

# UC Berkeley

## UC Berkeley Electronic Theses and Dissertations

### Title

A Micromechanical RF Channelizer

### Permalink

<https://escholarship.org/uc/item/5x25k2hw>

### Author

Akgul, Mehmet

### Publication Date

2014

Peer reviewed|Thesis/dissertation

# A Micromechanical RF Channelizer

By

Mehmet Akgul

A dissertation submitted in partial satisfaction of the  
requirements for the degree of

Doctor of Philosophy

in

Engineering – Electrical Engineering and Computer Sciences

in the

Graduate Division

of the

University of California, Berkeley

Committee in charge:

Professor Clark T.-C. Nguyen, Chair  
Professor Ming C. Wu  
Professor Liwei Lin

Fall 2014

Copyright © 2014, by the author(s).

All rights reserved.

Permission to make digital or hard copies of all or part of this work for personal or classroom use is granted without fee provided that copies are not made or distributed for profit or commercial advantage and that copies bear this notice and the full citation on the first page. To copy otherwise, to republish, to post on servers or to redistribute to lists, requires specific permission from the copyright holders.

## **Abstract**

### **A Micromechanical RF Channelizer**

by

Mehmet Akgul

Doctor of Philosophy in Engineering – Electrical Engineering and Computer Sciences

University of California, Berkeley

Professor Clark T.-C. Nguyen, Chair

The power consumption of a radio generally goes as the number and strength of the RF signals it must process. In particular, a radio receiver would consume much less power if the signal presented to its electronics contained only the desired signal in a tiny percent bandwidth frequency channel, rather than the typical mix of signals containing unwanted energy outside the desired channel. Unfortunately, a lack of filters capable of selecting single channel bandwidths at RF forces the front-ends of contemporary receivers to accept unwanted signals, and thus, to operate with sub-optimal efficiency.

This dissertation focuses on the degree to which capacitive-gap transduced micromechanical resonators can achieve the aforementioned RF channel-selecting filters. It aims to first show theoretically that with appropriate scaling capacitive-gap transducers are strong enough to meet the needed coupling requirements; and second, to fully detail an architecture and design procedure needed to realize said filters. Finally, this dissertation provides an actual experimentally demonstrated RF channel-select filter designed using the developed procedures and confirming theoretical predictions.

Specifically, this dissertation introduces four methods that make possible the design and fabrication of RF channel-select filters. The first of these introduces a small-signal equivalent circuit for parallel-plate capacitive-gap transduced micromechanical resonators that employs negative capacitance to model the dependence of resonance frequency on electrical stiffness in a way that facilitates the analysis of micromechanical circuits loaded with arbitrary electrical impedances. The new circuit model not only correctly predicts the dependence of electrical stiffness on the impedances loading the input and output electrodes of parallel-plate capacitive-gap transduced micromechanical device, but does so in a visually intuitive way that identifies current drive as most appropriate for applications that must be stable against environmental perturbations, such as acceleration or power supply variations. Measurements on fabricated devices in fact confirm predictions by the new model of up to 4× improvement in frequency stability against DC-bias voltage variations for contour-mode disk resonators as the resistance

loading their ports increases. By enhancing circuit visualization, this circuit model makes more obvious the circuit design procedures and topologies most beneficial for certain mechanical circuits, e.g., filters and oscillators.

The second method enables simultaneous low motional resistance ( $R_x < 130 \Omega$ ) and high  $Q$  ( $>70,000$ ) at 61 MHz using an improved ALD-partial electrode-to-resonator gap filling technique that reduces the  $Q$ -limiting surface losses of previous renditions by adding an alumina pre-coating before ALD of the gap-filling high- $k$  dielectric. This effort increases the  $Q$  over the  $\sim 10,000$  of previous renditions by more than  $6\times$  towards demonstration of the first VHF micromechanical resonators in any material, piezoelectric or not, to meet the simultaneous high  $Q$  ( $>50,000$ ) and low motional resistance  $R_x$  ( $< 200\Omega$ ) specs highly desired for front-end frequency channelizer requirements in cognitive and software-defined radio architectures. The methods presented in this chapter finally overcome the high impedance bottleneck that has plagued capacitively transduced micro-mechanical resonators over the past decade.

The third method introduces a capacitively transduced micromechanical resonator constructed in hot filament CVD boron-doped microcrystalline diamond (MCD) structural material that posts a measured  $Q$  of 146,580 at 232.441 kHz, which is  $3\times$  higher than the previous high for conductive polydiamond. Moreover, radial-contour mode disk resonators fabricated in the same MCD film and using material mismatched stems exhibit a  $Q$  of 71,400 at 299.86 MHz. The material used here further exhibits an acoustic velocity of 18,516 m/s, which is now the highest to date among available surface micromachinable materials. For many potential applications, the hot filament CVD method demonstrated in this work is quite enabling, since it provides a much less expensive method than microwave CVD based alternatives for depositing doped CVD diamond over large wafers (e.g., 8") for batch fabrication.

The first three methods described so far focus on a single vibrating disk resonator and improve its electrical equivalent modeling,  $C_x/C_0$ , and  $Q$ . Once we craft the resonator that meets the challenging design requirements of RF channel-select filters, the last method presents a design hierarchy that achieves the desired filter response with a specific center frequency, bandwidth, and filter termination resistance. The design procedure culminates in specific values for all mechanical geometry variables necessary for the filter layout, such as disk radii, and beam widths; and process design variables such as resonator material thickness and capacitive actuation gap spacing.

Finally, the experimental results introduce a 39nm-gap capacitive transducer, voltage-controlled frequency tuning, and a stress relieving coupled array design that enable a 0.09% bandwidth 223.4 MHz channel-select filter with only 2.7dB of in-band insertion loss and 50dB rejection of out-of-band interferers. This amount of rejection is more than 23dB better than previous capacitive-gap transduced filter designs that did not benefit from sub-50nm gaps. It also comes in tandem with a 20dB shape factor of 2.7 realized by a hierarchical mechanical circuit design utilizing 206 micromechanical circuit elements, all contained in an area footprint of only  $600\mu\text{m}\times 420\mu\text{m}$ . The key to such low insertion loss for this tiny percent bandwidth is  $Q$ 's  $>8,800$

supplied by polysilicon disk resonators employing for the first time capacitive transducer gaps small enough to generate coupling strengths of  $C_x/C_o \sim 0.1\%$ , which is a  $6.1\times$  improvement over previous efforts. The filter structure utilizes electrical tuning to correct frequency mismatches due to process variations, where a dc tuning voltage of 12.1 V improves the filter insertion loss by 1.8 dB and yields the desired equiripple passband shape. An electrical equivalent circuit is presented that captures not only the ideal filter response, but also parasitic non-idealities that create electrical feed-through, where simulation of the derived equivalent circuit matches the measured filter spectrum closely both in-band and out-of-band.

The combined 2.7dB passband insertion loss and 50dB stopband rejection of the demonstrated 206-element 0.09% bandwidth 223.4-MHz differential micromechanical disk filter represents a landmark for capacitive-gap transduced micromechanical resonator technology. This demonstration proves that the mere introduction of small gaps, on the order of 39 nm, goes a long way towards moving this technology from a research curiosity to practical performance specs commensurate with the needs of actual RF channel-selecting receiver front-ends. It also emphasizes the need for tuning and defensive stress-relieving structural design when percent bandwidths and gaps shrink, all demonstrated by the work herein.

Perhaps most encouraging is that the models presented in dissertation used to design the filter and predict its behavior seem to be all be spot on. This means that predictions using these models foretelling 1-GHz filters with sub-200 $\Omega$  impedances enabled by 20nm-gaps might soon come true, bringing this technology ever closer to someday realizing the ultra-low power channel-selecting communication front-ends targeted for autonomous set-and-forget sensor networks. Work towards these goals continues.

*Dedicated to my parents and my dear wife Hatice.*

*None of this would have been possible without their  
unconditional love and support.*

## Table of Contents

<b>CHAPTER 1 INTRODUCTION.....</b>	<b>1</b>
1.1 Conventional Wireless Receiver Design Architectures .....	2
1.1.1 The Superheterodyne Receiver .....	4
1.1.2 Direct Conversion Receivers .....	7
1.2 RF-Channel Selecting Front-Ends .....	8
1.2.1 Software Defined Cognitive Radio .....	10
1.3 A Review of Previous Vibrating Micromechanical RF Channel-Select Filter Efforts ..	12
1.3.1 Summary of Improvements to Previous Work by this Dissertation .....	13
1.4 Micromechanical Vibrating Disk Filter Design Basics.....	14
1.4.1 Contributors to Filter Insertion Loss.....	16
1.4.2 Filter Termination Impedance & Electromechanical Coupling Strength .....	19
1.5 High- $Q$ Micromachined Vibrating Resonators for Low Loss RF Channel-Selection ...	20
1.6 Dissertation Overview.....	22
 <b>CHAPTER 2 A NEGATIVE CAPACITANCE EQUIVALENT CIRCUIT MODEL FOR PARALLEL- PLATE CAPACITIVE-GAP TRANSDUCED MICROMECHANICAL RESONATORS.....</b>	 <b>25</b>
2.1 Negative Capacitance Equivalent Circuit .....	29
2.2 Negative $C_o$ Equivalent Circuit for a Capacitive-Gap Transduced Radial Contour Mode Disk.....	34
2.2.1 Design Example: 218-MHz Radial-Contour Mode Disk.....	36
2.3 Negative $C_o$ Equivalent Circuit for a Capacitive-Gap Transduced Wine-Glass Mode Disk.....	36
2.3.1 Core $LCR$ .....	38
2.3.2 Static Electrode-to-Resonator Overlap Capacitance.....	42
2.3.3 Electromechanical Coupling Factor.....	42
2.3.4 Motional Current.....	45
2.3.5 Electrical Spring Stiffness.....	46
2.3.6 Wine-Glass Disk Equivalent Circuit Summary .....	48
2.3.7 Design Example: 61-MHz Wine-Glass Mode Disk.....	49



	iii
2.4 Efficacy of the Equivalent Circuit: Theory vs. Measurement.....	50
2.4.1 Fabrication Process .....	50
2.4.2 Measurement and Simulation Circuits.....	52
2.4.3 Frequency Response versus DC-Bias .....	55
2.4.4 Frequency Response versus Resonator Port Resistance .....	56
2.4.5 Frequency Versus DC-Bias, Termination Resistance, and Electrode-to-Resonator Gap Spacing .....	58
2.4.6 Electrode-to-Resonator Gap Extraction.....	61
2.4.7 Effect of Parasitic Trace and Bond-Pad Capacitance .....	62
2.5 Impact on Applications .....	66
2.5.1 Reference Oscillator Design Insights.....	66
2.5.2 Device Design Insights .....	66
2.6 Conclusions on the Negative-Capacitance Equivalent Circuit Model.....	67

**CHAPTER 3 CAPACITIVELY TRANSDUCED MICROMECHANICAL RESONATORS WITH SIMULTANEOUS LOW MOTIONAL RESISTANCE AND  $Q > 70,000$ ..... 68**

3.1 Introduction .....	68
3.2 Methods to Improve the Electromechanical Coupling of Capacitive Actuated Vibrating Disk.....	71
3.3 ALD Partial Electrode-to-Resonator Gap Filling Technique.....	74
3.4 Improving ALD Film Quality .....	76
3.5 ALD Partial Gap Filling Process Flow .....	78
3.6 Experimental Results.....	81
3.6.1 Effect of Parasitic Resistance on Resonator $Q$ .....	82
3.6.2 Extraction of the gap spacing $d_o$ .....	83
3.7 Oscillator Far-from-Carrier Phase Noise Reduction via Nano-Scale Gap Tuning of MEMS Micromechanical Resonators .....	84
3.7.1 Oscillator Phase Noise .....	85
3.7.2 ALD Partial Gap Filling for Stronger Power Handling.....	87
3.7.3 Experimental Results .....	88
3.7.4 Oscillator Design Insights via ALD Gap Scaling Technique .....	92
3.8 Conclusion.....	93

<b>CHAPTER 4 HOT FILAMENT CVD CONDUCTIVE MICROCRYSTALLINE DIAMOND FOR HIGH Q, HIGH ACOUSTIC VELOCITY MICROMECHANICAL RESONATORS.....</b>	<b>94</b>
4.1 Introduction .....	94
4.2 High Quality Factor and Acoustic Velocity Advantage of CVD Polydiamond .....	96
4.3 Polydiamond Deposition Techniques.....	97
4.4 Hot Filament CVD Polydiamond for High $Q$ Low Frequency Micromechanical Combdrive Resonators .....	99
4.4.1 Two-Mask HFCVD Polydiamond Fabrication Process.....	100
4.4.2 Measurement Results .....	102
4.4.3 HFCVD Diamond Recipe Optimization.....	104
4.5 Hot Filament CVD Polydiamond for High $Q$ & High Frequency Micromechanical Disk Resonators .....	107
4.5.1 Material Mismatched Stems for Suppressing Anchor Loss.....	108
4.5.2 Five-Mask Fabrication Process for High Frequency Contour Mode Micromechanical Disk Resonators.....	110
4.5.3 Measurement Results .....	113
4.5.4 Finite Element Analysis of Acoustic Impedance Mismatched Stems .....	114
4.6 Conclusion.....	118
<b>CHAPTER 5 PASSBAND-CORRECTED HIGH REJECTION RF CHANNEL-SELECT MICROMECHANICAL VIBRATING DISK FILTERS.....</b>	<b>120</b>
5.1 Introduction .....	120
5.2 Filter Design Specifications .....	124
5.3 Needed $Q$ and Coupling .....	125
5.3.1 Needed Quality Factor .....	126
5.3.2 Needed Electromechanical Coupling Strength .....	128
5.4 Simplified Description of the Vibrating Disk Filter Operation.....	130
5.5 Actual Filter Structure and Operation .....	135
5.6 Detailed Filter Design .....	137
5.7 Radial Contour-Mode Disk Design.....	138
5.8 Disk Array-Composite Design.....	141
5.8.1 Array-Composite Equivalent Circuit .....	144

5.8.2	Array-Composite Motional Resistance.....	145
5.8.3	Array-Composite Power Handling .....	146
5.8.4	Array-Based Mechanical Impedance Tailoring .....	147
5.8.5	Non-I/O Disks .....	148
5.9	Minimum Electromechanical Coupling Strength for the Chosen Bandwidth.....	148
5.10	Filter Passband Specification.....	149
5.10.1	Electrical Equivalent Circuit of $\lambda/4$ Coupling Beams .....	150
5.10.2	$\lambda/4$ Coupling Beam Width & Array Size .....	151
5.11	Differential Mechanical Design.....	153
5.11.1	Differential Filter Structure Design Summary .....	156
5.12	Filter Electrical Equivalent Circuit Model .....	156
5.13	Summary of Filter Design Procedure and Equations .....	157
5.13.1	Filter Design Examples .....	158
5.14	Conclusion .....	159
<b>CHAPTER 6 PRACTICAL FILTER IMPLEMENTATION &amp; EXPERIMENTAL RESULTS .....</b>		<b>160</b>
6.1	Introduction .....	161
6.2	Defensive Design against Film Stress .....	163
6.3	Electrical Equivalent Circuit with Parasitic Elements & Modeling Electrical Feedthrough .....	164
6.3.1	Filter Electrical Equivalent Circuit with Parasitic Elements .....	165
6.3.2	Filter Design Insights from Inspection of the Electrical Equivalent Circuit .....	167
6.4	Electrical Stiffness Tuning of Frequency Mismatches .....	170
6.5	Design Parameters for the Fabricated 224 MHz, 0.1% Bandwidth Channel-Select Filter	171
6.6	Fabrication Process .....	173
6.7	Measurement Results .....	176
6.7.1	Verification of $\lambda/2$ Coupled Array-Composite Operation .....	177
6.7.2	Terminated and Electrically Tuned Filter Spectrum.....	178
6.7.3	Comparison of Measured & Simulated Results.....	180
6.7.4	Measured Comparison of Differential & Single-Ended Filters .....	181
6.8	Electrical Stiffness Tuning Strategy.....	182

	vi
6.9 Filter Power Handling Capability and Linearity .....	183
6.10 Conclusion .....	185
<b>CHAPTER 7 CONCLUSIONS.....</b>	<b>186</b>
7.1 Achievements .....	186
7.2 Future Research Directions .....	188
<b>REFERENCES.....</b>	<b>190</b>
<b>APPENDIX A THICK-POLY INTERCONNECT FABRICATION PROCESS TRAVELER .....</b>	<b>198</b>

## Acknowledgments

I would like to convey my gratitude to all of the wonderful people who shared with me not only their technical insight, but also their friendship and company throughout the seven years we spent together at UC Berkeley. Your presence made the journey as interesting and enjoyable as the destination that this dissertation culminates.

First of all, I would like to thank my research adviser Prof. Clark T.-C. Nguyen for his continued support in my growth as a researcher in the RF MEMS field. His advisement provided freedom in the way I conducted research and managed my time that allowed me to build my independence and confidence; but also provided feedback and guidance in every little step of the way, for which I am very grateful. Perhaps the most important thing I learned from him is the importance of paying attention to detail in everything I do, not necessarily in research but in all aspects of life. The results presented in this dissertation are possible thanks to him sharing his vision and prowess of the RF MEMS field with me and my colleagues. Certainly, the field will advance and the results presented in this dissertation will not be as exciting and relevant as they are today in the near future. However, learning how to identify the important aspects of a complex looking problem using a disciplined mind, and never to shy away from trying the seemingly impossible from Prof. Nguyen will stay with me for the rest of my career.

I also would like to thank Prof. Ming Wu, Prof. Liwei Lin, and Prof. Elad Alon for serving on my qualifying exam committee and reviewing my dissertation. Their feedback improved the quality of my research and this dissertation.

I was blessed with numerous mentors throughout my PhD. I would like to especially thank to Dr. Bongsang Kim for sharing his experience and knowledge with me when I first started my studies at UC Berkeley, and I still cherish his friendship today. He generously shared his expertise in microfabrication, automated measurement setups, and general advice that was very valuable. I am also indebted to Zeying Ren, who not only shared her expertise on the specific processes our group runs with me, but also has been a valuable friend during the long days in the cleanroom. Her cheerful attitude was a constant support to me during my PhD. I thank Dr. Tommi Riekkinen for sharing his knowledge in metallurgy and metal MEMS structures, and the fun he brought to the group picnics we had. I also would like to thank Dr. Tristan Rocheleau for teaching me how to design elaborate custom measurement setups and how to work with the practical aspects of experiment design, such as working with machine shops and procuring the right parts by designing everything meticulously and well in advance. Discussions with him on how to fabricate and measure the structures presented in this dissertation has been very valuable.

I thank the Berkeley Nanolab staff for continuously doing their best to upkeep the lab. I especially thank Dr. Bill Flounders, Ryan Rivers, and Jay Morford for helping me maintain the polydi- amond tool that played an important role in my PhD. And Joe Donnelly and Rich Hemphill were

always very kind and available to fix the CMP tools, etchers, and furnaces that somehow seem to go down right before the important deadlines.

I am proud to be a BSAC member, and I thank the BSAC co-directors, John Huggins, and the BSAC staff for keeping a tradition going forward with momentum over the years. Their efforts made sure our research is well exposed to the MEMS industry via the semi-annual IAB meetings. I would like to thank Helen Kim for shielding us from the bureaucracy and paperwork with great enthusiasm, and for being so understanding and friendly all the time. Richard Lossing and Kim Ly also deserve special thanks for making sure the IAB experience went as close to perfect as possible every single time.

Financial support from the DARPA CSSA program for most of the work presented in this dissertation is also gratefully acknowledged.

I cherish all my friends that I acquainted during my PhD at UC Berkeley. Berkeley is known for its colorful personalities, out of the box thinking, and a unique and dynamic way of life. These traits definitely reflected in all the people I had the chance to work with in our group. The sense of solidarity and support we shared during the all-nighters we had to pull before paper submission deadlines, and the lively discussions we had when we were faced with a challenging research problem made it a lot easier to believe that our collective efforts will succeed. I would like to thank Yang Lin, Wei-chang Li, Ashkan Borna, Thura Lin Naing, Turker Beyazoglu, Alper Ozgurluk, Robert Shneider, Henry Barrow, Linqi Wu, Jalal Nilchi, Ruonan Liu, and numerous others that are too many to name here. I hope to continue my friendship with all of these wonderful people in the years to come.

I thank my parents with endless gratitude for their love and support through all my life. I would not be able to finish my PhD without their continuous belief in me. Finally, I thank my wife Hatice for her unconditional love and encouragement. Her love and presence in my life puts everything else into perspective, and turns everything into a more enjoyable and meaningful experience.

# *Chapter 1*

## *INTRODUCTION*

---

---

Wireless communications has become an integral part of our daily lives, and revolutionized this century by fundamentally changing the way we connect to each other with unprecedented ease and speed. Today we expect all of the gadgets that make our lives easier to connect with each other and create a hive mind, and bring us copious amounts of information on topics ranging from real time traffic conditions as we commute to work, to air quality monitoring information collected from autonomous wireless motes spread over hundreds of miles. Information is the fuel that the modern society runs on, and enabling masses with easy access to free flow of information with a simple tap on a smart phone is a game changer that will snowball into even more acceleration for innovation.

Of course, trying to scale connectivity on such a massive scale using wired networks would be highly impractical, and it is no coincidence that the rise of today's information society coincides with the emergence of low cost and reliable wireless technologies. Since Marconi performed the landmark experiment that sent messages wirelessly over the English Channel in 1897, the way we build radios improved continuously due to a strong demand from numerous markets. Research on radars and microwave theory has been at the very center of our technological advances in particular during WWI and WWII. The following advances in transistor technology and RF circuit fabrication driven by scaling have continuously reduced the cost, power consumption, and area footprint of transceivers to eventually bring the ubiquitous use of voice telephony and wireless internet access to the back pockets of more than a billion users worldwide.

The adoption of wireless technologies at such a staggering pace; however, brings certain challenges with it. The wireless spectrum is a shared and limited resource, and it is already crowded and tightly regulated to ensure various technologies can coexist without compromising the quality of service of each other. The conventional way we have been building our radios to operate in a statically assigned band, where one's transmission acts as a strong blocker for devices operating

in adjacent channels, does not easily scale to accommodate the ever-increasing number of users that compete over the same spectrum. There are numerous efforts to address this problem by increasing the spectral efficiency of radios using both software techniques, such as by using compression or spread spectrum coding techniques like CDMA [1]; and by improving hardware to use available spectrum most effectively, such as spectrum sensing cognitive radios [2]. Here, the radio hardware improvements play a much more important role in increasing the reliability of the communication channel, as well as introducing drastic changes to reduce the cost and power consumption of transceiver systems.

## 1.1 Conventional Wireless Receiver Design Architectures

Wireless transceivers are designed to transmit and receive signals over a frequency band allocated for a specific transmission protocol within a spectrum crowded with many other strong interfering signals, some, in fact, may be actively trying to disrupt communications by jamming. As Figure 1.1 describes, the transceiver consists of two main paths, a receiver path to sense incoming data, and a transmit path to broadcast information. The transmitter performs modulation of baseband data, and up-converts it to transmission frequency with a high frequency carrier and uses a power amplifier to send the signal with a controlled dynamic range, where transmit filters that precede the antenna prevent leakage to adjacent channels as tightly regulated by wireless transmission protocols.

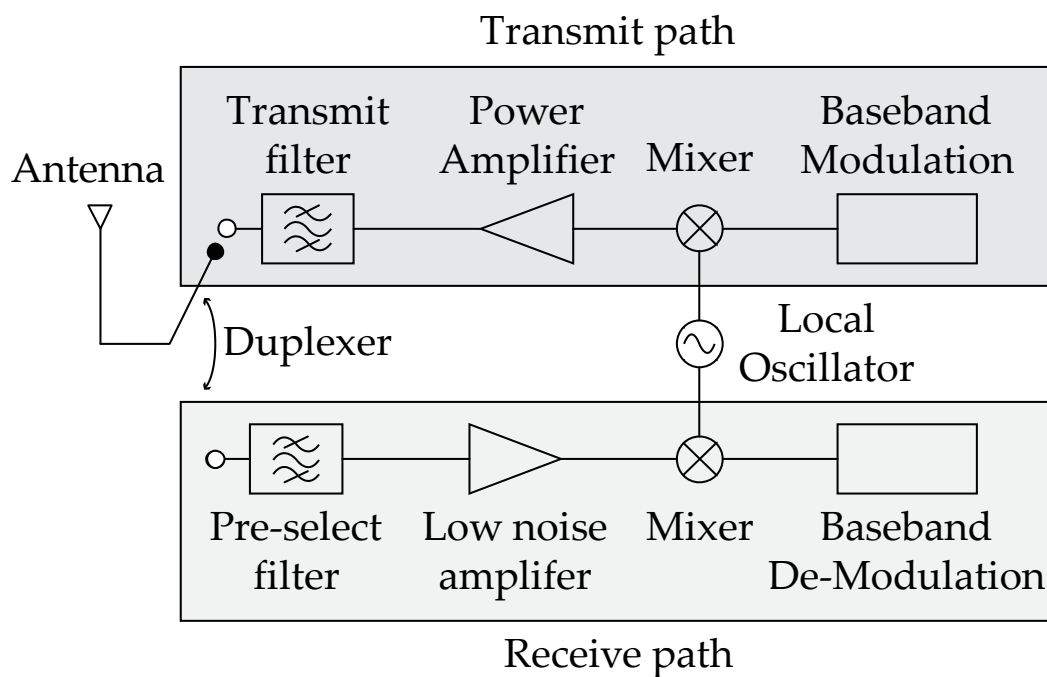


Figure 1.1: Simplified schematic of a conventional transceiver that identifies the transmit and receive paths.



In contrast, the receiver must be able to sense the desired signal while suppressing unwanted signals, such as interference. Unlike the transmitter, the receiver does not have active control over the dynamic range of the received signal power, where communication standards define the operating conditions that the receiver is expected to perform. The power difference between the desired signal and the unwanted blockers that falls in the vicinity of the desired communication frequency can be as high as 100dB, e.g. as in the 3G GSM specification [3]. In addition to handling the high power dynamic range, the receiver sensitivity, which defines the minimum detectable signal level over input referred noise figure of the receiver that enables reliable demodulation of the information, poses another challenge. Therefore, the receiver architecture is more demanding to optimize compared to a transmitter due to challenges posed by noise, interference rejection, high dynamic range, and frequency selectivity.

Among various receiver architectures that employ creative methods to mitigate these challenges, the superheterodyne [4] and direct conversion [5] architectures are the most widely used ones due to their distinctive advantages. The direct conversion receiver, also known as zero-IF, uses the simplest method capable of demodulating the received signal by directly converting it to the baseband, where a low-pass filter recovers the original signal. However, this seemingly simple scheme has major design challenges due to dc-offsets stemming from local oscillator leakage from the mixer and  $1/f$  noise of the baseband electronics, and has only recently become popular in contemporary receiver handsets once recent advances in RFIC design tackled these challenges. In comparison, the super heterodyne receiver relaxes these issues by introducing the intermediate frequency, commonly referred as IF, concept that improves the robustness of the receiver significantly at the expense of increased number of components, and thus cost. Instead of down-converting the received signal directly to the baseband, the superheterodyne receiver first mixes the input signal to IF, where it performs channel-selection by using a filter with narrow enough bandwidth to eliminate all blockers, which eliminates high dynamic range burden for the succeeding demodulation electronics. Despite using more off-chip components, primarily the bulky IF channel-select filter, the performance requirements for the superheterodyne receiver is in fact easier to realize compared to the direct receiver. In addition, superheterodyne achieves better dynamic range performance than that of the direct conversion architecture.

The following sections will describe the basic details of these two architectures as case studies and identify the primary issues that pose bottlenecks for further performance improvements. Finally, a novel, single-chip, low cost and low power MEMS-based RF front-end architecture will be presented that improves over these conventional methods by eliminating off chip passives that pose the fundamental size and performance improvement bottlenecks for future multi-band receiver architectures.

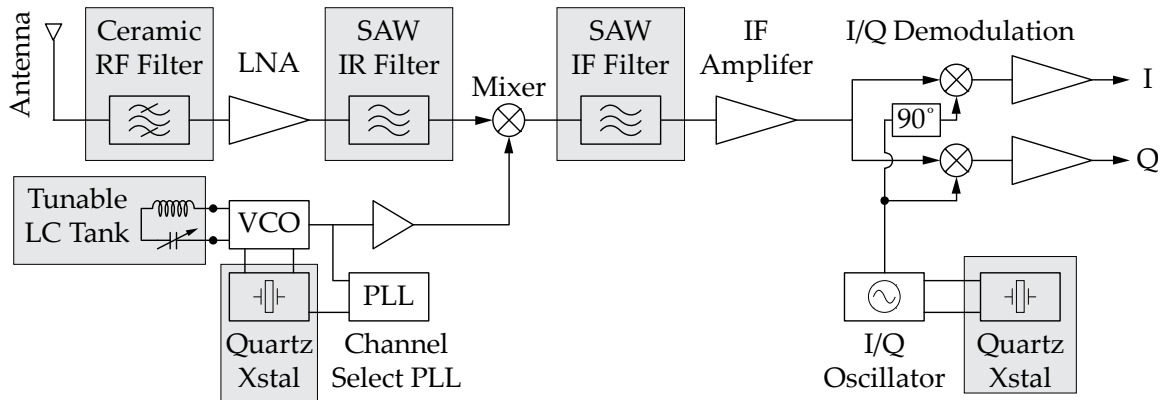


Figure 1.2: Schematic description of a conventional superheterodyne receiver diagram. The highlighted elements indicate off-chip components that pose a bottleneck for miniaturization, parasitic elimination and cost reduction.

### 1.1.1 The Superheterodyne Receiver

The superheterodyne receiver was originally designed by Edwin Armstrong [4] during WWI to overcome the poor RF performance of vacuum triodes as high frequency amplifiers used in radars by implementing channel selection at low IF frequency, where design requirements for very narrow bandwidths capable of selecting individual channels is much more relaxed compared to that of RF channel-select filters. Initial implementations used self-resonance of iron core coupling transformers to filter the IF frequency, which implemented the characteristic IF channel-selection operation of superheterodyne receivers performed by low frequency tuned circuits to ease the high dynamic range burden imposed by strong interferers for the demodulation circuitry that follows the IF stage.

Figure 1.2 schematically describes a conventional superheterodyne receiver, where the RF pre-select filter placed directly after the antenna performs band-selection to remove interferers that fall outside its bandwidth. However, the information bandwidth of the desired signal is still a fraction of this wideband filter and close-to-carrier interferers also pass to the succeeding stages since the pre-select filter fails to perform channel-selection directly at RF, i.e. to achieve a narrow enough bandwidth for selecting *only* the frequency of interest and rejecting everything else. The received desired signal is typically very low in power as it weakens due to path losses across the transmission distance (unlike interferers that can be coming from much nearer transmitters), and also to save power at the transmitter end of the communication channel.

The noise performance of the amplifier that follows the pre-select filter is of critical importance for good receiver sensitivity, because the noise performance of the components that precede the initial high gain elements primarily determine the overall noise figure of the receiver. Friis' formula calculates the input referred noise figure of a system consisting of cascaded stages like filters, amplifiers, mixers, etc. to form a receiver, such as the one depicted in Figure 1.2, given by [6]

$$F = F_1 + \frac{F_2 - 1}{G_1} + \frac{F_3 - 1}{G_1 G_2} + \dots + \frac{F_n - 1}{G_1 G_2 \dots G_{n-1}} \quad (1.1)$$

where  $F_i$  and  $G_i$  represent the noise factor and gain for stage  $i$ , respectively. Inspection of this expression clearly identifies the critical importance of the first two terms that dominate the overall receiver noise factor  $F$  assuming the first amplifier has high gain  $G_1 > 10$ , so that the noise contribution from stages following the first antenna gets suppressed. This amplifier is called a low noise amplifier, commonly referred to as LNA, with special attention paid during its design to minimize its noise figure to amplify the pre-select filtered signals with little noise added.

Clearly, all filters preceding the LNA should have very low insertion loss, because the noise figure of a passive system equals its insertion loss. A high pre-select filter insertion loss would increase the  $F_1$  term in (1.1), and thus directly add to the noise figure of the receiver. This observation is key to understand why current receiver designs have to be contented with band-select filters at the RF front-end that have bandwidths wider than that is actually needed to select only the frequency channel of interest, and thus allow undesired interferers through, as well. As it will be the primary focus of this thesis, true RF channel-select filters that can realize the very narrow bandwidths capable of selecting individual channels right at RF frequencies require resonator technologies with quality factors exceeding 30,000. Indeed, capacitive transduced micromechanical disk resonators demonstrated such high  $Q$ 's and constantly improve other design variables, such as electromechanical coupling and motional resistance, to potentially realize RF channel-selection. Nonetheless, currently commercialized resonator technologies, such as FBARs [7] or quartz crystals [8] fall rather short of such high  $Q$ 's at GHz frequencies. Therefore, filter designers compromise the filter bandwidth to achieve acceptably low filter insertion loss, as seen in the widely used RF duplexers [9] used for RF pre-selection in modern transceivers.

After the LNA boosts the received signal level, an image reject (IR) filter removes the image signal [6] to prevent down-converting both the desired signal and its image to the same IF frequency during the following mixing operation. The desired signal and its image are separated by  $2 \times f_{IF}$  in the frequency domain, where  $f_{IF}$  is the chosen IF frequency. This creates a trade-off between design parameters of the image reject (IR) filter that operates at the RF frequency and the IF filter that operates at a much lower frequency. Choosing a low  $f_{IF}$ , referred to as low IF receivers, makes it much easier to design a channel-select filter at the low IF frequency using low- $Q$  resonators. However, the reduced frequency separation between the desired signal and its image band requires the image reject filter to have a narrower bandwidth and sharper roll-offs to sufficiently suppress the image signal at RF frequencies, which is a challenging task for conventional filters. Once more, the ability to realize narrow-band filters at RF frequencies as a highly desired design tool emerges clearly. However, lacking the required currently commercially available RF frequency high- $Q$  resonators, the system designer makes a compromise between the IR filter design specifications and the IF operation frequency to ensure sufficient image rejection before mixing.

After solving the image frequency problem via the IR filter, the mixer down-converts the signal frequency to IF using a local oscillator (LO) signal generated by a voltage controlled oscillator (VCO) controlled by a phase locked loop system (PLL) that is referenced to a lower frequency, but very low phase noise mechanical quartz crystal oscillator. Quartz crystal oscillators provide a very stable output with impressive phase noise performance to provide a frequency reference that is resilient to aging and temperature changes. However, they are off-chip components with a large area footprint, and their frequency range is typically limited to 10-20 MHz, which is too low for mixing the RF signal down to IF. Therefore, the PLL locks into the low phase noise reference of the quartz crystal to suppress the phase noise of the much higher frequency VCO that serves as the mixing tone that down-converts the desired signal to IF. The PLL also provides a flexible and wide tuning range for the mixing LO frequency, which allows using a constant IF frequency regardless of the RF signal frequency. Otherwise, a constant LO frequency would require an IF filter tunable over a wide frequency range, which would be a challenging design for the high order filters required to achieve sharp stop-band roll-offs required from the IF filter. However, the reduced LO phase noise and tuning range benefits provided by the PLL comes with a hefty power consumption penalty that typically comprises a major portion of the overall power consumption of the receiver.

Once again, if channel-selection directly at RF were possible to remove all blocker signals right after the antenna, a much higher phase noise VCO signal would be sufficient for mixing, and eliminate the design complexity and high power consumption that the PLLs require [10]. After the down-conversion mixer, a passive off-chip high order filter operating at the IF frequency with very sharp stop-band roll-offs and high stop-band rejection performs channel selection to eliminate undesired out-of-channel blockers and decreases the dynamic range requirement of the following I/Q demodulation circuitry.

As a second best alternative to RF channel-selection that eludes the quality factor performance of commercially available on-chip resonators, the superheterodyne receiver uses channel-selection at IF to create a robust receiver that performs well even when strong blockers interfering with the desired signal are present. As a result, it has found use in virtually all modern receiver systems until the recent popularity of the direct conversion architecture that reduces the number of components in the receiver chain, i.e. cost at the expense of increased design complexity. The robustness that stems from the multiple off-chip filters placed along the receiver chain as shown by the shaded elements in Figure 1.2; however, increases the number of components and area that raises the cost of the receiver. Furthermore, the input and output ports of these off-chip filters require impedance matching to maximize power transfer between the elements linked to them, unlike single-chip integrated components that can work with higher impedances without worrying about transmission line effects due to the orders-of-magnitude smaller compactness of connected components. Moreover, receiver architectures aiming to support multiple transmission standards like GSM, CDMA, etc. simultaneously require more of such off-chip filters to be able to operate at different frequency bands. Clearly, these off-chip components pose a bottleneck in miniaturization, power reduction, and production cost of next generation multi-mode receivers.

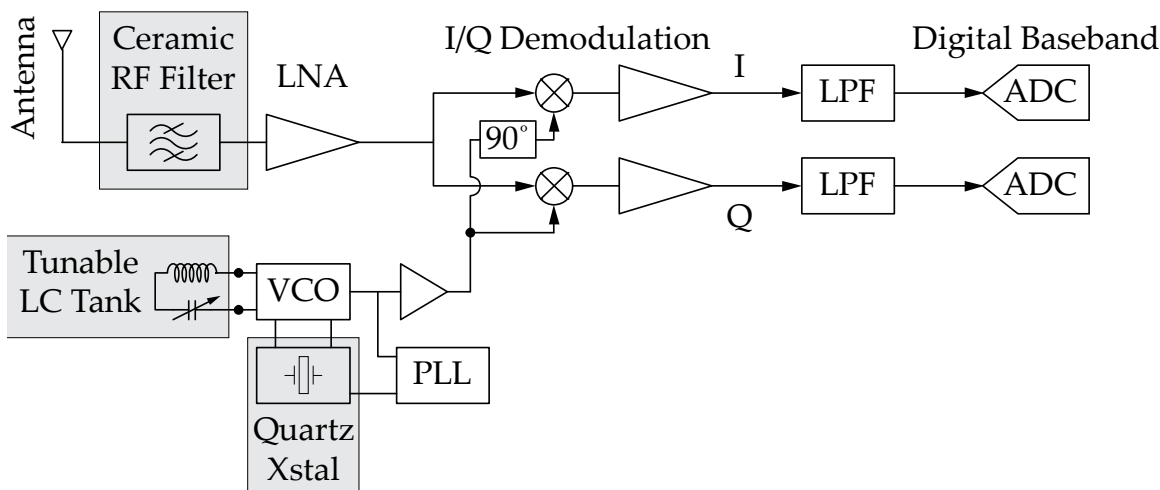


Figure 1.3: Schematic description of a conventional direct-conversion receiver diagram. The highlighted elements indicate off-chip components that pose a bottleneck for miniaturization, parasitic elimination and cost reduction.

### 1.1.2 Direct Conversion Receivers

The superheterodyne receiver explained in the previous section revolutionized receiver design by introducing the IF channel-selection concept that modulates the RF signal to a much lower frequency for easier signal processing; but at the expense of increased number of components, cost, and design complexity. The direct receiver architecture goes one more step ahead and asks the question “what would happen if we down-convert the RF signal even further from low-IF to DC?” The direct receiver architecture is commonly referred to as the zero-IF receiver for this reason. Since the LO and RF frequencies match in the zero-IF scheme, there is no image frequency problem and thus no need for an image-reject filter between the LNA and the mixer. As a result, the LNA drives only on-chip loads, typically the input stage of the mixer with relatively high impedance. Therefore, the output impedance of the LNA does not need to be  $50\Omega$ , since impedance matching to off-chip IR filters is eliminated, which relaxes the design requirements of the LNA and the mixer significantly.

Figure 1.3 presents the schematic diagram for a typical direct-conversion receiver, where the highlighted building blocks indicate the off-chip components. Here, the preselect filter is the only filter in the receive path that cannot be on-chip integrated with contemporary resonator technology. Compared to the superheterodyne receiver illustrated in Figure 1.2 that requires three off-chip filters, the direct conversion receiver achieves significantly better integration that makes it more suitable for today’s multi-mode receiver handsets. In fact, the lower cost and smaller form factor advantages make the direct conversion receiver the most widely used architecture in conventional receiver design. However, these benefits trade-off design complexity and challenges that include high sensitivity to dc offsets, I/Q mismatch, even order distortion, and baseband  $1/f$  noise [6].

The direct conversion receiver minimizes the need to interface to off-chip components, and thus saves power compared to the superheterodyne receiver with multiple off-chip filters. On the other hand, the superheterodyne receiver performs signal processing at a much lower frequency at IF that consumes less power compared to the processing performed at RF for the zero-IF receiver. In addition, eliminating the IF-channel select filters significantly increases the dynamic range that the baseband has to handle for the direct conversion receiver, which increases the linearity and power consumption. Therefore, both receiver architectures experience bottlenecks that prevent them from achieving very low receiver power consumption. Furthermore, both architectures require an off-chip RF duplexer after the antenna, and a high- $Q$  external crystal for a stable and low phase noise frequency reference, both of which impose area and cost penalties. In order to achieve a single-chip multi-mode ultra low power receiver, an architecture that uses on-chip high- $Q$  passives towards enhancing the robustness and power efficiency of the complete receiver chain is needed.

## 1.2 RF-Channel Selecting Front-Ends

The power consumption of a radio generally goes as the number and strength of the RF signals it must process [10]. In particular, a radio receiver would consume much less power if the signal presented to its electronics contained only the desired signal in a tiny percent bandwidth frequency channel, rather than the typical mix of signals containing unwanted energy outside the desired channel that may be much stronger than the desired signal, e.g. by 70dB for the W-CDMA standard

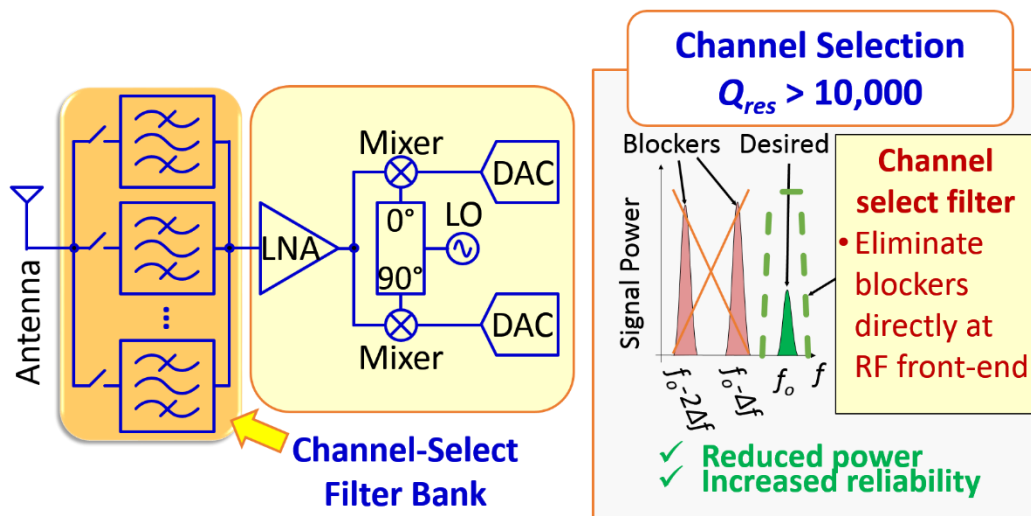


Figure 1.4: Proposed RF channel-select filter bank architecture that eliminates blockers directly at RF front-end right after the antenna. Therefore, electronics working at RF frequency, e.g. LNA, mixers, etc. have reduced dynamic range requirements with lower power consumption.

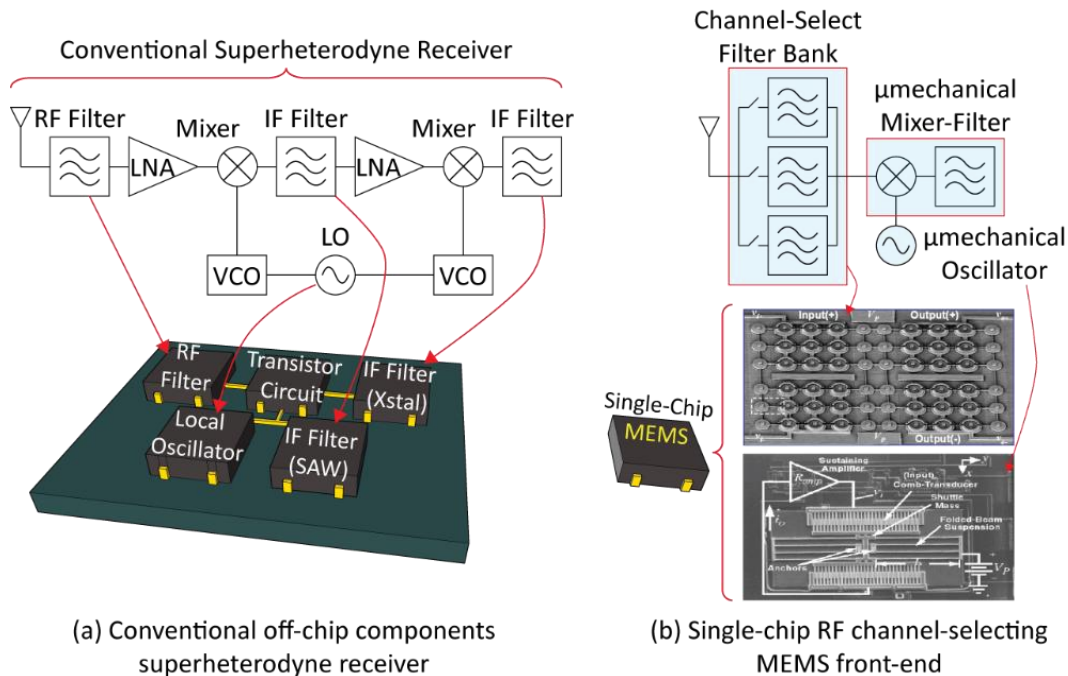


Figure 1.5: (a) The standard superheterodyne architecture with multiple off-chip components. (b) MEMS based RF channelizer single-chip front-end architecture.

[3]. Unfortunately, a lack of filters capable of selecting single channel bandwidths at RF forces the front-ends of contemporary receivers to accept unwanted signals, and thus, to operate with sub-optimal efficiency.

Figure 1.4 presents an alternative receiver architecture with an RF channel-selecting front-end filter bank. Here, a parallel bank of filter capable of selecting individual frequency channels matching the desired information bandwidths for various communication standards come right after the antenna. The key goal here is to select just the signal of interest and eliminate all the unwanted blockers, and thus the dynamic range they impose, before any further signal processing down the receiver chain occurs. If channel-selection occurs directly at RF frequencies as proposed in Figure 1.4, rather than just at IF as in the superheterodyne receiver, electronics blocks working at RF frequencies would no longer need to handle the power of alternate channel interferers, which would enable significant power reductions and a much more robust receiver. This proposed receiver topology uses an abundance of micromechanical circuits to realize an RF-channelizer [10], an IF mixer+filter [11], and stable LO synthesizers [12] by taking advantage of the small footprint and low cost of MEMS technology. Unlike the superheterodyne architecture that is bogged with multiple high cost off-chip components as illustrated in Figure 1.5(a), a large number of on-chip high- $Q$  vibrating micromechanical signal processors, *cf.* Figure 1.5(b), can potentially enable a low cost multi-mode receiver very extremely low power consumption. In this way, the high quality factor, stability, small size, and low cost of these devices enable a paradigm shift in transceiver design.

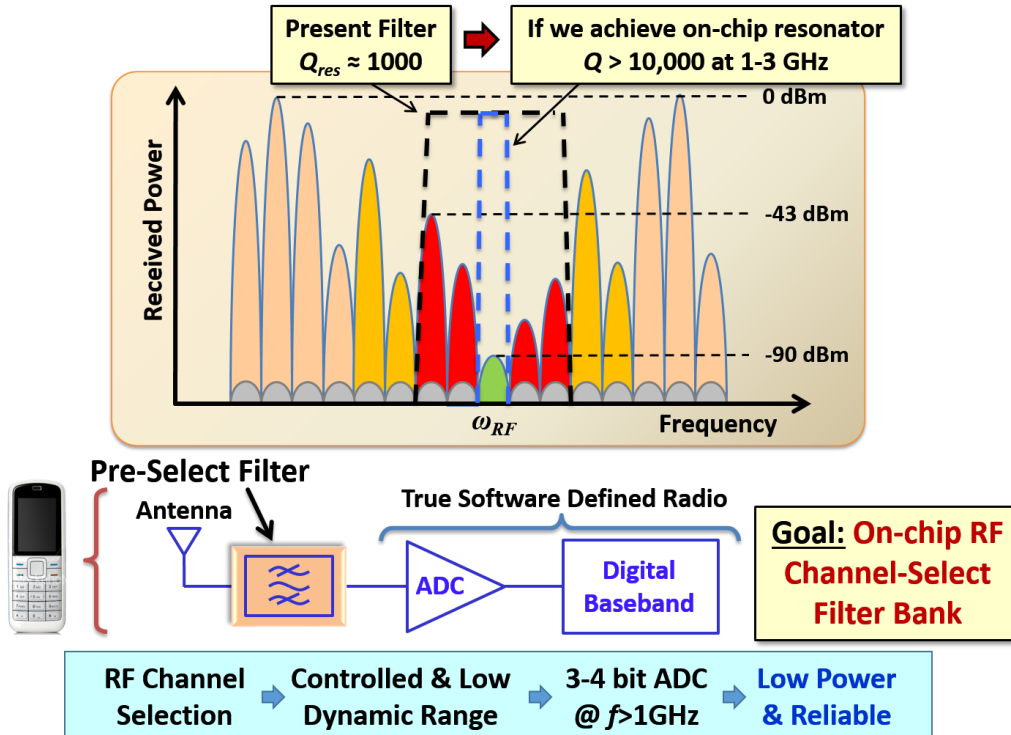


Figure 1.6: A software defined radio architecture operating in a GSM-like spectrum. The bandwidth of the pre-select filter determines the dynamic range the ADC must handle, where RF channel-selection enables practical ADC designs with low power consumption.

### 1.2.1 Software Defined Cognitive Radio

Reconfigurable radios capable of adapting to any communication standard at any location worldwide is of great interest, and is commonly referred as software defined radio (SDR) [13][14], which produces the frequencies and modulation schemes of any existing communication standard in real time by simply using an appropriate software implementation. The ideal rendition of such a radio would digitally realize all radio functions, including the RF front-end, using a programmable microprocessor, e.g. an FPGA. Towards performing as much signal processing as possible digitally, the ADC that normally resides near the baseband circuits of a conventional receiver would need to be placed as close to the antenna as illustrated in Figure 1.6. Practically, a frequency gating function must precede the ADC to remove blockers (i.e., out-of-channel interferers) that can be many orders stronger than the desired signal at the receive antenna [3]. For reasonable ADC power consumption, all blockers, even those within its communication standard's band very close to the desired channel must be removed. Removing such blockers relaxes the ADC's dynamic range and power requirements, which otherwise would be too excessive for portable applications.

Figure 1.7 conveys the importance of filtering out interferers before they reach the ADC input, by summarizing the SNR and the consequent power consumption requirement for an ADC with 3 GHz bandwidth, i.e. 6 GHz sampling rate, to digitize to complete RF spectrum directly after the



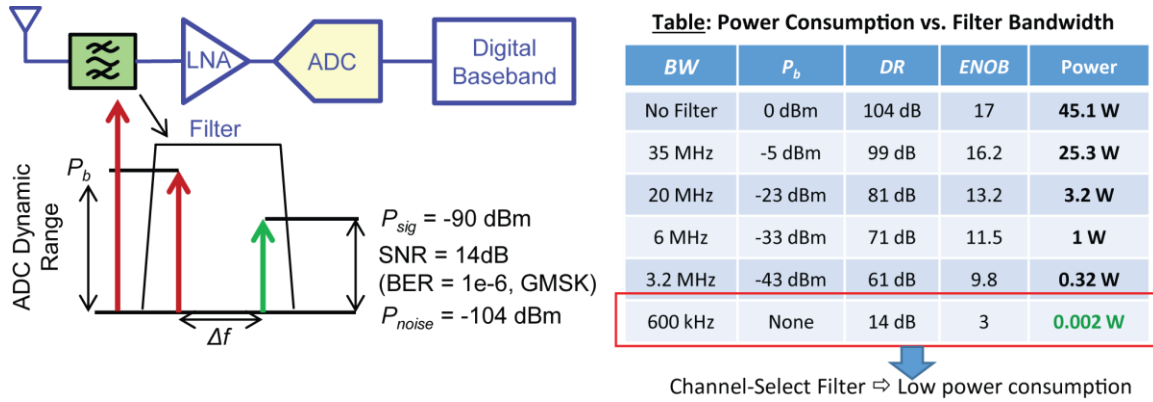


Figure 1.7: Power consumption as a function of dynamic range for an ADC designed to sample a 3GHz-wide RF spectrum assuming an SDR in a blocker environment identical to that assumed by the GSM standard.

antenna. A state-of-the-art ADC published by [15] that achieves an impressively low figure-of-merit 58 fJ/conversion is used for the power consumption calculations. The analysis assumes a GSM-like blocking scenario with an input sensitivity requirement of  $-104$  dBm in a 200 kHz bandwidth [16]. With no RF front-end filtering, the 0 dBm out-of-band blockers assumed in the GSM standard [16] demand an ADC dynamic range of  $DR = 104$  dB. This dynamic range would correspond to an equivalent number of bits (ENOB) of 17 according to

$$DR = 6.02 \times ENOB + 1.76dB \quad (1.2)$$

The power consumed by 16 17-bit ADC using the  $FOM = 58$  fJ/conversion with  $f_s = 6$  GHz sampling rate can be approximated by

$$Power = f_s \times FOM \times 2^{ENOB} \quad (1.3)$$

that demands 45.1 W power consumption. Clearly, this would be excessive power consumption even for a table-top receiver setup and definitely impossible for a mobile receiver. Decreasing the bandwidth of pre-select filter suppresses more interferers and relaxes the dynamic range of the ADC. As Figure 1.7 shows, however, even the 35 MHz bandwidth of a conventional duplexer filter widely used in receivers today is still grossly insufficient for low power portable software defined radio since the interferers impose 25.3 W power consumption.

As Figure 1.7 shows, low ADC power consumption on the order of 2 mW is only achieved when the filter bandwidth corresponds to that needed to eliminate all interferers. i.e., by selecting the desired channel and only this channel. For GSM, emissions are regulated such that each 200 kHz information bandwidth allocated in any time division multiple access (TDMA) slot has 200 kHz guard-bands around it. Therefore, a filter bandwidth of 600 kHz operating at 1800 MHz carrier, i.e. 0.03% fractional bandwidth, would be necessary to achieve RF channel-selection that reduces the ADC power consumption by four order-of-magnitude compared to the no-filtering case. Here, rather than relying on a single very narrow band filter to sweep a much wider band, a

bank of RF channel-select filters in parallel, *cf.* Figure 1.4, solves the impractically high sweeping time and the tuning range requirements. Depending upon the standard, this could involve hundreds of filters in parallel, which would be an irrational design if today's off-chip macroscopic filters were to be used, which; however, maybe perfectly reasonable for filters comprising micromachined vibrating resonators. MEMS technology offers the desired programmable frequency gate and encourages designers to use mechanical devices the same way transistors are used: in massive numbers. This would conceivably realize a programmable frequency gate via a bank of on/off switchable micromechanical filters, where each filter is realized using an interconnected network of micromechanical resonators, which will be focus of this dissertation as described in the following sections.

### 1.3 A Review of Previous Vibrating Micromechanical RF Channel-Select Filter Efforts

Given their potential for improving the robustness and power consumption of receivers, it is not surprising that attempts to realize RF filters with percent bandwidths on the order of 0.1% sufficient to remove all interfering signals, leaving only energy in the desired RF channel, are abundant in the literature. These studies employ various resonator technologies using piezoelectric [17][18][19][20], internal dielectric [21][22], and capacitive [23][24] actuation. Unfortunately, so

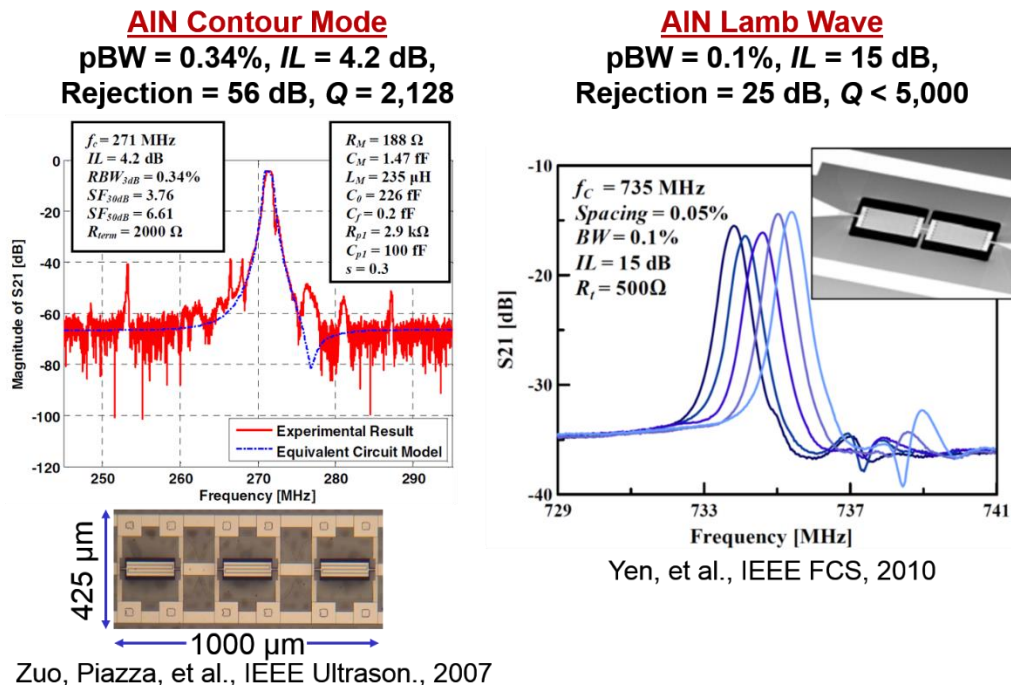


Figure 1.8: Previous vibrating channel-select filter work using piezoelectric actuation.

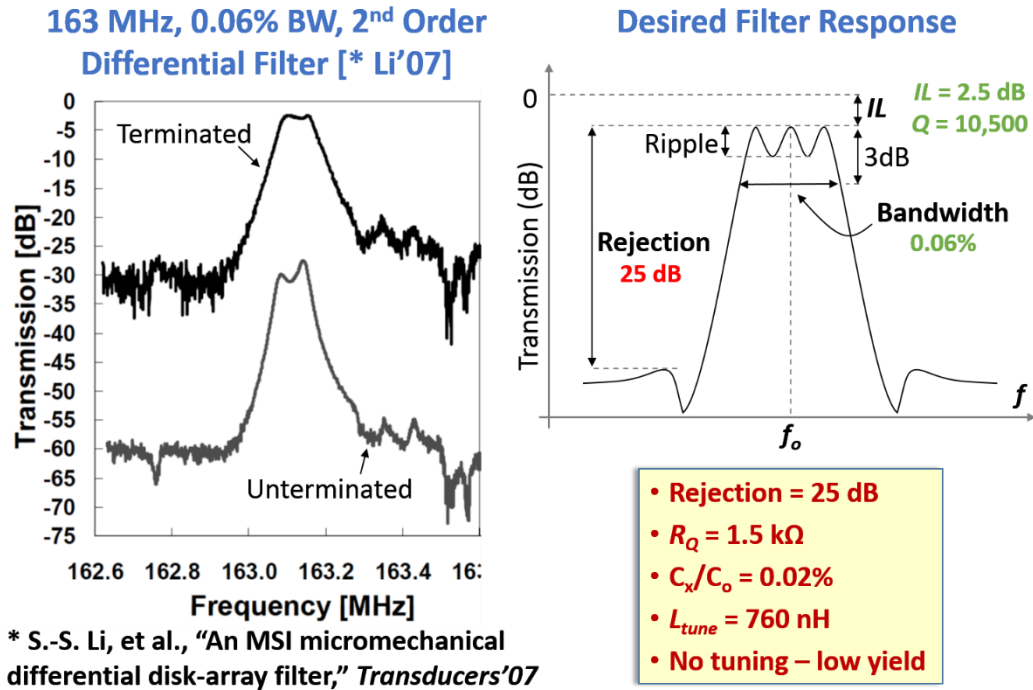


Figure 1.9: Previous work on capacitive actuated vibrating disk channel-select filters.

far none of the explored approaches truly achieves the needed performance, which demands not only small percent bandwidth, but also low passband insertion loss and high stop-band rejection. Piezoelectric materials lack the needed  $Q$  to achieve low insertion loss in so small a percent bandwidth, and lead to high passband losses that exceed 15 dB for 0.1% bandwidths [5] as a result, as shown in Figure 1.8.

On the other hand, approaches that attain sufficient  $Q$ 's on the order of 10,000, e.g., capacitive-gap transduced resonators, so far do not possess enough electromechanical coupling to attain 50dB stop-band rejection at UHF. Nonetheless, capacitive actuated filters come closest to achieving low loss RF channel-selection by demonstrating <0.1% bandwidth passbands with less than 3 dB insertion loss [23][24], as presented in Figure 1.9. However, previous capacitive actuated filter studies left a lot of room for improvement. Specifically, capacitive actuation gaps  $> 80 \text{ nm}$  limits their stopband rejection to a mere 25 dB, and requires rather large termination impedances exceeding  $1.5 \text{ k}\Omega$  that necessitate the use of inductors to resonate out shunt input and output capacitance. Finally, their yield of devices with adequately small passband ripple is quite low.

### 1.3.1 Summary of Improvements to Previous Work by this Dissertation

Pursuant to fixing these deficiencies, the work presented in this dissertation modifies the design of [23] presented in Figure 1.10-(a) to that of Figure 1.10-(b), which points out the major design changes. Now, smaller electrode-to-resonator gaps on the order of 39nm amplify the input/output

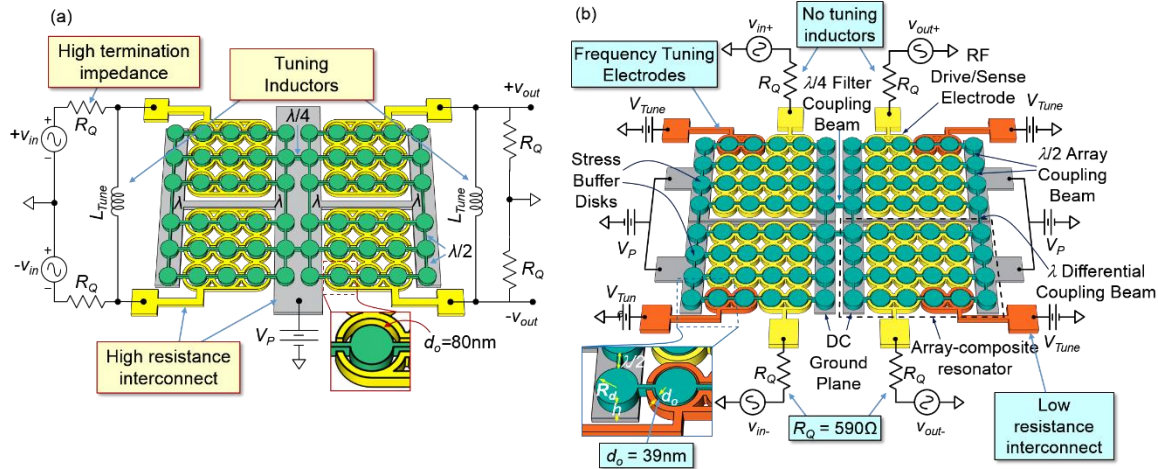


Figure 1.10: Comparison of (a) the filter design presented in [23] with labels indicating limitations that hinder performance; and (b) the improved design of this work with indicated improvements; both in preferred bias and excitation configurations used to evaluate filter performance.

electromechanical coupling by more than  $8.6\times$ , which directly contributes to larger stop-band rejection and removes the need for inductors. The new design also introduces additional electrodes around disks specifically tasked for frequency tuning towards higher device yield; as well as carefully designed electrode-less buffer devices that alleviate post-fabrication stress, thereby also contributing to higher yield. Combined, these design changes yield a 223.4-MHz two-resonator filter that employs 206 resonant micromechanical elements to realize a channel-selecting 0.09%-bandwidth while achieving only 2.7dB of in-band insertion loss together with 50dB of out-of-channel stop-band rejection. This amount of rejection is more than 25dB better than that of [23] and comes in tandem with a 20dB shape factor of 2.7 commensurate with its use of two array-composite resonators. The following chapters of this dissertation will elaborate on the milestones achieved that contributed to the aforementioned performance boost with the new design approach.

## 1.4 Micromechanical Vibrating Disk Filter Design Basics

Figure 1.11 describes the transmission response of a typical bandpass filter and identifies the commonly used performance metrics [25]. Such filter characteristics are typically achieved using the coupled-resonator network topology shown in Figure 1.12-(a) [25][26]. Here, each resonator element implements a frequency selective bi-quad transfer function with an associated resonator  $Q$  and the electrical equivalent LCR tank representation as shown in Figure 1.12-(b). When the filter is terminated, loading of the resonators with the termination resistors  $R_Q$  widens their frequency response spectra, allowing them to add constructively between peaks and subtract outside, yielding the desired filter spectrum.

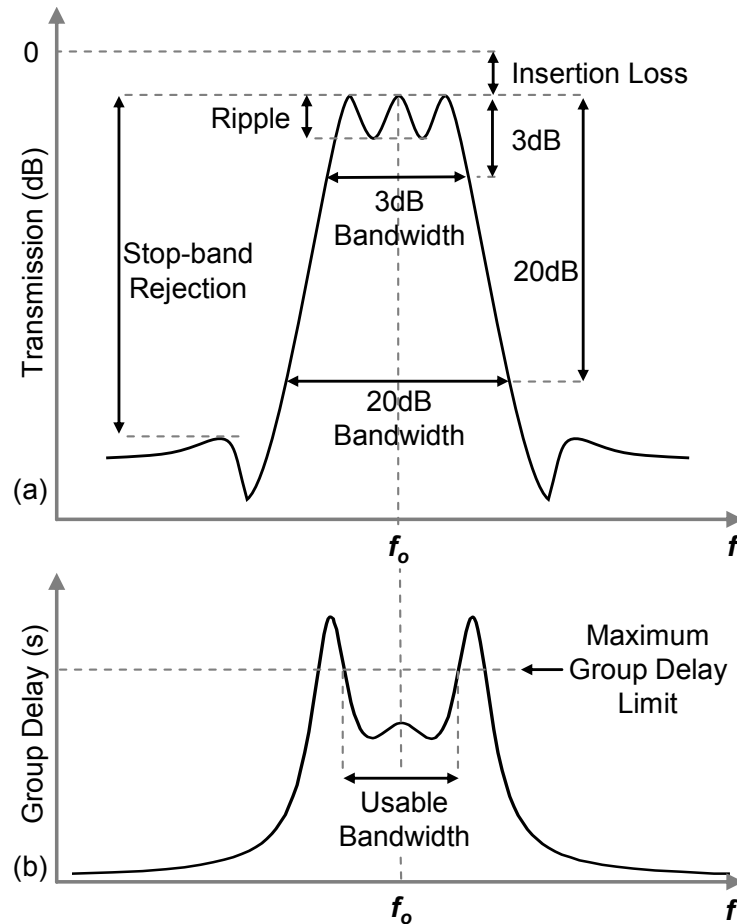


Figure 1.11: Schematic description of (a) transmission amplitude, and (b) group delay response metrics used to specify a bandpass filter.

The desired filter amplitude response, *cf.* Figure 1.11-(a), minimizes the passband insertion loss, ripple, and the filter shape factor defined here by the ratio of the 20dB band-width to the 3dB bandwidth; and maximizes the stopband rejection. The group delay characteristic illustrated in Figure 1.11-(b) is a measure of how much the filter phase response deviates from the ideal linear-phase response. The group delay is inversely proportional to the filter bandwidth, and its variation characteristic over the passband depends on the filter type and order. Chebyshev and Elliptic type filters display a rippled group delay over the pass-band as seen in Figure 1.11-(b), whereas Bessel type filters achieve maximally flat group delay at the expense of increased shape factor [25]. The communication standards specify the maximum allowed group delay ripple that sets the usable bandwidth of the filter as described in Figure 1.11-(b). The ultimately achievable performance of a filter relies primarily on the properties of its constituent resonators; therefore, the following sections will investigate the basic resonator requirements to meet the design goals described above.

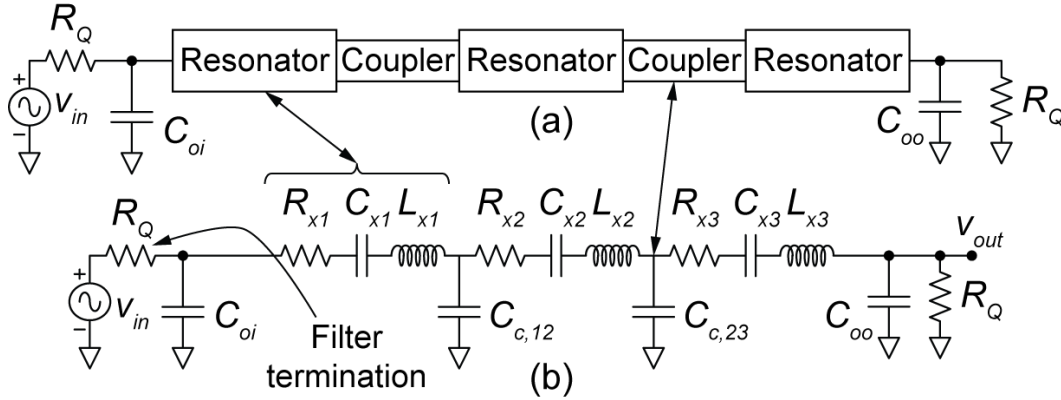


Figure 1.12: (a) Schematic description of general implementation topology of a band-pass filter consisting of a chain of discrete resonator tanks linked with coupling elements. (b) Electrical equivalent circuit representation of the generic filter.

### 1.4.1 Contributors to Filter Insertion Loss

The passband insertion loss, denoted as  $IL$ , of a pre-select filter is perhaps the most important performance metric because it strongly affects the receiver sensitivity due to the position of this filter in the receiver chain, *cf.* Figure 1.4. The noise figure of a passive filter equals its  $IL$  and adds directly to the overall noise figure of the receiver since the pre-select filter precedes the low noise amplifier (LNA) [6]. Any resonator targeting the needs of an RF channel-selecting filter must possess both sufficient  $Q$  to prevent undue insertion loss, and enough input/output (I/O) electro-mechanical coupling to overpower feed-through currents that would otherwise exert additional passband loss. Given their critical importance, the following sections will outline the minimum sufficient resonator  $Q$  and electromechanical coupling strength requirements towards minimizing the  $IL$  of RF channel-select filters.

#### 1.4.1.1 High Resonator Quality Factor

The insertion loss of any coupled-resonator filter is primarily determined by the following figure of merit [26]

$$q_o = \frac{Q}{Q_f} \quad (1.4)$$

defined as the ratio of the  $Q$  of resonators comprising the filter and the quality factor  $Q_f$  of the filter itself defined as

$$Q_f = \frac{f_o}{B} \quad (1.5)$$

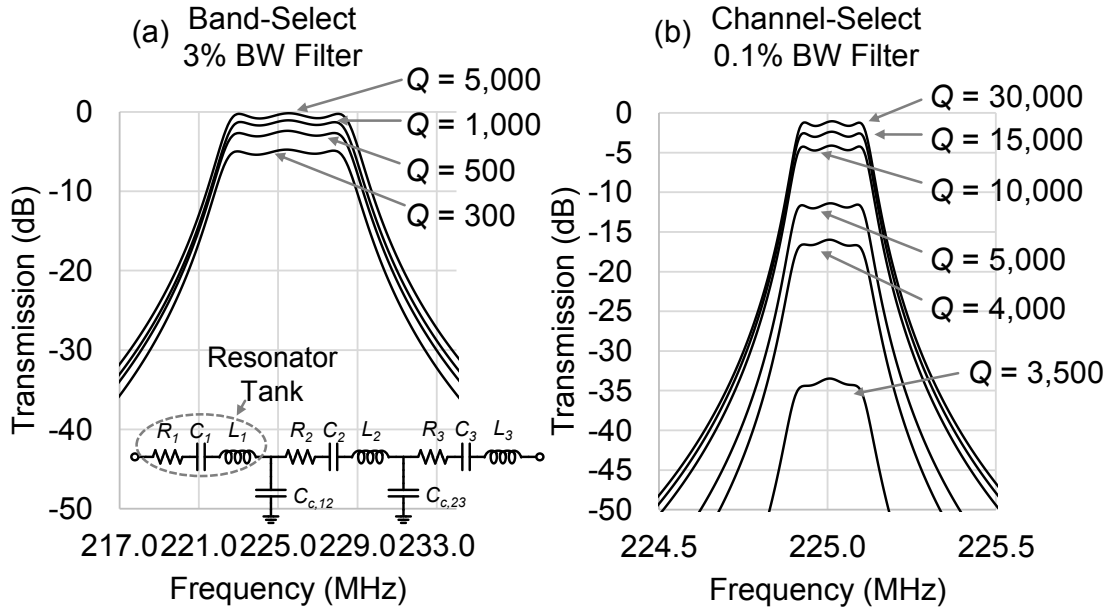


Figure 1.13: Simulated frequency spectrum for a 3<sup>rd</sup> order Chebyshev filter operating at  $f_o = 225$  MHz with (a) 3% bandwidth for a wideband band-select application, and (b) 0.1% bandwidth for a narrow band channel-select application for varying resonator tank  $Q$ 's.

where  $f_o$  is the filter center frequency and  $B$  is the filter 3 dB bandwidth. The filter type and order set the minimum  $q_o$  required to achieve the desired  $IL$ , which is tabulated in filter cookbooks [26]. For example, the minimum  $q_o$  required for less than 2 dB  $IL$  for a 2<sup>nd</sup> order Chebyshev filter is 9.7; and increases to 18.6 and 31.1 for third and fourth order filters, respectively [26]. It is important to note that the relation between the figure of merit set by (1.4) and the filter  $IL$  is independent of the resonator technology used to implement the filter.

Evidently from (1.4), filters with higher  $Q_f$ , i.e. narrower fractional bandwidth, require a proportionally higher resonator  $Q$  to sustain the high  $q_o$  and the resulting low insertion loss. This observation sets the design requirements of RF channel-select filters with high  $Q_f$  distinctly apart from those of band-select duplexers with much larger bandwidths, i.e. lower  $Q_f$ , that fall short of rejecting adjacent-channel blockers.

Figure 1.13 illustrates the vital importance of high resonator  $Q > 10,000$  in achieving low  $IL$  for filters with high  $Q_f > 1,000$  (i.e. fractional bandwidth  $< 0.1\%$ ) by comparing the simulated frequency spectrum of a three-resonator Chebyshev filter operating at 225 MHz for band-select and channel-select cases with 3% and 0.1% fractional bandwidths, respectively. This simulation varies the  $Q$  of the resonator tanks comprising the filter to gauge influence of  $Q$  on the filter  $IL$  for both cases. As Figure 1.13-(a) indicates, the band-select filter with 3% fractional bandwidth achieves less than 3 dB insertion loss with resonator  $Q$ 's as low as 500. In contrast, the insertion loss of the channel-select filter with 0.1% fractional bandwidth, i.e.  $Q_f = 1,000$ , shown in Figure 1.13-(b)

displays a much stronger dependence on resonator quality factor, where  $Q$ 's  $< 10,000$  lead to unacceptably high  $IL$  for an RF front-end filter.

#### 1.4.1.2 Sufficient Electromechanical Coupling Strength

Sufficient electromechanical coupling strength must accompany the high resonator  $Q$  to mitigate the passband loss and distortion levied by the input and output capacitance of the filter. Here, the ratio  $C_x/C_o$  [27] from the circuit of Figure 1.12 provides a convenient measure of electromechanical coupling strength, the value of which must exceed the fractional bandwidth of the filter to avoid excessive passband distortion. The degree by which it must exceed the fractional bandwidth depends upon the filter type and order, i.e., the number of resonators used. For example, if the three-resonator filter depicted in Figure 1.12 aims to effect a Chebyshev response, then the  $(C_x/C_o)$ 's of the I/O resonators must be  $2.5\times$  larger than the filter fractional bandwidth. Frequency spectrum for a 3<sup>rd</sup> order Chebyshev filter operating at  $f_o = 225$  MHz with (a) 3% bandwidth for a wideband band-select application, and (b) 0.1% bandwidth for a narrow band channel-select application for varying resonator tank  $Q$ 's.

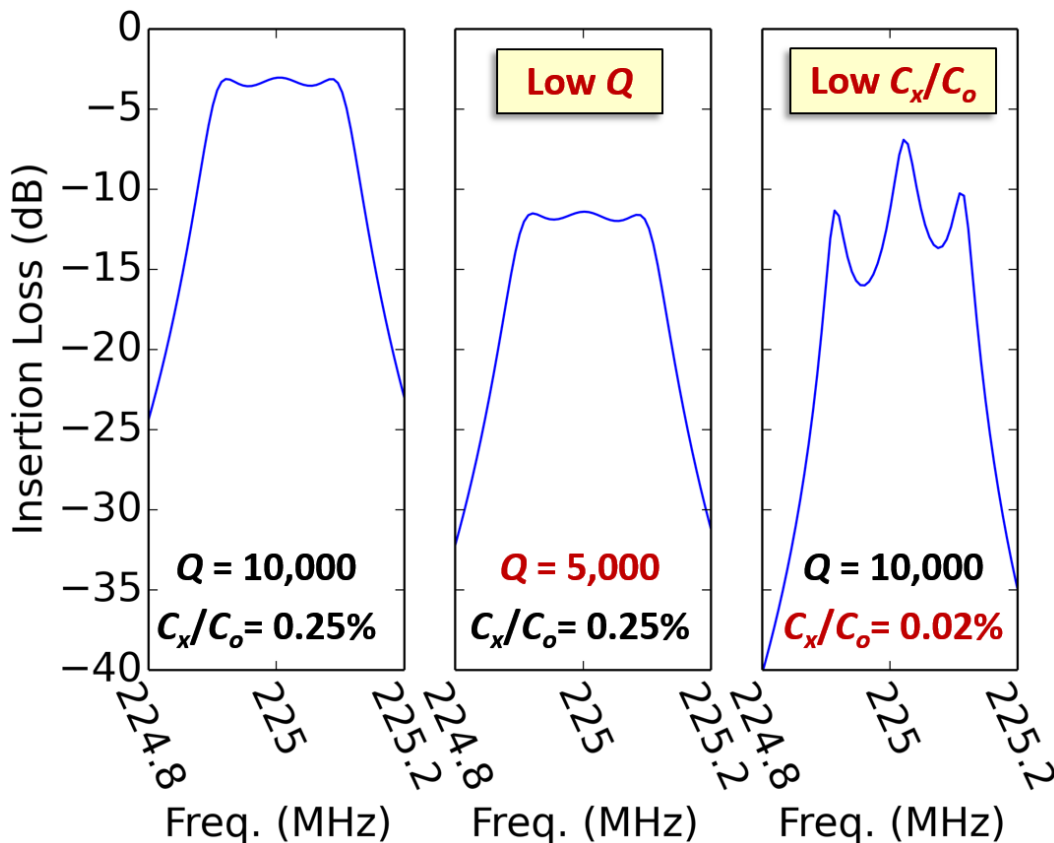


Figure 1.14: Simulated frequency response of a three-resonator RF channel-select filter with 0.1% fractional bandwidth for different resonator  $Q$  and  $C_x/C_o$  combinations as (a)  $Q = 15,000$  and  $C_x/C_o = 0.25\%$ , (b)  $Q = 5,000$  and  $C_x/C_o = 0.25\%$ , and (c)  $Q = 15,000$  and  $C_x/C_o = 0.01\%$ .



Figure 1.14 illustrates the importance of  $Q$  and  $(C_x/C_o)$  for an example three-resonator Chebyshev filter, this one centered at 225 MHz with a 0.1% bandwidth. When using resonators with  $Q$ 's at least  $15\times$  the filter  $Q_f$  and  $(C_x/C_o)$  at least  $2.5\times$  the fractional bandwidth, the desired response in Figure 1.14-(a) results. A drop in resonator  $Q$  from the desired 15,000 to just 5,000 yields the response in Figure 1.14-(b), which now sports 11.4 dB of insertion loss—clearly too much loss. On the other hand, a drop in resonator  $(C_x/C_o)$  from the desired 0.25% to 0.01% introduces undue passband ripple, as shown in Figure 1.14-(c). Clearly, the filter response is good only when its constituent resonators possess sufficient quantities of both  $Q$  and I/O coupling.

It is important to note that the needs of a 0.1% RF channel-select filter differ significantly from those of conventional 3% band-select filters used in today's handsets. In particular, conventional 3% filters put a premium on strong coupling, where  $(C_x/C_o) \sim 7\%$  is often needed, and not so much on  $Q$ , for which 500 is often acceptable as in Figure 1.13-(a). On the other hand, a 0.1% RF channel-select filter places a high premium on  $Q$ , which must often be greater than 10,000, and not so much on  $(C_x/C_o)$ , for which values on the order of only 0.25% are acceptable.

## 1.4.2 Filter Termination Impedance & Electromechanical Coupling Strength

RF channel-selects filter must not only provide low passband loss to avoid taxing the overall receiver noise figure, but also attain high stopband rejection towards sufficiently suppressing strong adjacent channel blockers. To this end, the value of the termination resistors  $R_{Qi}$ , *cf.* Figure 1.12, must be minimized, because these resistors form voltage dividers with the parasitic feed-through current paths that shunt the desired micromechanical signal processing path. Consequently, low filter termination resistor values reduce the coupling of the parasitic electrical feed-through paths to the I/O ports of the filter.

The filter termination resistors, denoted as  $R_Q$ , provide  $Q$ -control for the end resonators to flatten the otherwise jagged filter passband, and the required termination resistor value is given by [26]

$$R_Q = \left( \frac{Q}{Q_f q_i} - 1 \right) R_x \quad (1.6)$$

where  $q_i$  is a normalized termination constant obtained from filter cookbooks [17], and  $R_x$  is the motional resistance of the resonator terminated by  $R_Q$ . The desired  $R_Q$  value is typically set by the system requirements, such as the impedance of the preceding antenna and the succeeding LNA, and is typically less than  $1\text{k}\Omega$ .

Evidently from (1.6), reducing  $R_x$  is key to achieve low  $R_Q$ ; however, even though a higher resonator  $Q$  reduces  $R_x$ , the  $Q$  term cancels in (1.6) and does not affect  $R_Q$  for  $Q \gg Q_f$  that must hold for low passband loss. Instead, increasing the electromechanical coupling coefficient  $\eta$ , defined as the ratio of resonant force applied to a resonator to the applied input voltage [28], serves

as the key strategy to minimize  $R_Q$ . For this very reason, the filter design hierarchy presented in this dissertation incorporates various methods that increase electromechanical coupling.

## 1.5 High- $Q$ Micromachined Vibrating Resonators for Low Loss RF Channel-Selection

Much like individual transistors in a VLSI circuit, the vibrating micromechanical resonators are the unit cell components for realizing complex micromechanical signal processor circuits, such as filters [23] and oscillators [12]. Signal processing using vibrating mechanical elements, initially in the macro-level using quartz [8] and relatively large SAW filters [29], became ubiquitous in modern receiver design for frequency control and synthesizer circuitry design. However, a potentially CMOS compatible and very small footprint solution is needed to realize the multi-mode filter bank solution illustrated in Figure 1.4 to avoid excessive area and cost. The advances in micromachined resonator technology gets us ever closer to this goal by scaling the resonator dimensions and increasing operation frequency and performance. However, the requirements for a micromachined channel-selecting RF front-end include much more than merely small size. The piezoelectric FBARs [7], for example, that have already become a successful high volume product in the wireless handset arena, although small, are perhaps not suitable for circuit design, since their frequencies are governed almost entirely by thickness, which is not a parameter that can be specified via computer-aided design (CAD) layout. Given how instrumental CAD has been to the success of VLSI transistor IC design, one would expect CAD amenability to be equally important for micromechanical ICs. In this respect, the resonators and other elements in the repertoire of a micromechanical circuit design environment should have frequencies or other characteristics definable by lateral dimensions easily specifiable by CAD. A list of requirements necessary for creating micromechanical circuit design environment can be listed as:

- $Q$ 's  $> 10,000$  from 1–3000 MHz.  $Q$ 's this high are needed to allow cascading of circuit blocks without accumulating excessive loss, and to allow channel selection at RF.
- *Strong electromechanical coupling.*  $C_x/C_o$  on the order of 0.1-1% is highly desired for RF channel-select front end designs. A technology that scales the  $C_x/C_o$  coupling figure of merit with smaller dimensions, much like the effect of scaling on the  $f_t$  of transistors, is needed to retain sufficient coupling at high operation frequencies.
- *CAD-amenable design.* Frequencies should be determined by lateral dimensions that can be specified via CAD, which makes possible an ability to attain many different frequencies in a single layer on a single chip. Relying on vertical dimensions for vertical dimensions for frequency control is incompatible with automated CAD design, as well as impose a fabrication challenge that requires very uniform and repeatable control of film thickness over multiple large area wafers.

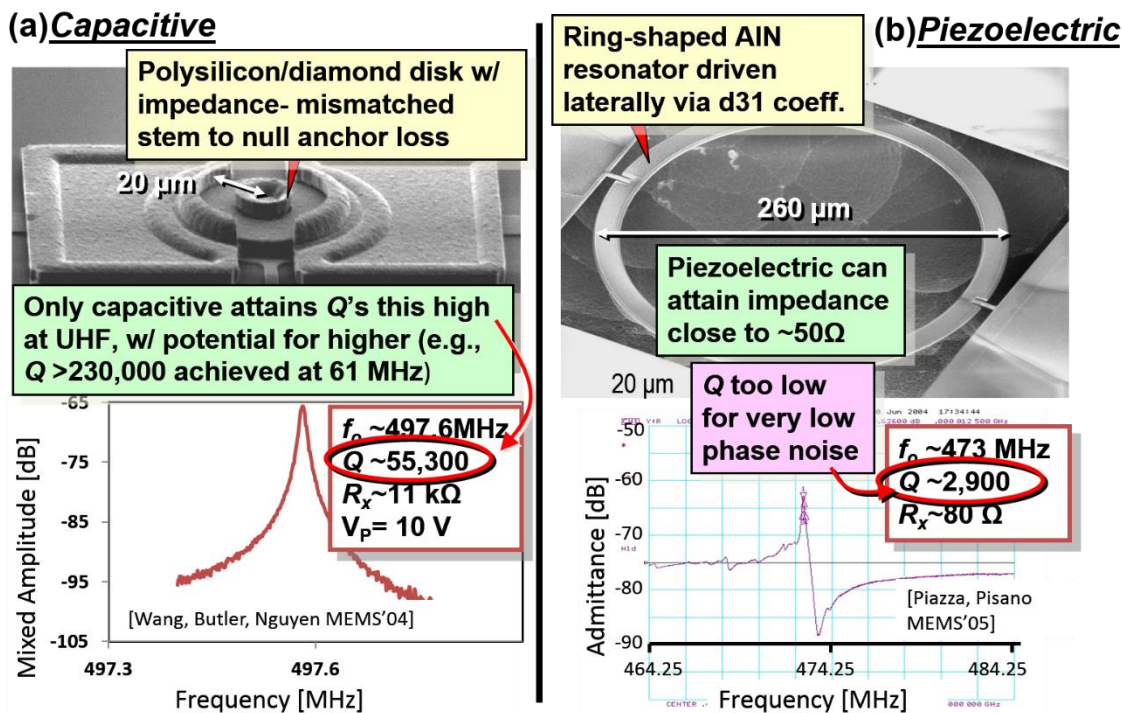


Figure 1.15: (a) Previous work on capacitive transduced vibrating disks that attains extremely high  $Q$ 's exceeding 50,000 at  $\sim 500$  MHz, but high motional resistance  $R_x$ . (b) Piezoelectric actuated vibrating ring resonator with impressively low motional resistance, but low  $Q \sim 3,000$ .

- On/off switchability. Here, the overriding preference is for vibrating micromechanical devices that can switch themselves, i.e., that do not require extra series switches to do so, and that thus avoid the extra cost and insertion loss.
- Thermal and aging stability to better than 2 ppm, or at least amenable to compensation or control to this level.
- Nonlinear characteristics that enable such functions as mixing, amplification, limiting, and other useful signal processing abilities.

A mechanical circuit technology with the attributes mentioned above might make possible filter banks capable of selecting channels (as opposed to just bands) right at RF with zero switching loss added by series on/off switches. Similarly, these properties would enable oscillators using multiple high- $Q$  resonators to attain improved long- and short-term stability; oscillators with oven-control-like temperature stability, but consuming only milliwatts of power; ultra-low power completely mechanical RF front ends for wireless handsets; and all of these realized on a single silicon chip.

Figure 1.15 compares the two major micro-resonator actuation technologies that find the most common use in contemporary vibrating micromechanical resonator design. Figure 1.15-(a) presents an example capacitive actuated vibrating disk resonator that is capable of attaining  $Q$ 's exceeding 50,000 at  $\sim 500$  MHz [30] and  $Q > 230,000$  at 61 MHz. In addition to impressively high  $Q$ , capacitive transduction also achieves flexible geometries with CAD-definable frequencies ranging from HF [31] to UHF [30], voltage controlled tuning [28], thermal stability [32], and on/off switching capability [33]. Clearly, the capacitive transduction method exemplified in Figure 1.15-(a) satisfies the list of requirements necessary for an RF channel-selecting front end, which makes it a very attractive technology candidate for future RF-MEMS front-end designs. Especially the high  $Q > 10,000$  enabled by capacitive transduction is indispensable for low loss RF channel-selection, as demonstrated in Figure 1.13-(b). However, in the past, the electromechanical coupling strength of capacitive actuators was limited because of actuation gaps were restricted to 100 nm or wider due to fabrication constraints. Fortunately, as the following chapters of this dissertation will illustrate, recent techniques such as partial gap filling via ALD high-k dielectrics [34][35] enable gaps as small as 25nm. Such small gaps overcome the high impedance barrier that hindered the adaptation of capacitive transducers in practical systems and provide the designers with a wide range of  $C_x/C_o$  and motional resistance using capacitive actuated micromechanical circuits.

In comparison, the piezoelectric actuation technique, *cf.* Figure 1.15-(b), excels in very strong electromechanical coupling with its inherent  $C_x/C_o$  in the 1-10% range. However, the  $Q$  of piezoelectric actuated resonators have historically been limited to 3,000 [36]. Piezoelectric actuation also lacks inherent electrical tuning, such the electrical spring softening effect [37] that capacitive actuators leverage for frequency control. It is possible to use varactors or switchable bank of capacitors as external elements to affect the resonance frequency of a piezoelectric resonator, but such solutions are bulky and do not scale well for large scale mechanical circuits. The low  $Q$  and tuning limitations render the current generation of piezoelectric actuated resonators hard to adapt to low loss RF channel-select circuits. However, for wideband systems, such the typical 3% band-select filters, *cf.* Figure 1.13-(a), that can tolerate high frequency variations without requiring tuning and low  $Q \sim 500$ ; piezoelectric actuators present a very good solution. In fact, they are ubiquitous in contemporary wideband front-ends as duplexer filters and frequency sources [9]. The trade-off by choosing to work with low  $Q$  resonators and wideband front-ends; however, is being forced to work with a very high dynamic range exceeding 100 dB and the resulting high power consumption.

## 1.6 Dissertation Overview

This dissertation focuses on very narrow band,  $< 0.1\%$  fractional bandwidth RF front-end filters. Therefore, the primary focus will be on capacitive actuated micromechanical circuits. To this end, Chapter 2 will introduce the high- $Q$  micromechanical vibrating disk resonators that forms the

unit element of the ensuing low loss RF channel-select vibrating disk filters. This chapter will also develop a small-signal equivalent circuit for parallel-plate capacitive-gap transduced micromechanical disk resonators that employs negative capacitance to model the dependence of resonance frequency on electrical stiffness. This negative-capacitance model will prove very valuable in accurate modelling of electrical tuning of filters, as well as thoroughly capturing the effects of arbitrary port termination impedances on the filter pole locations.

Chapter 3 will follow up the electromechanical coupling model presented in Chapter 2 by introducing a capacitive actuation gap scaling that uses high- $k$  ALD dielectric films to partially fill the electrode-to-resonator gap. Capacitive actuation gap scaling is perhaps the most pressing need for capacitive actuated vibrating disk filters to complement the very high  $Q$  of the capacitive resonators with sufficient electromechanical coupling. The  $\text{Al}_2\text{O}_3$ - $\text{TiO}_2$  bi-layer ALD partial gap filling approach presented in Chapter 3 achieves just this by demonstrating 61 MHz wineglass resonators with simultaneous high  $Q > 70,000$  and motional resistance  $R_x < 140\Omega$ . This result demonstrates the first VHF micromechanical resonators in any material, piezoelectric or not, to meet the simultaneous high  $Q (>50,000)$  and low motional resistance ( $<200\Omega$ ) commonly desired in many RF and frequency control applications.

After presenting a method that not only boosts electromechanical coupling but also preserves the high  $Q$  of capacitive actuated vibrating disks in Chapter 3, Chapter 4 delves into resonator materials that will sustain the high  $Q$  and sufficient electromechanical coupling at frequencies beyond 1 GHz. Chapter 4 introduces a capacitively transduced micromechanical resonator constructed in hot filament CVD (HFCVD) boron-doped microcrystalline diamond (MCD) structural material that posts a measured  $Q$  of 146,580 at 232.441 kHz, which is  $3\times$  higher than the previous high for conductive polydiamond fabricated using the costlier MPCVD method. Moreover, radial-contour mode disk resonators fabricated in the same MCD film and using material mismatched stems exhibit a  $Q$  of 71,400 at 299.86 MHz, which is the highest series-resonant  $Q$  yet measured for any on-chip resonator at this frequency. For many potential applications, the hot filament CVD method demonstrated in this work is quite enabling, since it provides a much less expensive method than microwave CVD based alternatives for depositing doped CVD diamond over large wafers (e.g., 8") for batch fabrication.

Having covered the two primary needs for RF channel selection, i.e. sufficient electromechanical coupling  $> 0.1\%$  and high  $Q > 10,000$ , Chapter 5 introduces a design flow for micromechanical RF channel-select filters capable of eliminating strong adjacent channel blockers directly after the antenna, which greatly reduces power consumption in RF front-ends. The presented design hierarchy achieves the desired filter response with a specific center frequency, bandwidth, and filter termination resistance. The design procedure culminates in specific values for all mechanical geometry variables necessary for the filter layout, such as disk radii, and beam widths; and process design variables such as resonator material thickness and capacitive actuation gap spacing. Perhaps

the most significant contribution of Chapter 5 is the demonstration of an intuition based mechanical circuit design flow that works just as powerful as those used in the transistor world to enhance functionality via a hierarchical building block approach.

Finally, Chapter 6 presents the fabrication and measurement results of an RF channel-select filter created using the theory and design procedure elaborated in Chapter 5. Unlike the ideal filter treated in Chapter 5, the real filter has non-idealities such as structural film stress, parasitic trace resistance, and process variations. Therefore, this chapter focuses on the practical implementation of a filter that accounts for these non-idealities. The introduction of a 39nm-gap capacitive transducer, voltage-controlled frequency tuning, and a stress relieving coupled array design has enabled a 0.09% bandwidth 223.4 MHz channel-select filter with only 2.7dB of in-band insertion loss and 50dB rejection of out-of-band interferers. This amount of rejection is more than 23dB better than a previous capacitive-gap transduced filter design [23] that did not benefit from sub-50nm gaps. It also comes in tandem with a 20dB shape factor of 2.7 realized by a hierarchical mechanical circuit design utilizing 206 micromechanical circuit elements, all contained in an area footprint of only  $600\mu\text{m}\times 420\mu\text{m}$ . The key to such low insertion loss for this tiny percent bandwidth is  $Q's > 8,800$  supplied by polysilicon disk resonators employing for the first time capacitive transducer gaps small enough to generate coupling strengths of  $C_x/C_o \sim 0.1\%$ , which is a  $6.1\times$  improvement over previous efforts [23]. The filter structure utilizes electrical tuning to correct frequency mismatches due to process variations, where a dc tuning voltage of 12.1 V improves the filter insertion loss by 1.8 dB and yields the desired equiripple passband shape. An electrical equivalent circuit is presented that captures not only the ideal filter response, but also parasitic non-idealities that create electrical feed-through, where simulation of the derived equivalent circuit matches measured filter spectrum closely both in-band and out-of-band.

The combined 2.7dB passband insertion loss and 50dB stopband rejection of the demonstrated 206-element 0.09% bandwidth 223.4-MHz differential micromechanical disk filter represents a landmark for capacitive-gap transduced micromechanical resonator technology. This demonstration proves that the mere introduction of small gaps, on the order of 39 nm, goes a long way towards moving this technology from a research curiosity to practical performance specs commensurate with the needs of actual RF channel-selecting receiver front-ends. It also emphasizes the need for tuning and defensive stress-relieving structural design when percent bandwidths and gaps shrink, all demonstrated by the work herein.

The kernel at the center of all these results is the unit element: the capacitive actuated vibrating disk resonators with very high  $Q$ . Consequently, Chapter 2 will ensue with an elaborate analysis of the parallel plate capacitor actuated vibrating disks.

## *Chapter 2*

# *A NEGATIVE CAPACITANCE EQUIVALENT CIRCUIT MODEL FOR PARALLEL-PLATE CAPACITIVE-GAP TRANSDUCED MICROMECHANICAL RESONATORS*

---

---

This chapter introduces a small-signal equivalent circuit for parallel-plate capacitive-gap transduced micromechanical resonators that employs negative capacitance to model the dependence of resonance frequency on electrical stiffness in a way that facilitates circuit analysis, that better elucidates the mechanisms behind certain potentially puzzling measured phenomena, and that inspires circuit topologies that maximize performance in specific applications. For this study, a micromechanical disk resonator serves as the vehicle with which to derive the equivalent circuits for both radial-contour and wine-glass modes, which are then used in circuit simulations (via SPICE) to match measurements on actual fabricated devices. The new circuit model not only correctly predicts the dependence of electrical stiffness on the impedances loading the input and output electrodes of parallel-plate capacitive-gap transduced micromechanical device, but does so in a visually intuitive way that identifies current drive as most appropriate for applications that must be stable against environmental perturbations, such as acceleration or power supply variations. Measurements on fabricated devices in fact confirm predictions by the new model of up to 4× improvement in frequency stability against DC-bias voltage variations for contour-mode disk resonators as the resistance loading their ports increases. By enhancing circuit visualization, this circuit model makes more obvious the circuit design procedures and topologies most beneficial for certain mechanical circuits, e.g., filters and oscillators.

Parallel-plate capacitive transducers enjoy widespread use in the MEMS industry, where they are employed in applications ranging from accelerometers [38], to gyroscopes [39] and other resonant sensors [40], to RF MEMS switches [41], to vibrating RF MEMS resonators [10]. The last of these often employ relatively large circuits of resonant MEMS devices [23] coupled electrically

or mechanical at very specific locations, so requires models for such devices that are accurate, scalable, location de-pendent, and amenable to simulation via established soft-ware, like SPICE [42].

Unfortunately, several of the classic equivalent circuit models for capacitive-gap transduced micromechanical resonators lack sufficient location dependence [43][44], and one is curiously asymmetric in that it models voltage-to-force and velocity-to-current coupling via different coupling coefficients [43]. All of the above, plus those of [31] and [45], do not allow sufficient visualization for insightful circuit design, to the point where they actually hide important aspects of capacitive-gap transduced device behavior in circuit networks. Since circuit design and analysis is largely a skill of recognition, insufficient visualization is a significant shortcoming for any equivalent circuit.

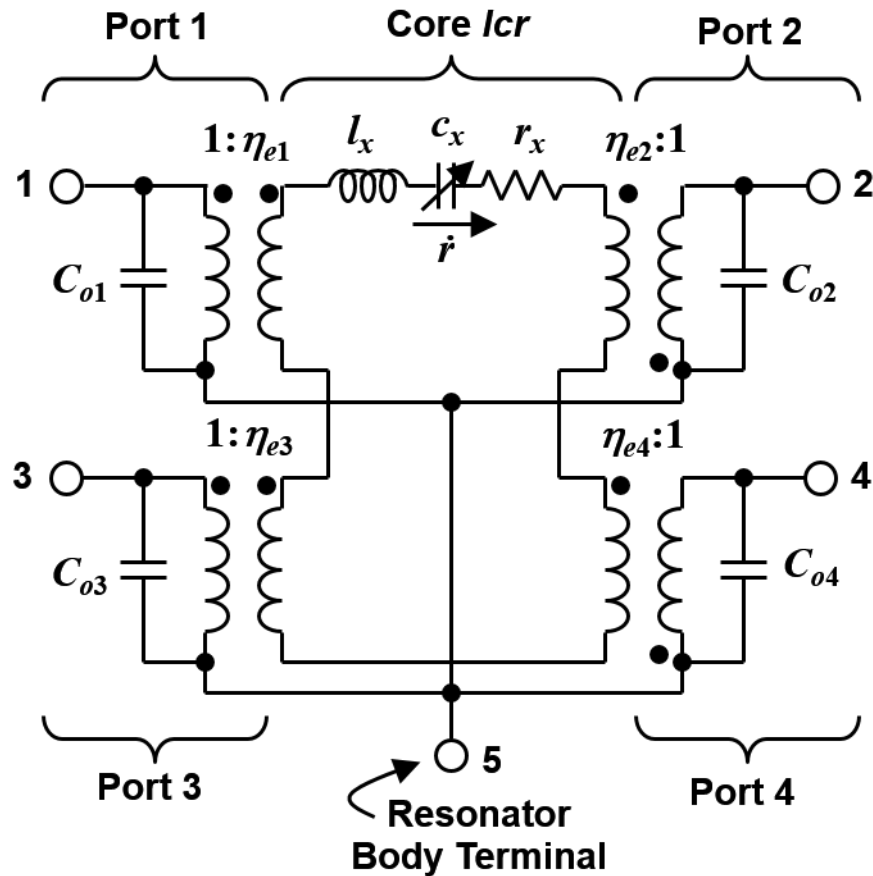


Figure 2.1: Conventional small-signal AC equivalent circuit for a four-port capacitive-gap transduced micromechanical resonator, such as that of Figure 2.2, when operating in the radial-contour mode of Figure 2.2-(d). Here, terminal 1 corresponds to the electrode 1, terminal 2 to electrode 2, terminal 3 to electrode 3, terminal 4 to electrode 4, and terminal 5 to the body of the conductive resonant structure. The core  $lcr$  models the dynamic behavior of the resonant structure, where the variable capacitor  $c_x$  includes the effects of electrical stiffness.



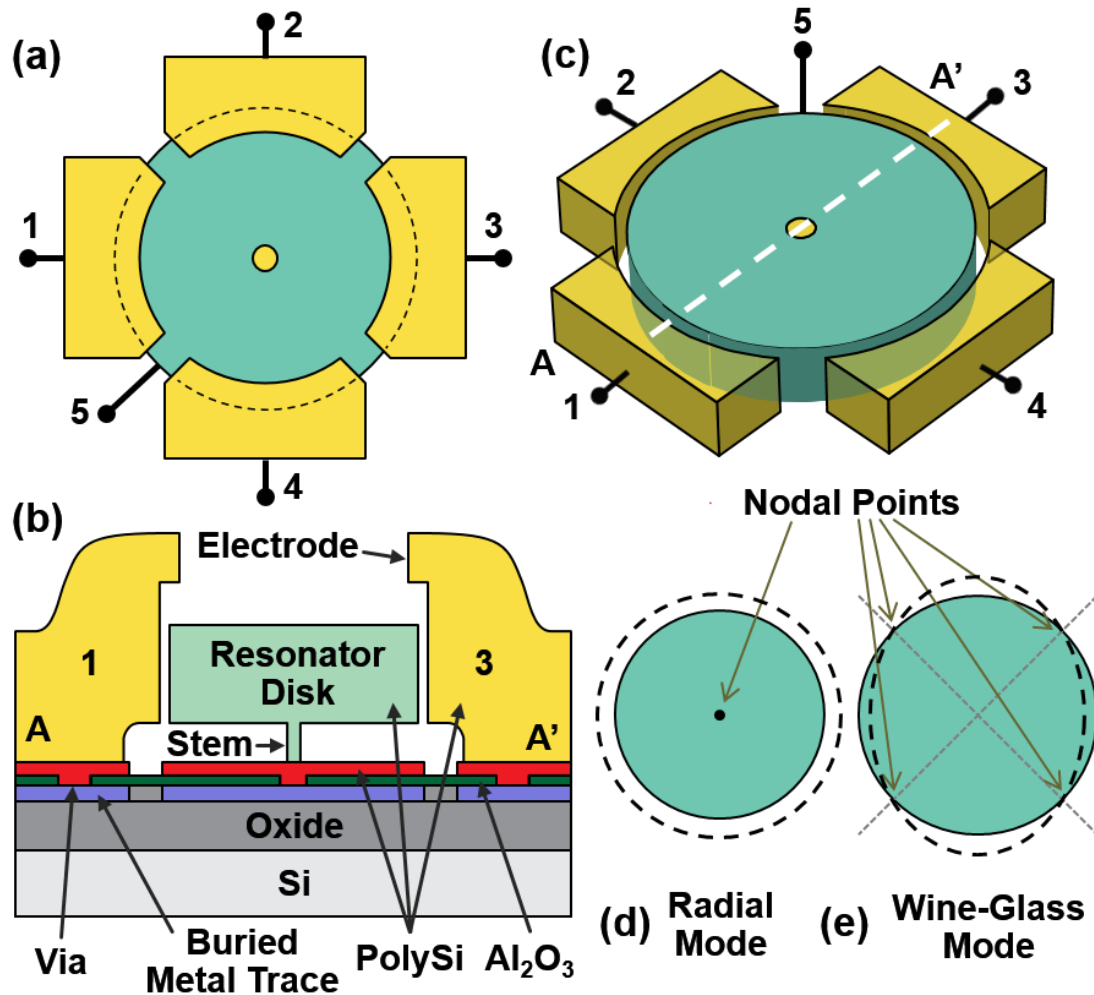


Figure 2.2: Pictorial summary for a micromechanical disk resonator with four in-put/output ports and a resonator body port. (a) Layout view. (b) Cross-section view. (c) Perspective view. (d) Radial-contour mode shape. (e) Wine-glass mode shape.

Take for example the small-signal dynamic equivalent circuit of Figure 2.1 [31][44] [46] that models the disk micro-mechanical resonator depicted in Figure 2.2-(a) and (b) when operating in its radial-contour mode, *cf.* Figure 2.2-(d). This particular circuit has been used successfully in various incarnations to design micromechanical resonator oscillators [45] and even much more complex filters [23][31][46]. It is perhaps the best to date for mechanical circuit design, since it captures the full flexibility of inputs and outputs for any capacitive-gap transduced micromechanical resonator by using transformers to couple location dependent electrical and mechanical input energy to the mechanical response of the structure, and vice versa. It also conveniently uses actual values of dynamic mass, inverse stiffness, and damping, as values for its core motional inductance  $l_x$ , motional capacitance  $c_x$ , and motional resistance  $r_x$ . The motional resistance  $r_x$  further captures the complete noise performance of the device, where a noise force generator with value  $4kTr_x$  placed in series with  $r_x$  fully models the thermal noise.

This circuit, however, has faults. In particular, it models the influence of electrical stiffness [37] on the resonance frequency of the device via the arrow through the capacitor  $c_x$  (that indicates this capacitor is tunable) and by setting the value of  $c_x$  equal to  $1/(k_m - k_e)$ , where  $k_m$  is the mechanical stiffness and  $k_e$  the voltage-tunable electrical stiffness. Although this method for capturing electrical stiffness adequately predicts the frequency, it does not convey clearly to a circuit designer the impact of electrical stiffness on the overall circuit performance. Modeling the electrical stiffness in this way in fact hides some very important capacitive-gap transduced resonator behaviors when emplaced into certain circuits. This model also encourages designers to dismiss the impact of electrical stiffness, since many designers just neglect the  $k_e$  part in the value of  $c_x$  when drawing up mechanical circuits.

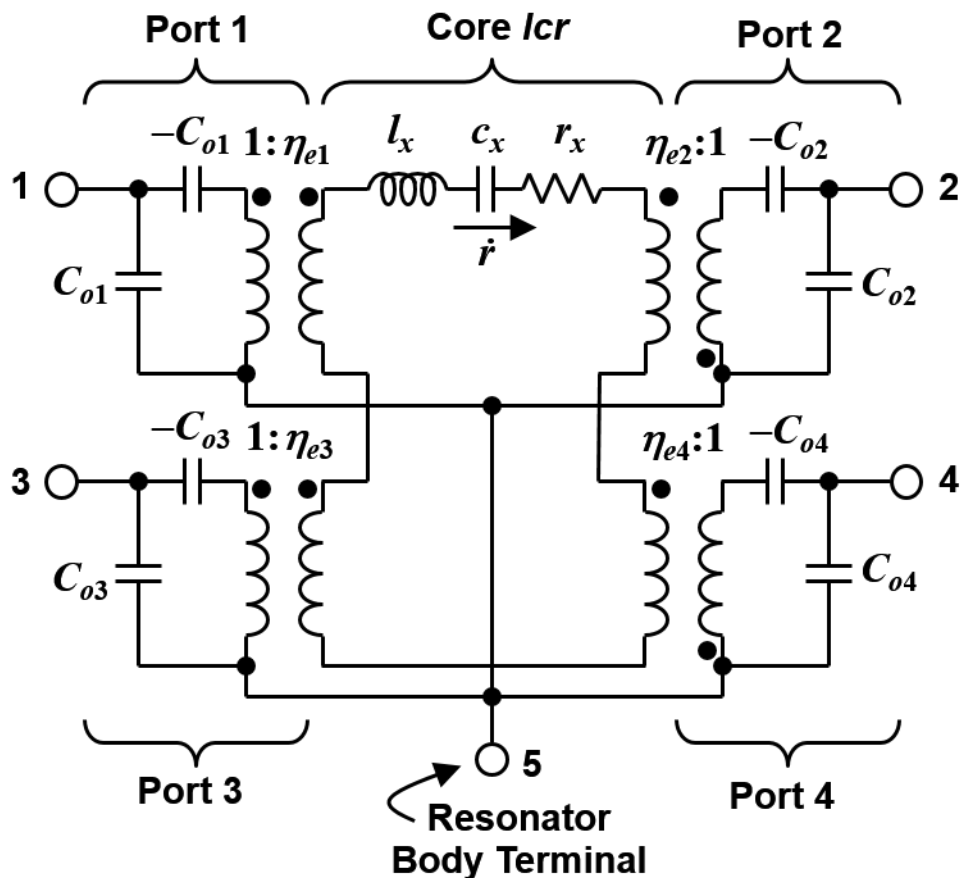


Figure 2.3: Negative capacitance small-signal AC equivalent circuit for a two-port capacitive-gap transduced micromechanical resonator, such as that of Figure 2.2, when operating in the radial-contour mode shown in Figure 2.2(d). Here, negative capacitors exactly equal to the shunt electrode-to-resonator static overlap capacitors are used to model the effect of electrical stiffness in a way that more clearly conveys interaction between them and the static electrode-to-resonator overlap capacitance at each port.

To remedy the above deficiencies, this chapter introduces a more circuit design-friendly model presented in Figure 2.3 that captures the influence of electrical stiffness on device and circuit behavior using a negative capacitance exactly equal in magnitude to the shunt static electrode-to-resonator overlap capacitance  $C_o$  at each electrode terminal. The presence of this negative circuit element obviously presents opportunities to negate the effect of the shunt  $C_o$ , which has historically proven troublesome for certain oscillator, filter, and sensor designs. As will be seen, recognition of the negative  $C_o$  also suggests circuit topologies for oscillators that should greatly enhance their stabilities against environmental perturbations, such as temperature-induced drift or acceleration.

This chapter begins in Section 2.1 with a simple derivation for the circuit model of Figure 2.3 and follows in Sections 2.2 and 2.3 with the complete development of element expressions for the specific cases of capacitive-gap transduced disk resonators operating in the radial-contour mode and the wineglass mode. After establishing proper design procedures via actual design examples in Sections 2.2 and 2.3, Section 2.4 then confirms model accuracy by comparison with measured data that includes frequency response matching, as well as plots of frequency versus DC-bias versus input/output load impedance, where the new equivalent circuit proves especially adept at explaining the behavior of these curves. Section 2.5 finally explores the impact that use of this equivalent circuit should have on practical applications.

## 2.1 Negative Capacitance Equivalent Circuit

A succinct derivation of the equivalent circuit of Figure 2.3 follows directly from consideration of the forces generated by voltages applied to terminals of the disk resonator device depicted in Figure 2.2. As shown, this device comprises a conductive disk surrounded by electrodes spaced

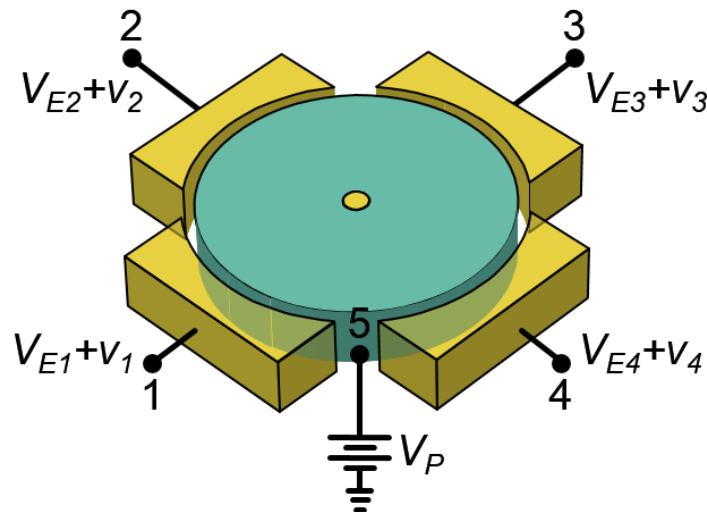


Figure 2.4: Schematic showing the general electrical input/output configuration for a capacitive-gap transduced micromechanical disk resonator.

very close to its edges and supported at its center by a conductive stem above a uniform ground plane at the same potential as the disk.

Figure 2.4 presents a general electrical input/output configuration that can excite the disk into either of the modes shown in Figure 2.2-(d, e). Here, a DC-bias voltage  $V_P$  is applied to the conductive structure (i.e., at terminal 5) and in general combinations of dc  $V_{Ei}$  and ac voltages  $v_i$  either applied or generated (e.g., by transistor circuit inputs) at each of the electrodes. The combination of these voltages generates a force from each electrode  $i$  to the disk structure given by

$$F_i = \frac{1}{2} \frac{\partial C_i}{\partial r} (V_{Pi} - v_i)^2 \quad (2.1)$$

where  $\partial C_i/\partial r$  is the change in port  $i$  electrode-to-resonator capacitance per unit radial displacement of the disk, and  $V_{Pi}$  is the dc voltage applied across the resonator-to-electrode gap at port  $i$ . For the simple case where the radial displacement of the disk remains the same over the span where the electrode at port  $i$  overlaps the disk,  $\partial C_i/\partial r$  can be obtained from the port  $i$  electrode-to-resonator capacitance  $C_i(r)$  as follows:

$$C_i(r) = C_{oi} \left(1 - \frac{r}{d_o}\right)^{-1} \Rightarrow \frac{\partial C_i}{\partial r} = \frac{C_{oi}}{d_o} \left(1 - \frac{r}{d_o}\right)^{-2} \quad (2.2)$$

where  $C_{oi}$  is the static electrode-to-resonator overlap capacitance at port  $i$ ,  $d_o$  is the electrode-to-resonator gap spacing (assumed the same for all ports), and  $r$  is radial displacement. For small displacements, (2) Taylor expands to

$$\frac{\partial C_i}{\partial r} = \frac{C_{oi}}{d_o} (1 + A_1 r + A_2 r^2 + A_3 r^3 + \dots) \quad (2.3)$$

where

$$A_1 = \frac{2}{d_o}, A_2 = \frac{3}{d_o^2}, A_3 = \frac{4}{d_o^3}, \dots \quad (2.4)$$

Inserting (2.3) into (2.1), taking only the first two terms of (2.3), yields

$$\begin{aligned} F_i &= \frac{1}{2} \frac{C_{oi}}{d_o} (V_{Pi}^2 - 2V_{Pi}v_i + v_i^2 + A_1 V_{Pi}^2 r - 2A_1 V_{Pi} v_i r + A_1 v_i^2 r) \\ &= \frac{1}{2} \frac{C_{oi}}{d_o} (\dots - 2V_{Pi}v_i + A_1 V_{Pi}^2 r + A_1 v_i^2 r + \dots) \end{aligned} \quad (2.5)$$

where the last form includes only terms that can generate force components at the frequency of the input voltage  $v_i$ . Recognizing that at resonance the displacement is  $90^\circ$  phase-shifted from the drive

voltage, so  $r = \mathcal{R} \sin \omega_o t$  when  $v_i = V_i \cos \omega_o t$ , then inserting these plus the first term of (2.4) into (2.5) yields for the force at resonance

$$F_i = - \left\{ V_{Pi} \frac{C_{oi}}{d_o} V_i \cos \omega_o t - \left( V_{Pi}^2 + \frac{V_i^2}{2} \right) \frac{C_{oi}}{d_o^2} \mathcal{R} \sin \omega_o t \right\} \quad (2.6)$$

where  $t$  is time.

The first term of (2.6) represents the force at resonance generated by the input voltage  $v_i$ , which is of course in phase with  $v_i$ . In transformer-based equivalent circuits, such as those of Figure 2.1 and Figure 2.3, this force is often written as

$$F_i = -\eta_{ei} V_i \cos \omega_o t \quad (2.7)$$

where

$$\eta_{ei} = V_{Pi} \frac{\partial C_i}{\partial x} = V_{Pi} \kappa_i \frac{C_{oi}}{d_o} \quad (2.8)$$

is the electromechanical coupling factor that defines the value of the transformer turns ratio at port  $i$  in Figure 2.3. In the last form of (2.8),  $\kappa_i$  is a modifying factor (to be derived later) that applies when the displacement amplitude of the resonator varies over the span of overlap by electrode  $i$ . (When the displacement amplitude is constant over this span,  $\kappa_i$  equals 1.) As will be seen,  $\kappa_i$  mainly modifies  $(C_{oi}/d_o)$ . So in general, formulas derived assuming a constant displacement amplitude over a given electrode span can be generalized to the non-constant case by merely multiplying any  $(C_{oi}/d_o)$  term by  $\kappa_i$  calculated for the corresponding vibration mode shape.

At resonance, the second term of (2.6) is  $90^\circ$  phase-shifted from the input, which means it is in phase with the displacement. This, together with the fact that it is also proportional to the displacement amplitude  $\mathcal{R}$ , identifies this force component as equivalent to a stiffness, but in this case, one generated via electrical means. In particular, this component arises from the increase and decrease in electric field strength across the electrode-to-resonator gap as the gap shrinks and grows, respectively, during mechanical resonance vibration. When the disk sidewall gets close to the electrode, the force pulling it into the electrode grows, and vice versa for the other direction, i.e., it shrinks as the disk sidewall moves away from the electrode. Thus, rather than acting to oppose displacement, as is the case for mechanical stiffness, this force acts to enhance it, which effectively makes it a negative electrical stiffness at port  $i$ , with spring constant magnitude equal to (using (2.6))

$$k_{ei} = \left( V_{Pi}^2 + \frac{V_i^2}{2} \right) \frac{C_{oi}}{d_o^2} \approx V_{Pi}^2 \frac{C_{oi}}{d_o^2} \quad (2.9)$$

where the last form assumes that  $V_i$  is much smaller than  $V_{Pi}$ —a condition for which the reader is cautioned isn't always the case, such as in micromechanical mixers [11]. For the case where the dynamic stiffness of the resonator varies over the span of the electrode-to-resonator overlap, Section 2.3 will show that the  $\kappa_i$  factor once again applies, and (2.9) becomes

$$k_{ei} = V_{Pi}^2 \left( \kappa_i \frac{C_{oi}}{d_o} \right)^2 \frac{1}{C_{oi}} = \frac{\eta_{ei}^2}{C_{oi}} \quad (2.10)$$

When the frequency of  $v_i$  matches one of the mode frequencies of the disk, the force given by (2.6) ensues, and the disk begins to vibrate in (essentially) that mode shape, with a resonance frequency shifted by the electrical stiffnesses generated by the electrode-to-resonator voltage drops at each port  $i$  according to [47]

$$\begin{aligned} f_o &= \frac{1}{2\pi} \sqrt{\frac{k_r}{m_m}} = \frac{1}{2\pi} \sqrt{\frac{k_m - \sum_{i=1}^n k_{ei}}{m_m}} \\ &= \frac{1}{2\pi} \sqrt{\frac{k_m}{m_m}} \left[ 1 - \sum_{i=1}^n \frac{k_{ei}}{k_m} \right]^{1/2} = f_{nom} \left[ 1 - \sum_{i=1}^n \frac{k_{ei}}{k_m} \right]^{1/2} \end{aligned} \quad (2.11)$$

where  $f_{nom}$  is the nominal resonance frequency of the disk (i.e., with no voltages applied),  $k_r$  is the total stiffness including mechanical and electrical components of the resonator at a maximum amplitude location,  $n$  is the number of parallel-plate electrodes overlapping the disk, and  $m_m$  and  $k_m$  are its dynamic mechanical mass and stiffness, respectively, again at the specified maximum amplitude location.

To attain the circuit of Figure 2.3, we start with the circuit of Figure 2.1 and first separate  $c_x$  into four capacitors:  $c_x = 1/k_m$  to model the mechanical stiffness of the resonator structure, and four negative capacitors of the form

$$-c_{ei} = -\frac{1}{k_{ei}} = -\frac{C_{oi}}{\eta_{ei}^2} \quad (2.12)$$

to model electrical stiffnesses generated at the  $i$  ports, as shown in Figure 2.5. Reflecting the electrical stiffness-based capacitors through the transformers to outside the core  $lcr$  loop yields the circuit Figure 2.3, where the physical shunt electrode-to-resonator capacitors  $C_{oi}$  are now matched by series negative capacitors of exactly the same values.

Note that the disk's resonance frequency dependence on DC-bias voltage  $V_P$  is now entirely captured by the electromechanical coupling coefficients  $\eta_{ei}$ . Thus, no arrow is needed through the motional capacitor, as needed in the conventional circuit of Figure 2.1, although one might want to draw arrows through the  $\eta_{ei}$ 's as reminders that they are tunable via the  $V_{Pi}$ 's. More importantly,

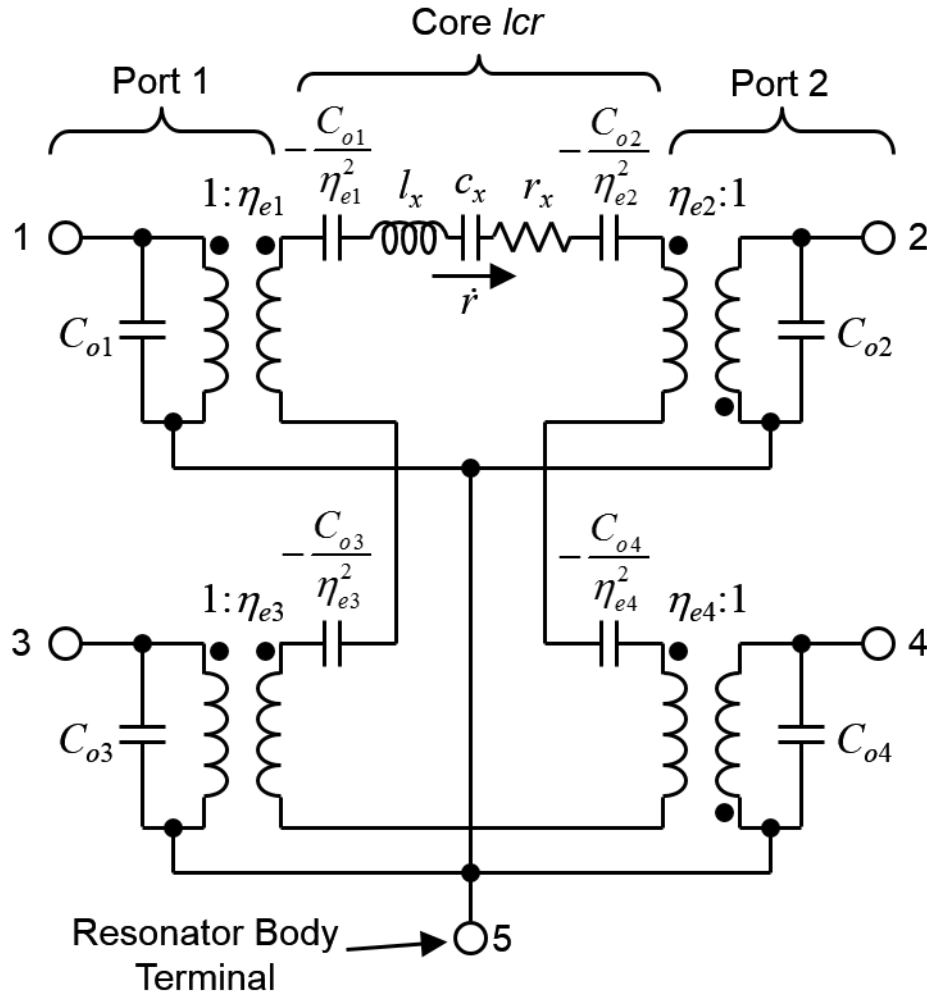


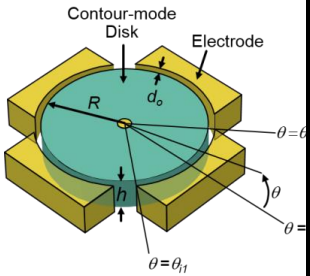
Figure 2.5: Circuit for the device of Figure 2.4 explicitly showing capacitors modeling the mechanical stiffness and electrical stiffness normally combined into  $c_x$ . Here, negative capacitors modeling electrical stiffnesses from ports 1 and 2, and equal to  $-1/k_{e1}$  and  $-1/k_{e2}$ , respectively, are shown with their actual values (in terms of  $C_o$  and  $\eta_e$ ).

the value of the core  $c_x$  element stays constant, as it should. The negative  $C_o$  is also a static capacitor, just like the positive  $C_o$  of the physical shunt electrode-to-resonator capacitance. With this circuit, by mere inspection, a designer can now immediately see that the electrical stiffness phenomenon presents the opportunity to effectively cancel the shunt  $C_o$  in certain circuit configurations—something often desirable in filter applications—or vice versa, i.e., the shunt  $C_o$  negates the electrical stiffness—something often desirable in some oscillator applications. These opportunities will be explored later in Section 2.5.

First, however, explicit expressions for the equivalent circuit elements in Figure 2.3 for a disk operating in its radial-contour and wine-glass modes are needed.

## 2.2 Negative $C_o$ Equivalent Circuit for a Capacitive-Gap Transduced Radial Contour Mode Disk

Table 2-I: Radial-Contour Mode Design Equations and Procedure Summary

Objective/Procedure	Parameter	Relevant Design Equations for a Given Parameter	Eq.
	Solve For $\zeta$	$\frac{\zeta}{\xi} \cdot \frac{J_0(\zeta/\xi)}{J_1(\zeta/\xi)} = 1 - \sigma$ $\zeta = 2\pi f_{nom} R \sqrt{\frac{\rho(2+2\sigma)}{E}}$ $\xi = \sqrt{\frac{2}{1-\sigma}}$	(2.13)
	Resonance Frequency	$f_{nom} = \frac{K_{(R,m),mat}}{2R} \sqrt{\frac{E}{\rho}}$ , where $K_{(R,m),mat} = \frac{\zeta_{(R,m),mat}}{\pi} (2+2\sigma)^{-1/2}$ <p>where <math>R</math> denotes the disk radius, <math>E</math> and <math>\sigma</math> are the Young's modulus and Poisson ratio, and <math>m =</math> mode number</p>	(2.14)
<p><u>Given:</u> <math>f_{nom}</math>, <math>V_P</math>, <math>R_{xij}</math> (= resistance between terminals <math>i</math> and <math>j</math>).</p> <p><u>Find:</u> radius <math>R</math>, electrode-to-resonator gap spacing <math>d_o</math>.</p> <ol style="list-style-type: none"> <li>Choose <math>E</math>, <math>\rho</math>, and <math>\sigma</math> by choice of structural material.</li> <li>Choose thickness <math>h</math>.</li> <li>Use (2.14) to find the <math>R</math> needed to achieve <math>f_{nom}</math>. Use (2.13) to get <math>\zeta</math> in the process.</li> <li>Use (2.18) to find the <math>d_o</math> needed to achieve <math>R_x</math>.</li> <li>(2.15)-(2.18) yield all needed values in the transformer-based negative <math>C_o</math> equivalent circuit.</li> </ol>	Core Equiv. Circuit Elements	$l_x = m_m(R) = \frac{2\pi\rho h \int_0^R r J_1^2(\varphi r) dr}{J_1^2(\varphi R)}$ , $\varphi = \sqrt{\frac{\omega_o^2 \rho}{\left(\frac{2E}{2+2\sigma} + \frac{E\sigma}{1-\sigma^2}\right)}}$ $c_x = \frac{1}{k_m(R)} = \frac{1}{\omega_{nom}^2 m_m}$ $r_x = b_m(R) = \frac{\sqrt{k_m m_m}}{Q} = \frac{\omega_{nom} m_m}{Q}$	(2.15)
	Static Overlap Capacitor	$C_{oi} = \frac{\epsilon_o(\theta_{i2} - \theta_{i1})Rh}{d_o}$	(2.16)
	Electro-mech. Coupling Coefficient	$\eta_{ei} = V_{Pi} \frac{C_{oi}}{d_o}$	(2.17)
	Motional Resistance, Capacitance, and Inductance	$R_{xij} = \frac{r_x}{\eta_{ei}\eta_{ej}}$ , $C_{xij} = c_x \eta_{ei}\eta_{ej}$ , $L_{xij} = \frac{l_x}{\eta_{ei}\eta_{ej}}$	(2.18)



As shown in Figure 2.2(d), the radial-contour mode shape is one where all points on the side-walls of the vibrating disk move the same amount, with the same velocity. As such, displacement as a function of angle  $\theta$  is constant, so  $\kappa_i = 1$  in the formulations of the previous section. In particular, (2.8) with  $\kappa_i = 1$  provides the needed value of turns ratios  $\eta_{ei}$  for each of the transformers in Figure 2.3.

With knowledge of the transformer turns ratios, all that remains to specify the entire equivalent circuit is specification of the core  $lcr$ . In the circuit of Figure 2.3, the values for the core  $lcr$  elements take on the actual values of dynamic mass, stiffness, and damping, for the resonator being modeled at the core  $lcr$  location. Each of these can be derived by consideration of the total kinetic energy of resonant disk structure and its radial velocity at the disk edges. Reference [47] has actually already correctly derived expressions for the core  $lcr$  of a radial-contour mode disk resonator, as well as associated mathematical expressions describing its mode shape and resonance frequency. Thus, there is no need to do this, here. Instead, Table 2-I summarizes the needed expressions while also succinctly presenting a design flow to achieve a radial-contour mode disk resonator like that of Figure 2.2 with a specific operating frequency and with specific motional resistances  $R_{xij}$  between its electrode terminals.

Since the displacement amplitude is the same at all locations along the perimeter of a disk vibrating in the radial-contour mode shape, the expressions for the turns ratios in Figure 2.3 are quite simple, requiring no integration. In addition, the integral formulation of (2.15) needed to determine the dynamic mass  $m_m$  of a disk operating in its  $m^{\text{th}}$  radial-contour mode always yields the same factor  $\chi$  modifying the physical mass of disk for that value of  $m$ , regardless of disk radius. In other words, for a radial-contour mode disk of any radius, the dynamic mass expression in (2.15) reduces to

$$m_m = \chi M_{tot} = \chi \rho \pi R^2 h \quad (2.19)$$

where  $\rho$ ,  $R$ , and  $h$  are the mass density, radius, and thick-ness, respectively, of the disk, and  $\chi = 0.763, 0.967, 0.987$  for a disk operating in its first, second, and third radial-contour modes, respectively. Note how the disk dynamic mass approaches its physical static mass as mode number rises. The simplicity of its equivalent circuit model afforded by equal displacements along its contour makes a radial-contour mode disk resonator ideal for use in complex mechanical circuits, such as that of [23][48], which employs large arrays of such disks.

One consequence of a mode shape with equal displacements at all points on the disk perimeter is that all currents flow in the same direction, i.e., either into the port or out of the port. They thus sum and flow into the DC-bias voltage source in phase. This by itself is not overly problematic. However, if there is any resistance in series with the DC-bias voltage source, e.g., interconnect or contact resistance, currents flowing through this resistance manifests as loss that lowers the  $Q$  of the device. In other words, radial-contour mode devices suffer from  $Q$ -loading by not only parasitic input and output interconnect resistance, but also from the DC-bias interconnect line. To correctly

model this important behavior, the radial-contour mode equivalent circuit of Figure 2.3 reverses the polarities of the transformers on the right side with respect to those on the left. (Note that the circuit could also be drawn with all ports on the left, in which case all transformers would have the same turns polarity.) As will be seen, when used in a multiple port configuration with designated inputs and outputs, the above makes the device appear inductive when interacting with feedthrough currents—something that could be used to advantage to effect loss poles below the pass-band in certain filters [31].

### 2.2.1 Design Example: 218-MHz Radial-Contour Mode Disk

Table 2-III presents the results of using the procedure of Table 2-I to design a 218-MHz radial-contour mode disk with characteristics as presented in the top “Design Variables” section. Given the desired resonance frequency and thickness, solution of (2.14) yields a needed radius of 12.1  $\mu\text{m}$ . With all dimensions now established, and assuming an electrode configuration like that of Figure 2.2(c) the values for the equivalent circuit elements of Figure 2.3 now follow from (2.15)-(2.18) and are summarized in the “4-Port Equivalent Circuit Variables” section of Table 2-III.

The actual radial-contour mode device to be evaluated in Section 2.4 was designed to resonate at 218 MHz, but is actually a two-port device that essentially combines ports 1 and 2 to form an input port A and ports 3 and 4 to form an output port B. This electrode configuration favors the radial-contour mode and suppresses to some degree the wine-glass and other modes. The actual tested device uses electrodes that do not quite span half the disk’s circumference, each rather spanning only  $-65^\circ$  to  $+65^\circ$ . The “2-Port Equivalent Circuit Variables” section of Values of the electromechanical couplings for ports A and B of the fabricated two-port version of this device, plus element values seen looking across its two opposing electrodes, are listed in the “2-Port Equivalent Circuit Variables” section of Table 2-III.

It should be noted that there are many other electrode configurations capable of exciting this mode, using any number of electrodes, including just one fully surrounding electrode [49], which is actually the most effective way to excite this mode, since it suppresses other modes and provides the largest electromechanical coupling. It, however, does not suppress parasitic feedthrough currents the way a multiple electrode device can, so is useful mainly when disks are coupled to form a separate input and output, as in [23][48].

## 2.3 Negative $C_o$ Equivalent Circuit for a Capacitive-Gap Transduced Wine-Glass Mode Disk

Figure 2.2(e) presents the wine-glass disk (or more precisely, compound-(2,1)) mode shape [43][45][50], in which the disk expands along one axis while contracting along the orthogonal

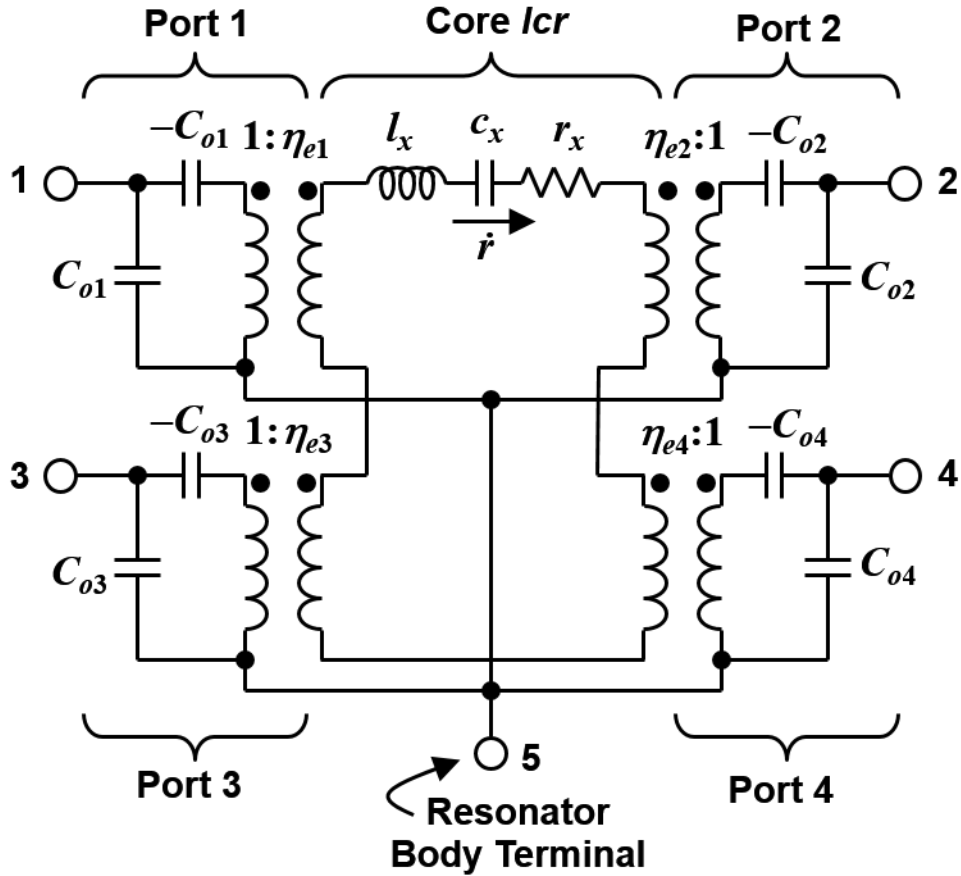


Figure 2.6: Negative capacitance small-signal AC equivalent circuit for a four-port capacitive-gap transduced micromechanical resonator, such as that of Figure 2.2, when operating in the wine-glass mode shown in Figure 2.2(e). Here, the polarities of the right side transformers are opposite to those in Figure 2.3.

axis. As shown, the wine-glass mode exhibits a perimeter displacement that varies over its electrode lengths. Thus,  $\kappa_i$  is not equal to 1, and determination of values for the effective electromechanical coupling and the electrical stiffness imposed by each electrode requires integration.

The mode shape further features sections on the disk edges that move out of phase. In particular, sections overlapping electrodes 1 and 3 move in phase, while those overlapping 2 and 4 move in the opposite phase. Their currents are thus similarly out-of-phase. For the case where the combination of all electrodes fully covers the edge of the disk, e.g., as in Figure 2.1, the total current going into the disk equals that exiting, and (ideally) none of the current enters the DC-bias source, VP. This then eliminates loss due to resistance in series with the DC-bias voltage source, giving the wine-glass disk a  $Q$ -advantage over its radial-contour mode counterpart. Figure 2.6 presents the wine-glass disk negative capacitance equivalent circuit for the device of Figure 2.2(c), where ports 2 and 4 on the right side possess transformer polarities that reflect the stated current directions.

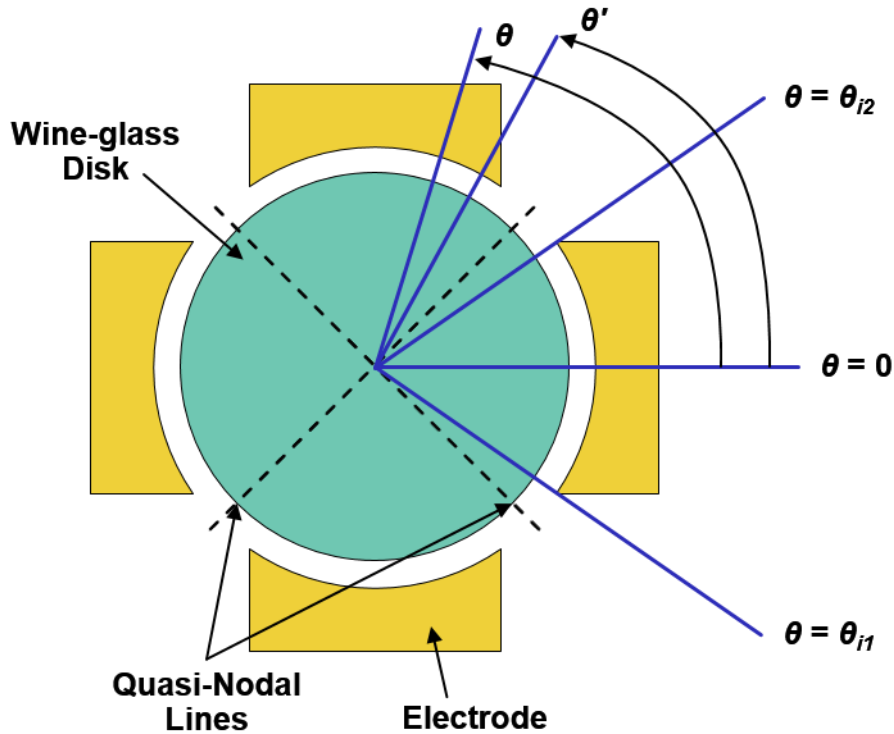


Figure 2.7: Schematic showing variables used in the derivation of the negative capacitance equivalent circuit for a capacitive-gap transduced disk operating in its wine-glass mode shape.

The device of Figure 2.2(c) situates its four electrodes such that their midpoints overlap the disk at anti-nodes, where the dynamic mass and stiffness are minimized. Alignment of electrode midpoints with anti-nodes, together with proper phasing of signals applied to these electrodes, is key to selecting the mode in question. In general, however, any number of electrodes can be used, and they can span any angular range over the disk circumference that still excites the wine-glass mode. Thus, for greatest generality, the formulation for equivalent circuit elements should be applicable to an electrode with any span over the disk perimeter.

### 2.3.1 Core *LCR*

As with the radial-contour mode version, the element values of the core *lcr* in Figure 2.6 are specified by the actual values of dynamic mass, stiffness, and damping, for the resonator being modeled. The equivalent dynamic mass at a location  $(r, \theta)$  on a disk operating in its wine-glass disk mode can be obtained by dividing the total kinetic energy of the disk by one-half the square of the velocity at that location [27] [31]. Doing so, with reference to Figure 2.7, yields

$$\begin{aligned}
m_m(r, \theta) &= \frac{KE_{tot}}{(1/2)[v(r, \theta)]^2} = \frac{\frac{1}{2} \int_0^{2\pi} \int_0^R dm \times [v(r', \theta')]^2}{(1/2)[v(r, \theta)]^2} \\
&= \frac{\rho h \int_0^{2\pi} \int_0^R [\mathfrak{R}_{mode}(r', \theta')]^2 r' dr' d\theta'}{[\mathfrak{R}_{mode}(r, \theta)]^2}
\end{aligned} \tag{2.20}$$

where  $v(r, \theta) = \omega_o \mathfrak{R}(r, \theta)$  is the resonance radial velocity amplitude at location  $(r, \theta)$ ,  $\mathfrak{R}(r, \theta)$  is the radial displacement amplitude at location  $(r, \theta)$ ,  $dm$  is a differential mass element,  $R$  is the disk radius, and  $\mathfrak{R}_{mode}(r, \theta)$  describes the mode shape, essentially giving the relative radial amplitude of vibration at a point  $(r, \theta)$  versus a point  $(r', \theta')$  on the disk. For the wine-glass mode, the mode shape function takes on the approximate form [50]

$$\mathfrak{R}_{mode}(r, \theta) = \left[ \frac{\partial}{\partial r} J_n \left( \frac{\zeta}{\xi R} r \right) + \frac{nB}{A} \frac{1}{r} J_n \left( \frac{\zeta}{R} r \right) \right] \cos n\theta \tag{2.21}$$

where

$$\zeta = 2\pi f_{nom} R \sqrt{\frac{\rho(2+2\sigma)}{E}}, \quad \xi = \sqrt{\frac{2}{1-\sigma}}, \quad n = 2 \tag{2.22}$$

and where  $J_n(x)$  is the Bessel function of the first kind,  $E$  and  $\sigma$  are the Young's modulus and Poisson ratio, respectively, of the resonator structural material,  $B/A = -4.5236$  and  $n = 2$  for the wine-glass mode, and  $f_{nom}$  is the nominal resonance frequency of the disk (in this case, when operating in the wine-glass mode).

The resonance frequency  $f_{nom}$  can be determined by simultaneously solving (2.22) with [50]

$$\left[ \Psi_n \left( \frac{\zeta}{\xi} \right) - n - q \right] \cdot \left[ \Psi_n(\zeta) - n - q \right] = (nq - n)^2 \tag{2.23}$$

where

$$\Psi_n(x) = \frac{xJ_{n-1}(x)}{J_n(x)}, \quad q = \frac{\zeta^2}{2n^2 - 2} \tag{2.24}$$

and where  $n$  denotes the compound mode in question. As previously mentioned, the wine-glass disk mode corresponds to the  $(n, m) = (2, 1)$  compound mode, where the "1" denotes the fundamental of this mode. Although higher modes exist for  $m > 1$ , this discussion focuses on the compound  $(2, 1)$  mode.

Although solution of (2.22)-(2.24) as described provides an accurate value for the resonance frequency of the wine-glass (i.e., compound-(2,1)) mode, it does not readily impart design insight.

To provide better insight to variable dependencies, rearrangement and simplification of (2.22)-(2.24) yields the closed form

$$f_{nom} = \frac{K_{(n,m),mat}}{2R} \sqrt{\frac{E}{\rho}} \quad (2.25)$$

where the constant

$$K_{(n,m),mat} = \frac{\zeta_{(n,m),mat}}{\pi} (2 + 2\sigma)^{-1/2} \quad (2.26)$$

is a dimensionless frequency parameter that depends upon the structural material and is independent of radius. It can be obtained by first solving (2.22)-(2.24) for  $\zeta = \zeta_{(n,m),mat}$  then substituting this value into (2.26). For polysilicon structural material (with  $E = 150$  GPa,  $\rho = 2,300$  kg/m<sup>3</sup>, and  $\sigma = 0.226$ ),  $\zeta_{(2,1),polySi} = 2.344$ , and  $K_{(2,1),polySi} = 0.476$ . For polydiamond (with  $E = 1,198$  GPa,  $\rho = 3,500$  kg/m<sup>3</sup>, and  $\sigma = 0.0691$  [51]),  $\zeta_{(2,1),polyDiamond} = 2.339$ , and  $K_{(2,1),polyDiamond} = 0.509$ .

With knowledge of the resonance frequency, the expression for dynamic stiffness follows readily from that for mass via the relationship between resonance frequency, mass, and stiffness, given by (2.11). Use of (2.11) yields

$$k_m(R, \theta) = \omega_{nom}^2 \cdot m_m(R, \theta) \quad (2.27)$$

where  $\omega_{nom}$  is the nominal radian resonance frequency of the disk (with no voltages applied).

Using (2.20) and (2.27), Figure 2.8 plots the dynamic mass and stiffness at locations on the edge of a disk, i.e., at  $r = R$ , vibrating in the wine-glass mode as a function of  $\theta$ , showing minima in both at mode shape maxima, i.e., at anti-nodes. By convention, the point where the equivalent mass minimizes is taken as the location governing the core  $lcr$  in the equivalent circuit of Figure 2.6, which in the coordinate system of Figure 2.8 occurs at  $\theta = \theta_{core} = 0^\circ$  for electrode 3. Of course, there are other minimum mass locations, e.g.,  $\theta = 90^\circ$  for electrode 2, and any of these can also be selected as the core location, but for this analysis, we choose  $\theta_{core} = 0^\circ$ . At this location, the values of the elements in the core  $lcr$  become

$$l_x = m_m(R, \theta_{core}) = \frac{\rho h \int_0^{2\pi} \int_0^R [\Re_{mode}(r', \theta')]^2 r' dr' d\theta'}{[\Re_{mode}(R, \theta_{core})]^2} \quad (2.28)$$

$$\frac{1}{c_x} = k_m(R, \theta_{core}) = \frac{\omega_{nom}^2 \rho h \int_0^{2\pi} \int_0^R [\Re_{mode}(r', \theta')]^2 r' dr' d\theta'}{[\Re_{mode}(R, \theta_{core})]^2} \quad (2.29)$$

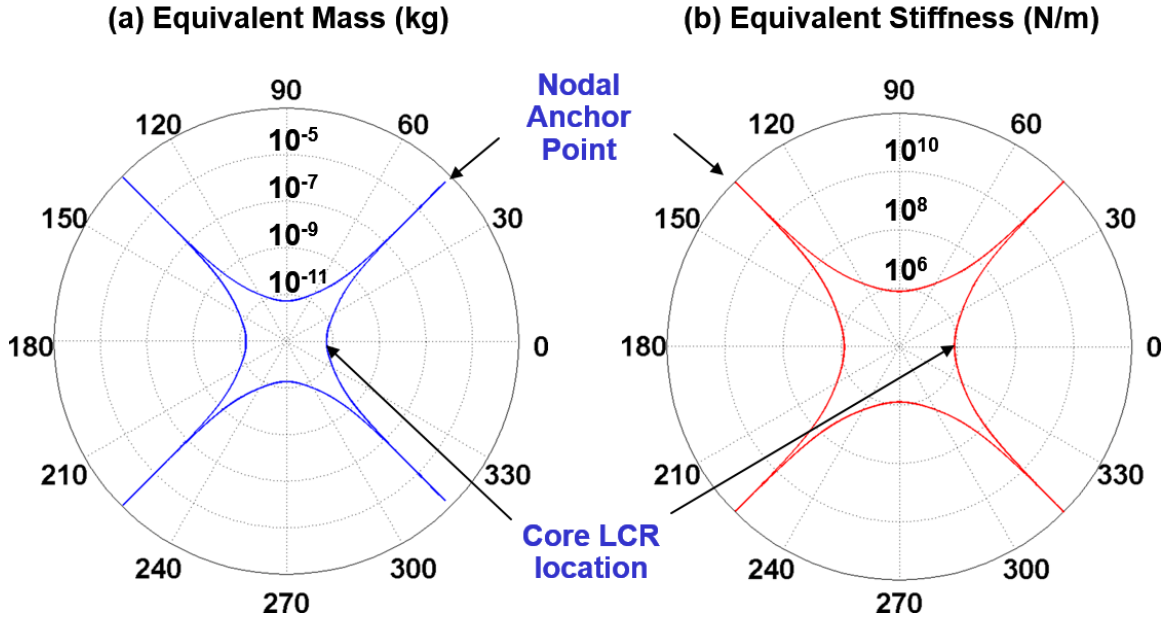


Figure 2.8: Plot of dynamic (a) mass and (b) stiffness at locations on the edge of a disk, i.e., at  $r = R$ , vibrating in the wine-glass mode as a function of angle  $\theta$ . The circular axis convey lines of (a) equal mass and (b) equal stiffness.

$$\begin{aligned}
 r_x = b_m(R, \theta_{core}) &= \frac{\sqrt{k_m(R, \theta_{core}) \cdot m_m(R, \theta_{core})}}{Q} \\
 &= \frac{\omega_{nom} \rho h \int_0^{2\pi} \int_0^R [\Re_{mode}(r', \theta')]^2 r' dr' d\theta'}{Q [\Re_{mode}(R, \theta_{core})]^2}
 \end{aligned} \tag{2.30}$$

where the  $b_m$  in (2.30) is the damping constant from the equation of motion describing this system:

$$m_m \ddot{r} + b_m \dot{r} + k_m r = F_i(t) \tag{2.31}$$

Using (2.28), the mass modifier factor in (2.19) that relates the actual physical mass of a disk to its dynamic mass at  $\theta_{core} = 0^\circ$  on its perimeter when vibrating in its wine-glass mode is found to be  $\chi = 0.360$ . As with the radial-contour mode, this value is largely independent of radius, thickness, and material type.

From (2.19), the dynamic mass at the core *lcr* location  $\theta_{core} = 0^\circ$  of a disk vibrating in its wine-glass mode has a quadratic dependence on disk radius. The dynamic stiffness at this location, on the other hand, is independent of radius and depends mainly on thickness, as can easily be seen using (2.19), (2.25), (2.26), and (2.27) to yield

$$k_m(R, 0) = \pi^3 K_{(2,1),mat}^2 \chi E h \tag{2.32}$$

As similar analysis for the damper constant yields

$$b_m(R, 0) = \frac{1}{Q} \pi^2 K_{(2,1),mat}^2 \chi \sqrt{\rho E R h} \quad (2.33)$$

which clearly has a linear dependence on radius  $R$  that, from (2.25), amounts to a reciprocal dependence on frequency, i.e., it gets smaller as frequency increases. (But note that, as will be seen, motional resistance rises linearly with frequency, since the electrode-to-resonator overlap shrinks as radius decreases.)

### 2.3.2 Static Electrode-to-Resonator Overlap Capacitance

For the case of an electrode spanning  $\theta = \theta_{i1}$  to  $\theta_{i2}$  as shown in Figure 2.7, the static overlap capacitance is given by

$$C_{oi} = \frac{\varepsilon_o (\theta_{i2} - \theta_{i1}) R h}{d_o} \quad (2.34)$$

where  $\varepsilon_o$  is the permittivity of vacuum. This equation holds whether the disk operates in the radial-contour or wine-glass mode. As will be seen, this equation forms the starting point from which the electromechanical coupling factor for a capacitive transducer can be derived.

### 2.3.3 Electromechanical Coupling Factor

As mentioned in Section 2.1, the electromechanical coupling factor  $\eta_{ei}$  at port  $i$  determines the turns ratio of the transformer used to model the input voltage-to-force and/or input current-to-velocity transfer functions at that port. As such, it can be expressed as either

$$\begin{aligned} \eta_{ei} &= \frac{F_i}{V_i} = \frac{F(R, \theta_{core})}{V_i} \quad \text{or} \\ \eta_{ei} &= \frac{I_{ri}}{\dot{\mathcal{R}}_i} = \frac{I_{ri}}{j\omega \mathcal{R}_i} = \frac{I_{ri}}{j\omega \mathcal{R}(R, \theta_{core})} \end{aligned} \quad (2.35)$$

where  $V_i$  is the magnitude of the AC voltage applied across the electrode-to-resonator gap at port  $i$ ,  $F_i$  is the magnitude of the total lumped force generated by  $V_i$  and applied to the disk sidewall at the core  $lcr$  location  $(R, \theta_{core})$ ,  $\mathcal{R}_i$  is the ensuing radial displacement amplitude at that same location, and  $I_{ri}$  is the resulting current going into the electrode. Note that there should be only one coupling factor to simultaneously model both transfer functions—something that [43] lacks.

Derivation of the electromechanical coupling factor from the voltage-to-force relationship starts with the general expression for force at resonance, which from (2.1) takes the form

$$F_i = V_{pi} \frac{\partial C_i}{\partial r} V_i \quad (2.36)$$



Because the dynamic mass and stiffness for the wine-glass mode are not constant over the length of (or angle subtended by) the electrode, determination of the  $\partial C_i/\partial x$  term requires a double integration over the electrode length to first obtain an expression for the resonance displacement at the core *lcr* reference location as a function of the excitation voltage across the electrode-to-resonator gap.

To do this, referring to Figure 2.7, the electrode is first sectioned into infinitesimally small portions  $d\theta$  along its length, each of which contributes a radial force

$$dF = V_{Pi}V_i \frac{\epsilon_o R h d\theta}{d_o^2} \quad (2.37)$$

Each such force induces a radial displacement amplitude at its location (i.e., at  $\theta$ ) given by

$$d\mathfrak{R}(R, \theta) = \frac{Q}{k_m(R, \theta)} V_{Pi}V_i \frac{\epsilon_o R h d\theta}{d_o^2} \quad (2.38)$$

At resonance, the radial displacement amplitude at each location is related to that at another location by the mode shape expression, given by (2.21) for the wine-glass mode. In particular, the radial displacement amplitude contribution at location  $\theta$  generated by a force at  $\theta'$  is

$$d\mathfrak{R}(R, \theta) = \frac{\mathfrak{R}_{\text{mode}}(R, \theta)}{\mathfrak{R}_{\text{mode}}(R, \theta')} \cdot d\mathfrak{R}(R, \theta') \quad (2.39)$$

To obtain the total resonance displacement amplitude at a location  $\theta$ , one must sum, i.e., integrate, all displacement contributions to location  $\theta$  from forces at all other port  $i$  electrode-to-resonator overlap locations  $\theta'$  as follows:

$$\begin{aligned} \mathfrak{R}(R, \theta) &= \int_{\theta_{i1}}^{\theta_{i2}} d\mathfrak{R}(R, \theta) \\ &= Q V_{Pi}V_i \frac{\epsilon_o R h}{d_o^2} \int_{\theta_{i1}}^{\theta_{i2}} \frac{\mathfrak{R}_{\text{mode}}(R, \theta)}{\mathfrak{R}_{\text{mode}}(R, \theta')} \cdot \frac{d\theta'}{k_m(R, \theta')} \end{aligned} \quad (2.40)$$

Again, for equivalent circuit purposes, the resonance displacement amplitude at the core *lcr* location  $\theta_{\text{core}}$ , where the displacement amplitude is greatest, is of particular interest and can be found by evaluating (40) at  $\theta = \theta_{\text{core}}$ . For the electrode of Figure 2.7,  $\theta_{\text{core}} = 0^\circ$  for the wine-glass mode shape shown.

To obtain an expression for electromechanical coupling  $\eta_{ei}$ , (2.40) can be used to express the resonance lumped force  $F_i$  at port  $i$  as a function of input voltage amplitude  $V_i$  as follows:

$$\begin{aligned}
F_i &= \frac{k_m(R, \theta_{core}) \cdot \Re(R, \theta_{core})}{Q} \\
&= V_{Pi} V_i \frac{\varepsilon_o R h}{d_o^2} \int_{\theta_{i1}}^{\theta_{i2}} \frac{\Re_{mode}(R, \theta_{core})}{\Re_{mode}(R, \theta')} \cdot \frac{k_m(R, \theta_{core})}{k_m(R, \theta')} \cdot d\theta' \\
&= V_i V_{Pi} \frac{C_{oi}}{d_o} \frac{1}{(\theta_{i2} - \theta_{i1})} \int_{\theta_{i1}}^{\theta_{i2}} \frac{\Re_{mode}(R, \theta')}{\Re_{mode}(R, \theta_{core})} \cdot d\theta' \\
&= V_{Pi} \kappa_i \frac{C_{oi}}{d_o} V_i \\
&= \eta_{ei} V_i
\end{aligned} \tag{2.41}$$

where (2.34) has been used along with (2.29), and where the electromechanical coupling factor is seen to be

$$\eta_{ei} = V_{Pi} \kappa_i \frac{C_{oi}}{d_o} \tag{2.42}$$

where

$$\kappa_i = \frac{1}{(\theta_{i2} - \theta_{i1})} \int_{\theta_{i1}}^{\theta_{i2}} \frac{\Re_{mode}(R, \theta')}{\Re_{mode}(R, \theta_{core})} \cdot d\theta' \tag{2.43}$$

is a factor that modifies the (easy to remember) electromechanical coupling of an ideal parallel-plate capacitive-gap transducer to account for a non-constant resonance displacement (or velocity) profile over the electrode length. Equation (2.43) should be evaluated for each electrode  $i$  overlapping the disk sidewalls to obtain the turns ratio  $\eta_{ei}$  for each transformer modeling electromechanical couplings through the electrodes. Doing so for  $\theta_{core} = 0^\circ$  reveals that  $\kappa_i$  remains constant as disk radius changes, posting a value of 0.724 for the wine-glass mode shape for a layout defined electrode span angle of  $\theta_{i2} = -\theta_{i1} = 38.6^\circ$ , which is the angle used for the measured devices to be described later.

To provide a sense of how strongly  $\kappa_i$  changes with the length of an electrode centered at  $\theta_{core} = 0^\circ$ , Figure 2.9 plots  $\kappa_i$  versus electrode length, as defined by the inset figure. Here,  $\kappa_i = 1$  when the electrode length is infinitesimally small, as expected, but decreases steadily as the electrode grows, until the electrode angle subtends the entire right half of the disk, at which point  $\kappa_i$  goes to zero. This makes sense, since a semicircular electrode should (ideally) not be able to excite the wine-glass disk mode (although it can certainly excite the radial-contour mode).

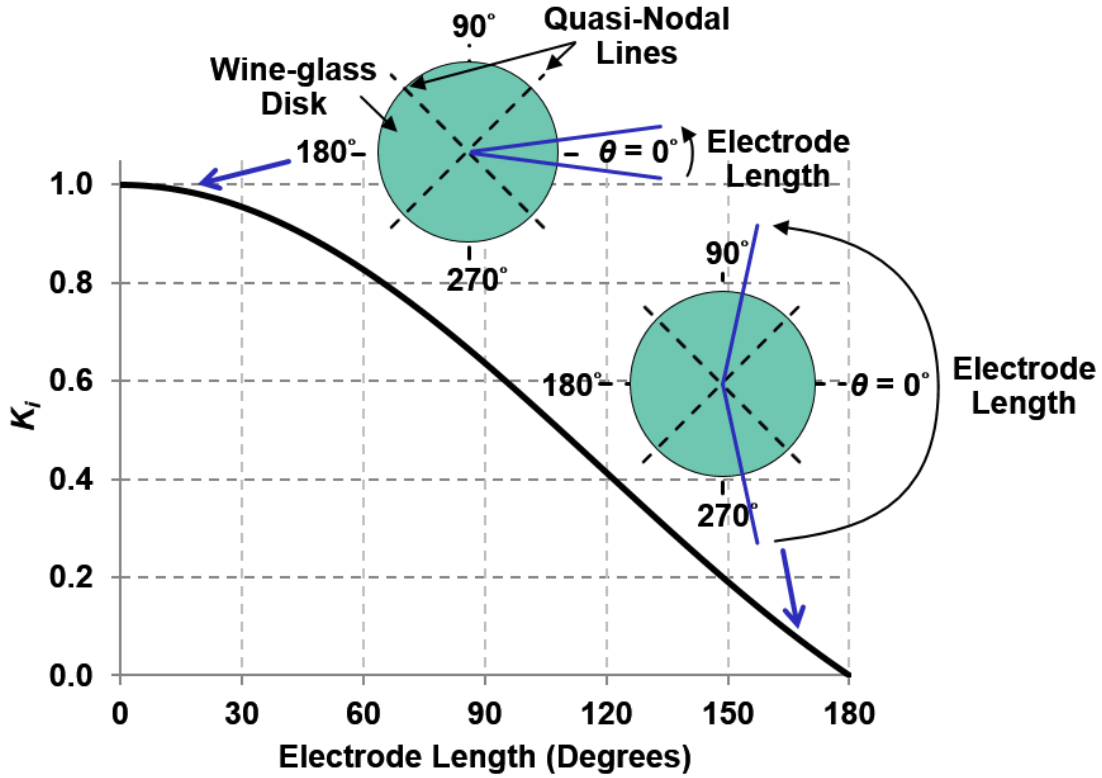


Figure 2.9: Plot of electromechanical coupling modification factor  $\kappa_i$  versus electrode length.

### 2.3.4 Motional Current

To obtain an expression for the motional current into port  $i$ , integration is also required, since the velocity term  $\partial r / \partial t$  in the general expression for output current at port  $i$

$$i_{ri} = V_{pi} \frac{dC_i}{dt} = V_{pi} \frac{\partial C_i}{\partial r} \frac{\partial r}{\partial t} \quad (2.44)$$

varies with angle  $\theta$ . Pursuant to performing this integration, the current flowing through a differential slice of electrode-to-resonator overlap  $d\theta$  at  $\theta$  takes on the form

$$\begin{aligned} di_{ri}(\theta) &= j\omega_o V_{pi} \frac{\epsilon_o R h}{d_o^2} \Re(R, \theta) d\theta \\ &= j\omega_o V_{pi} \frac{\epsilon_o R h}{d_o^2} \Re(R, \theta_{core}) \cdot \frac{\Re_{mode}(R, \theta)}{\Re_{mode}(R, \theta_{core})} \cdot d\theta \end{aligned} \quad (2.45)$$

where  $\omega_o$  is the frequency of vibration. Integrating this over the electrode overlap length yields

$$\begin{aligned}
i_{ri} &= j\omega_o V_{Pi} \frac{\varepsilon_o Rh}{d_o^2} \Re(R, \theta_{core}) \cdot \int_{\theta_{i1}}^{\theta_{i2}} \frac{\Re_{mode}(R, \theta)}{\Re_{mode}(R, \theta_{core})} d\theta \\
&= j\omega_o V_{Pi} \frac{C_{oi}}{d_o} \Re(R, \theta_{core}) \cdot \frac{1}{(\theta_{i2} - \theta_{i1})} \int_{\theta_{i1}}^{\theta_{i2}} \frac{\Re_{mode}(R, \theta)}{\Re_{mode}(R, \theta_{core})} d\theta \\
&= j\omega_o V_{Pi} \kappa_i \frac{C_{oi}}{d_o} \Re(R, \theta_{core}) \\
&= j\omega_o \eta_{ei} \Re(R, \theta_{core})
\end{aligned} \tag{2.46}$$

where (2.29), (2.34), (2.42), and (2.43) have been used to obtain the final form. Note that the value of  $\eta_{ei}$  given by (2.46) is identical to that for the voltage-to-force expression of (2.41), as it should be.

### 2.3.5 Electrical Spring Stiffness

The second term of (2.6) indicates that the force generated by the electrical stiffness phenomenon is a function of the displacement amplitude  $\Re$ . Thus, for a disk vibrating in the wine-glass mode, the variation of displacement amplitude along the angle subtended by an electrode-to-resonator overlap requires that integration be employed to obtain an accurate expression for the frequency-pulling electrical spring stiffness at that electrode.

Using the second term of (2.6), the differential element of electrical spring force over a differential angle  $d\theta'$  at location  $(R, \theta')$  along the  $i^{\text{th}}$  electrode-to-resonator overlap can be expressed as

$$\begin{aligned}
dF_{kei}(R, \theta') &= V_{Pi}^2 \frac{\varepsilon_o Rh d\theta'}{d_o^3} \Re(R, \theta') \\
&= V_{Pi}^2 \frac{\varepsilon_o Rh}{d_o^3} \Re(R, \theta) \cdot \frac{\Re_{mode}(R, \theta')}{\Re_{mode}(R, \theta)} \cdot d\theta'
\end{aligned} \tag{2.47}$$

Integrating over the angle subtended by the electrode yields for the total force (in quadrature with the input force at resonance) due to electrical stiffness

$$\begin{aligned}
F_{kei}(R, \theta) &= V_{Pi}^2 \frac{\varepsilon_o Rh}{d_o^3} \Re(R, \theta) \cdot \int_{\theta_{i1}}^{\theta_{i2}} \frac{\Re_{mode}(R, \theta')}{\Re_{mode}(R, \theta)} \cdot d\theta' \\
&= \left\{ V_{Pi}^2 \frac{C_{oi}}{d_o^2} \frac{1}{(\theta_{i2} - \theta_{i1})} \int_{\theta_{i1}}^{\theta_{i2}} \frac{\Re_{mode}(R, \theta')}{\Re_{mode}(R, \theta)} \cdot d\theta' \right\} \Re(R, \theta) \\
&= k_{ei}(R, \theta) \Re(R, \theta)
\end{aligned} \tag{2.48}$$

where

$$k_{ei}(R, \theta) = V_{Pi}^2 \frac{C_{oi}}{d_o^2} \left\{ \frac{1}{(\theta_{i2} - \theta_{i1})} \int_{\theta_{i1}}^{\theta_{i2}} \frac{\Re_{\text{mode}}(R, \theta')}{\Re_{\text{mode}}(R, \theta)} \cdot d\theta' \right\} \quad (2.49)$$

is the electrical stiffness as a function of angular location  $\theta$ . Again, the location dependence of (2.49) comes about due to the variation of displacement amplitude over the angle subtended by the electrode in question. The dependence modeled in (2.49) is not, however, sufficient to correctly model the frequency pulling afforded by the electrical stiffness. This is because the frequency pulling efficacy of electrical stiffness also depends on the mechanical stiffness over the electrode length, which also depends on angular location.

Indeed, from (2.11), the important parameter that gauges the frequency pulling efficacy of the electrical stiffness is the effective integrated ratio of the electrical stiffness to the mechanical stiffness averaged over the electrode length, which can be expressed as

$$\left\langle \frac{k_{ei}}{k_m} \right\rangle = \int_{\theta_{i1}}^{\theta_{i2}} \frac{k_{ei}(R, \theta)}{k_m(R, \theta)} \cdot \frac{d\theta}{(\theta_{i2} - \theta_{i1})} \quad (2.50)$$

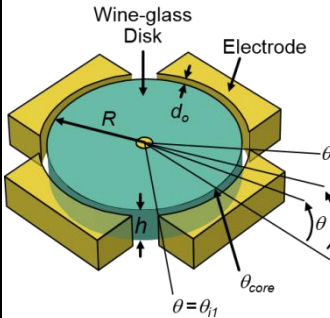
The expression for the total effective electrical stiffness (to be used in (2.11)) at port  $i$  then becomes

$$\begin{aligned} k_{ei} &= \left\langle \frac{k_{ei}}{k_m} \right\rangle \cdot k_m(R, \theta_{\text{core}}) \\ &= V_{Pi}^2 \frac{C_{oi}}{d_o^2} \frac{1}{(\theta_{i2} - \theta_{i1})^2} \cdot \int_{\theta_{i1}}^{\theta_{i2}} \int_{\theta_{i1}}^{\theta_{i2}} \frac{\Re_{\text{mode}}(R, \theta')}{\Re_{\text{mode}}(R, \theta)} \cdot \frac{k_m(R, \theta_{\text{core}})}{k_m(R, \theta)} \cdot d\theta d\theta' \\ &= V_{Pi}^2 \frac{C_{oi}}{d_o^2} \left\{ \frac{1}{(\theta_{i2} - \theta_{i1})} \int_{\theta_{i1}}^{\theta_{i2}} \frac{\Re_{\text{mode}}(R, \theta')}{\Re_{\text{mode}}(R, \theta_{\text{core}})} \cdot d\theta' \right\}^2 \\ &= V_{Pi}^2 \kappa_i^2 \frac{C_{oi}}{d_o^2} = \frac{\eta_{ei}^2}{C_{oi}} \end{aligned} \quad (2.51)$$

where (2.42) and (2.43) have been used to match (2.10).

It should be noted that all of the above formulations, specifically (2.41)-(2.43), (2.46), and (2.51), are completely consistent with the general ones of Section 2.1.

Table 2-II: Wine-Glass Mode Design Equations and Procedure Summary

Objective/Procedure	Parameter	Relevant Design Equations for a Given Parameter	Eq.
	Solve For $\zeta$	$\left[ \Psi_n \left( \frac{\zeta}{\xi} \right) - n - q \right] \cdot \left[ \Psi_n (\zeta) - n - q \right] = (nq - n)^2$ $\Psi_n (x) = \frac{x J_{n-1}(x)}{J_n(x)}, \quad q = \frac{\zeta^2}{2n^2 - 2},$ $\zeta = 2\pi f_{nom} R \sqrt{\frac{\rho(2+2\sigma)}{E}}, \quad \xi = \sqrt{\frac{2}{1-\sigma}},$	(2.52)
	Resonance Frequency	$f_{nom} = \frac{K_{(n,m),mat}}{2R} \sqrt{\frac{E}{\rho}}, \text{ where}$ $K_{(n,m),mat} = \frac{\zeta_{(n,m),mat}}{\pi} (2+2\sigma)^{-1/2}$	(2.53)
<p><u>Given:</u> <math>f_{nom}, R_x, V_p</math>.  <u>Find:</u> <math>R, d_o</math>.</p> <ol style="list-style-type: none"> <li>1. Choose <math>E, \rho</math>, and <math>\sigma</math> by choice of structural material.</li> <li>2. Choose thickness <math>h</math>.</li> <li>3. Use (2.53) to find the <math>R</math> needed to achieve <math>f_{nom}</math>.</li> <li>4. Use (2.57) to find the <math>d_o</math> needed to achieve <math>R_x</math>.</li> <li>5. (2.54)-(2.56) yield all needed values in the transformer-based negative <math>C_o</math> equivalent circuit.</li> </ol>	Core Equiv. Circuit Elements	$l_x = m_m(R, \theta_{core}) = \frac{\rho h \int_0^{2\pi} \int_0^R [R_{mode}(r', \theta')]^2 r' dr' d\theta'}{[R_{mode}(R, \theta_{core})]^2}$ $c_x = \frac{1}{k_m(R)} = \frac{1}{\omega_{nom}^2 m_m},$ $r_x = b_m(R) = \frac{\sqrt{k_m m_m}}{Q} = \frac{\omega_{nom} m_m}{Q}$ $R_{mode}(r, \theta) = \left[ \frac{\partial}{\partial r} J_n \left( \frac{\zeta}{\xi R} r \right) + \frac{nB}{A} \frac{1}{r} J_n \left( \frac{\zeta}{\xi R} r \right) \right] \cos n\theta$	(2.54)
	Static Overlap Capacitor	$C_{oi} = \frac{\epsilon_o (\theta_{i2} - \theta_{i1}) R h}{d_o}$	(2.55)
	Electromech. Coupling Coefficient	$\eta_{ei} = V_{Pi} \kappa_i \frac{C_{oi}}{d_o},$ $\kappa_i = \frac{1}{(\theta_{i2} - \theta_{i1})} \int_{\theta_{i1}}^{\theta_{i2}} \frac{R_{mode}(R, \theta')}{R_{mode}(R, \theta_{core})} \cdot d\theta'$	(2.56)
	Motional Resistance, Capacitance, and Inductance	$R_x = \frac{r_x}{\eta_{ei}^2}, \quad C_x = c_x \eta_{ei}^2, \quad L_x = \frac{l_x}{\eta_{ei}^2}$	(2.57)

### 2.3.6 Wine-Glass Disk Equivalent Circuit Summary

Table 2-II summarizes the equations needed to generate specific values for the elements in the small-signal equivalent circuit of Figure 2.6 for a wine-glass disk resonator. Like Table 2-I, the

Table 2-III: Summary of Designed and Simulated Disk Equivalent Circuit Element Values

	Parameter	Source	Radial-Contour Mode		Wine-Glass Mode		Units
			Designed	Simulated	Designed	Simulated	
Design Variables	Disk Radius, $R$	Layout	12.10	<b>12.15</b>	32.0	<b>32.07</b>	$\mu\text{m}$
	Frequency, $f_o$	(2.11)	218.138	<b>217.170</b>	61.181	<b>61.033</b>	MHz
	Nominal resonance frequency, $f_{nom}$	(2.14) (2.53)	218.260	<b>217.288</b>	61.201	<b>61.055</b>	MHz
	Electrode Span Angle, $-\theta_{i1}, \theta_{i2}$	Layout	65°	65°	38.6°	38.6°	°
	Disk Thickness, $h$	Layout	2.1	2.1	2.1	2.1	$\mu\text{m}$
	Resonator Quality Factor, $Q$	Measured	15,000	<b>12,392</b>	50,000	<b>46,560</b>	–
	DC Bias Voltage, $V_P$	Measured	15	15	14	14	V
	Electrode-to-Resonator Gap, $d_o$	Measured	40.0	<b>40.56</b>	85.0	<b>84.1</b>	nm
4-Port Equivalent Circuit Variables	Inductance at $\theta_{core}, l_x$	(2.15) (2.54)	1695.410	<b>1710.623</b>	5395.005	<b>5420.964</b>	fH
	Capacitance at $\theta_{core}, c_x$	(2.15) (2.54)	313.628	313.628	1253.507	1253.507	nF
	Resistance at $\theta_{core}, r_x$	(2.15) (2.54)	155.002	<b>188.464</b>	41.492	<b>44.664</b>	n $\Omega$
	Static Overlap Capacitance, $C_o$	(2.34)	12.762	<b>12.643</b>	18.863	<b>19.111</b>	fF
	Electromech. Coupling, $\eta_{ei}$	(2.17) (2.56)	4785.600	<b>4676.075</b>	1124.270	<b>1151.220</b>	nC/m
2-Port Eq. Circuit Variables	Electromech. Coupling, $\eta_{eA} = \eta_{eB}$	(2.58)	4785.600	<b>4676.075</b>	2248.540	<b>2302.440</b>	nC/m
	Motional Resistance, $R_{x12}$	(2.18) (2.57)	6768.1	<b>8618.9</b>	8812.9	<b>8425.3</b>	$\Omega$
	Motional Capacitance, $C_{x12}$	(2.18) (2.57)	0.007	<b>0.007</b>	0.006	<b>0.007</b>	fF
	Motional Inductance, $L_{x12}$	(2.18) (2.57)	0.074	<b>0.078</b>	1.067	<b>1.023</b>	H
Parasitic Elements	Bond Pad Capacitance, $C_{pad}$	Measured	362	<b>300</b>	186	160	fF
	Parasitic Tuning Inductor, $L_{Tune}$	(2.59)	1.469	<b>1.788</b>	36.368	<b>42.479</b>	$\mu\text{H}$
	Interconnect Trace Resistance, $R_p$	Measured	0.8	<b>5</b>	1,080	<b>1200</b>	$\Omega$
	Feedthrough Capacitance, $C_f$	Measured	–	7.3	–	5.9	fF

\* Boldface value indicates a change from the design value needed to curve fit the simulation to the actual measured data.

expressions are presented in a design flow that achieves a wine-glass mode disk resonator with a specific operating frequency and with specific motional resistances  $R_{xij}$  between its electrode terminals.

### 2.3.7 Design Example: 61-MHz Wine-Glass Mode Disk

Table 2-III presents the results of using the procedure of Table 2-II to design a 61.2-MHz wine-glass mode disk using the electrode configuration of Figure 2.1(c) with characteristics as presented in the top “Design Variables” section. Here, given the desired resonance frequency and thickness, solution of (2.53) yields a needed radius of 12.1  $\mu\text{m}$ . With all dimensions now established, the values for the equivalent circuit elements now follow from (2.54)-(2.56), and are summarized in the “4-Port Equivalent Circuit Variables” section of Table 2-III.

The wine-glass mode device to be evaluated by measurement in Section 2.4 is operated as a two-port device that combines ports 1 with 3 to form an input port A, and ports 2 with 4 to form an output port B. In this configuration, electrodes on opposite sides of the disk are electrically connected, one pair serving to excite the disk, the other to detect output currents. With the disk perimeter moving in opposite directions over the input and output electrodes, currents that go into the disk at the input electrode leave the disk at the output electrode, with ideally none of the current flowing through the DC-bias voltage source,  $V_P$ , thus avoiding loss from resistance in series with the DC-bias supply voltage.

Since the wine-glass mode shape is identical along ports 1 and 3, and ports 2 and 4, merging of these electrodes generates an electromechanical coupling turns ratio given by the sum of the individual electrode turns ratios, or

$$\eta_{ei+j} = \eta_{ei} + \eta_{ej} \longrightarrow \begin{cases} \eta_{eA} = \eta_{e1} + \eta_{e3} \\ \eta_{eB} = \eta_{e2} + \eta_{e4} \end{cases} \quad (2.58)$$

The “2-Port Equivalent Circuit Variables” section of Table 2-III provides the turns ratio values associated with ports A and B.

## 2.4 Efficacy of the Equivalent Circuit: Theory vs. Measurement

Since the described negative capacitance alters device behavior under different input/output port load conditions, the described negative capacitive circuit model is perhaps best confirmed by

1. comparison with measured S21 plots as a function of DC-bias and port loading; and
2. comparison with measured plots of resonance frequency as a function of DC-bias and port loading.

### 2.4.1 Fabrication Process

Pursuant to obtaining such plots, disks designed to operate in radial-contour and wine-glass modes were fabricated using a process flow similar to that of [47], but for the case of radial-contour mode devices, using tungsten metal in contact with and buried under its conventional polysilicon interconnect; and using  $\text{Al}_2\text{O}_3$  as the release etch-resistant isolation layer, rather than the usual



$\text{Si}_3\text{N}_4$ , in order to allow vapor phase HF release; all depicted in the cross-section of Figure 2.2(b). The metal reduces the typical bond pad-to-device interconnect resistance to values around  $5\Omega$ , which is much lower than the  $1.2\text{k}\Omega$  of polysilicon-only interconnect. The use of low resistance interconnect becomes more important as electrode-to-resonator gaps shrink to yield correspondingly smaller motional resistances that are more easily loaded by interconnect resistance. Metal lines are especially beneficial for disks operating in radial-contour modes, since as described in Section 2.2 their currents enter or leave both input and output electrodes in phase, so are subject to resistive loading from DC-bias lines, as well as from the input/output lines.

Figure 2.10 presents scanning electron micrographs (SEMs) of a fabricated 218-MHz radial-contour mode disk with 40nm gaps and submerged metal interconnect; while Figure 2.11 presents the same for a 61-MHz wine-glass disk with 80nm gaps large enough to not require metal lines. For this reason, the wine-glass disks did not employ buried metal interconnect, and were fabricated using a process identical to that of [47].

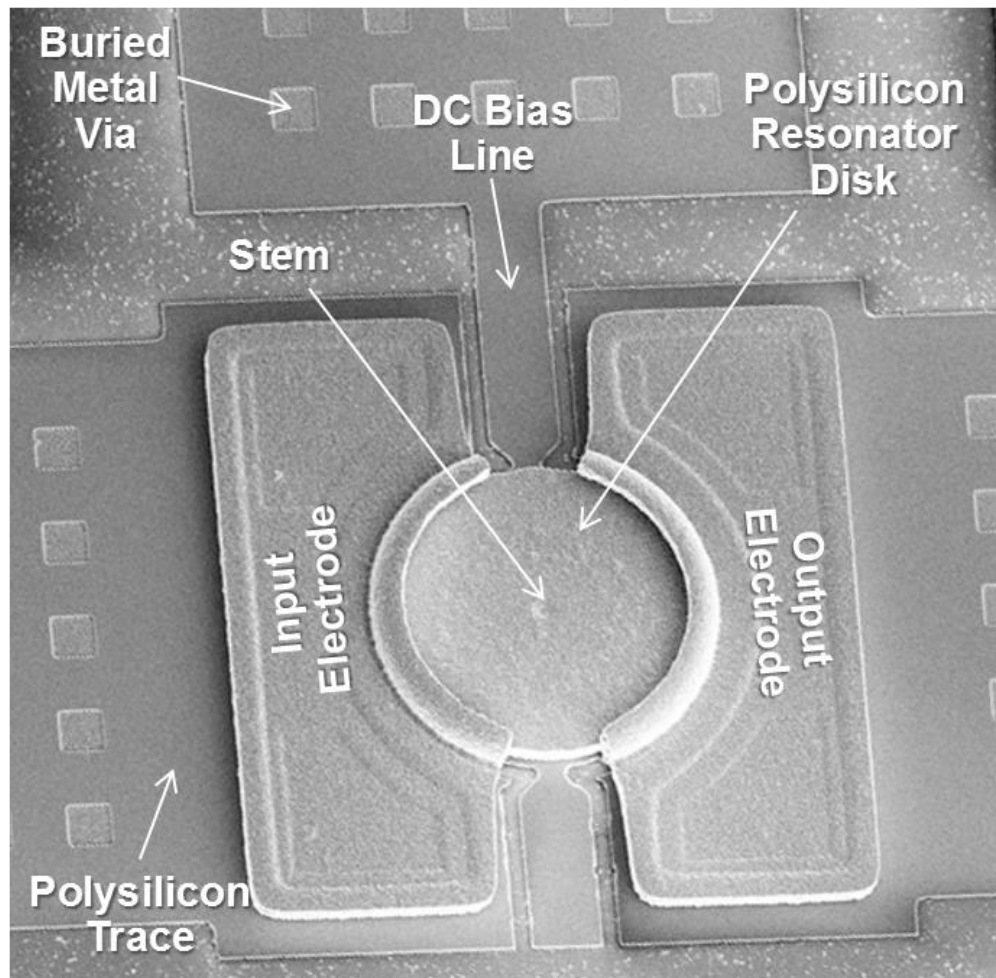


Figure 2.10: Scanning electron micrograph (SEM) of the fabricated 218-MHz radial-contour mode disk.

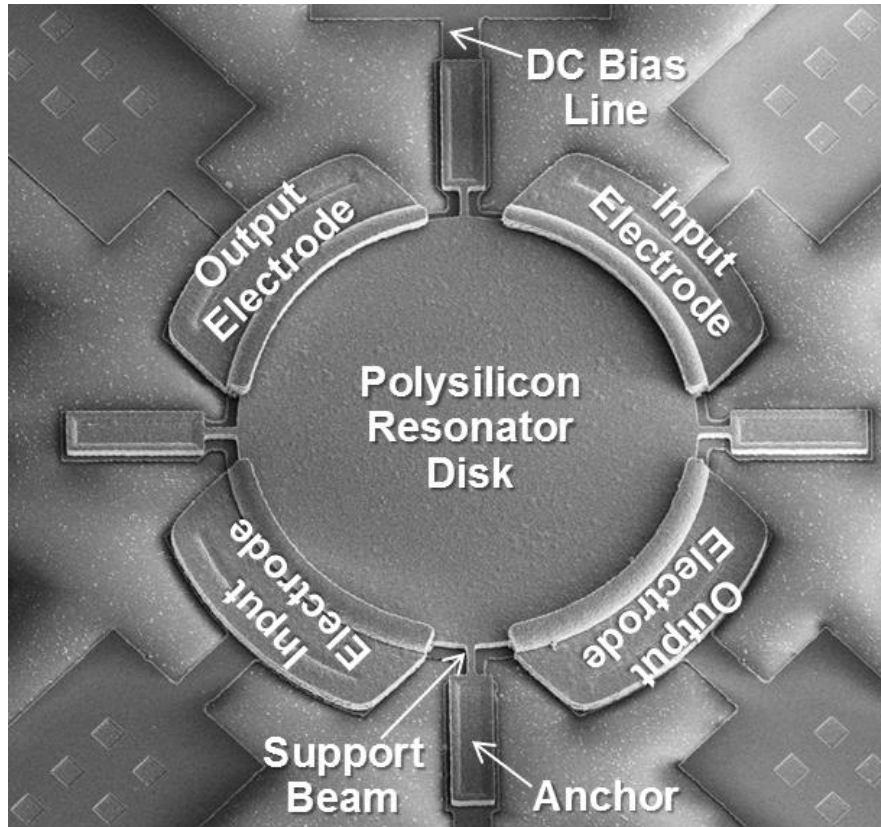


Figure 2.11: Scanning electron micrograph (SEM) of the fabricated 61-MHz wine-glass mode disk.

#### 2.4.2 Measurement and Simulation Circuits

The measurement circuit and corresponding simulation circuits used to compare measured and predicted frequency characteristics for the radial-contour mode and wine-glass mode devices are presented in Figure 2.12. During measurement, the die containing each device sits atop the chuck of a Lakeshore Model FWPX probe station that maintains a 100  $\mu$ Torr vacuum environment while providing electrical probe access to devices and electrical feedthroughs to connect them to outside measurement instrumentation. An Agilent E5071C network analyzer allows software emulated placement of potentially large resistors  $R_S$  and  $R_L$  as port impedances to gauge the effect of termination resistance on frequency tuning range. Standard SOLT calibration on a CS5 substrate moves the measurement plane to the tips of the GSG probes used for RF input and output to the device bond pads as seen in Figure 2.12, and nulls the signal line-to-shield capacitors of the coaxial cables and probes to eliminate frequency cutoff concerns for measurements that use large source and load resistors. Shunt inductors can also be simulated by the E5071C to resonate out bond pad capacitance, allowing observation of performance that would ensue under fully on-chip integrated environments with no bond pads. All measured results are obtained using two-port direct measurement with the network analyzer, hooked up as shown in Figure 2.12(a). As shown in Figure

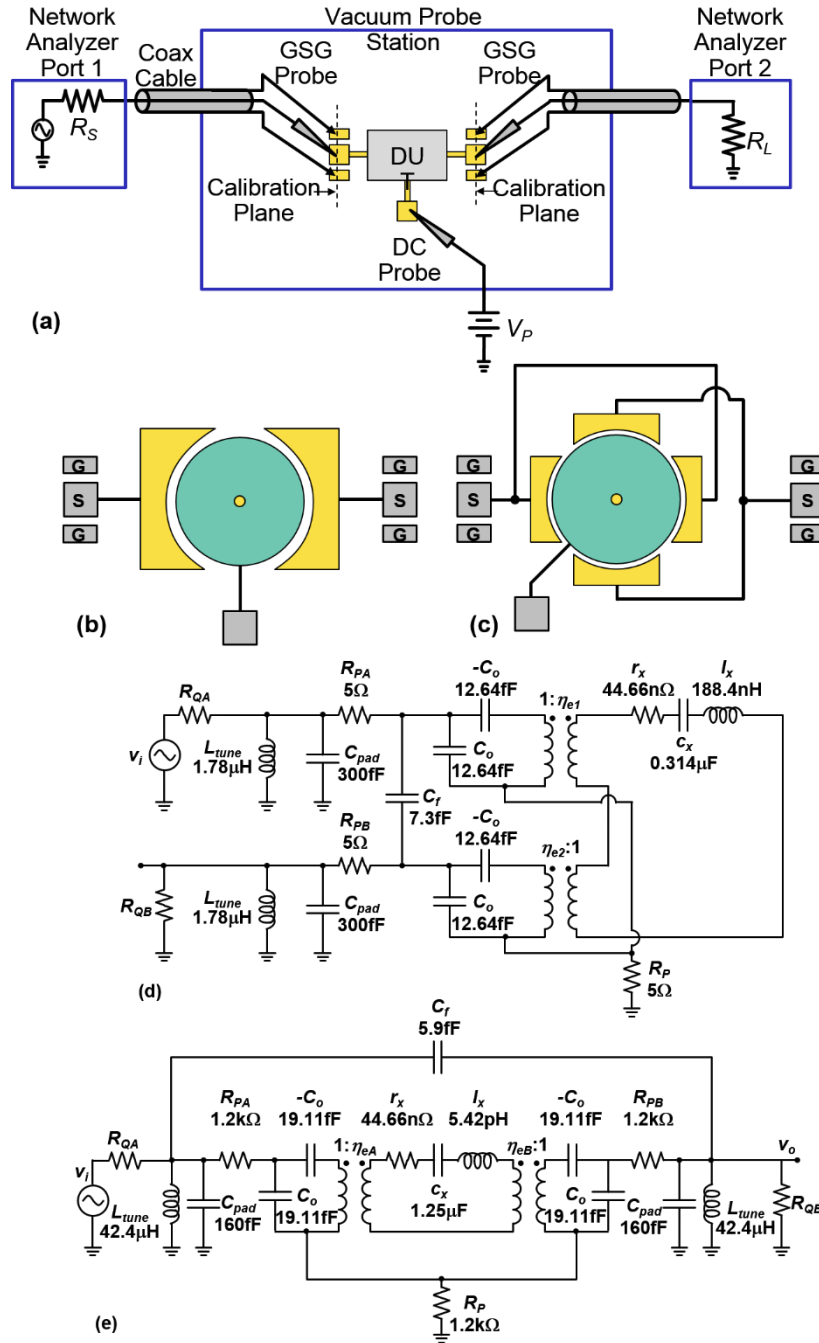


Figure 2.12: (a) Schematic description of the measurement system used to test the disk resonators of this work, (b) schematic of the electrode configuration of the contour-mode device and (c) the wine-glass mode device; and the electrical equivalent system circuit used to compare measurement with theory for (d) the contour-mode resonator and (e) wine-glass mode resonator.

2.12(d) and Figure 2.12(e), each of the circuits used for simulation include not only the base device as modeled by two-port versions of Figure 2.3 or Figure 2.6, but also measured values of parasitic interconnect resistance, and bond pad capacitance.

Table 2-III summarizes the device dimensions and parameters used to generate the simulation circuits of Figure 2.12(d, e) as covered in the design Sections 2.2 and 2.3. For each device, the first column presents direct design values, obtained using the procedures of Table 2-I and Table 2-II; and the columns to the right of these (to be referred to as the second columns) the actual values simulated to match measured curves. The values in the second columns comprise a combination of direct design values, i.e., the values used in layout and targeted in fabrication, and values (in boldface) either directly measured or extracted from sets of data using methods to be described in full detail. The latter is needed for elusive dimensions, like the electrode-to-resonator gap spacing, which if less than 100nm is very difficult to determine with the needed accuracy using SEM photos or capacitance measurements. Gap spacing is thus often determined indirectly from frequency versus DC-bias curves using a procedure that (as will be seen) can yield erroneous results if one does not utilize the negative capacitance equivalent circuit of Figure 2.3 or Figure 2.6.

The circuits of Figure 2.12(d) and (e) differ in not only their element values, but also in the polarity of the transformers at their output ports. As mentioned in Section 2.2, for the radial mode, since the disk moves in the same direction over all electrodes, if current flows into one electrode, it flows into all of them. This can be modeled by either a circuit like that of Figure 2.3, where the polarity of the output transformer is flipped relative to that of the input, or by merely situating the output transformer on the same side as the input, as is done in Figure 2.12(d). For the wine-glass mode, since the disk moves in the opposite direction at the input electrodes versus the output electrodes, when current goes into an input electrode, it goes out of an output terminal, and thus, the output transformer situated on the other side of the input in Figure 2.12 (e).

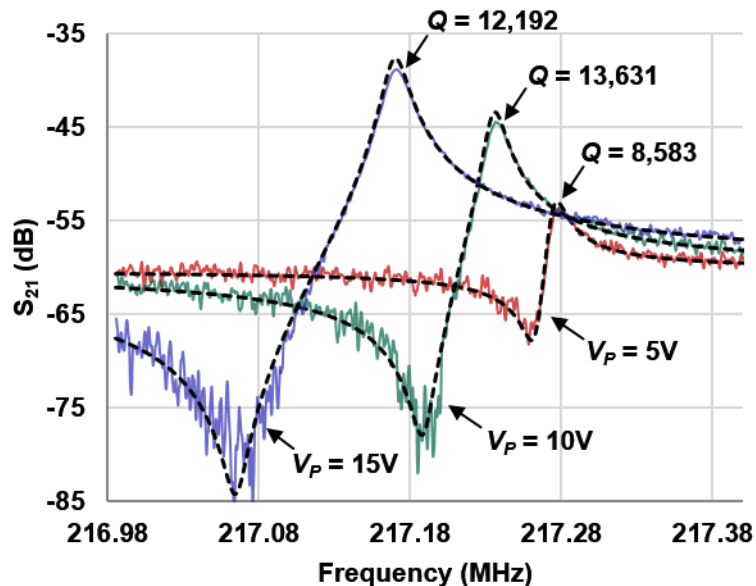


Figure 2.13: Measured and simulated (dashed lines)  $S_{21}$  plots for the radial-contour mode disk with  $50\Omega$  source and load termination resistors for varying values of DC-bias voltage  $V_P$  without using  $L_{tune}$ .

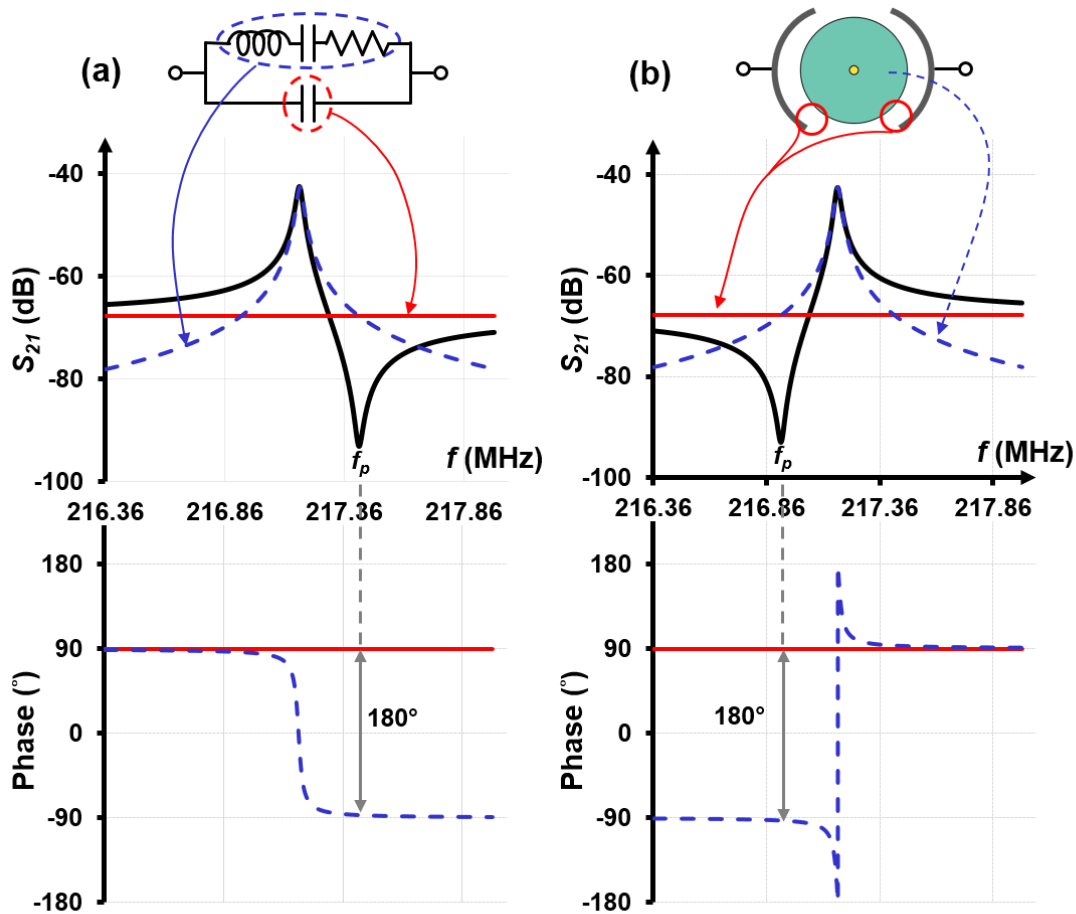


Figure 2.14: Simulated magnitude and phase curves contrasting parallel resonance peak formation for the case of (a) a quartz crystal, with circuit shown; and (b) a radial contour-mode disk resonator.

### 2.4.3 Frequency Response versus DC-Bias

Figure 2.13 presents measured and simulated  $S_{21}$  plots (using the Figure 2.12(d,e) circuit sans  $L_{tune}$ ) for the radial-contour mode disk for varying values of DC-bias voltage  $V_P$ . Here, the simulated plots not only match measured values at the peaks, but also match measured curves over the whole frequency range shown, from the slopes of the series resonant peaks, to the locations and depths of the parallel resonant zeros. Both theory and measurement indicate a series resonance frequency and motional resistance at  $V_P = 15\text{V}$  of 217.170 MHz and 8.6 k $\Omega$ , respectively.

One interesting difference between these curves and those for more common resonators, e.g., quartz crystals, is the location of the parallel resonance peak, which is now below the series resonance frequency, rather than above. That this should be the case comes from the fact that the current exiting the output electrode of a radial-contour mode disk is opposite in phase to that entering its input, meaning that current entering the input incites current entering the output. This to be contrasted with a typical two-terminal quartz crystal, where current entering the input terminal

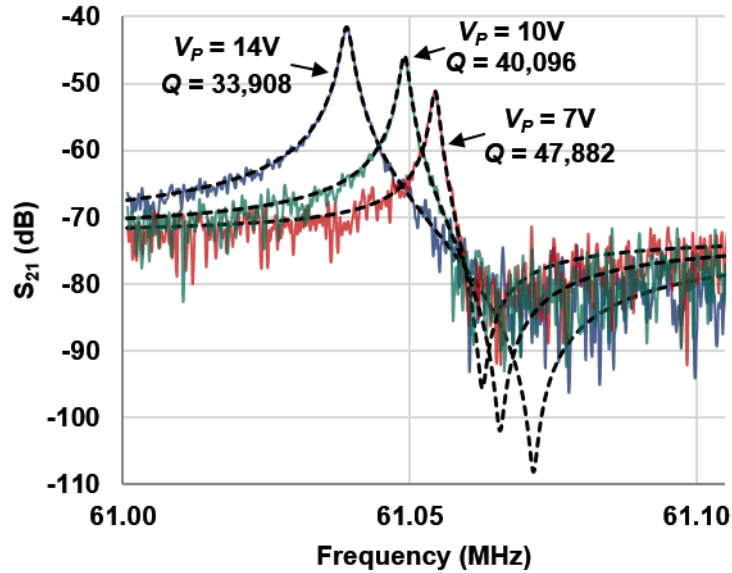


Figure 2.15: Measured and simulated (dashed lines)  $S_{21}$  plots for the wine-glass mode disk with  $50\Omega$  source and load termination resistors for varying values of DC-bias voltage  $V_P$  without using  $L_{tune}$ . (Note that the depths of the measured parallel resonance peaks are not as deep as predicted by theory only due to measurement instrument limitations, i.e., due to its insufficient noise floor.)

exits via the output terminal, i.e., current goes through a quartz crystal. As a result, as shown in Figure 2.14, the frequency at which the feedthrough current is opposite in phase to the radial-contour disk's output current occurs below the series resonance, where the phase is  $-90^\circ$  relative to the input voltage, and thus,  $180^\circ$  from the  $90^\circ$  feed-through current. Since the parallel resonance peak arises from cancellation of motional and feedthrough currents that add out-of-phase, this peak occurs below the series resonance peak for a radial-contour mode disk.

Figure 2.15 presents similar measured and simulated  $S_{21}$  curves for the wine-glass mode disk for varying values of DC-bias voltage  $V_P$ . Again, the curves are well predicted by the equivalent circuit of Figure 2.12(e). Both theory and measurement indicate a series resonance frequency and motional resistance at  $V_P = 14\text{V}$  of 61.03 MHz and 8.4 k $\Omega$ , respectively. Here, the parallel resonance peak occurs above the series resonance, just like in a quartz crystal. This makes perfect sense, since as described in Section 2.3, current flows through a wine-glass disk resonator, into the input electrode and out the output electrode, just as in a quartz crystal, so the relative output current-to-feedthrough phasing is the same.

#### 2.4.4 Frequency Response versus Resonator Port Resistance

Figure 2.16 presents measured and simulated  $S_{21}$  plots for the radial-contour mode disk for varying values of terminating port resistance  $R_{QA}$  and  $R_{QB}$  in series with the measured device and with  $L_{tune}$  engaged to null shunt bond pad capacitance at the device terminals. Here, the buried-

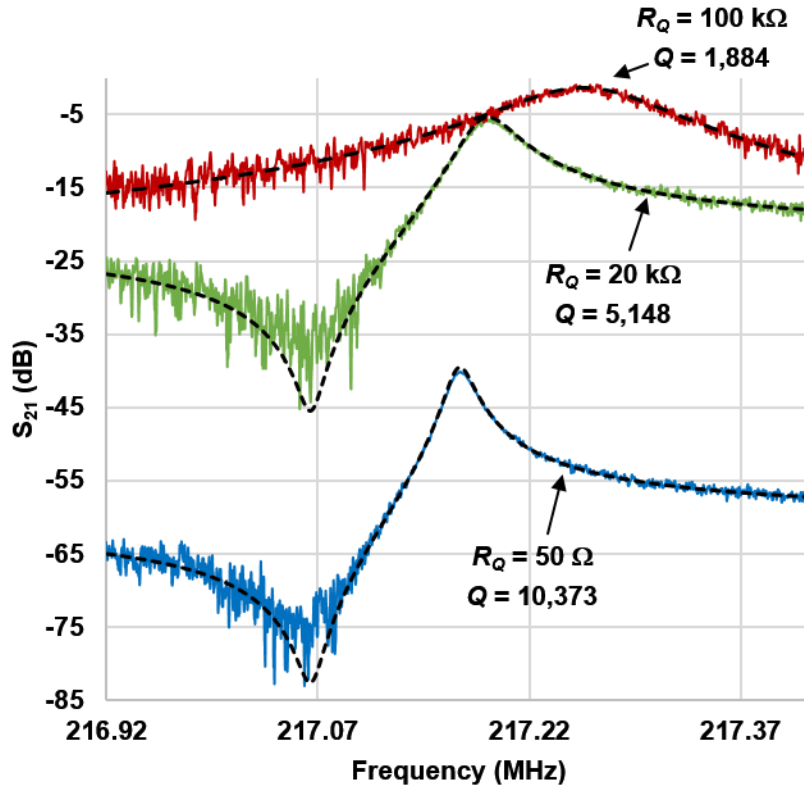


Figure 2.16: Measured and simulated (dashed lines)  $S_{21}$  plots for the radial-contour mode disk for varying values of termination resistance  $R_Q = R_{QA} = R_{QB}$  with  $L_{tunei}$ 's engaged to null  $C_{padi}$ 's, all measured under the conditions of Table 2-III.

metal interconnect described in Section 2.4.1 suppresses  $Q$  loading by parasitic resistance  $R_P$  from the DC-bias line to allow a more accurate determination of  $Q$  when the input/output termination resistors are small. Comparison of measured and simulated plots using the equivalent circuit of Figure 2.12(d) reveals excellent agreement.

Figure 2.17 presents measured and simulated  $S_{21}$  plots, this time for the wine-glass mode disk, again for varying values of port resistance values  $R_{QA}$  and  $R_{QB}$  in series with the measured device and with  $L_{tune}$  engaged. For this device, the DC-bias line trace parasitic  $R_P$  has no effect, since the polarity of motion at the input port is opposite that of the output port for this mode of vibration, so current flows into the input port and out the output port, i.e., it flows through the device. Thus, ideally none of it flows through  $R_P$ , so no power dissipates in the resistor, and the  $Q$  of the device is independent of  $R_P$ . Again, the simulated plots using the equivalent circuit of Figure 2.12(e) agree quite well with the measured plots.

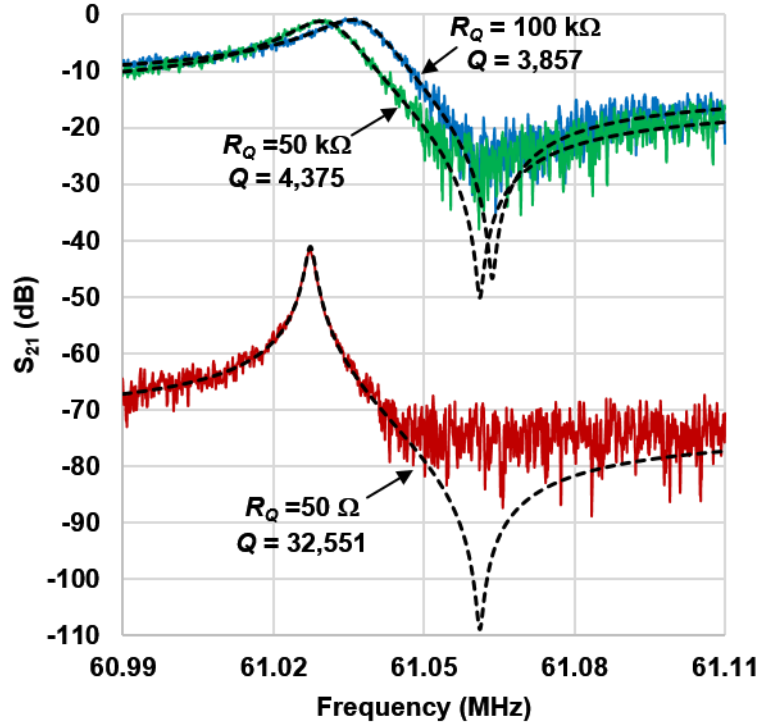


Figure 2.17: Measured and simulated (dashed lines)  $S_{21}$  plots for the wine-glass mode disk for varying values of termination resistance  $R_Q = R_{QA} = R_{QB}$  with  $L_{tunei}$ 's engaged to null  $C_{padi}$ 's, all measured under the conditions of Table 2-III. (Again, the measurement instrumentation noise floor limits the depth of the measured parallel resonance peak for the  $R_Q=50\Omega$  case.)

#### 2.4.5 Frequency Versus DC-Bias, Termination Resistance, and Electrode-to-Resonator Gap Spacing

The dependence of resonance frequency on DC-bias voltage  $V_P$  and electrode-to-resonator gap spacing do is well known for capacitive-gap transduced micromechanical resonators. What is less apparent is that the frequency versus DC-bias curve for a given capacitive-gap transduced micromechanical resonator is also a function of the termination resistances,  $R_{QA}$ ,  $R_{QB}$ , and  $R_{pC}$ , in Figure 2.12(d,e) in series with all ports of the device. More generally, it is a function of the termination impedance, to include reactive components, i.e., capacitance and inductance, as well. A lack of understanding of how termination impedance influences frequency dependence on electrode-to-resonator DC-bias voltage can in fact be responsible for incorrect experimental determination of electrode-to-resonator gap spacing for capacitive-gap transduced devices.

Pursuant to first exploring the ideal case where the resonator device is loaded only by pure resistance, with no reactance, the first set of measurements employ Figure 2.12(d) and (e) schemes that include the tuning inductor  $L_{tune}$ , given by



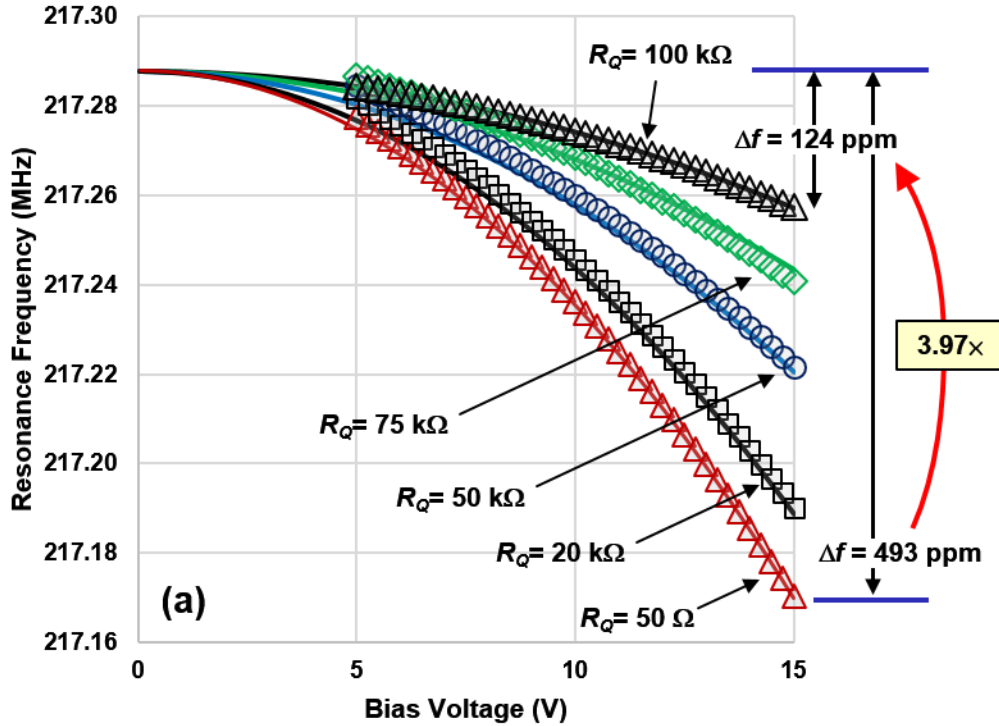


Figure 2.18: Measured plots of resonance frequency versus DC-bias after the parasitic capacitance  $C_{pad}$  is tuned out for varying values of source and load resistances denoted by  $R_Q$  as third variable for the radial-contour mode disk. Solid curves indicate simulated plots that fit the measured data point using the equivalent circuit of Figure 2.12(d).

$$L_{Tune} = \frac{1}{C_{pad} (2\pi f_o)^2} \quad (2.59)$$

to null out any non-device capacitance in shunt with the terminals, e.g., due to bond pads. Here, measurements indicate that the influence of termination resistance  $R_{Qi}$  at port  $i$  on DC-bias frequency dependence is a strong function of the size of the electrode-to-resonator overlap capacitance  $C_{oi}$  at that port. To illustrate, Figure 2.18 and Figure 2.19 present measured plots of resonance frequency versus DC-bias voltage  $V_P$ , also as a function of the time constant  $\tau = R_{Qi}C_{oi}$  formed by the product of the electrode-to-resonator overlap capacitance  $C_{oi}$  and termination resistance  $R_{Qi}$  applied to each I/O port of Figure 2.12, for disks vibrating in the radial-contour and wine-glass modes, respectively. As shown, the efficacy of the electrical stiffness is strongly dependent upon the relative values of  $C_{oi}$  and  $R_{Qi}$ , where large frequency shifts are observed when the product  $R_{Qi}C_{oi}$  is small, but the frequency shifts are much smaller over the same range of  $V_P$  when  $R_{Qi}C_{oi}$  is large. Specifically, from Figure 2.18, the contour mode devices with 40nm gaps reduce their frequency tuning range from 493ppm to 124ppm over a DC-bias sweep between 5V to 10V when their termination resistance increases from 50Ω to 100kΩ, which represents a 3.97× improvement in frequency stability against bias voltage fluctuations. Similarly, from Figure 2.19, larger gapped

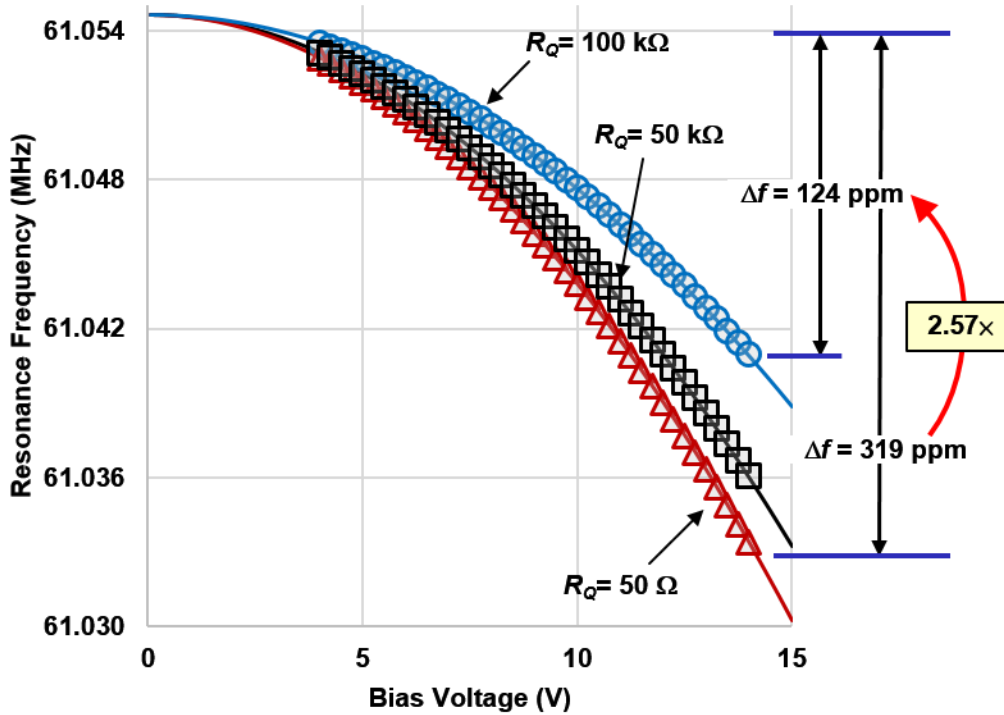


Figure 2.19: Measured plots of resonance frequency versus DC-bias after the parasitic capacitance  $C_{pad}$  is tuned out for varying values of source and load resistances denoted by  $R_Q$  as third variable for the wine-glass mode disk. Solid curves indicate simulated plots that fit the measured data point using the equivalent circuit of Figure 2.12(e).

wine-glass mode resonators improve their frequency stability by a smaller, but still significant,  $2.57\times$  from 319ppm to 124ppm measured over a DC-bias sweep between 5V and 14V when the termination resistance sweeps from  $50\Omega$  to  $100k\Omega$ .

The mechanism behind this dependence on  $R_{Qi}C_{oi}$  is not immediately apparent in the circuit of Figure 2.1, but quite easy to see in the negative capacitance circuit of Figure 2.12(d,e) with  $C_{pad}$  tuned out. In particular, since this circuit models the electrical stiffness by the  $-C_{oi}$  capacitor, the efficacy of the electrical stiffness depends upon the degree of cancellation of  $-C_{oi}$  by  $C_{oi}$ . When  $R_{Qi}$  is small, it effectively shorts the shunt electrode-to-resonator overlap capacitor  $C_{oi}$ , leaving the series  $-C_{oi}$  free to influence resonance frequency via changes in  $V_P$  that in turn change the transformer turns ratios  $\eta_{ei}$ . As  $R_{Qi}$  increases, the current into the parallel combination of  $R_{Qi}$  and  $C_{oi}$  prefers to pass through  $C_{oi}$  instead of  $R_{Qi}$ , effectively activating  $C_{oi}$  and allowing it to cancel  $-C_{oi}$ , negating the electrical stiffness in the process. When the impedance of  $R_{Qi}$  is considerably larger than that of  $C_{oi}$ , complete cancellation of electrical stiffness ensues, and the resonance frequency is no longer dependent upon dc-bias voltage  $V_P$ , electrode-to-resonator gap spacing, or any other parameter in (2.10).

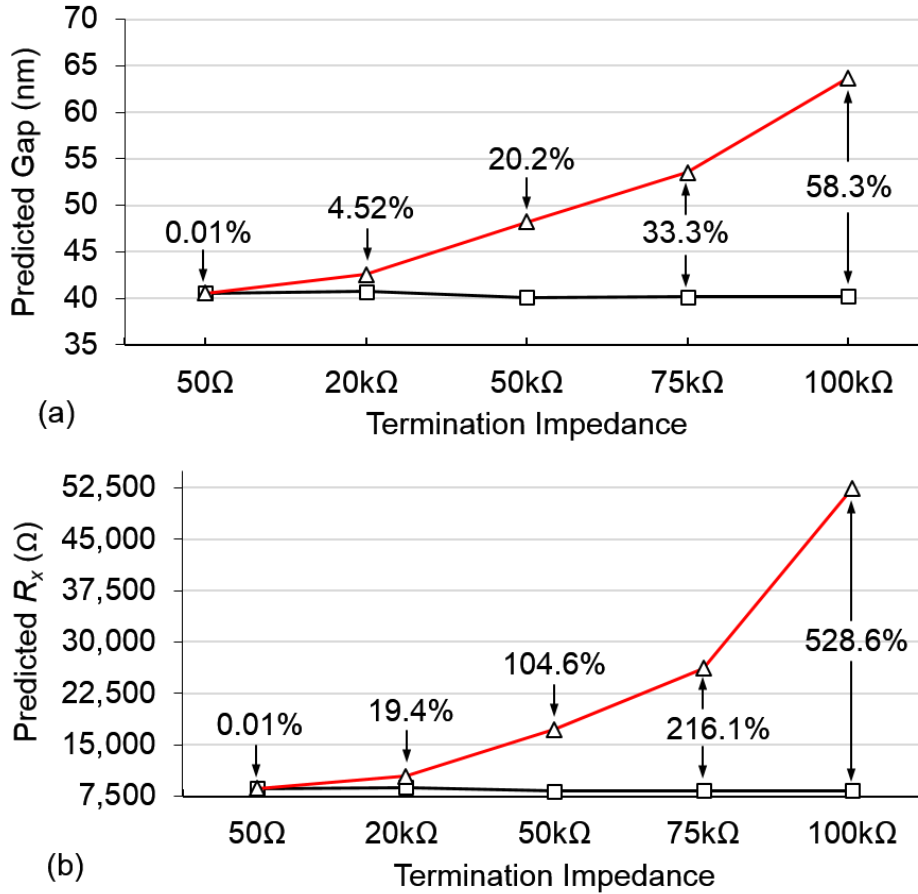


Figure 2.20: Plots of (a) extracted gap and (b) the corresponding motional resistance versus termination impedance using for extraction the circuit of Figure 2.12(d) (black curves) and the same circuit sans the negative capacitance (red curves). Percent discrepancy between the curves is also provided for each extracted point.

The efficacy of the negative capacitance equivalent circuit in predicting this dependency on  $R_{Qi}$  is clearly seen by the accuracy to which simulation of the circuits of Figure 2.12(d) and Figure 2.12(e) match the measured curves in Figure 2.18 and Figure 2.19, respectively.

#### 2.4.6 Electrode-to-Resonator Gap Extraction

With a better understanding of parameters (especially load resistances) that influence the frequency versus DC-bias  $V_P$  curve, one can now extract the average electrode-to-resonator gap spacing at a given port more accurately than previous work [31]. In particular, by fitting values of electrode-to-resonator gap spacing (for each set of resistances  $R_{QA}$  and  $R_{QB}$  used) so that simulated curves using the Figure 2.12(d) and Figure 2.12(e) circuits match those of measured data at all values of  $V_P$ , one obtains very accurate estimates of the average electrode-to-resonator gap spacing

for each device. Note that lack of knowledge of the influence of the  $R_{Qi}$ 's on the efficacy of electrical stiffness can lead to very incorrect estimates for gap spacing, especially when the gap is very small.

The above procedure yields for the wine-glass disk an average electrode-to-resonator gap spacing of 84.1 nm, and for the radial-contour more disk 40.56 nm. These values are in fact the ones used for all simulations in this section, i.e., Figure 2.18 and Figure 2.19 had to be measured before any of the simulations could be generated.

To convey the degree to which ignoring the influence of  $R_{Qi}$  on electrical stiffness impacts extracted parameters, Figure 2.20 plots the gap and corresponding motional resistance  $R_x$  versus termination impedance for the 40nm-gap radial-contour mode device using extraction based on 1) the negative capacitance circuit of Figure 2.12(d); and 2) the same circuit, but without the negative capacitance and without otherwise accounting for the change in  $c_x$  due to electrical stiffness. Here, the discrepancy between results yielded by each circuit increases with termination resistance, with errors for method 2 rising to 58.3% for gap spacing and an astonishing 529% for motional resistance when the termination resistance is 100k $\Omega$ . Plots for devices with different gaps reveals that errors are larger when the gap is small, emphasizing the importance of including negative capacitance when designing mechanical circuits composed of devices with aggressively small gaps.

#### 2.4.7 Effect of Parasitic Trace and Bond-Pad Capacitance

Of course, in any practical circuit not using  $L_{tune}$ , bond-pad and interconnect capacitance will change the load condition from the pure resistance considered in Sections 2.4.4 and 2.4.6 to a more general impedance that includes reactance from the bond-pad capacitance  $C_{pad}$ , shown in Figure 2.12(d,e). This extra capacitance not only steals current from the resistor  $R_{Qi}$ , but also changes the shunt capacitor value so that the  $-C_{oi}$  in the series arm cannot be cancelled completely, even if  $R_{Qi}$  becomes infinite. As a result, the frequency versus  $V_P$  dependence cannot be nulled.

For the simpler case of only one electrode in the Figure 2.12(d) circuit for the radial mode disk loaded by the parallel combination of  $R_{QA}$  and  $C_L=C_{pad}$ , the resonance frequency is found by equating the total reactance around the  $LCR$  loop to zero, i.e.,

$$j \frac{\eta_{eA}^2}{\omega_o C_{oA}} \frac{1 + \omega_o^2 R_{QA}^2 C_L (C_{oA} + C_L)}{1 + \omega_o^2 R_{QA}^2 (C_{oA} + C_L)^2} + j \omega_o l_x - j \frac{1}{\omega_o c_x} = 0 \quad (2.60)$$

which reduces to

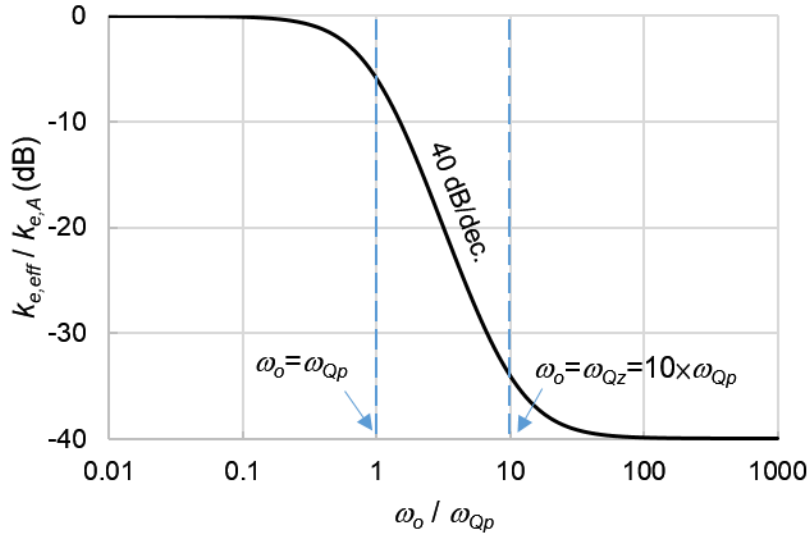


Figure 2.21: Plot of  $k_{e,eff}/k_{eA}$  in dB versus the log of resonance frequency normalized to  $\omega_{Qp}$  for the case where  $\omega_{Qz}=10\omega_{Qp}$ .

$$\begin{aligned} \omega_o &= \frac{1}{\sqrt{l_x c_x}} \left\{ 1 - \frac{\eta_{eA}^2 c_x}{C_{oA}} \frac{1 + \omega_o^2 R_{QA}^2 C_L (C_{oA} + C_L)}{1 + \omega_o^2 R_{QA}^2 (C_{oA} + C_L)^2} \right\}^{1/2} \\ &= \frac{1}{\sqrt{l_x c_x}} \left\{ 1 - \frac{k_{eA}}{k_m} \frac{1 + (\omega_o/\omega_{Qz})^2}{1 + (\omega_o/\omega_{Qp})^2} \right\}^{1/2} \end{aligned} \quad (2.61)$$

where

$$\omega_{Qz} = \frac{1}{R_{QA} \sqrt{C_L (C_{oA} + C_L)}} \quad \text{and} \quad \omega_{Qp} = \frac{1}{R_{QA} (C_{oA} + C_L)} \quad (2.62)$$

The frequencies  $\omega_{Qz}$  and  $\omega_{Qp}$  can be interpreted loosely as zero and pole locations that govern the frequency dependence of the electrical stiffness magnitude. In particular, the expression for electrical stiffness magnitude as a function of device resonance frequency is easily extracted from (2.61) to be

$$k_{e,eff} = k_{eA} \frac{1 + (\omega_o/\omega_{Qz})^2}{1 + (\omega_o/\omega_{Qp})^2} \quad (2.63)$$

Plotting (2.63) on a Bode plot-like graph for the case  $\omega_{Qz} = 10 \omega_{Qp}$  yields Figure 2.21, where the frequencies  $\omega_{Qz}$  and  $\omega_{Qp}$  clearly delineate the start and stop points, respectively, where the electrical stiffness magnitude drops at a rate of 40dB/dec towards a final value attained when  $\omega_o$  exceeds  $\omega_{Qz}$ , i.e., when the  $R_{QA}C_{oA}$  product is large.

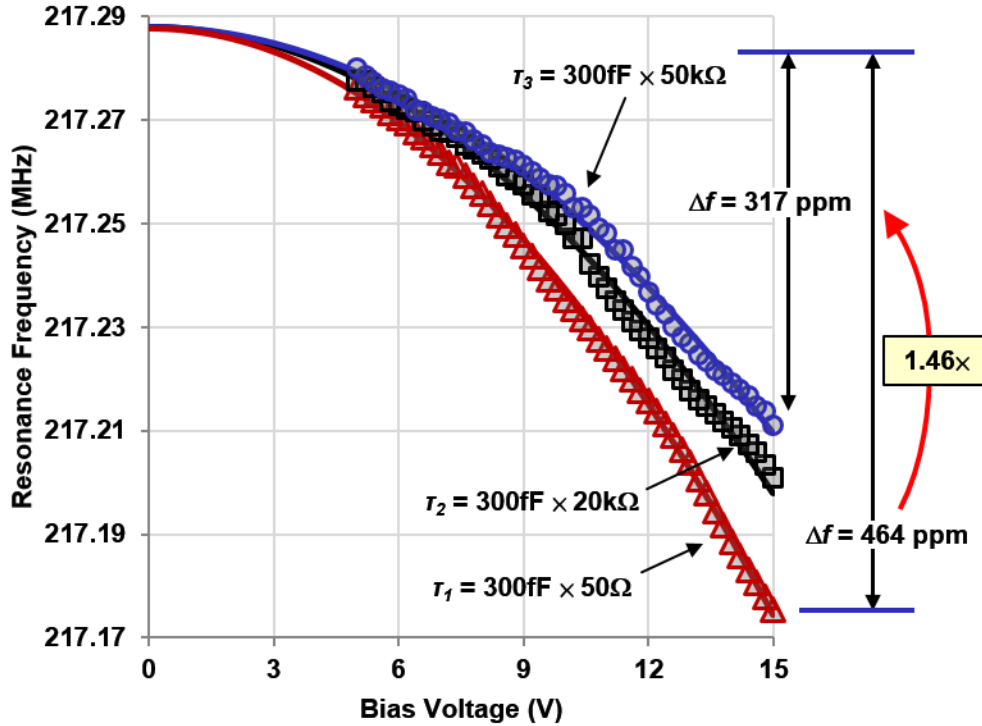


Figure 2.22: Measured plots of resonance frequency versus DC-bias, with termination impedance time constants  $\tau_i = R_{Qi}C_{pad}$  as a third variable without using  $L_{tune}$ , for the radial-contour mode disk. Solid curves indicate the theoretical expectation from the simulation of the circuit model presented in Figure 2.12(d). The identical least-square curve fitted electrode-to-resonator gap spacing of 40.56 nm is used for all simulated plots that match very well to the measured data points for different source and load termination resistors.

For useful insight, one can take (2.61) to extremes where  $\omega_{Qz}$  and  $\omega_{Qp}$  are both very small or both very large. For the latter, where  $\omega_o \ll \omega_Q$ , (2.61) reduces to

$$\omega_o = \frac{1}{\sqrt{l_x c_x}} \left\{ 1 - \frac{k_{eA}}{k_m} \right\}^{1/2} \quad (2.64)$$

which is the familiar equation for the case where frequency pulling via electrical stiffness is at maximum strength. This is consistent with the data in Figure 2.18 and Figure 2.19, since a large  $\omega_Q$  implies a small  $R_{QA}C_{oA}$  product.

On the other hand, when  $R_{QA}C_{oA}$  is large,  $\omega_Q$  is small, and  $\omega_o > \omega_Q$ . When  $\omega_o \gg \omega_Q$ , (2.61) reduces to

$$\omega_o = \frac{1}{\sqrt{l_x c_x}} \left\{ 1 - \frac{k_{eA}}{k_m} \frac{C_L}{C_{oA} + C_L} \right\}^{1/2} \quad (2.65)$$

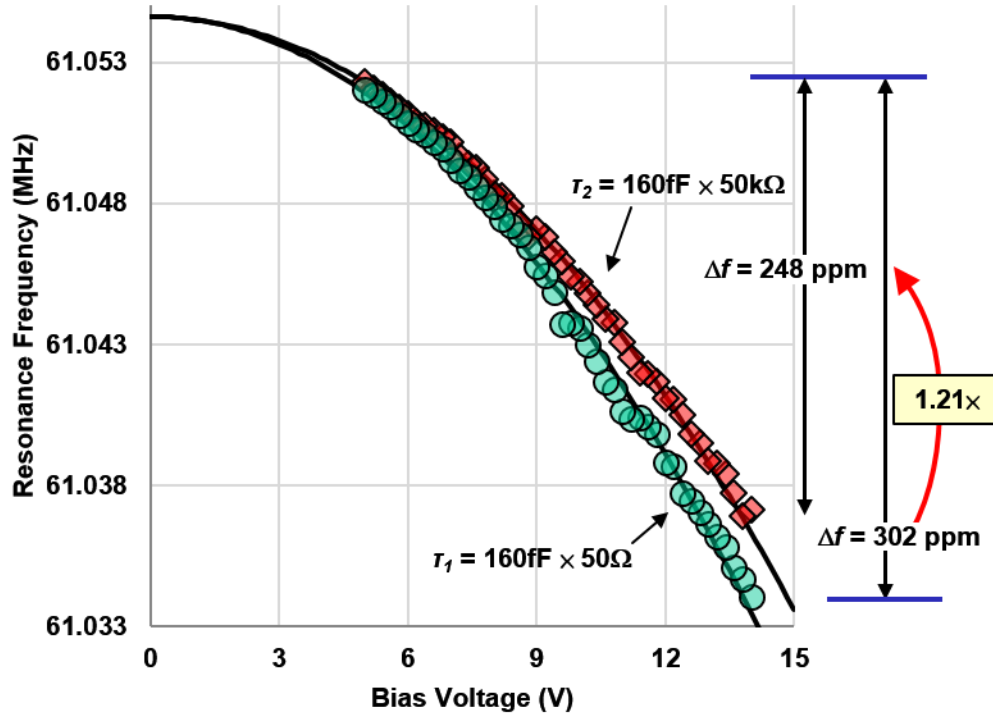


Figure 2.23: Measured plots of resonance frequency versus DC-bias, with termination impedance time constants  $\tau_i = R_{Qi} C_{pad}$  as a third variable without using  $L_{tune}$ , for the wine-glass mode disk. Solid curves indicate the theoretical expectation from the simulation of the circuit model presented in Figure 2.12(e). The identical least-square curve fitted electrode-to-resonator gap spacing of 84.1 nm is used for all simulated plots that match very well to the measured data points for different source and load termination resistors.

where the magnitude of the effective electrical stiffness can be extracted as

$$k_{e,eff} = k_{eA} \frac{C_L}{C_{oA} + C_L} \quad (2.66)$$

Note that if  $C_L = 0$ , or  $C_{oA} \gg C_L$ , the effective electrical stiffness would disappear. Thus, the presence of  $C_L$  prevents a large  $R_Q$  from nulling the DC-bias dependence of the resonance frequency. Overall, when extra shunt capacitance loads the device terminals, the degree to which  $-C_o$  series arm capacitance cancels reduces considerably, as shown in Figure 2.22 and Figure 2.23, which present measured curves of frequency versus DC-bias with bond-pad capacitance present, i.e., without use of the  $L_{tune}$ 's.

## 2.5 Impact on Applications

From a practical circuit perspective, the use of small source and load resistances equates to the use of voltage drive and current sensing. Conversely, the use of large source and load resistances equates to the use of current drive and voltage sensing. From the results of Section 2.4, voltage drive makes most sense where frequency tuning is needed, such as for a tunable filter passband application, or a voltage-controlled oscillator. On the other hand, current drive is most appropriate when frequency stability is paramount.

### 2.5.1 Reference Oscillator Design Insights

One example application where the choice of drive and sense type could make a big difference is that of a reference oscillator that must be stable against a variety of environmental perturbations. These include acceleration, power supply noise, drift, and undue charging (e.g., due to radiation), all of which can induce instability in the oscillator's frequency. Interestingly, the most significant mechanism for frequency instability caused by these particular perturbations ends up being instability in the electrical stiffness. For instance, theoretical analysis of micromechanical wine-glass disk resonators reveals that acceleration-induced changes in electrode-to-resonator gap spacing or overlap area that in turn induce shifts in electrical stiffness dominate among sources that shift frequency during accelerations [52]. In addition, noise or drift on the power supply manifests as fluctuations on the resonator DC-bias  $V_P$  that obviously destabilize the electrical stiffness, and thereby, resonance frequency.

As revealed by the negative capacitance equivalent circuit and verified by the measurements in Figure 2.18 and Figure 2.19, frequency dependence on electrical stiffness can essentially be nulled by using a high impedance input, high impedance output sustaining amplifier. Here, high impedance is defined relative to the impedance presented by the shunt  $C_{oi}$  at the resonator I/O terminals, i.e., the resistance presented by the drive/sense circuit loading each I/O port is considered "high" when it is at least 5 times larger than  $1/(sC_{oi})$ . This suggests that to maximize frequency stability against environmental variations, a Pierce oscillator [53] configuration would be a better choice than the commonly used transresistance sustaining amplifier.

On the other hand, if frequency tuning is important, and slight instabilities due to environmental perturbations can be tolerated, a low impedance input, low impedance output sustaining amplifier is most suitable, such as a transresistance amplifier, as used in [45].

### 2.5.2 Device Design Insights

For the case where frequency stability is of most interest, the negative capacitance equivalent circuit offers a very important insight: The highest stability against changes in bias voltage or overlap capacitance comes when the negative  $C_{oi}$ 's can cancel the positive ones. From Section



2.4.7, terminal load capacitance  $C_{Li}$  can limit the degree to which electrical stiffness can be negated, i.e., to which stability can be maximized. Indeed, if  $C_{oi}$  can be made much greater than any load capacitance on a given terminal, this ensures maximum stability.

This simple fact now reveals several methods by which the frequency stability of a capacitive-gap transduced resonator can be maximized:

- 1) Utilize solid dielectric gaps, such as demonstrated in [54] and [55]. Here, simply raising the gap permittivity raises  $C_{oi}$  so that it dominates over terminal parasites.
- 2) Utilize large arrays of resonators, perhaps mechanically coupled into array composites like that of [56] and [57]. Again, the use of many devices increases the total input or output  $C_{oi}$  so that it swamps terminal load capacitance.
- 3) Integrate resonators alongside transistors, removing large board-level capacitors to again allow intrinsic resonator input/output capacitance to swamp parasitics.

Note that all of the above methods increase  $C_{oi}$  without compromising the  $(C_x/C_{oi})$  ratio that governs transducer electromechanical coupling efficiency. Methods (1) and (3) in fact improve the  $(C_x/C_{oi})$  ratio.

Needless to say, design insights like these facilitated by the negative capacitance equivalent circuit are quite invaluable. There are sure to be many other examples, from oscillators, to filters, to mixers [11], where explicit representation of the negative capacitance in a micromechanical resonator's equivalent circuit proves instrumental to maximizing performance.

## 2.6 Conclusions on the Negative-Capacitance Equivalent Circuit Model

By explicitly modeling electrical stiffness in a capacitive-gap transduced micromechanical resonator via a negative capacitance, the equivalent circuit of this chapter provides design insights that explain certain previously unexplained measured behavior, such as the reduction in efficacy of electrical stiffness when the resistances loading a resonator's input/output ports are large, which in turn led to incorrect experimental extraction of electrode-to-resonator gap spacings. The equivalent circuit further provides designers with needed visual cues that enable them to more intelligently choose circuit topologies to maximize the performance of resonator applications, especially where frequency stability is paramount. These, together with more accurate methods for determining element values, where integration is employed to account for varying resonator mass and stiffness over a given electrode and where a single coupling coefficient models both electrical and mechanical aspects of a capacitive-gap transducer, make the described negative capacitance equivalent circuit a great tool for design of more complex micromechanical circuits to come in the following chapters.

# Chapter 3

## CAPACITIVELY TRANSDUCED MICROMECHANICAL RESONATORS WITH SIMULTANEOUS LOW MOTIONAL RESISTANCE AND $Q > 70,000$

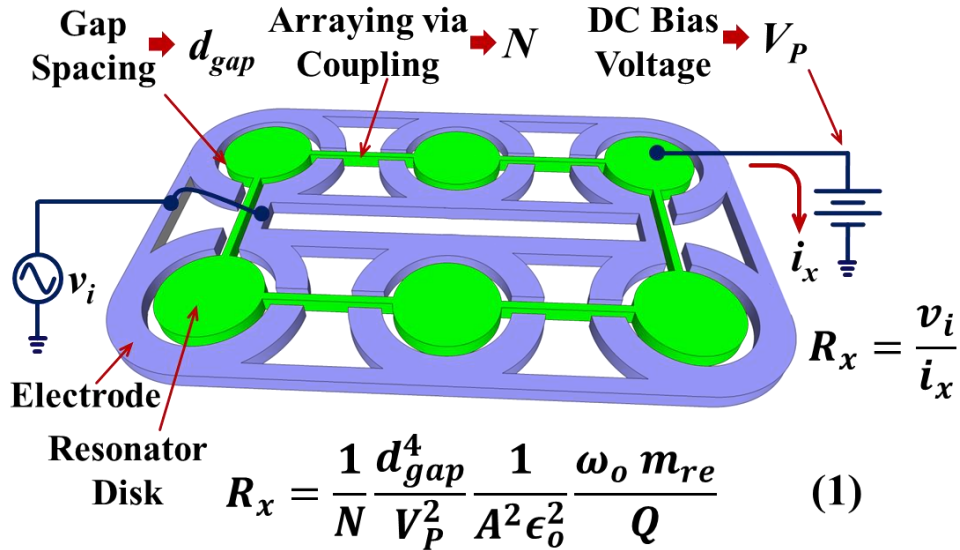
---

---

This chapter demonstrates capacitively transduced micromechanical disk resonators that exhibit simultaneous low motional resistance ( $< 130 \Omega$ ) and high  $Q$  ( $> 70,000$ ) at 61 MHz using an improved ALD-partial electrode-to-resonator gap filling technique that reduces the  $Q$ -limiting surface losses of previous renditions [34] by adding an alumina pre-coating before ALD of the gap-filling high- $k$  dielectric. This effort increases the  $Q$  over the  $\sim 10,000$  of previous renditions by more than  $6\times$  towards demonstration of the first VHF micromechanical resonators in any material, piezoelectric or not, to meet the simultaneous high  $Q$  ( $> 50,000$ ) and low motional resistance  $R_x$  ( $< 200\Omega$ ) specs highly desired for front-end frequency channelizer requirements in cognitive and software-defined radio architectures. The methods presented in this chapter finally over-come the high impedance bottleneck that has plagued capacitively transduced micromechanical resonators over the past decade.

### 3.1 Introduction

Capacitively transduced micromechanical resonators have historically achieved the highest  $Q$ 's among micro-scale counterparts using other technologies [7][58][59], reaching  $Q$ 's past 200,000 at VHF and 14,600 at 1.2 GHz [60]. Such  $Q$ 's are highly desired for a myriad of applications, from very narrow band low insertion loss filters for co-site interference suppression [61]; to low phase noise, low power oscillators for radar and communications [62]; to frequency gating spectrum analyzer functions for true software-defined cognitive radio [61]. Additional advantages,



$m_{re}$  : Equivalent dynamic mass       $Q$  : Resonator quality factor  
 $\omega_0$  : Resonance frequency in radians     $\epsilon_0$  : Permittivity of vacuum  
 $A$  : Overlap area between the electrode and resonator

Figure 3.1: Schematic of an array-composite disk resonator, showing a one-port excitation/readout scheme, identifying important variables, and providing the expression for the effective motional resistance  $R_x$  of the device.

like zero DC power consumption and the ability to self-switch, further bolster the argument for using these devices [33].

Still, adaptation of capacitive micromechanical resonators in these applications has so far been slowed by their higher than conventional impedances, which makes them difficult to interface with widely used  $50\Omega$  RF components. Theoretically, there is actually no good reason why the impedances of such resonators must be high. In particular, just a quick glance at

$$R_x = \frac{1}{N} \frac{d_o^4}{V_P^2} \frac{1}{A^2 \epsilon_o^2} \quad (3.1)$$

that governs the motional resistance  $R_x$  of the disk array-composite resonator shown in Figure 3.1 reveals that there are many knobs to turn that allow a designer to achieve a very wide range of motional resistances. A similar expression for  $R_x$  that uses the basic disk resonator design variables introduced in Chapter 2 can be written as

$$R_x = \frac{1}{N} \frac{d_o^4}{V_P^2} \cdot \frac{\pi^3 \chi K_{mat}^2 E}{Q \omega_o h (\epsilon_o \kappa_i (\theta_{i2} - \theta_{i1}) R)^2} \quad (3.2)$$

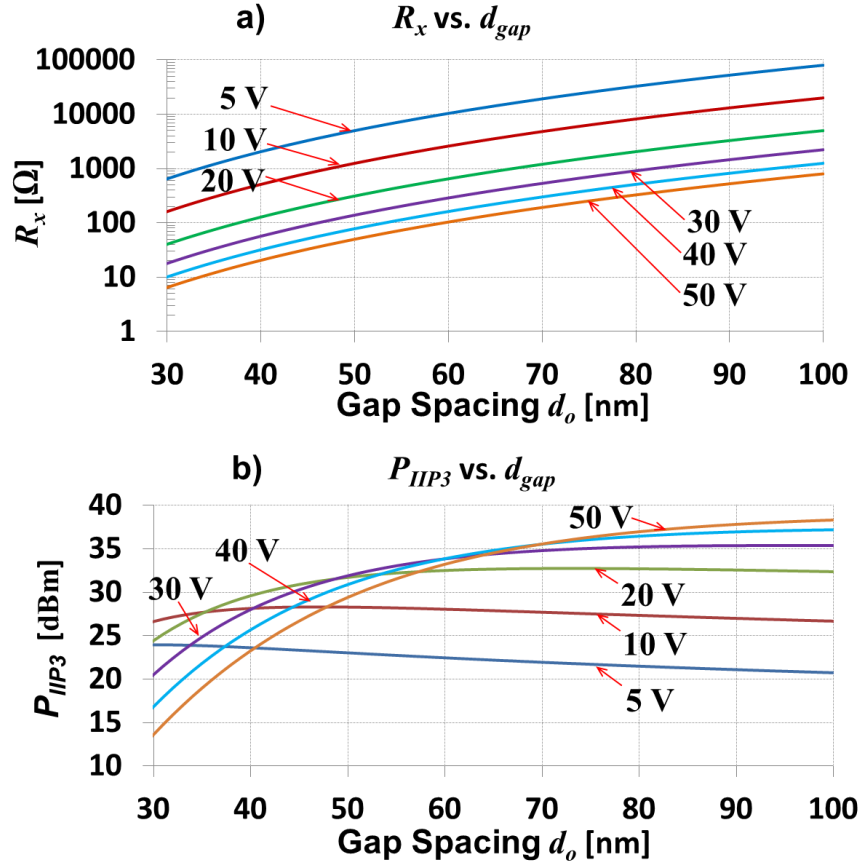


Figure 3.2: Simulated plots of (a) motional resistance and (b)  $IIP_3$  versus dc-bias voltage  $V_P$  and electrode-to-resonator gap spacing  $d_o$  for a 61-MHz wineglass disk resonator with  $Q = 70,000$ .

The motional resistance  $R_x$  given by (3.2) serves as a very intuitive metric for evaluating resonator coupling strength in applications where matching to a given system impedance is important, or evaluating required negative resistance for an oscillator circuit. However, another commonly used measure of electromechanical coupling strength is  $C_x/C_o$  [27][63] that provides greater insight for filter applications [48], and serves a common metric to compare performance of capacitive transducers to other technologies such as piezoelectric devices [58]. The  $C_x/C_o$  expression for a disk resonator array, such as the one described in Figure 3.1, in terms of the fundamental disk resonator design variables introduced in Chapter 2 is given by

$$\frac{C_x}{C_o} = \frac{V_P^2}{d_o^3} \frac{1}{f_o} \frac{\epsilon_o (\theta_{i2} - \theta_{i1})}{2\pi^3 \chi K \sqrt{E\rho}} \quad (3.3)$$

Of the variables in (3.2) and (3.3), only the dc-bias voltage  $V_P$  and the electrode-to-resonator gap spacing  $d_o$  are truly adjustable; whereas the remaining variables are anchored by the choice of resonator material, such as  $K_{mat}$ ,  $E$ ,  $\chi$ ; linked to operation frequency as in  $R$ ; or otherwise set in layout like the electrode angle span  $\theta_i$  and the related  $\kappa_i$ .

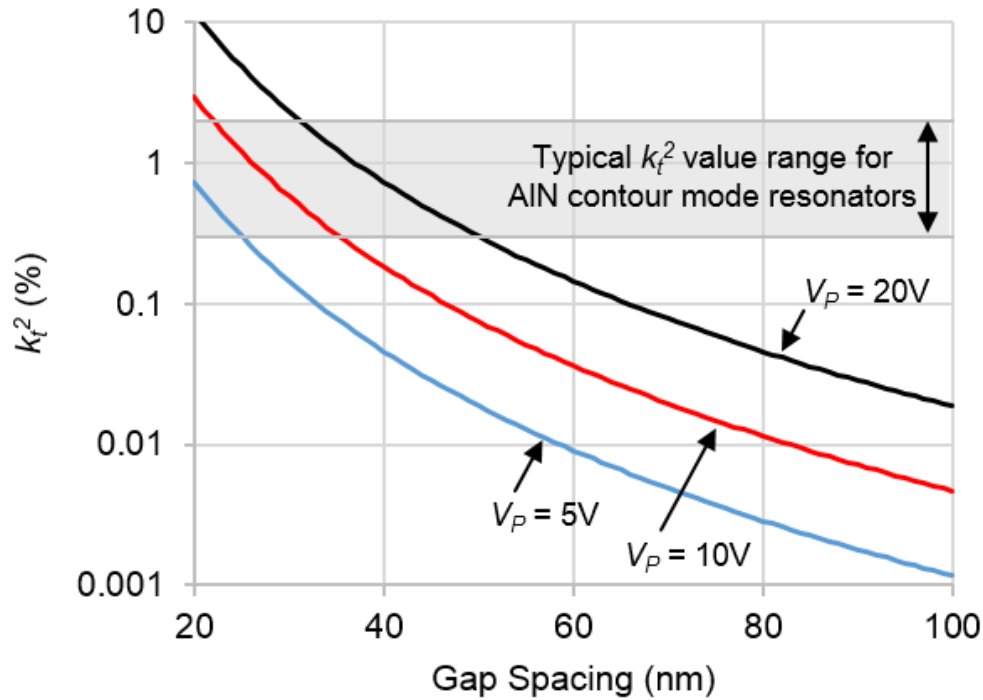


Figure 3.3: Simulated curves of  $C_x/C_o$  as a function of electrode-to-resonator gap spacing for different dc-bias voltages calculated for a 61MHz wineglass mode disk resonator fabricated in polysilicon.

### 3.2 Methods to Improve the Electromechanical Coupling of Capacitive Actuated Vibrating Disk

Although all the variables in (3.2) and (3.3) can (and have been) used as knobs to tailor  $R_x$  and  $C_x/C_o$ ; the electrode-to-resonator gap spacing do stands out as the most effective with its very strong 4<sup>th</sup> power and cubic relation to  $R_x$  and  $C_x/C_o$ , respectively [34][35]. Furthermore, as detailed in [34], reducing gap spacing is the most effective knob by which to maximize the  $\omega_{FOM}=1/(R_Q C_o)$  figure of merit that governs the efficacy of a given resonator for filter construction.

Similarly, the dc bias voltage  $V_P$  provides a convenient way of adjusting electromechanical coupling in real time by synthesizing the desired dc-bias voltage by a circuit. However, even though increasing  $V_P$  improves coupling with a quadratic dependence, it is limited by destructive electrostatic pull-in and ever-shrinking voltage supply rails in contemporary electronic circuit design, though the advent of MEMS based charge-pumps [64] can alleviate the latter given that capacitive disk resonators are passive devices and thus do not impose any dc-current load to the charge pump. Nevertheless, by eliminating the need for a charge pump for design simplicity and keeping operation voltages low for compatibility with standard CMOS, and more importantly by

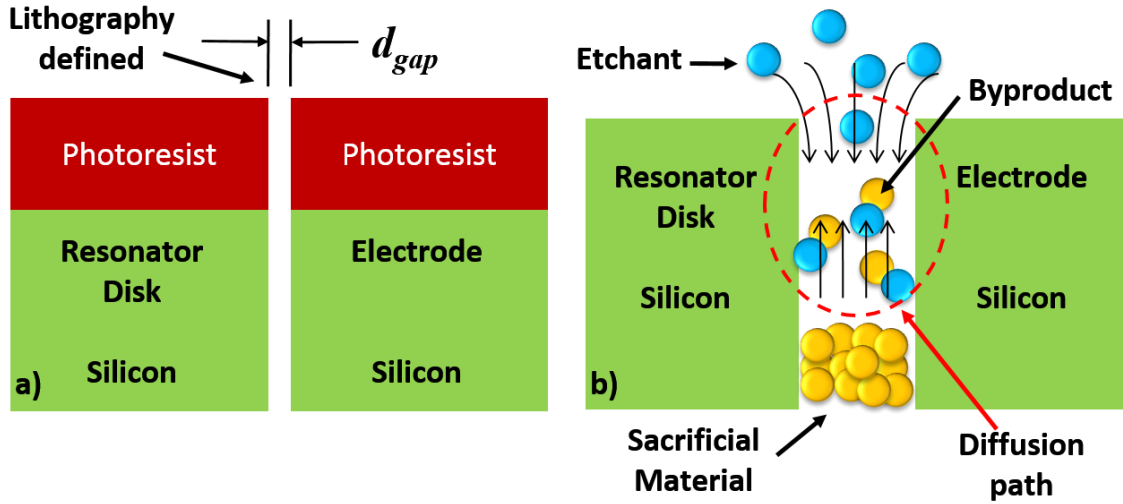


Figure 3.4: Defining the electrode-to-resonator gap spacing by (a) photolithography and dry etching, and (b) a sacrificial etch release.

having the strongest relation to  $C_x/C_o$  and  $R_x$  among all available design variables, scaling of the electrode-to-resonator gap spacing  $d_o$  presents the most advantageous method to increase electro-mechanical coupling of capacitive resonators. Figure 3.2(a) presents curves of  $R_x$  versus gap spacing and dc-bias that illustrate the efficacy of gap scaling and the wide range of  $R_x$  values attainable by capacitively transduced resonators.

And contrary to popular belief, shrinking  $d_o$  does not necessarily reduce resonator linearity, as clearly shown by the  $IIP_3$  versus gap spacing and dc-bias curves of Figure 3.2(b), generated using the theory of [65]. Here, for a dc-bias voltage of  $V_P = 20V$ , the  $IIP_3$  remains above 25 dBm at a gap spacing of  $d_o = 30$  nm. For lower dc-bias voltages, e.g., 5V, the  $IIP_3$  remains high for gap spacings well below 30 nm.

Similarly, Figure 3.3 presents simulated curves of  $C_x/C_o$  as a function of electrode-to-resonator gap spacing  $d_o$  for different values of dc-bias voltage calculated for a 61 MHz wineglass mode disk resonator fabricated in polysilicon, and illustrates the dramatic improvement in electromechanical coupling by scaling  $d_o$ . In fact, achieving a gap spacing in the 20nm – 40nm range enables capacitive transducers to perform on par, if not better, with alternative resonator technologies, such as AlN contour mode resonators [66][67]. However, achieving smooth and near vertical electrode and disk resonator sidewalls as shown in Figure 3.1 in a 100:1 aspect ratio trench for the typical resonator structural film thickness of  $3\mu m$  [35] necessary to avoid mode shape perturbations and  $Q$  reduction due to sidewall defects presents a challenge.

While it is conceivable to define the gap spacing lithographically in layout and a dry etch step as illustrated in Figure 3.4(a), this method would increase fabrication process complexity and does not scale well for increasing aspect ratios with the drive for smaller gap spacing. Furthermore,

lithographically defined gaps would significantly limit the choice of structural material because reliable dry etch methods that can conceivably achieve such high aspect ratios do not exist for some high  $Q$  resonator materials such as polydiamond [51] or nickel [54]. In addition, even though modern CMOS technology can reliably create sub-10nm transistor gates, the fabrication process is optimized for a uniformly repeated gate pattern that has a strictly Manhattan geometry and a periodic pitch. Also, the aspect ratio of the etching step is very small since the gate material is very thin. Attempting to resolve lateral critical dimensions as narrow as 20nm or below in circular geometries, such as the disk resonators illustrated in Figure 3.3, where the array composite resonator layout geometry is more irregularly shaped compared to that of standard CMOS cells, such as the 6-T SRAM [68], is beyond the capability of conventional fabrication methods.

A much simpler and reliable method utilizes a sidewall sacrificial oxide coated over the disk with a thickness matching the desired gap spacing [47]. Depositing the resonator disk, sidewall sacrificial and electrode films in sequence eliminates the need for a high aspect ratio dry etch. However, as illustrated in Figure 3.4(b), this method requires a release etch step where the reactants need to diffuse in to the very high aspect ratio gap and etch the sidewall sacrificial; and just as importantly, the reaction by products should diffuse out without leaving any residue on the resonator. Wet-release processes, such as the common liquid HF release step to clear pin-hole free and uniform oxide sacrificial layers, can reliably release gaps as small as 68nm [47]; however, fails to clear higher aspect ratio gaps where reactions get severely diffusion limited, and wet stiction can lead to catastrophic failure. Vapor phase HF release technique can alleviate stiction and diffusion concerns to some extent and can reportedly clear 10nm gaps [69]; however, brute force etching of such small gaps have very low yield, and the release etch setup costs significantly more and does not easily scale to high volume production. In addition, defining the electrode-to-resonator spacing solely during fabrication does not allow dynamic post-fabrication tuning of electromechanical coupling; which, if possible, would provide the designer with a very strong knob to adjust resonator specifications during R&D stage of the micromechanical circuits.

Of the approaches to reducing gap spacing towards lower impedance [69][70], the partial atomic layer deposition (ALD)-filled gap spacing method described in [34] combines the advantages of better yield relative to brute force gap-release approaches [65], and demonstrated application to a lateral disk resonator, to which the silicide gap method of [70] has not yet been applied. Unfortunately, the work of [34] lowered the  $Q$  of resonator devices from starting values over 150,000 without partial ALD-gap filling down to only  $\sim 10,000$ , supposedly due to surface losses introduced by the  $\text{HfO}_2$  high- $k$  dielectric film used to partially fill the gap and coat the resonator.

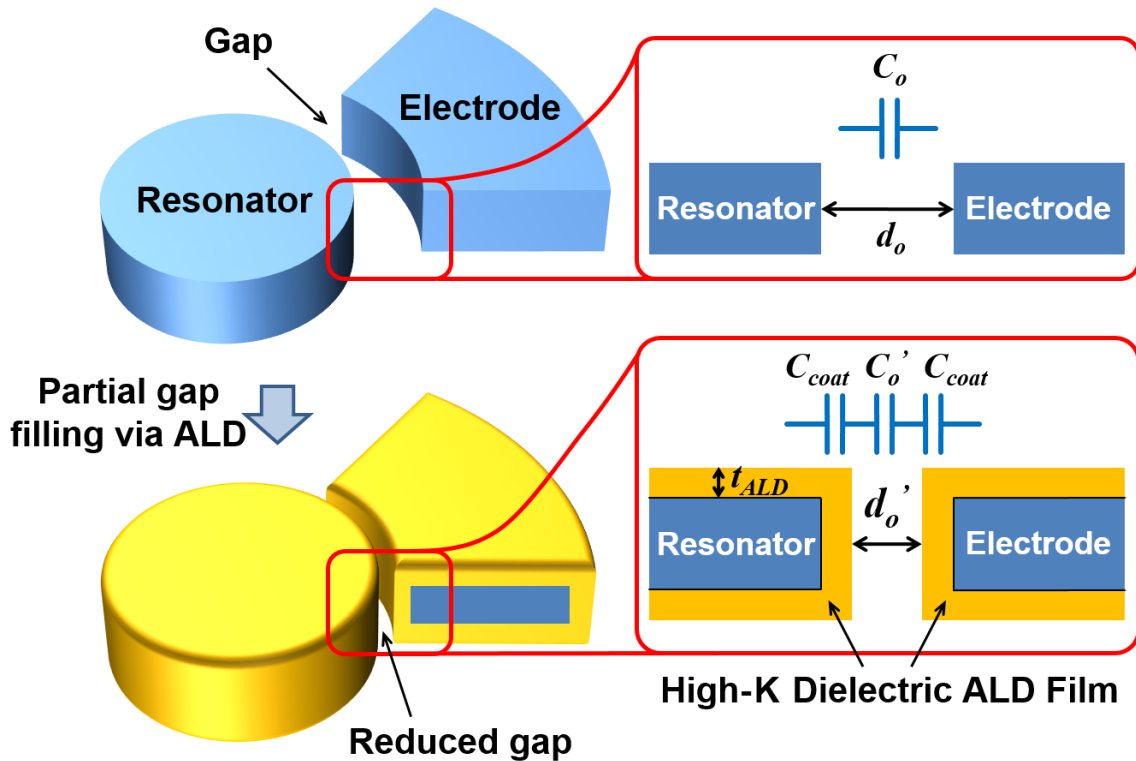


Figure 3.5: Schematics summarizing the partial gap-filling gap reduction method, where ALD of a high- $k$  dielectric film effectively reduces the gap distance between the electrode and the disk.

### 3.3 ALD Partial Electrode-to-Resonator Gap Filling Technique

Partial ALD gap-filling, first demonstrated in [34], comprises a clever way to achieve tiny sub-30nm electrode-to-resonator gaps without the need to etch tiny sacrificial spacer layers, and thus, without the associated yield losses. As described in Figure 3.5, the method involves first fabricating and releasing a micromechanical resonator, e.g., a disk resonator, with relatively wide initial electrode-to-resonator gap spacings that permit good device yield; then coating the resonator and its electrodes with a conformal high- $k$  dielectric ALD film. If the dielectric constant of the dielectric material is sufficiently high, i.e., if it is a “high- $k$ ” material, the effective electrode-to-resonator gap spacing of the coated device will be much smaller than the original spacing, and very close to the physical spacing between the dielectric surfaces, as shown in Figure 3.5. Since ALD [71] provides a very uniform and conformal film deposition with <1nm thickness accuracy controlled simply by the number of reaction half cycles used, one can tune the final gap spacing to any desired value very accurately, provided the initial gap spacing is well known. This equates to an ability to



achieve virtually any low motional resistance in accordance with (3.2), while simultaneously improving  $C_x/C_o$  and  $\omega_{FOM}$  and avoiding the excessive chip area (for arraying [56]) and high bias voltage that would otherwise be needed if large gaps are used.

Here, the total electrode-to-resonator capacitance after ALD coating of the resonator consists of series connection of three sub-capacitors as depicted in Figure 3.5, which can be modeled by an effective capacitance  $C_{o,eff}$

$$\frac{1}{C_{o,eff}} = \frac{1}{C_{ALD}} + \frac{1}{C_o'} + \frac{1}{C_{ALD}} \quad (3.4)$$

where  $C_o'$  and  $C_{ALD}$  are the capacitors that form across the reduced air gap after ALD coating and the high- $k$  ALD layers, respectively, and are given by

$$\begin{aligned} C_o' &= \frac{\epsilon_o (\theta_{i2} - \theta_{i1}) Rh}{d_o - 2t_{ALD}} \\ C_{ALD} &= \frac{\epsilon_o (\theta_{i2} - \theta_{i1}) Rh}{t_{ALD}} \end{aligned} \quad (3.5)$$

Inserting (3.5) into (3.4) leads to the expression for the effective electrode-to-resonator gap spacing  $d_{o,eff}$  achieved by partial ALD filling of the electrode-to-resonator gap as

$$d_{o,eff} = d_o - 2t_{ALD} + \frac{2t_{ALD}}{\epsilon_{r,ALD}} \quad (3.6)$$

where  $\epsilon_{r,ALD}$  denotes the dielectric constant of the ALD film. The advantage of using a very high- $k$  dielectric film, such as  $\text{TiO}_2$  with  $\epsilon_r = 80$  [72], is evident from (3.6) to ensure that the effective gap spacing that determines electro-mechanical coupling is very close to the physical gap spacing  $d_o - 2t_{ALD}$  term after ALD coating by making the last term in (3.6) negligible.

As mentioned, although the work of [34] successfully reduced the gap spacing of a 61-MHz wineglass mode disk resonator from 94 nm to 32 nm by coating the released resonator with a 30.7 nm  $\text{HfO}_2$  ALD film, it did so with a penalty amounting to a  $20\times$  reduction in resonator  $Q$ , from the original uncoated  $Q$  of 150,527 to a much lower value of 7,368. Needless to say, if not mitigated in some way, such a reduction in  $Q$  renders the described partial-gap filling approach quite ineffectual, since  $Q$ 's less than 30,000 are not sufficient for the RF channel-selection or low phase noise applications targeted by MEMS-based vibrating resonators [61]. With all other parameters that influence energy loss (e.g., pressure, temperature, device geometry, anchor size) held constant before and after the  $\text{HfO}_2$  ALD coating, the most probable explanation for the reduction in resonator  $Q$  is added surface loss due to the  $\text{HfO}_2$  ALD film, and this was indeed postulated in [34].

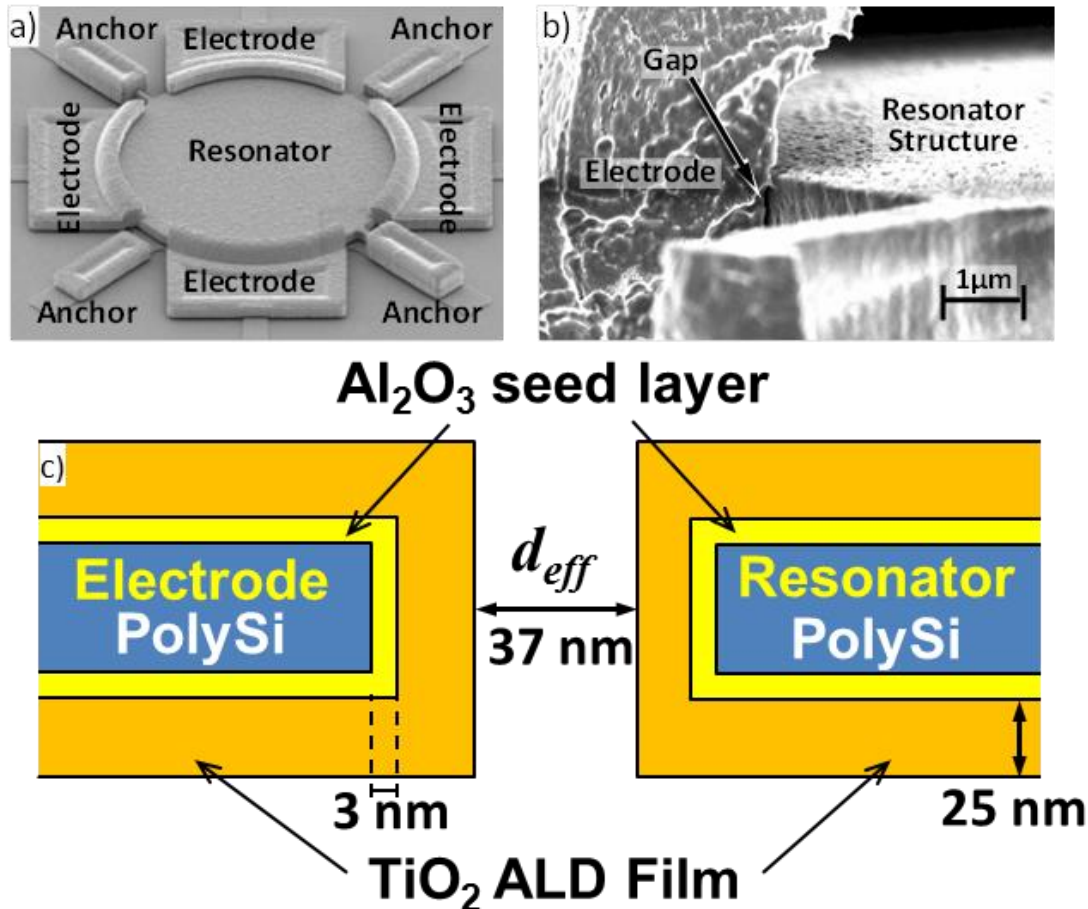


Figure 3.6: SEM images of a) a polysilicon micromachined wine-glass mode disk resonator before gap tuning and b) cross-section after conformal ALD of 3nm  $\text{Al}_2\text{O}_3$  + 25nm  $\text{TiO}_2$ . c) Schematic showing reduction of the resonator-to-electrode gap size from 87nm to 37nm via ALD partial-gap filling.

If surface losses are the main culprit here, then methods for improving ALD film quality are required. Especially, the need to mitigate surface film based losses become even more urgent as resonator dimensions scale down towards higher frequency operation, where the smaller disk radius raises the surface-to-volume ratio and makes surface-derived loss mechanisms even more prominent.

### 3.4 Improving ALD Film Quality

Pursuant to reducing surface-derived losses, this study attempts to improve the ALD film quality by more properly nucleating the high- $k$  dielectric ALD as it grows. The key to the order of magnitude performance  $Q$  boost in this work is the introduction of an interface 3nm  $\text{Al}_2\text{O}_3$  ALD

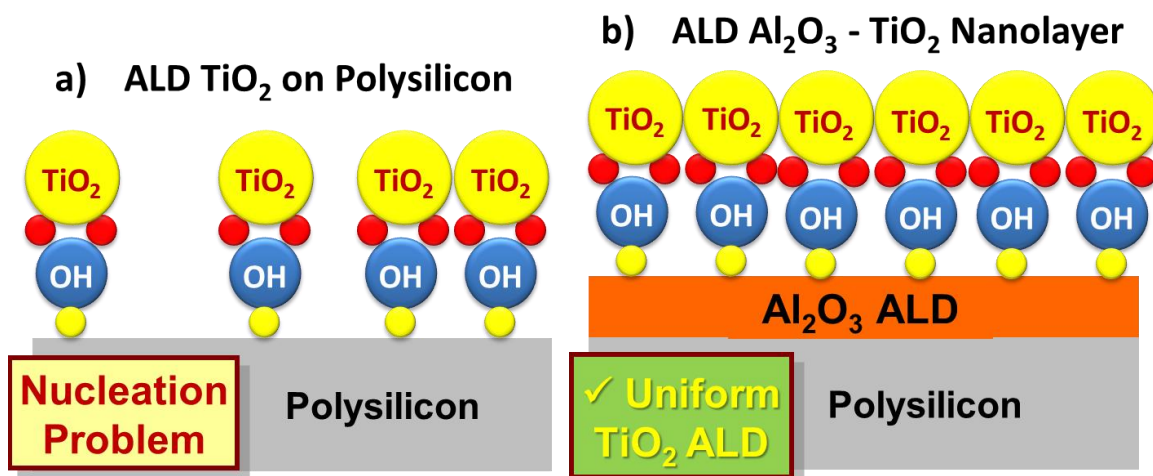


Figure 3.7: a) Good quality TiO<sub>2</sub> ALD film requires good surface hydroxylation, i.e. a rich and uniform OH (hydroxyl) layer, which silicon lacks, leading to a nucleation problem and resultant surface loss mechanism that reduces the resonator  $Q$ . b) Al<sub>2</sub>O<sub>3</sub> grows good quality films on various substrates, even without good hydroxylation, and also provides a dense and uniform forest of AlOH hydroxyl group. This then leads to a uniform subsequent TiO<sub>2</sub> ALD, eliminating surface loss mechanisms that otherwise limit the resonator  $Q$ .

pre-coating before the ALD coating of the much higher- $k$  gap-filling dielectric film—in this case, 25nm of TiO<sub>2</sub>—shown in Figure 3.6(c). The need for such a pre-coating is governed by the ALD deposition chemistry of TiO<sub>2</sub>, which requires a healthy forest of dangling OH bonds over the starting surface to achieve a conformal and high quality film [73]. Without the pre-coating of Al<sub>2</sub>O<sub>3</sub>, the number of free OH bonds on the silicon surface is comparatively sparse, resulting in nucleation problems for the TiO<sub>2</sub> film that in turn lead to  $Q$ -reducing surface defects and losses, *cf.* Figure 3.7(a). Al<sub>2</sub>O<sub>3</sub> is an excellent choice for the pre-coating, because it depends less on a perfectly hydroxylated surface, in other words, it ALDs into good quality films on various substrates, including silicon, whether or not the starting OH forest is sparse [74].

Of course, as seen from (3.6), Al<sub>2</sub>O<sub>3</sub>'s dielectric constant ( $k=9$ ) is too low to serve as the primary gap-filling material, so the thickness of the Al<sub>2</sub>O<sub>3</sub> film should be kept small: for this work, on the order of 3 nm. Although very thin, this Al<sub>2</sub>O<sub>3</sub> film still provides the desired OH surface for the much higher- $k$  ( $k=80$ ) TiO<sub>2</sub> film to follow [75], as described in Figure 3.7(b). Now, with Al<sub>2</sub>O<sub>3</sub> present, the TiO<sub>2</sub> film can be deposited free of nucleation defects, hence, with much better quality and fewer sites for defect-derived energy loss. As a result, this Al<sub>2</sub>O<sub>3</sub>-TiO<sub>2</sub> bilayer approach achieves an optimal solution that provides simultaneous narrow gaps for low motional resistance and low surface losses for high  $Q$ .

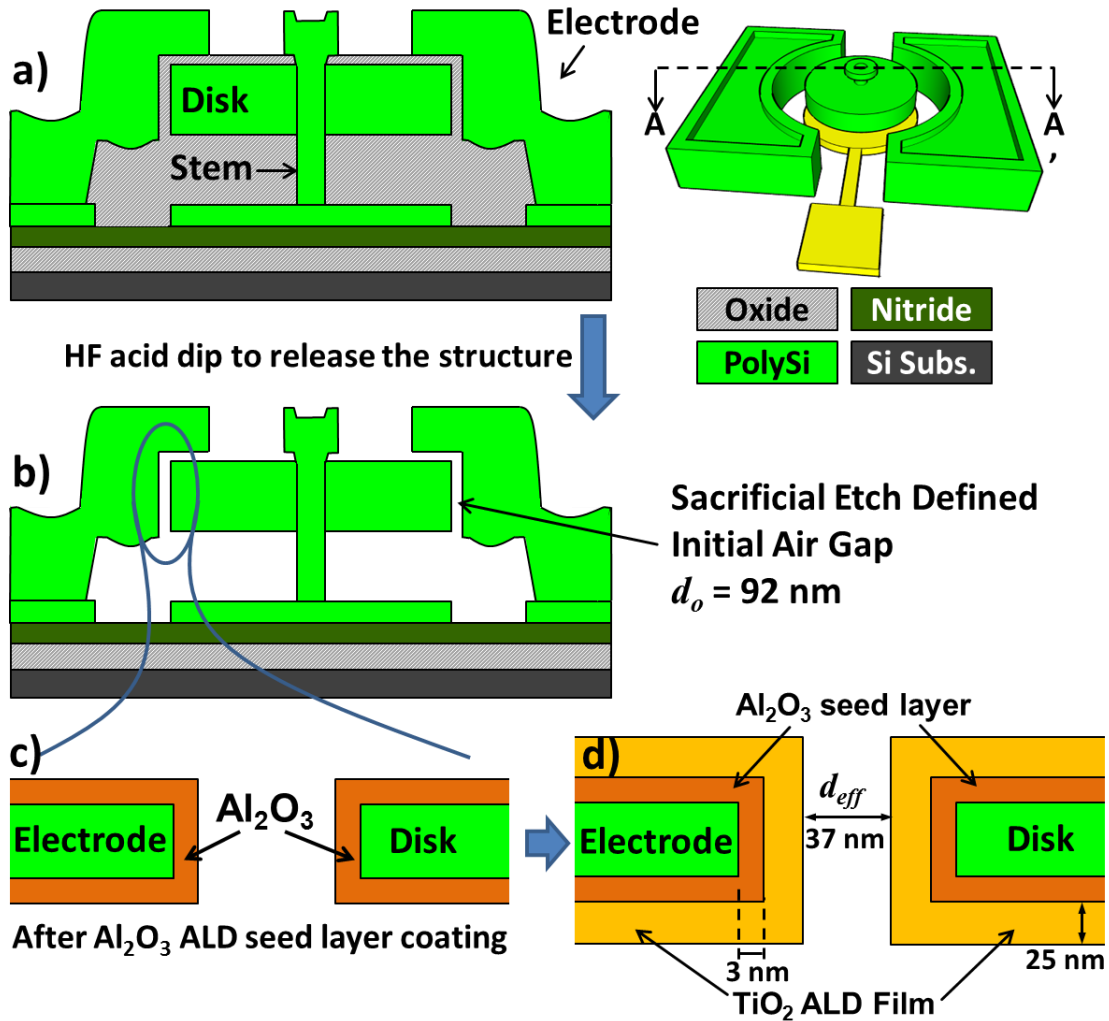


Figure 3.8: Cross-sections describing the process flow for Al<sub>2</sub>O<sub>3</sub>-TiO<sub>2</sub> nanolayer ALD partial-gap filling.

### 3.5 ALD Partial Gap Filling Process Flow

The ALD process is a self-limiting chemical reaction that uses metal precursors to coat an atomically thin layer of metal or metal oxide or metal nitride film on the substrate surface, which is the released polysilicon resonator in the partial gap filling process. The sources used in the ALD setup used in this study contains the desired metal for deposition, such Aluminum and Titanium in this work. This metal is bonded to a hydrophobic alkyl functional group such as Methyl (CH<sub>3</sub>), which will ultimately leave a monolayer of metal oxide behind on the substrate. The metal film is reacted with water vapor to form the metal oxide in the next half of the ALD process cycle. The precursor source bottle is pulsed open in specific intervals defined by the process recipe. A carrier

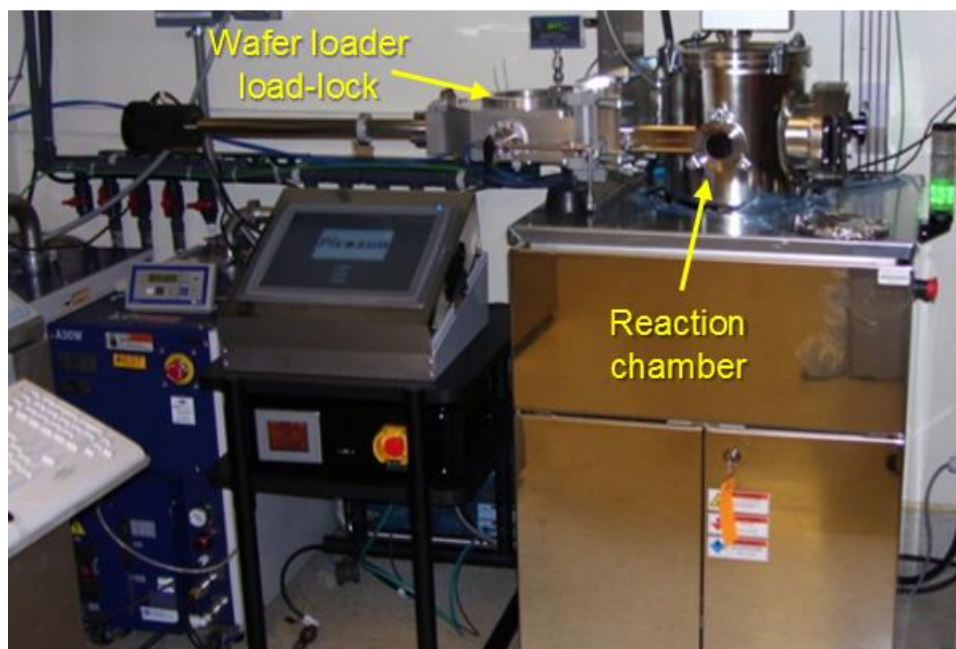


Figure 3.9: The Picosun Sunale R Series ALD system used for the  $\text{Al}_2\text{O}_3$  and  $\text{TiO}_2$  coating for the partial gap filling process.

$\text{N}_2$  gas delivers the precursor material to the reaction chamber in a sequence of pulses, where the number of pulse count determines the ALD film thickness.

Figure 3.8 summarizes the process flow for the ALD partial gap filling process, with the new measures described above to pre-coat structure surfaces with an  $\text{Al}_2\text{O}_3$  ALD seed layer prior to the ALD of the main partial gap filling high- $k$  dielectric  $\text{TiO}_2$ . The process starts with conventional steps [76] to achieve an unreleased 61-MHz wineglass mode disk resonator in polysilicon with 87 nm lateral electrode-to-resonator gaps filled with sacrificial high temperature oxide (HTO), as shown in Figure 3.8(a). The resonator is then dipped in a 49% HF acid bath for 30 minutes to etch the sacrificial oxide and release the structure, achieving the cross-section of Figure 3.8(b). Because the gaps are 87 nm, and not smaller, the yield of the release etch can be quite high, in excess of ~95%.

Next, the released resonator is coated with a 3nm  $\text{Al}_2\text{O}_3$  ALD to achieve the cross-section of Figure 3.8(c). This  $\text{Al}_2\text{O}_3$  layer is quite conformal over the polysilicon surface, which is necessary if it is to serve as a seed layer providing a uniform and dense AlOH hydroxylated surface for a subsequent ALD of 25 nm thick  $\text{TiO}_2$ . Figure 3.8(d) presents the final cross-section of the device, for which the final effective gap spacing is 37 nm. For comparative purposes, versions of the process were also run without the  $\text{Al}_2\text{O}_3$  pre-coating and just ALD'ing 25 nm  $\text{TiO}_2$  directly over the polysilicon resonator surfaces.

A Picosun Sunale R Series, cf. Figure 3.9, was used for all  $\text{Al}_2\text{O}_3$  and  $\text{TiO}_2$  depositions reported in this study. The Picosun ALD system comprises of the wafer load-lock loader station, deposition

Table 3-I: ALD deposition recipe parameters summary.

<b>Process Parameters</b>	<b>Al<sub>2</sub>O<sub>3</sub> ALD Recipe</b>	<b>TiO<sub>2</sub> ALD Recipe</b>
Substrate temperature	300°C	275°C
Deposition pressure	10 hPa	10 hPa
Metal source type	Al(CH <sub>3</sub> ) <sub>3</sub> (liquid)	TTIP (solid)
Metal source temperature	20°C	80°C
Oxidizer source type	H <sub>2</sub> O (liquid)	H <sub>2</sub> O (liquid)
Oxidizer source temperature	20°C	20°C
Pulse time	0.1 s	0.2 s
Chamber purge time	4 s	4 s
Deposition rate	1 Å/cycle	0.25 Å/cycle

chamber, and a source cabinet with the electronics and MFCs associated with it, all of which are controlled by the ALD software installed on device PLC. The system has three reactant source bottles designed to address different precursor materials at specific vapor pressure ranges. The two liquid source bottles installed on the system can store reactants with high vapor pressures above 10 mbar. The single Pico Solid source bottle can store liquid or solid sources with vapor pressures above 1 mbar at temperatures less than 200°C, where the adjustable source temperature provides a knob to achieve the desired reactant vapor pressure. The ability to house multiple reactant gases is a vital process capability of the Picosun ALD system, because it allows the user to deposit multiple ALD films in a sequence, such as the 3nm Al<sub>2</sub>O<sub>3</sub> – 25nm TiO<sub>2</sub> stack presented in this work, without breaking vacuum. Not breaking vacuum between the Al<sub>2</sub>O<sub>3</sub> and the TiO<sub>2</sub> ALD steps keeps the properly hydroxylated surface provided by the Al<sub>2</sub>O<sub>3</sub> pre-coating intact and pristine, so that the succeeding TiO<sub>2</sub> deposition does not have any nucleation problems and thus leads to high resonator Q as will be presented in the following section.

The Al<sub>2</sub>O<sub>3</sub> ALD deposition recipe employed in this study uses Trimethylaluminum Al(CH<sub>3</sub>)<sub>3</sub> stored at room temperature as a liquid Aluminum source, and H<sub>2</sub>O stored as a liquid source at room temperature as the oxidizing agent to form the Al<sub>2</sub>O<sub>3</sub> film. The substrate was kept at 300°C at 10 hPa pressure during the Al<sub>2</sub>O<sub>3</sub> ALD deposition, which leads to an Al<sub>2</sub>O<sub>3</sub> deposition rate of 1 Å/cycle. Similarly, the TiO<sub>2</sub> ALD recipe uses Titanium Tetrakis Isopropoxide (TTIP) stored as a solid source kept at 80°C to provide sufficient vapor pressure to serve as the Titanium source for the TiO<sub>2</sub> ALD formation. The substrate temperature and deposition pressure for the TiO<sub>2</sub> deposition are 275°C and 10 hPa, respectively, which leads to a TiO<sub>2</sub> deposition rate of 0.25 Å/cycle. Table 3-I summarizes the ALD deposition recipe parameters used to achieve the partial gap filling results presented in this chapter.

Finally, to allow for electrical connection to bond pads, a final lithography step was done to cover all released devices and expose their bond pads, after which a very short HF dip removed ALD material over the bond pads. Photoresist was then removed via acetone, and critical point drying was applied to clean devices.

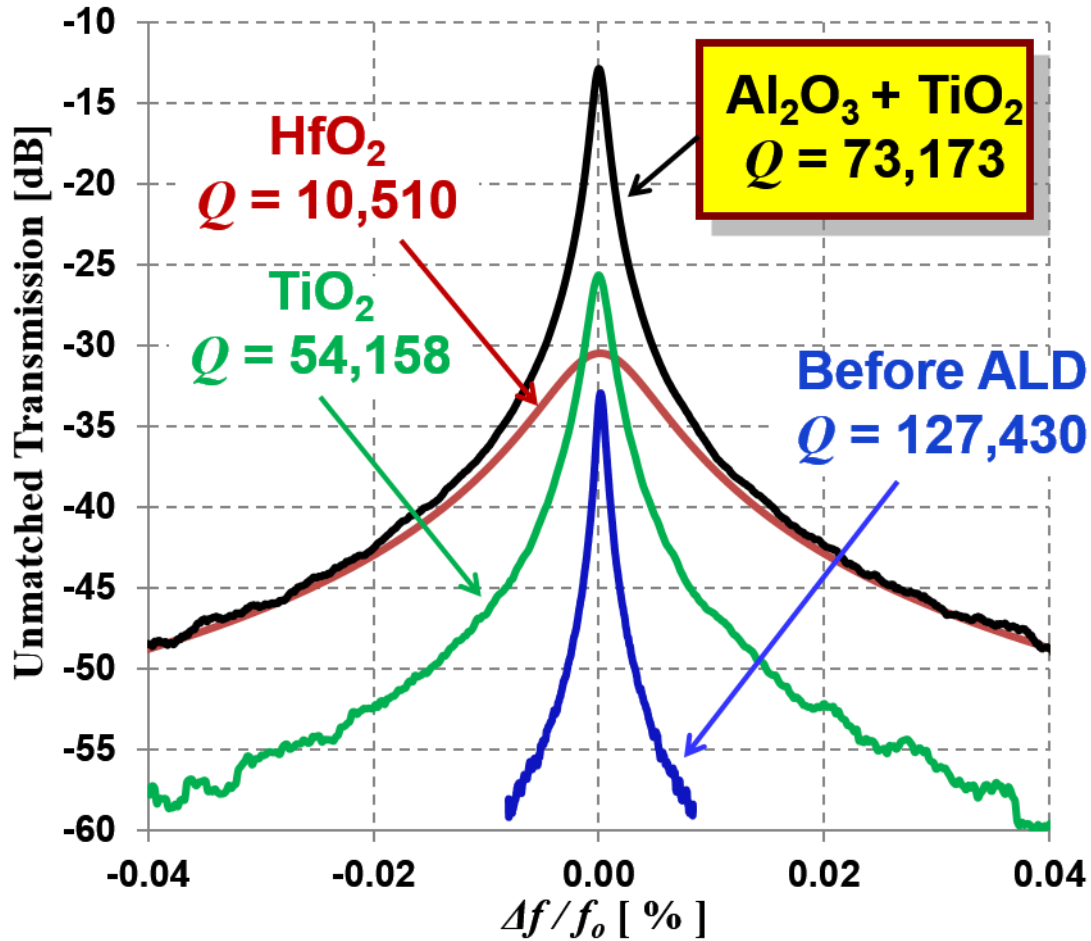


Figure 3.10: Comparison of measured frequency characteristics under vacuum with dc-bias voltage of 9V for 61-MHz wine-glass disk resonators treated with various ALD partial gap filling recipes.

### 3.6 Experimental Results

To verify the efficacy of  $\text{Al}_2\text{O}_3$  pre-coating as a method for reducing surface losses, the frequency characteristics of 61-MHz wine-glass disk resonators with various ALD-coating recipes were measured under 1  $\mu\text{Torr}$  vacuum in direct two-port configurations using an HP 5070B network analyzer. All tested devices were identical prior to ALD-coating, and all were measured under the exact same electrical connection and vacuum conditions. Figure 3.10 compares measured frequency characteristics for 61-MHz wine-glass disk resonators with electrode-to-resonator gaps partially filled with 25nm of  $\text{TiO}_2$  only, without the  $\text{Al}_2\text{O}_3$  seed layer; and 3nm  $\text{Al}_2\text{O}_3$ +25nm  $\text{TiO}_2$ ; showing  $Q$ 's of 54,158 and 73,173, respectively, which clearly indicates the benefits of  $\text{Al}_2\text{O}_3$  pre-coating. Comparison of these results with data from [34] (included in the plot) also

Table 3-II: Summary and comparison of measurement results for wineglass disk resonators treated with various ALD recipes.

	<b>Before ALD</b>	<b>HfO<sub>2</sub> [34]</b>	<b>TiO<sub>2</sub></b>	<b>Al<sub>2</sub>O<sub>3</sub> + TiO<sub>2</sub></b>
<b><math>Q</math></b>	127,430	10,510	54,158	73,173
<b><math>R_x</math></b>	10,180 $\Omega$	6,500 $\Omega$	512 $\Omega$	130 $\Omega$
<b><math>d_o</math></b>	92 nm	32 nm	35 nm	37 nm
<b><math>V_P</math></b>	9 V	5 V	9 V	17 V

makes clear the importance of the high- $k$  dielectric film type and quality, since the  $Q$  of 54,158 achieved via the TiO<sub>2</sub>-only case is still much higher than the HfO<sub>2</sub>-only case of [34], which used an inferior ALD tool to deposit HfO<sub>2</sub>.

It should be noted that ALD film coating does change the resonance frequency of each disk, most likely due to a combination of mass loading and an equivalent stiffness change caused by ALD film stress. Therefore, to better compare resonator  $Q$ 's and peak heights for different ALD coating experiments, the data in Figure 3.10 is normalized to a common frequency axis by applying to all data points the expression

$$\%f_{Norm} = \frac{f - f_o}{f_o} \times 100 \quad (3.7)$$

where  $f_o$  is the center frequency of each disk and  $f$  is the measurement frequency of the data point. Table 3-II provides a summary and comparison of all measured results.

### 3.6.1 Effect of Parasitic Resistance on Resonator $Q$

Parasitic trace resistance, denoted as  $R_P$ , can significantly degrade resonator  $Q$  when the impedance of the resonator is on the order of or lower than that of the parasite. Figure 3.11 explains how various parasitic elements like interconnect traces and bond-pad contacts can modify the electrical equivalent LCR circuit of the resonator and load the resonator  $Q$  via the expression:

$$Q = \frac{\omega_o L_x}{R_x} \Rightarrow Q_{Loaded} = \frac{\omega_o L_x}{R_x + 2R_P} \quad (3.8)$$

This work uses 400 nm-thick doped polysilicon traces as interconnect, as shown in Figure 3.11, for which the measured parasitic resistance is  $R_P = 1.2$  k $\Omega$ . Compared to the motional resistance  $R_x = 130$   $\Omega$  achieved by the Al<sub>2</sub>O<sub>3</sub>-TiO<sub>2</sub>-coated device of this work, such a large parasitic resistance leads to a loaded  $Q$  that is 10.2 $\times$  smaller than the actual  $Q$  of the device alone (without interconnects), and this is what is actually measured. Since the focus here is on the  $Q$  and  $R_x$  of the resonator device alone, sans the effect of interconnects, the data plotted in Figure 3.10 represents the actual  $Q$  of each device after extracting out loading by parasitic resistance using (3.8).



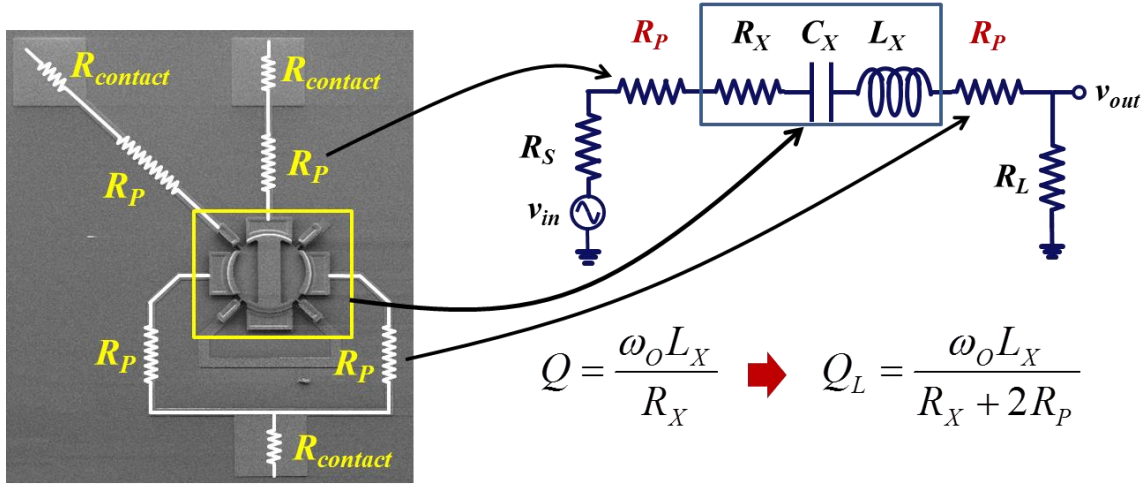


Figure 3.11: (Left) SEM of the 61-MHz wineglass disk resonator used in this work. The polysilicon traces and bond-pad contacts create parasitic resistance that then load the (right) electrical equivalent LCR circuit of the resonator, lowering its  $Q$  via the indicated expression.

### 3.6.2 Extraction of the gap spacing $d_o$

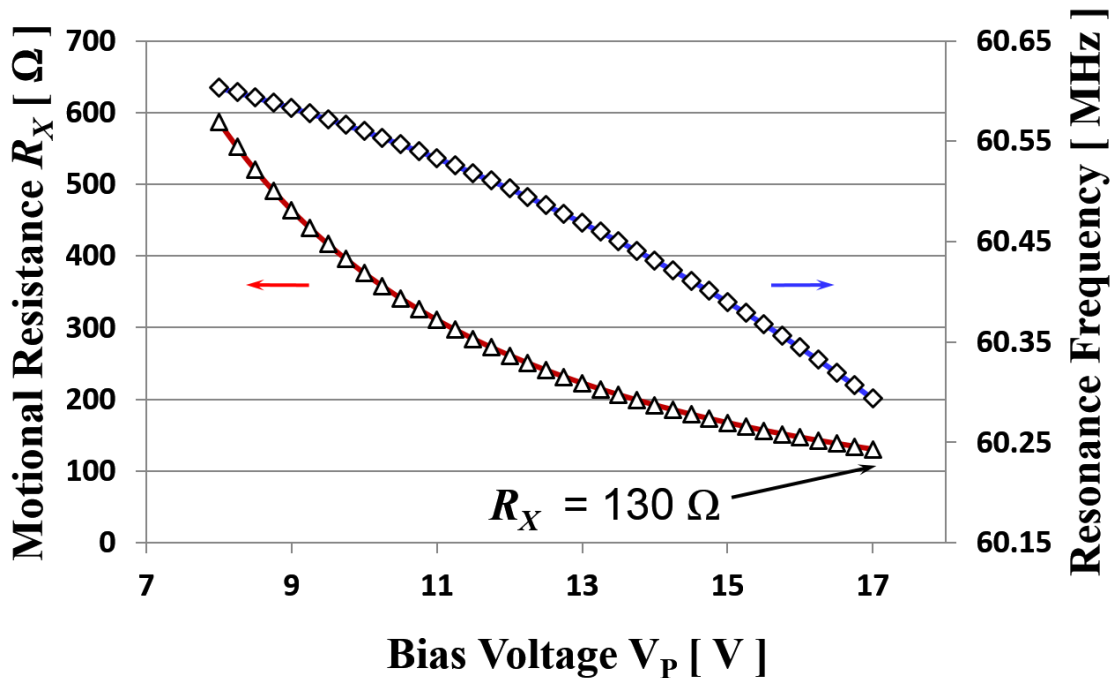


Figure 3.12: Measured curves of motional resistance (bottom curve) and resonance frequency (top curve) versus dc-bias. The electrical stiffness effect observed in the latter is used to extract the effective electrode-to-resonator gap spacing of a given device.

As previously elaborated in Section 2.4.6 of this dissertation, the effective gap spacing of any parallel plate capacitively transduced micromechanical resonator can be conveniently extracted by utilizing the electrical-stiffness [37] derived dependence of resonance frequency  $\omega_o$  on the applied bias voltage  $V_P$  and the gap spacing  $d_{gap}$ . Figure 3.12 presents measured curves of frequency and motional resistance vs. bias voltage for the  $\text{Al}_2\text{O}_3+\text{TiO}_2$ -coated resonator, all of which can be curve fitted simultaneously to reveal an effective gap spacing of  $d_o = 37\text{nm}$ ; nominal zero-bias resonance frequency and  $Q$ 's of 60.68 MHz and 73,173, respectively; and a motional resistance (with series interconnect resistance removed) of only  $R_x = 130 \Omega$ , as advertised.

### 3.7 Oscillator Far-from-Carrier Phase Noise Reduction via Nano-Scale Gap Tuning of MEMS Micromechanical Resonators

In addition to the significant motional resistance reduction demonstrated in the preceding sections, substantial improvements in the far-from-carrier phase noise of oscillators referenced to stand-alone (as opposed to arrayed [56]) capacitively transduced micromechanical disk resonators have been attained via the use of atomic layer deposition (ALD) to tune the electrode-to-resonator capacitive gaps. Specifically, ALD of about 30nm of hafnia ( $\text{HfO}_2$ ) onto the surface of a released 60-MHz micromechanical disk resonator to reduce its effective resonator-to electrode gap size from 92nm to 32nm provides an increase in power handling leading to more than 15-20dB reduction in the far-from-carrier phase noise of an oscillator referenced to this resonator. This ALD-enabled nano-scale gap tuning provides a simple and effective method to satisfy increasing demands for higher short-term stability in frequency references for electronic applications.

With measured on-chip  $Q$ 's exceeding 150,000 at VHF and 15,000 at UHF, surface-micromachined capacitively transduced micromechanical disk resonators have already combined with properly-designed sustaining circuits to achieve phase noise marks commensurate with the reference oscillator specifications required by the GSM cellular phone standard [45]. Specifically, GSM demands phase noise  $< -130\text{dBc/Hz}$  at 1 kHz offset from a 13-MHz carrier, and  $< -150\text{dBc/Hz}$  at far-from-carrier offsets. In satisfying these specs, the sheer  $Q$  of a capacitively transduced micromechanical resonator easily makes the close-to-carrier number. The far-from-carrier number, on the other hand, is much less dependent on  $Q$  and rather relies more on the power handling capability of the resonator, which for capacitive transduction is smaller than that of quartz crystals.

To overcome the power handling deficiencies of capacitively transduced disks, [77] mechanically coupled many disks into an array composite resonator that behaved like a single high- $Q$  resonator, but with a power handling capability larger than that of a single resonator by a factor equal to the number of resonators used in the array. The solution of [77] comprises a mechanical circuit approach to raising power handling, so requires no changes in technology to achieve the needed performance. Arguably, such a circuit approach is perhaps the most elegant solution to the far-

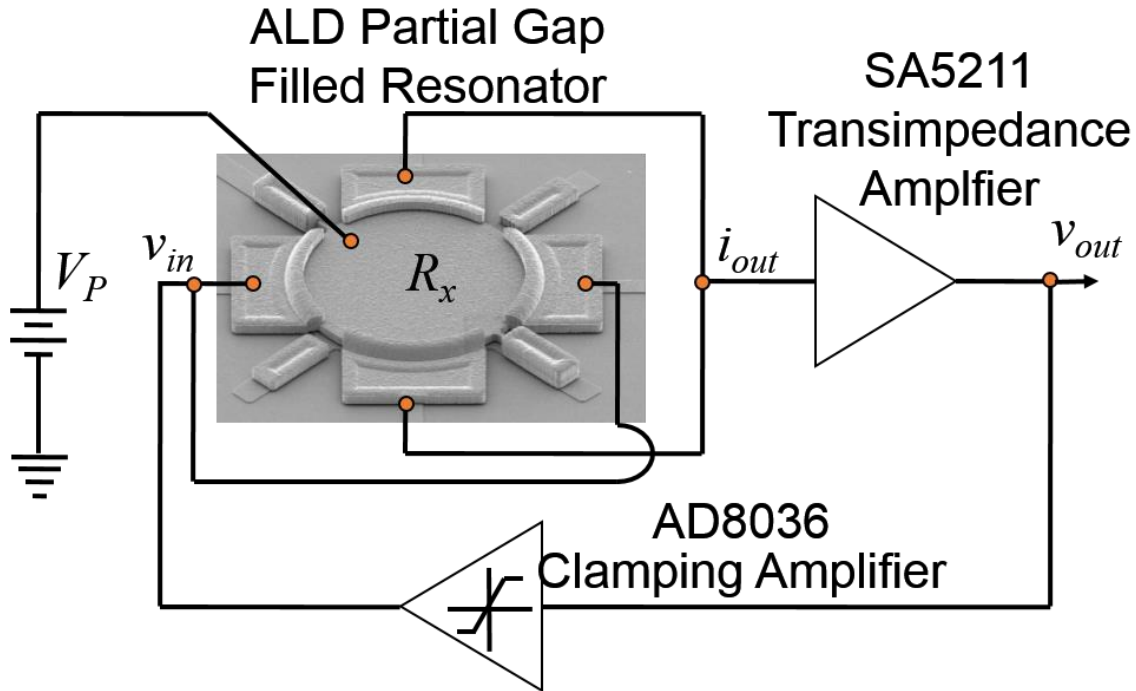


Figure 3.13: Schematic of the oscillator circuit used in this work, which comprises a micromechanical disk resonator, a transimpedance amplifier, and a clamping amplifier.

from-carrier phase noise issue for commercial wireless needs. However, another method to raise the current handling ability of a capacitively transduced micromechanical resonator is to reduce its electrode-to-resonator gap spacing, which essentially provides it with a more efficient electro-mechanical transducer.

Pursuant to investigating the efficacy of this approach, this work explores the use of ALD gap-filling methods introduced in Section 3.3 to reduce gaps towards a 15-20dB improvement in the far-from-carrier phase noise of an oscillator referenced to a micromechanical disk resonator. Although impressive, this figure comes at the expense of the close-to-carrier phase noise, which ends up suffering from 1) a lower  $Q$  caused by ALD; and 2) noise aliased by the larger non-linearity arising from smaller electrode-to-resonator gap spacing. Before delving in, some review of phase noise theory is in order.

### 3.7.1 Oscillator Phase Noise

Figure 3.13 presents a schematic of the circuit used in this work to sustain the oscillation of a micromechanical disk resonator. Briefly, in order to start up oscillations, the loop gain must be larger than 1 and its phase shift must be  $0^\circ$ . One way to insure this is to use a transresistance sustaining amplifier with current-to-voltage gain larger than the motional resistance of the resonator. Once oscillation begins, the amplitude of oscillation grows until some form of non-linearity limits the amplitude, after which steady-state oscillation ensues. Unlike quartz crystal oscillators,

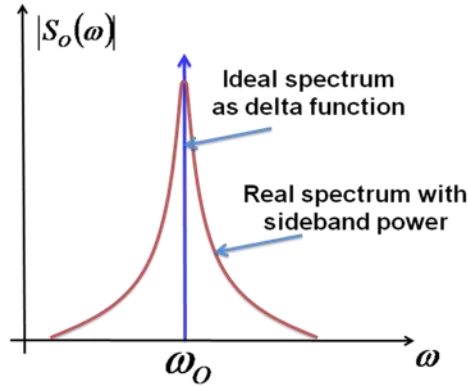


Figure 3.14: Schematic comparing the ideal delta function output signal of a noiseless oscillator with the actual output of a real oscillator possessing sideband noise components.

where the oscillation amplitude is generally limited by amplifier nonlinearity, MEMS resonator-based oscillators limit via either a nonlinearity in the resonator itself, or by a limiter circuit placed in the feedback loop.

As shown in Figure 3.13, this work takes the latter approach. In particular, the circuit utilizes an SA5211 transimpedance amplifier with a transresistance gain of 14 k $\Omega$ , together with an AD8036 clamping amplifier that clamps the voltage applied to the micromechanical disk resonator to a specifiable value, thereby limiting the oscillation amplitude of the overall oscillator.

Given that the main function of an oscillator is to provide a very distinct and stable frequency, the output of an ideal oscillator should in principal be a delta function in frequency domain, where all energy is at one and only one frequency. However, in practice, noise from the electronics or the resonator element superposes itself onto the output sinusoid, generating power at frequencies adjacent to the output frequency as shown in Figure 3.14. This adjacent power is considered undesired noise. In general, this noise comprises both amplitude and phase components. However, when the oscillation amplitude is limited at a constant level during steady state operation, e.g., by the limiter in circuit of Figure 3.13, only phase noise remains.

Leeson's model describes the oscillator phase noise as the single-side band noise-to-carrier power ratio at an offset frequency  $\Delta f$  from the oscillator's carrier frequency  $f_o$  via the expression [78]

$$L\{\Delta f\} = 10 \log \left( \frac{k_b T F}{P} \left( \frac{1}{4Q^2} \left( \frac{f}{\Delta f} \right)^2 + 1 \right) \right) \quad (3.9)$$

where  $k_b$  is the Boltzmann constant;  $T$  is the absolute temperature in Kelvin;  $F$  is the noise factor of the sustaining amplifier;  $Q$  is the loaded quality factor of the resonator; and the oscillator carrier power  $P$  is given by

$$P \approx \frac{v_{in}^2}{R_x} \quad (3.10)$$

where  $v_{in}$  is the voltage applied to the resonator input and  $R_x$  is the resonator motional resistance, given approximately by

$$R_x = \frac{m_r \omega_o}{(\epsilon_o A_o)^2 V_P} \cdot \frac{d_o^4}{Q} \quad (3.11)$$

where  $A$  and  $d_o$  are the electrode-to-resonator overlap area and gap spacing, respectively,  $m_r$  is the equivalent dynamic mass of the disk,  $\omega_o$  is the radian resonance frequency of the disk,  $V_P$  is the dc-bias voltage, and  $\epsilon_o$  is the permittivity of air. Assuming that the first term in the product in (3.9) remains constant, and given that the clamping amplifier sets  $v_{in}$  constant, (3.10) can be rewritten as

$$P \propto \frac{Q}{d_o^4} \quad (3.12)$$

Inserting (3.12) into (3.9) leads to the oscillator far-from-carrier phase noise (when  $\Delta f$  is large)

$$L(\Delta f) = 10 \log \left( \frac{k_b TF}{P} \right) = 10 \log \left( \frac{k_b TF}{c \cdot Q / d_o^4} \right) \quad (3.13)$$

where “ $c$ ” is a constant. Using reduction scale factors, the change in far-from-carrier phase noise can be expressed as

$$\Delta L = -10 \log(n_Q) + 40 \log(n_d) \quad (3.14)$$

where  $n_d$  is the gap reduction scale factor and  $n_Q$  is the  $Q$  reduction scale factor. From (3.14), although  $Q$  influences the far-from-carrier phase noise, the gap spacing  $d_o$  has a much stronger pull, with a fourth power dependence.

### 3.7.2 ALD Partial Gap Filling for Stronger Power Handling

One very effective way to reduce the electrode to resonator gap spacing of a lateral micromechanical resonator is the ALD partial-gap filling method first described in Section 3.3 and depicted in Figure 3.5. Here, ALD is used to conformally deposit a thin high- $k$  dielectric film on all surfaces of a micromechanical disk resonator, including within the electrode-to-resonator gaps. Upon doing this, the capacitance between the electrode and resonator becomes the series of three capacitors,  $C_{coat}$ ,  $C_o'$ , and  $C_{coat}$ , where  $C_o'$  is much smaller than  $C_{coat}$ . Since the smallest value dominates when

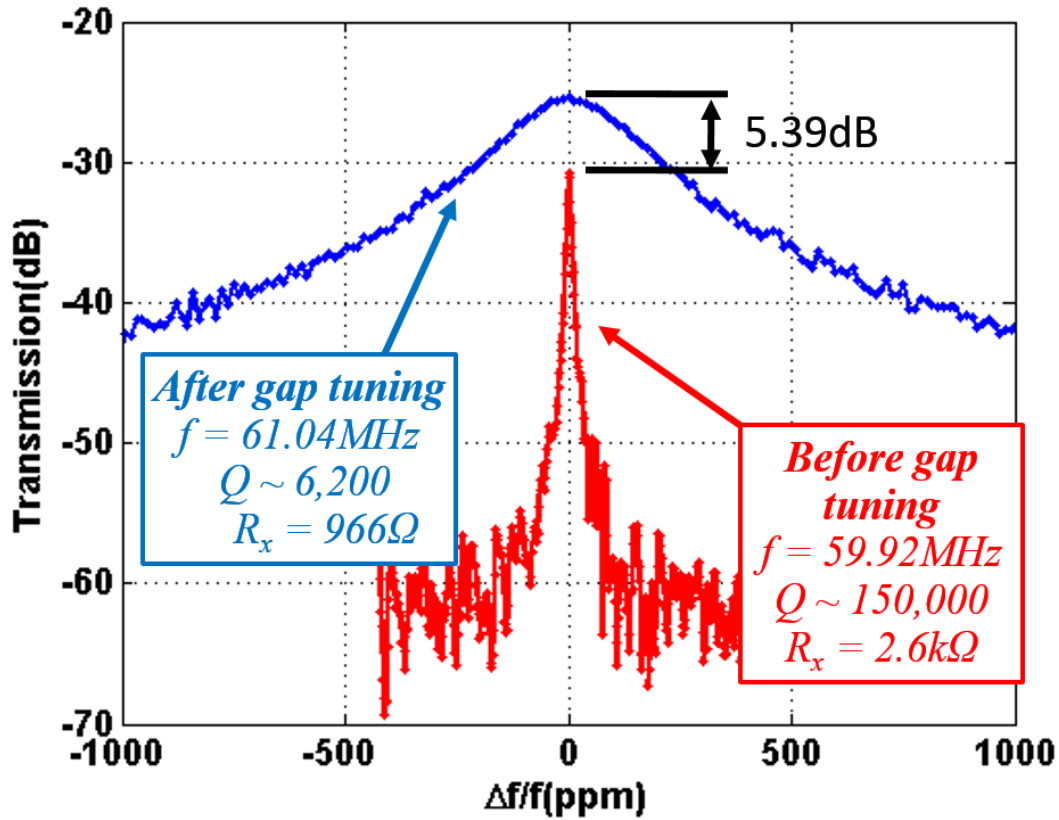


Figure 3.15: Comparison of frequency response before and after gap tuning. The loss after gap tuning is 5.39dB less than before gap tuning, due to enhanced power handling by reduced gap size, although quality factor was lowered after the ALD. In both cases, the bias voltage was the same ( $V_P=16V$ ).

capacitors are in series, the resonator-to-electrode capacitance boils down to the capacitance between the two coated surfaces, or  $C_o'$ . This effectively reduces the gap spacing to the distance between the surfaces of dielectric coating.

To capitalize on this, micromechanical disk resonators were first fabricated by a small-lateral gap polysilicon surface micromachining process similar to that previously used in [34][45]. Devices were patterned in a 3 $\mu$ m-thick polysilicon layer and a conformal sacrificial sidewall spacer high temperature oxide (HTO) deposition that provided 92nm lateral gaps between resonator structure and electrodes. Next, devices were released using hydrofluoric acid wet etching followed by critical point drying. Figure 3.6(a) shows the SEM of the resonator device at this point in the fabrication process. Next, atomic layer deposition was used to coat the surfaces of devices with 30nm of HfO<sub>2</sub> ( $\kappa\sim 30$ ), which reduced electrode-to-resonator gap spacings down to  $\sim 32$ nm. Figure 3.6(b) presents the device cross-section after this partial-gap filling process.

### 3.7.3 Experimental Results

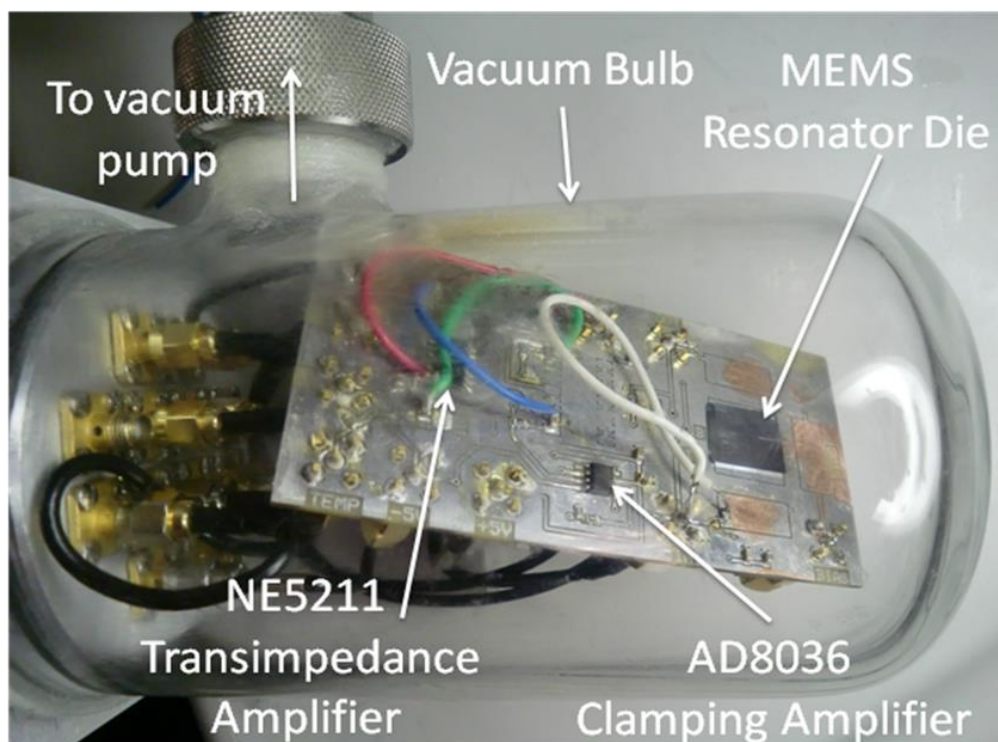


Figure 3.16: The oscillator test setup. Here, the resonator die is mounted on the circuit board and installed in a custom-made chamber for phase noise measurement under high vacuum ( $\sim\mu\text{Torr}$ ).

### 3.7.3.1 Resonator Frequency Response Measurement

Frequency response spectra for the fabricated micromechanical disks were measured under  $1\ \mu\text{Torr}$  vacuum before and after gap reduction via ALD. Figure 3.15 compares the measured characteristics after normalization to their respective center frequencies by making the  $x$ -axis fractional frequency offset from resonance. (This normalization was necessary, since the added mass (and stiffness) of the ALD film shifted the resonance frequency from  $61.04\ \text{MHz}$  without ALD, to  $59.82\ \text{MHz}$  with it.) The plot clearly shows a  $5.39\ \text{dB}$  increase in the (unmatched) transmission at resonance for the partial ALD-gap-filled device over the unfilled one, even after a significant reduction in quality factor (from  $150,000$  to  $10,000$ ). This reduction in quality factor was discussed in Section 3.4 and is probably caused by added surface losses induced by the deposited  $\text{HfO}_2$  film.

### 3.7.3.2 Oscillator Phase Noise Measurement

Both ALD partial-gap-filled and non-filled disk resonators were mounted and bond-wired to the circuit of Figure 3.13, then placed into a custom-built vacuum chamber with electrical feed-throughs to allow connection to external power sources and measurement instrumentation. Figure 3.16 presents a photo of the “glass bulb” vacuum chamber with the oscillator board within. During testing, a turbomolecular pump provided vacuums down to  $1\ \mu\text{Torr}$ , which eliminates gas damping and allows a given resonator to take on its highest  $Q$  value.

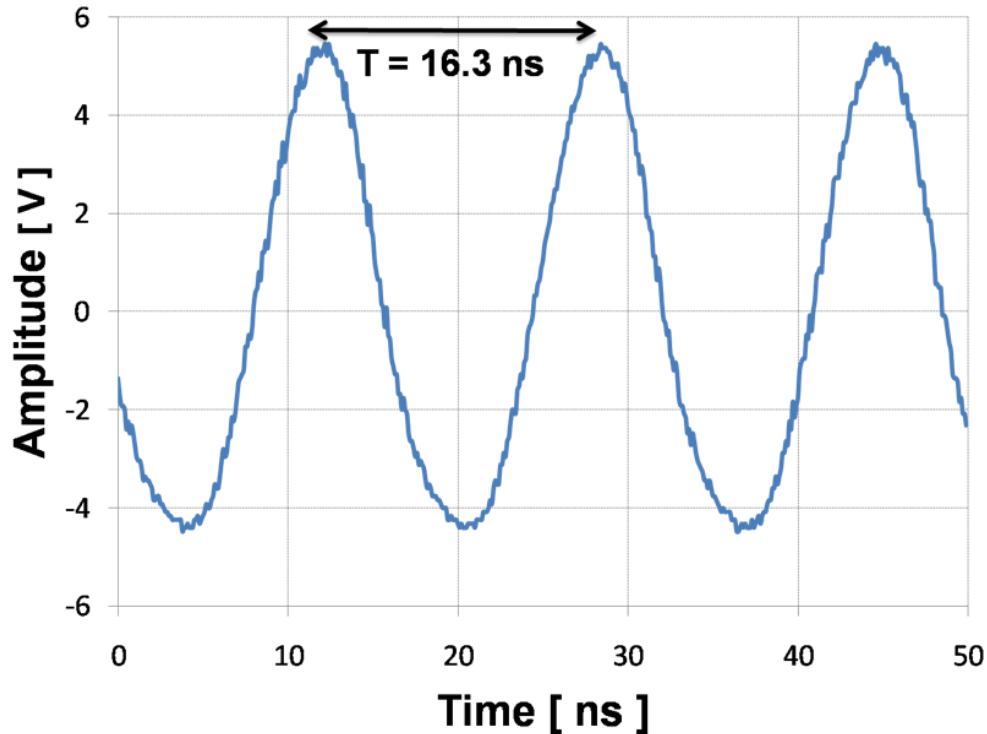


Figure 3.17: Oscilloscope waveform of the oscillator output.

The application of a dc-bias voltage  $V_P$  (c.f., Figure 3.13) to the disk resonator and supply power to the sustaining circuit was all that was needed to induce startup of oscillations. Figure 3.17 presents the oscillation waveform produced by the oscillator circuit referenced to a 32  $\mu\text{m}$  radius wine-glass disk without ALD operating in its 61-MHz wine-glass disk mode. Given that the output voltage was clamped at 10mV by the AD8036, it is no surprise that the ALD partial-gap filled devices gave similar output waveforms.

An Agilent E5500 Phase Noise Measurement System was utilized to accurately measure the phase noise of a 32  $\mu\text{m}$  radius disk

- 1) without ALD gap-filling, so with an electrode-to-resonator gap spacing of 92nm; and
- 2) with an ALD partial-gap-filled electrode- to-resonator gap spacing of 32nm.

Figure 3.18 plots the respective phase noise curves, each divided down to a common carrier frequency of 13MHz for fair comparison. Here, ALD partial-gap filling is seen to provide an improvement in far-from-carrier phase noise by more than 15dB, and up to 20dB at certain far-from-carrier frequency offsets!

It should be noted that the observed improvement in far-from-carrier phase noise actually does not match the prediction of (3.14). In particular, if the measured gap spacing and  $Q$  reduction factors of  $\sim 3$  and  $\sim 15$ , respectively, are inserted into (3.14), the predicted improvement in far-



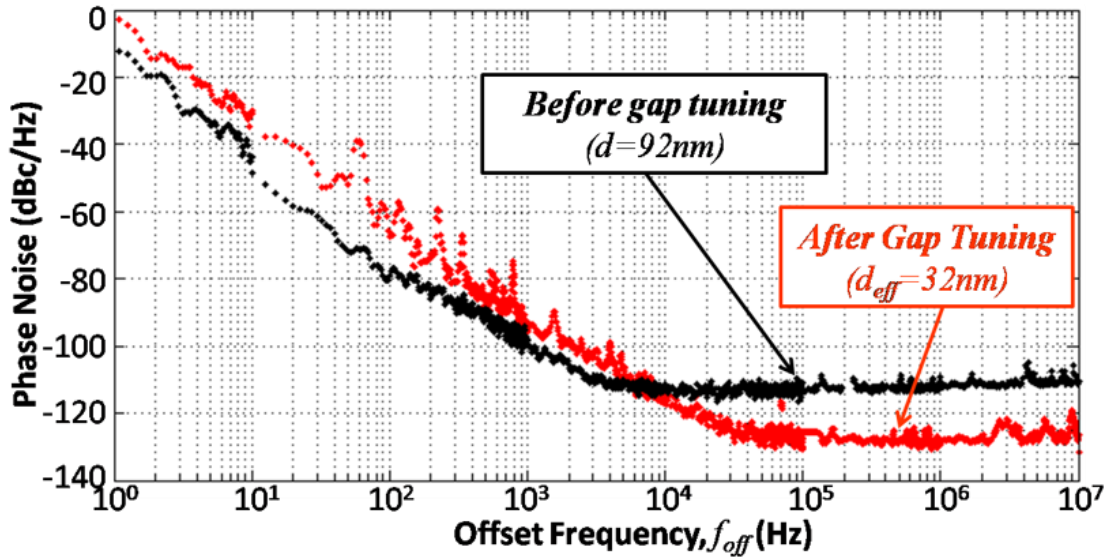


Figure 3.18: Plot comparing the phase noise of the 60-MHz wine-glass mode disk resonator oscillator before and after ALD gap tuning. As can be seen, the “far-from-carrier” phase noise has been improved by more than 15dB.

from-carrier phase noise is only 7dB. This is much smaller than the observed 15-20dB. At present, this is difficult to explain, although there are two plausible possibilities:

- 1) It is possible (but not likely) that the AD8036 clamping circuit increased its clamping voltage value when the ALD partial-gap-filled disk was inserted in to the oscillator loop, which would then raise the power level.
- 2) The very small gap of the ALD’ed disk incites nonlinearity at much smaller displacement amplitudes, leading to much larger output current amplitudes than predicted by linear theory for any given input voltage, and thus, generating more power than expected.

If either of the above occurred, then the loop power given by (3.10) would be larger and more capable of achieving the 15-20dB improvement in phase noise.

Regardless of the above discussion, the observed improvement in far-from-carrier phase noise comes at a heavy cost to the close-to-carrier phase noise, which becomes considerably poorer after ALD-coating of the disk resonator. Much of the poorer close-to-carrier phase noise derives directly from the fact that the  $Q$  of the ALD’ed disk dropped by a factor of  $\sim 15\times$ . Since (3.9) has a  $1/Q^2$  dependence, this factor is equivalent to a 23dB increase in phase noise at close-to-carrier offsets, which then negates the apparent 20dB improvement afforded by the higher power handling ability of the ALD partial-gap-filled disk.

But there’s actually more to it than this. In particular, some portions of the ALD partial gap-filled resonator oscillator’s close-to-carrier curve are more than 20dB higher than that of the non-

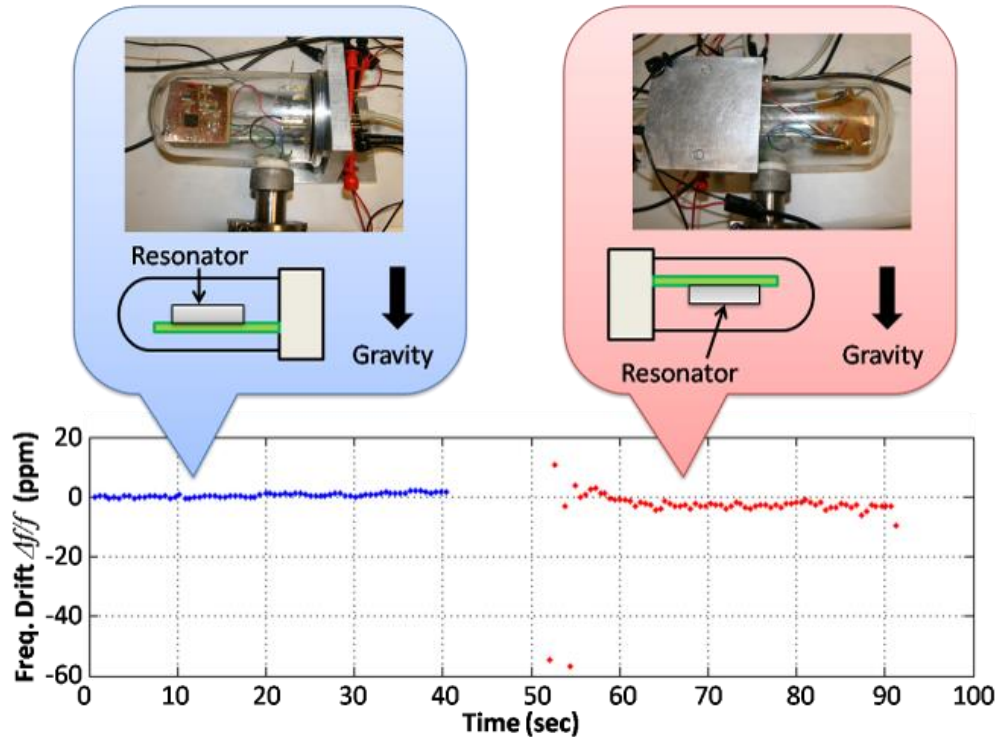


Figure 3.19: Preliminary experimental result of g-force sensitivity test. The frequency change of the oscillator was measured continuously while the gap tuned resonator experienced 2g difference, and very small trend in frequency drift has been detected.

ALD case, and this cannot be explained by the observed  $Q$  reduction due to  $\text{HfO}_2$  coating. Closer inspection of the close-to-carrier region on the ALD'ed resonator oscillator curve shows that this curve exhibits a  $1/f^3$  dependence, whereas the non-ALD curve has a  $1/f^2$  dependence. From [53] and [79], this suggests that the ALD partial-filled gap resonator was driven to amplitudes large compared to its static gap spacing, which is not surprising given the tiny size of the gap. As explained in [53], operation at such large amplitudes induces nonlinearities that can then alias transistor  $1/f$  noise into the oscillator passband, where they are then filtered by the oscillator transfer function to generate  $1/f^3$  noise. This would also support mechanism (2) above in explaining the larger far-from-carrier phase noise improvement. Finally, Figure 3.19 presents the preliminary vibration sensitivity test. Here, the frequency change of the oscillator was measured continuously while the gap tuned resonator experienced 2g difference, where a small trend in frequency drift is observed. This result indicates that the very narrow capacitive actuation gaps obtained by the ALD gap scaling technique does not adversely affect the vibration sensitivity of the oscillator.

### 3.7.4 Oscillator Design Insights via ALD Gap Scaling Technique

Although it requires some sacrifice in close-to-carrier phase noise and exhibits some unexpected performance enhancement, the 15-20dB increase in far-from-carrier phase noise obtained via ALD partial-gap filling in this work is nevertheless very impressive. Given that present

MEMS-based GSM-phase-noise-compliant oscillators actually beat the GSM close-to-carrier phase noise requirements by a fairly large margin (e.g., by 10dB in [77]), there is actually some room to sacrifice in close-to-carrier phase noise.

Furthermore, as discussed in Sections 3.4, the quality factor restoration techniques using high temperature annealing for HfO<sub>2</sub>, as well as the Al<sub>2</sub>O<sub>3</sub> – TiO<sub>2</sub> bi-layer for high  $Q$  will eventually improve the closed-to-carrier phase noise as well. Restoring the post ALD gap scaling  $Q$  by optimized ALD coating processes as elaborated in Section 3.4, together with a reduction in the number of resonators needed over the array approach of [77] makes the described ALD partial-gap filling approach quite compelling for future high performance MEMS-based oscillators.

### 3.8 Conclusion

This work demonstrates the first VHF micromechanical resonators in any material, piezoelectric or not, to meet the simultaneous high  $Q$  ( $>50,000$ ) and low motional resistance ( $<200\Omega$ ) commonly desired in many RF and frequency control applications. In doing so, it disproves to a large extent the common misconception that capacitively transduced resonators always exhibit high impedance. Interestingly, however, even as this work confirms the low impedance prowess of capacitive micromechanical resonators, other research begins to question the need for such low impedance in RF and other applications, and actually makes a case that higher impedance is preferred when a system can be fully integrated onto a single chip [80]. Whether or not low impedance is actually needed in the end, one can at least rest assured that capacitive resonators can provide it, while also simultaneously delivering  $Q$ 's in the tens of thousands.

The same ALD technique was also used to demonstrate substantial improvements in the far-from-carrier phase noise of oscillators referenced to stand-alone (as opposed to arrayed) capacitively transduced micromechanical disk resonators. The phase noise improvement is attained via the use of atomic layer deposition (ALD) to tune the electrode-to-resonator capacitive gaps. Specifically, ALD of about 30nm of hafnia (HfO<sub>2</sub>) onto the surface of a released 60-MHz micromechanical disk resonator to reduce its effective resonator-to electrode gap size from 92nm to 32nm provides an increase in power handling leading to more than 15-20dB reduction in the far-from-carrier phase noise of an oscillator referenced to this resonator. This ALD-enabled nano-scale gap tuning provides a simple and effective method to satisfy increasing demands for higher short-term stability in frequency references for electronic applications.

# *Chapter 4*

## *HOT FILAMENT CVD CONDUCTIVE MICROCRYSTALLINE DIAMOND FOR HIGH $Q$ , HIGH ACOUSTIC VELOCITY MICROMECHANICAL RESONATORS*

---

---

This chapter introduces a capacitively transduced micromechanical resonator constructed in hot filament CVD boron-doped microcrystalline diamond (MCD) structural material that posts a measured  $Q$  of 146,580 at 232.441 kHz, which is  $3\times$  higher than the previous high for conductive polydiamond. Moreover, radial-contour mode disk resonators fabricated in the same MCD film and using material mismatched stems exhibit a  $Q$  of 71,400 at 299.86 MHz, which is the highest series-resonant  $Q$  yet measured for any on-chip resonator at this frequency. The material used here further exhibits an acoustic velocity of 18,516 m/s, which is now the highest to date among available surface micromachinable materials. For many potential applications, the hot filament CVD method demonstrated in this work is quite enabling, since it provides a much less expensive method than microwave CVD based alternatives for depositing doped CVD diamond over large wafers (e.g., 8") for batch fabrication.

### 4.1 Introduction

Frequency-selective resonators with on-chip  $Q$ 's  $>30,000$  at GHz frequencies, if possible, would offer a paradigm shift in transceiver design by enabling narrow band low insertion loss RF channel-select filters capable of suppressing adjacent-channel interferers directly after the antenna in the receive chain, thereby significantly improving robustness and power consumption [81]. Unfortunately, no existing room temperature on-chip resonator can yet achieve such  $Q$ 's at GHz frequencies.

Nevertheless, the consistent improvement in the performance of capacitively transduced micromechanical resonators demonstrate results that get closer to make this goal a reality, with quality factors exceeding 200,000 at HF [82], 160,000 at VHF [77], and 14,600 at 1.2 GHz [60]. The choice of structural materials plays a crucial role in engineering high- $Q$  resonators to minimize acoustic damping not only stemming from intrinsic material losses but also energy dissipated by anchors. Among various surface-micromachinable materials, conductive polydiamond stands out as perhaps the most compelling option for high frequency resonators due to its high acoustic velocity that surpasses polysilicon by  $2.3\times$  and SiC by  $1.6\times$  to realize GHz frequencies with larger and more reliably definable dimensions. In addition, phonon-phonon interaction based damping models predict polydiamond to achieve the highest  $f\times Q$  product at GHz frequencies to surpass more conventional alternatives such as silicon, quartz, SiC and AlN [83][84]. Beyond just theoretical predictions, micromechanical contour mode disk resonators fabricated in polydiamond with acoustic impedance mismatched polysilicon anchors have already demonstrated  $Q$ 's of 11,555 at 1.14 GHz and 55,300 at 498 MHz [30], and the highest published  $f\times Q$  product diamond ring resonator posting  $Q$  of 42,900 at 2.9 GHz [85].

However, the majority of previous efforts that aim for high frequency and high  $Q$  polydiamond resonators [30][86] use microwave plasma CVD (MPCVD) technique [87] that typically constrains the uniform film deposition over small areas due to high cost of generating a uniform high energy density plasma over large wafers. In contrast, the hot filament CVD (HFCVD) technique [88] provides an easier to implement alternative that can uniformly deposit polydiamond simultaneously over multiple large area wafers at much lower cost. However, previous attempts using HFCVD diamond as structural resonator material yielded inferior performance compared to MPCVD technique that causes some to dismiss HFCVD as a viable option for MEMS-based resonators.

This chapter dispels such doubts by demonstrating HFCVD diamond MEMS resonators with unprecedented performance. Specifically, optimization of boron-doped HFCVD polydiamond deposition recipes and comparison of nano-crystalline diamond (NCD) and micro-crystalline diamond (MCD) is performed by using the measured quality factor of electrostatic combdrive resonators as a measure of intrinsic material losses. The results present a capacitive-comb driven resonator fabricated using the optimized HFCVD micro-crystalline diamond material posting a two-port electrically direct measured  $Q$  of 146,580 at 232.4 kHz, which is  $3\times$  higher than the previous high mark for MPCVD based resonators [86].

In addition, contour-mode disk resonators fabricated using the same optimized HFCVD recipe with acoustic impedance mismatched stems achieved a  $Q$  of 71,400 at 327.8 MHz, posting the highest series resonant  $Q$  measured at this frequency for an on-chip room temperature micromechanical resonator. This result records an  $f\times Q$  product of  $2.34\times 10^{13}$  Hz that is on par with similar resonators fabricated using MPCVD deposited diamond [30], but this time achieved on 6" wafer level with a lower cost system; instead of the die-level contact lithography limited fabrication process that plagued the previous MPCVD approach. The material demonstrated here further exhibits

Table 4-I: Comparison of Acoustic Velocities and Theoretically Calculated Quality Factors at 1 GHz and 3 GHz

<b>Material</b>	<b>Acoustic Velocity (m/s)</b>	$Q_{Theory @ 1GHz}$ [83]	$Q_{Theory @ 3GHz}$ [83]
Diamond	18,500	380,000	380,000
SiC	13,300	320,000	116,000
Quartz	5,720	39,000	13,000
Si	8,500	36,000	36,000
AlN	10,970	8,700	3,400

an acoustic velocity of 18,516 m/s that marks the highest to date among surface-micromachinable materials.

It is conceivable that this new polydiamond recipe that achieves high performance at low cost can eventually lead to  $Q$ 's  $>30,000$  at GHz frequencies and enable RF channel-selection for next generation transceiver front-ends [81]. The high performance of the HFCVD method reported in this work is promising towards enabling potentially high volume applications since it provides a lower cost and easier to scale fabrication technology than the microwave based CVD alternatives for uniformly depositing conductive polydiamond over multiple large area, e.g. 8", wafers.

## 4.2 High Quality Factor and Acoustic Velocity Advantage of CVD Polydiamond

Acoustic energy dissipation in micromechanical resonators stems from various mechanisms such as thermo elastic damping [89], phonon-phonon interaction dissipation [90], viscous damping [91], and anchor losses that can be treated as dampers in parallel [92]. The resonance frequency, operating temperature and environment such as air or vacuum, resonator geometry, and vibration mode shape determine the dominant loss mechanisms that limit the resonator quality factor.

For the UHF frequency vibrating contour mode disk resonators at the focus of this dissertation, phonon-phonon interaction based damping and anchor losses are the two dominant loss mechanisms at room temperature under vacuum [93]. Here, anchor losses are typically the more dominant one, and various anchor design practices ranging from the use of Bragg reflectors [94] to quarter-wavelength support design [60] aim to reduce acoustic energy lost to the substrate through the anchors.

Once anchor losses are sufficiently suppressed (if ever), intrinsic material losses remain to limit the  $Q$ . While a comprehensive understanding of intrinsic energy dissipation mechanisms remains elusive, recent studies predict an  $f \times Q$  product that is linearly proportional with frequency in the Landau-Rumer vibration frequency regime [83][84], which is a prediction that significantly differs from earlier studies that predicted a frequency independent upper limit. Table 4-I presents

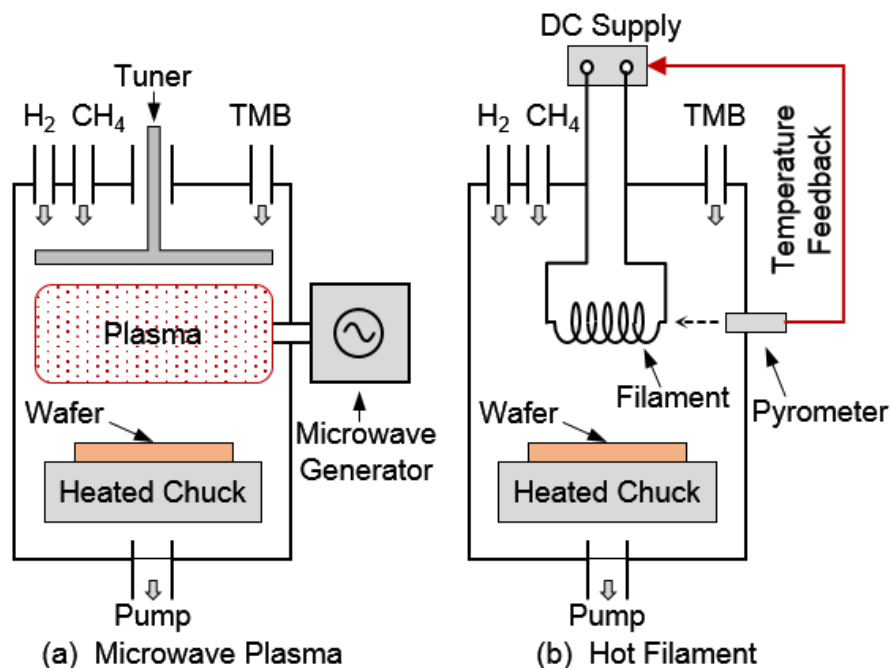


Figure 4.1: Schematic descriptions of (a) microwave plasma, and (b) hot filament CVD polydiamond deposition systems.

a comparison of predicted material  $Q$ 's based on phonon-phonon interaction based dissipation calculations [83][84] at 1-3 GHz for common MEMS resonator materials together with nominal acoustic velocities. Here, polydiamond clearly stands out as the material of choice for high  $Q$ , high frequency micromechanical resonators by having more than  $3\times$  the predicted  $Q$  and  $1.4\times$  the acoustic velocity of its closest competitors.

### 4.3 Polydiamond Deposition Techniques

Polydiamond deposition requires the presence of hydrocarbon radicals and high density atomic hydrogen to create a chemical dynamic that favors tetrahedrally bonded  $sp^3$  carbon over  $sp^2$  graphite. The key to achieving a high quality film amenable to large-scale batch production is a reliable and low cost method that can generate a high energy density plasma uniformly over a large area to excite the reactant gases to radicals. Typical reactant gases include  $CH_4$  to yield the hydrocarbon radicals that supply carbon, and  $H_2$  to form atomic H that eliminates the  $sp^2$  bonded graphite and establishes dangling bonds of  $sp^3$  diamond.

Various prominent techniques in the literature use essentially the same chemistry, but differ in their plasma generation technology, such as combustion flame [95], DC arc-jet [96], microwave plasma [87], and hot filament [88] methods. These methods all strive to minimize the impurities in the diamond film such as graphite,  $H_2$ ,  $N_2$ ,  $O_2$ , etc. to increase desired properties such as high

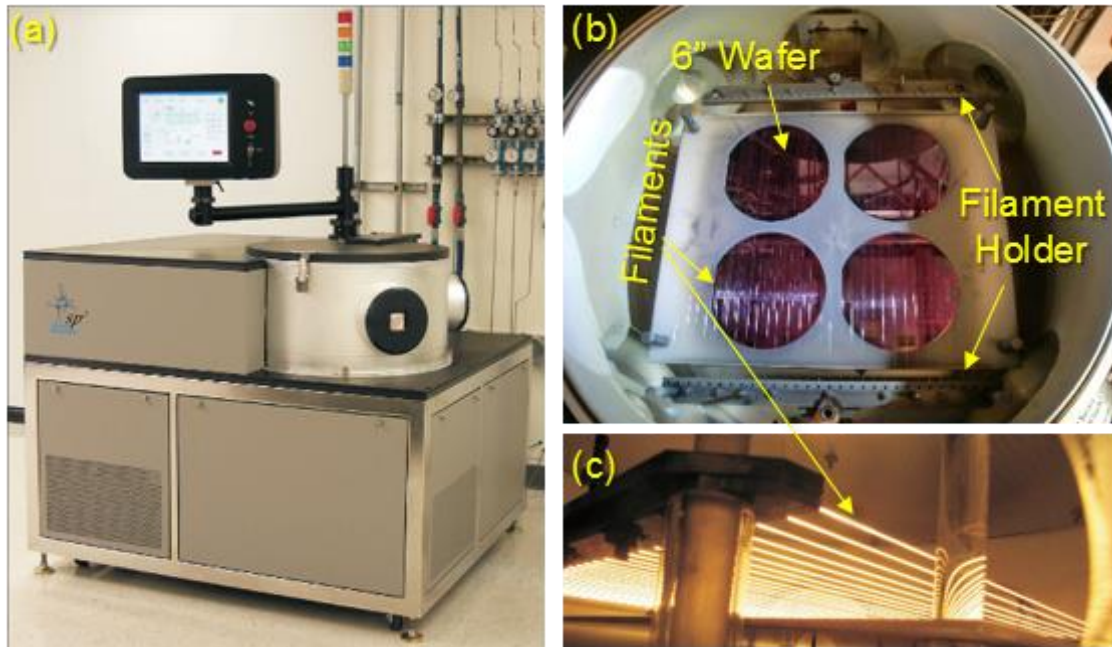


Figure 4.2: (a) Photo of the sp3 Model 650 HFCVD diamond reactor used in this work. (b) For 6" wafers loaded into the reactor for uniform film deposition ensured by tungsten filaments spanning over the substrates, and (c) picture of glowing filaments during deposition.

thermal conductivity and low acoustic energy dissipation. Among these methods, microwave plasma CVD (MPCVD) and hot filament CVD (HFCVD) techniques described in Figure 4.1 find the most common use in microfabrication applications because they are more amenable to wafer level surface micromachining, and can yield high quality and high purity films.

The microwave plasma setup depicted in Figure 4.1(a) provides energy for CVD through a microwave plasma that must be uniform over the receiving wafer to ensure uniform film thickness and quality. The high cost of the technology required to generate uniform and high energy density plasma over large substrates often constraints MPCVD diamond tools to small area depositions, which makes them less suitable for high volume batch production despite their established prowess in achieving high resonator  $Q$  at high frequency [30].

In contrast, a hot filament CVD tool creates a plasma around a glowing filament to supply energy for chemical reactions via filaments long enough to extend over several wafer-sized substrates. The filaments, typically made of tungsten, are low cost and easy to replace, and the tool is much simpler to build, operate, and scale for larger volume production. Before this work, HFCVD had not been able to produce diamond micromechanical resonators with  $Q$  and acoustic velocity performance matching that of more expensive MPCVD, causing diamond resonator endeavors to shy away from the former.



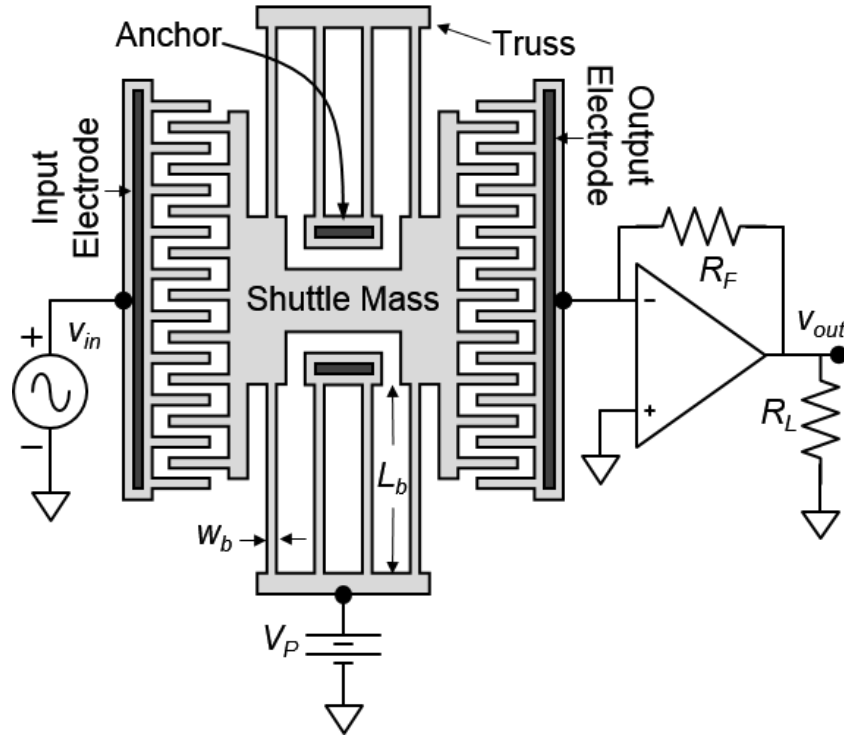


Figure 4.3: Schematic description of the folded-beam electrostatic comb-driven resonator used to evaluate intrinsic material loss dominated  $Q$ , and the electrical measurement setup.

This work uses an sp3 Model 650 HFCVD reactor, shown in Figure 4.2, to investigate the efficacy of the hot filament approach for microfabrication of micromechanical resonators and engineer deposition recipes that can match, or potentially go beyond the high performance of the high cost MPCVD technique. Since vibrating resonators for RF applications is the primary interest, resonator  $Q$  and acoustic velocity are the main metrics used to gauge performance in this work. Since the mechanisms for  $Q$ -limiting losses are often frequency and device geometry dependent [92], evaluations are performed at both low and high frequencies, as detailed in the following sections.

#### 4.4 Hot Filament CVD Polydiamond for High $Q$ Low Frequency Micromechanical Combedrive Resonators

In order to find the optimum HFCVD deposition conditions that minimizes intrinsic material losses, folded beam electrostatic comb-driven resonators [97] schematically described in Figure 4.3 are used to evaluate polydiamond films deposited under varying conditions. As thoroughly covered in the literature, these devices utilize capacitive comb transducers to linearize the ac voltage-to-force transfer function, and mitigate residual in-plane stress via their compliant folded-

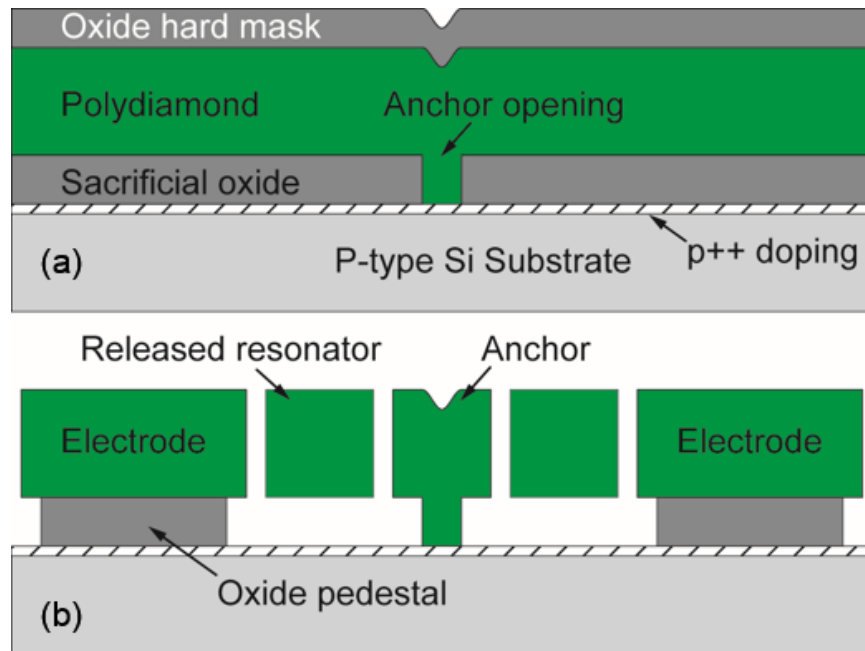


Figure 4.4: Process flow cross-section of the two-mask polydiamond combdrive resonator fabrication process after (a) polydiamond and oxide hard mask deposition, and (b) polydiamond etch and timed HF release.

beam suspensions. Such devices make for excellent gauges of intrinsic material  $Q$  since their dynamic stiffness on the order of 1 N/m are very low, therefore acoustic energy losses to the substrate through the anchors is quite small. If anchor losses can be made significantly smaller than the intrinsic material losses, then the measured resonator  $Q$  accurately represents the intrinsic material  $Q$ .

#### 4.4.1 Two-Mask HFCVD Polydiamond Fabrication Process

A simple two-mask process with fast turn around time is designed for fabricating the electrostatic comb-driven resonators to investigate the effects of various HFCVD polydiamond deposition recipe parameters, such as wafer temperature, doping level, grain size on polydiamond film quality factor and acoustic velocity. Figure 4.4 summarizes the cross-section views of the process flow. The process starts with forming an electrical ground plane by p++ doping of p-type 6" silicon wafers, followed by 2 $\mu$ m LPCVD oxide furnace deposited at 450°C to serve as the bottom sacrificial oxide layer. Then, the first mask lithographically defines the resonator anchors that are dry etched into the oxide, followed by HFCVD deposition of boron doped conductive polydiamond via recipes summarized in Table 4-II. Here, an array of recipes is used in consecutive runs to find optimum conditions that maximize the material  $Q$ . For each wafer batch run with the recipes given in Table 4-II, oxide coated wafers with anchors already etched are piranha cleaned, followed by seeding of nano-diamond particles by spin coating a liquid loaded with hydrocarbon nanoparticles as prepared via ultrasonic agitation of fine diamond powder in methanol [98].

Table 4-II: Measured hot filament deposited CVD diamond properties for different deposition conditions.

Parameter	NCD <sup>1</sup>	NCD <sup>2</sup>	MCD <sup>1</sup>	MCD <sup>2</sup>	Unit
CH <sub>4</sub> Concentration	2.7	1.5	1.5	1.0	%
Dopant TMB:CH <sub>4</sub>	7500	1350	2250	675	ppm
Wafer Temperature	720	720	710	730	°C
Filament Temp.	2285	2200	1975	2010	°C
Mean $Q$	10,228	15,789	23,477	127,330	-
Maximum $Q$	12,171	18,246	25,580	146,580	-
Mean Resonance $f_0$	41.477	36.164	210.852	232.220	kHz
Young's modulus	984	730	998	1198	GPa
Density, $\rho$	3,500	3,500	3,500	3,500	kg/m <sup>3</sup>

A blanket deposited LPCVD oxide is deposited in the next step to serve as a hard mask during the following diamond etch, as seen in Figure 4.4(a). The resonator structure and electrodes are defined by the second photolithography step, followed by first dry etching the oxide hard mask. The following diamond etch is performed in an RIE chamber at 50 mTorr pressure with 50 sccm O<sub>2</sub> and 2 sccm CF<sub>4</sub> gas flow rates and 750W power. This etch recipe yields a vertical etch sidewall profile, which is important for accurately interpreting comb-drive resonator measurements through

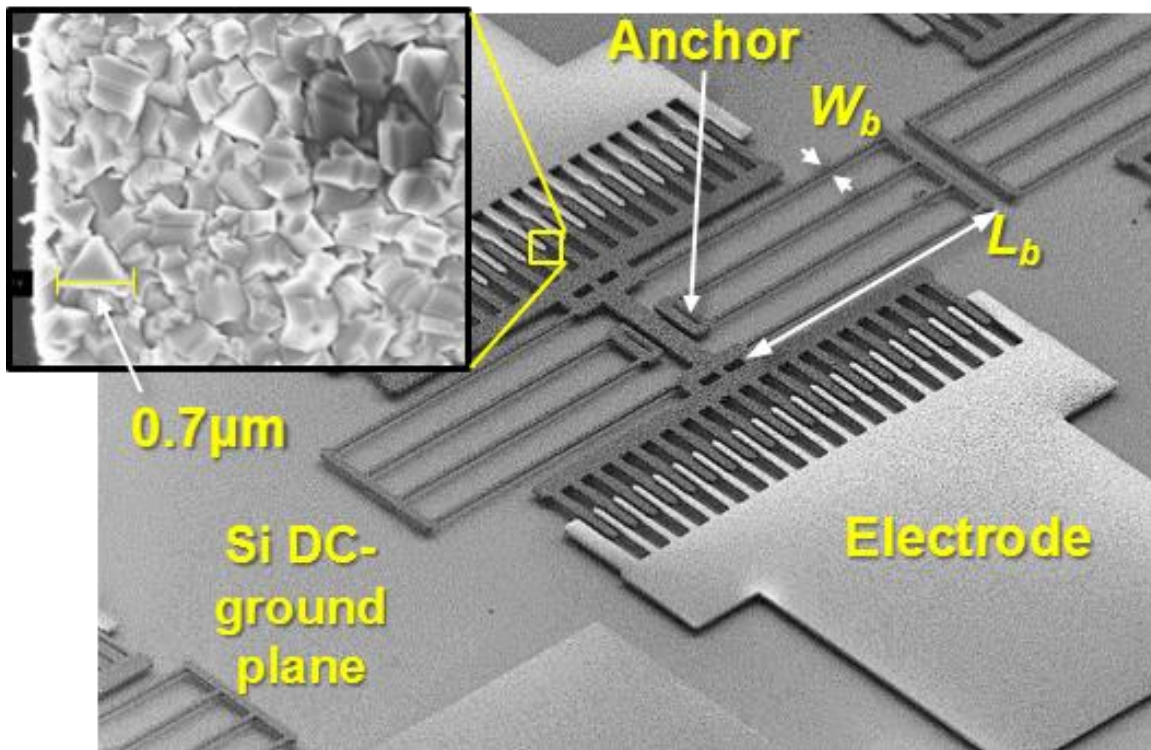


Figure 4.5: SEM image of a released polydiamond combdrive resonator fabricated using the process flow summarized in Figure 4.4, where the inset figure shows the zoomed-in view of the diamond film obtained using the MCD2 recipe with average grain size of  $0.7\mu\text{m}$ .

Table 4-III: Summary of combdrive resonator measurement results for different structural material types.

<b>Measured Resonator Quality Factors &amp; Statistics</b>					
Device	Resonator Material Type				
	NCD <sup>1</sup>	NCD <sup>2</sup>	MCD <sup>1</sup>	MCD <sup>2</sup>	PolySi
Res. 1	9,832	15,010	16,705	128,003	51,447
Res. 2	10,821	18,154	20,750	113,287	41,781
Res. 3	9,074	13,636	23,916	116,254	48,912
Res. 4	10,106	16,760	25,093	130,944	53,501
Res. 5	11,686	16,364	24,579	127,095	40,159
Res. 6	12,171	14,755	24,462	146,580	31,039
Res. 7	8,548	13,383	24,447	135,466	58,901
Res. 8	9,589	18,246	25,580	120,977	48,109
Max. $Q$	12,171	18,246	25,580	146,580	60,127
Mean $Q$	10,228	15,789	23,477	127,330	50,522
$\sigma_Q$	1,253	1,891	3,218	10,761	9,561
<b>Measured Resonance Frequency Statistics</b>					
Mean $f_o$ [Hz]	41,477	36,164	210,852	232,220	21,067
$\sigma_{freq.}$ [Hz]	472.6	334.7	943.7	606.5	570.3

lumped parameter modelling to extract material properties such as acoustic velocity. A trapezoidal etch cross-section would adversely affect the acoustic velocity extraction from the measured resonance frequencies. Finally, the wafer is diced and individual dies are released in 49 wt. % HF via a timed wet etch that releases the resonator structure, but leaves the electrodes on oxide pedestals rigidly anchored to the substrate, as depicted in Figure 4.4(b). Figure 4.5 presents the SEM image of a released HFCVD diamond combdrive resonator, with a zoom in showing the 0.7  $\mu\text{m}$  grain size obtained by recipe MCD<sup>2</sup>.

#### 4.4.2 Measurement Results

Fabricated diamond combdrive resonators were measured using the electrical measurement setup described in Figure 4.3 at room temperature under 10  $\mu\text{Torr}$  vacuum. A dc-bias voltage is applied to the conductive p++-doped silicon field of the die that serves as a dc-ground plane to mitigate levitation effects, which also dc-biases the resonator body with the same dc voltage through the anchor contact. An ac input voltage is applied to the input electrode from the input port of an Agilent E5071C network analyzer, and the output current is amplified with a trans-resistance amplifier to achieve a detectable signal to counter the very high motional resistance of comb-driven resonators, which then goes to the output port of the network analyzer.

The frequency response of eight identical resonators obtained from the same wafer fabricated for each of the recipes outlined in Table 4-II are measured under identical conditions, where resonator quality factor and resonance frequency are the main observed metrics used to evaluate the

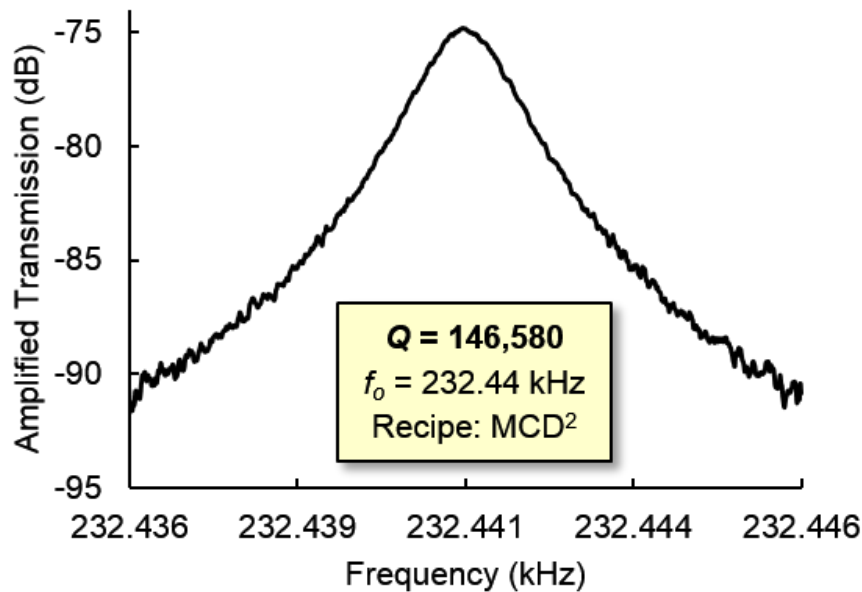


Figure 4.6: Measured frequency response for the microcrystalline polydiamond combdrive resonator achieving the highest  $Q$  using the best HFCVD recipe.

performance of each HFCVD deposition condition. In addition, polysilicon combdrive resonators with geometry similar to that of the polydiamond versions were also fabricated using LPCVD deposited in-situ phosphorus doped polysilicon as the structural material, and measured with the same measurement setup and identical conditions to facilitate comparison of conventional polysilicon and HFCVD polydiamond. Table 4-III presents the summary of measurement results that tabulates the measured quality factors for eight-resonator batches for each structural material type investigated using the combdrive resonators. It also presents the least-square fitted normal distribution metrics for extracting the mean quality factor and resonance frequency and standard deviations from the measured data sets.

Figure 4.6 presents the measured frequency response of the resonator fabricated using the best HFCVD polydiamond recipe, demonstrating a measured  $Q$  of 146,580 at 232.441 kHz that surpasses the previous high for microwave plasma deposited conductive polydiamond [86] by  $3\times$ . In comparison, polysilicon folded-beam resonators with similar geometry their polydiamond counterparts exhibit a measured  $Q$  of 60,127 at 21.065 kHz as presented in Figure 4.7. The polydiamond version bests the polysilicon  $Q$  by  $2.4\times$ , and does so at  $10.6\times$  higher frequency where anchor losses are higher for the stiffer diamond resonator. Therefore, if one assumes that other loss mechanisms such as surface contamination, etc., are relatively negligible, then these results demonstrate that the intrinsic material  $Q$  of HFCVD polydiamond is at least  $2.4\times$  that of polysilicon. Furthermore, given that the previous best  $Q$  reported for conductive MPCVD diamond material is 47,900 [86], this result shows that it is possible to deposit lower loss materials using HFCVD technique than MPCVD, with the additional benefits of higher throughput and lower cost.

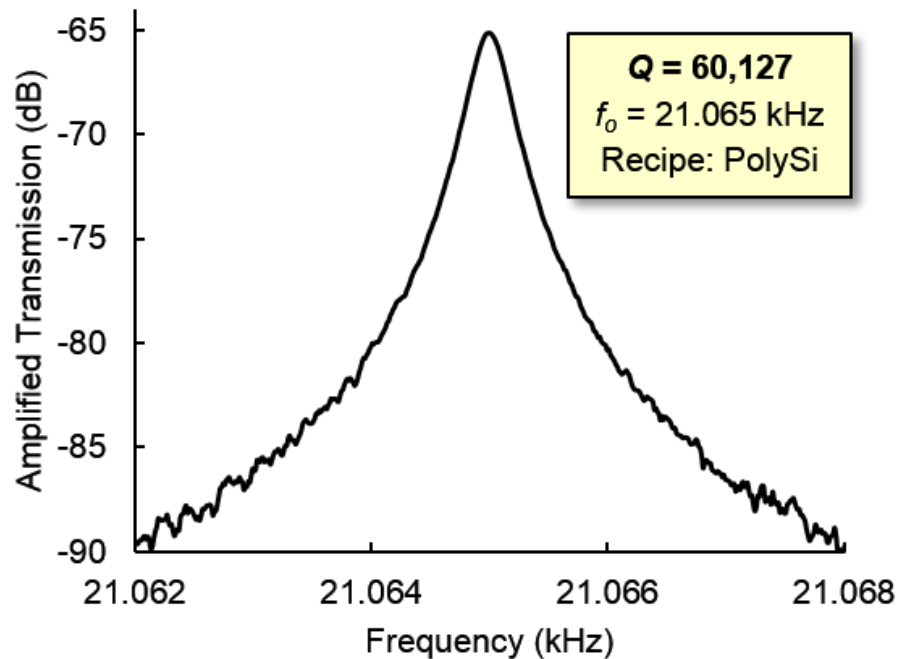


Figure 4.7: Measured frequency response for a polysilicon combdrive resonator with similar geometry to that of the device measured in Figure 4.6, showing  $2.4\times$  lower  $Q$  compared to the HFCVD polydiamond material.

#### 4.4.3 HFCVD Diamond Recipe Optimization

To identify the optimum HFCVD polydiamond deposition conditions that maximize  $Q$ , resonators fabricated using varying deposition recipes were measured and compared. Specifically, eight resonators from each fabrication batch were measured to observe consistent and statistically significant improvement between the developed recipes presented in Table 4-II. Table 4-III summarizes the measurement results by tabulating the measured quality factors of tested resonators coming from four polydiamond runs with varying structural polydiamond recipes denoted NCD<sup>1</sup>, NCD<sup>2</sup>, MCD<sup>1</sup>, and MCD<sup>2</sup>, as well as the polysilicon run for comparison. The tabulated results include the maximum  $Q$ , as well as least-square fitted normal distribution to the measured quality factors to identify the mean and standard deviation  $\sigma_Q$ ; and the mean and standard deviation of the measured resonance frequencies for each structural material recipe.

Each recipe shown in Table 4-II minimizes the residual stress by proper adjustment of the filament and wafer temperature during deposition that allows non-curved folded-beam resonators as seen in the SEM image of Figure 4.5. The reported Young's modulus values are extracted from the mean value of the measured resonance frequencies for each recipe using well known equations [97] that relate material density  $\rho$  and Young's modulus  $E$  to resonator geometry, e.g. folded beam

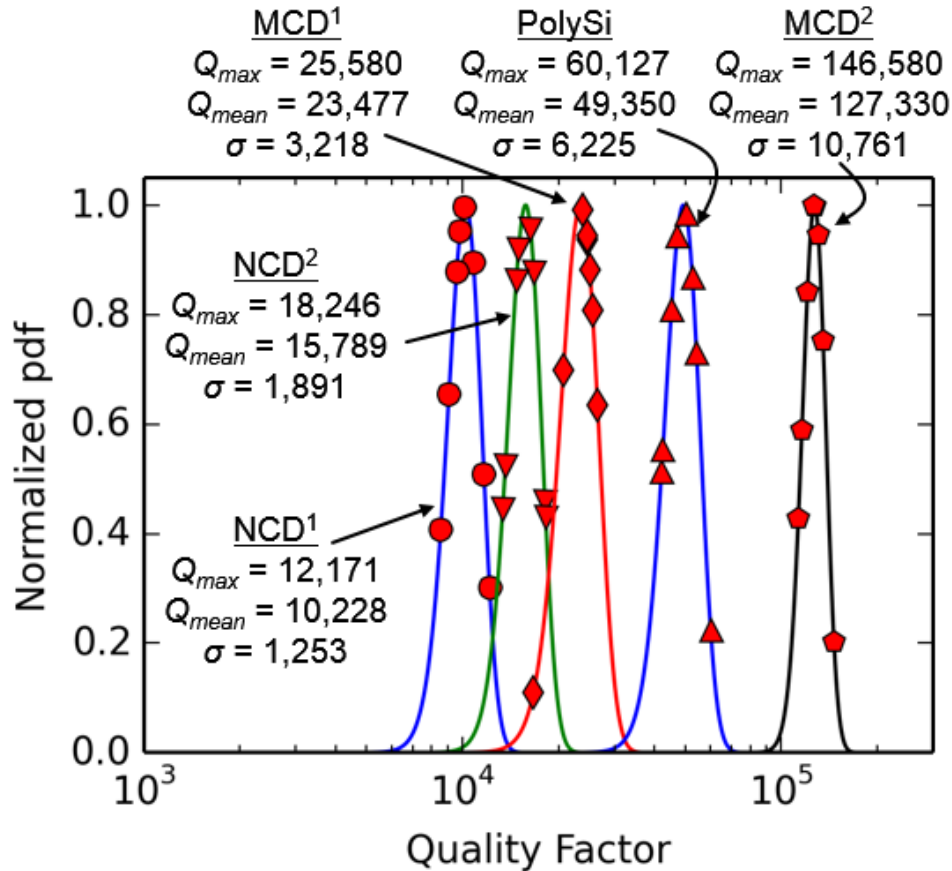


Figure 4.8: Normal probability distribution functions (pdf) with maximum values normalized to one (shown as solid line curves) least-square fitted to the measured quality factors tabulated in Table 4-III (shown as data markers) for each recipe studied in this work, where the  $x$ -axis is the quality factor values in log-scale, and  $y$ -axis shows the fitted  $Q$  histogram assuming a normal distribution. The labels indicate the maximum, mean, and standard deviation value for the  $Q$  data sets for each material type.

length, width and shuttle mass area, assuming the polydiamond density is constant as  $3500 \text{ kg/m}^3$  as reported in literature [99].

The comparison of measured quality factors achieved by each recipe as shown in Table 4-II demonstrates  $12.4\times$  improvement in the mean quality factor, and  $12\times$  improvement in the maximum measured quality factor between the initial (NCD<sup>1</sup>) and the final (MCD<sup>2</sup>) optimized recipes. The column denoted as MCD<sup>2</sup> indicates the best deposition conditions for microcrystalline diamond as indicated by the highest measured  $Q$  of 146,580, as well as the highest mean  $Q$  of 127,330, which also achieves the highest acoustic velocity defined as  $\sqrt{(E/\rho)}$  of 18,516 m/s that marks a record to date among other conventional surface micromachinable materials.

Finally, Figure 4.8 shows the normal probability distribution function with maximum value normalized to one least-square fitted to the measured quality factors tabulated in Table 4-III shown

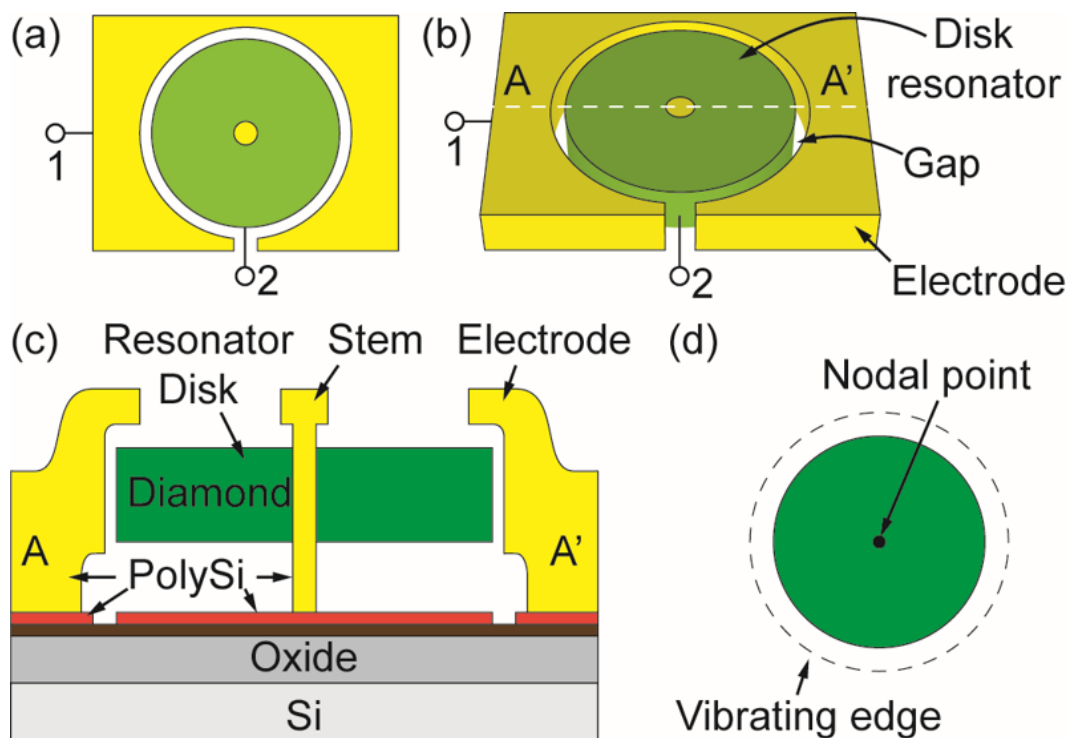


Figure 4.9: Schematic summary of a contour mode disk resonator with one fully surrounding electrode shown in (a) layout view, (b) perspective view, (c) cross-section view, and (d) radial contour mode shape.

with the data markers, where the  $x$ -axis shows the quality factors in log-scale and  $y$ -axis shows the least-square fitted  $Q$  histogram assuming a normal distribution. As the markers showing the maximum mean and standard deviation values of the measured quality factors indicate, this plot demonstrates consistent and statistically significant enhancement as the recipes improve to reduce energy losses. The important strategies for raising  $Q$  can be inferred from Table 4-II:

1. Use microcrystalline polydiamond (MCD) films instead of nanocrystalline polydiamond (NCD), since the former attains significantly higher  $Q$  as seen from the comparison of recipes MCD<sup>2</sup> and MCD<sup>1</sup> vs. NCD<sup>2</sup> and NCD<sup>1</sup>. The difference can be attributed to the increased phonon scattering by the higher number of grain boundaries per volume for smaller grain sizes. Studies in literature that report higher thermal conductivity for larger grain size polydiamond films due to reduced phonon scattering [100] support this hypothesis, as higher thermal conductivity is correlated to lower phonon-phonon scattering induced energy loss [84].

2. Reduce the CH<sub>4</sub> flow rate, which reduces the non-diamond carbon formation and thus creates a lower loss film. This comes at the expense of reduced growth rate; however, the increased H radicals to carbon ratio better favors the desired sp<sup>3</sup> bonded diamond over sp<sup>2</sup> bonded graphite, and the reduced impurity concentration in-creases the quality factor.



3. Reduce the TMB: CH<sub>4</sub> ratio, which reduces the doping level. Boron dopants tend to accumulate primarily in the grain boundaries and form an additional energy scattering mechanism. Therefore, keeping the boron level as low as possible while maintaining sufficient electrical conductivity for capacitive actuation is the desired strategy to maximize  $Q$ .

## 4.5 Hot Filament CVD Polydiamond for High $Q$ & High Frequency Micromechanical Disk Resonators

Having historically achieved the highest  $Q$  resonators operating past VHF [30] and their prominent use in micro-mechanical RF channel-select filter applications [23][48], this study employs radial contour mode disk resonators [101], schematically described in Figure 4.9, to evaluate the  $Q$  achievable at high frequency attained by HFCVD diamond material. The device consists of a polydiamond disk suspended 700nm above a polysilicon dc-ground plane tethered by a polysilicon stem at its very center created with a self-aligned process [102]. A polysilicon electrode fully surrounds the disk with a lateral capacitive actuation gap spacing of only 80nm. All structural, electrode and inter-connect layers are boron doped to make them electrically conductive.

The disk resonator is driven to resonance using capacitive actuation, much like the previous folded-beam resonators, where a combination of dc-bias and ac-excitation voltages applied across the electrode-to-resonator gap exerts a force to the disk and excites resonance in the radial contour mode shape, cf. Figure 4.9(d), and creates a time-varying dc-biased capacitance across the disk and the surrounding electrode. Sensing the resultant output current provides a measure of the resonance displacement against frequency that yields the quality factor and oscillation frequency as the main observed variables. The resonance frequency of a radial contour mode disk is inversely proportional to its radius and directly proportional to its acoustic velocity as elaborated in Section 2.2, where diamond has a major advantage for the latter.

Achieving  $Q$ 's at high frequencies as high as those observed for low frequency folded-beam devices of Section 4.4 is a major challenge primarily because anchor losses are very small for the low frequency devices, and therefore the dominant loss mechanisms stem from intrinsic material properties where diamond performs impressively. At the much higher frequencies needed for RF applications, the orders of magnitude increase in the stiffnesses required to attain the high frequency greatly accentuates the role of supports and anchors as conduits for energy loss, generally to the point where anchors dominate over other loss mechanisms for resonators operating under vacuum. In fact, anchor losses have historically prevented attaining quality factors as high as those predicted by theoretical models of intrinsic material  $Q$  at UHF frequencies [83]. As a result, the key to achieving the closest estimate of the  $Q$  set by intrinsic HFCVD material loss mechanisms at high frequency is to suppress anchor losses.

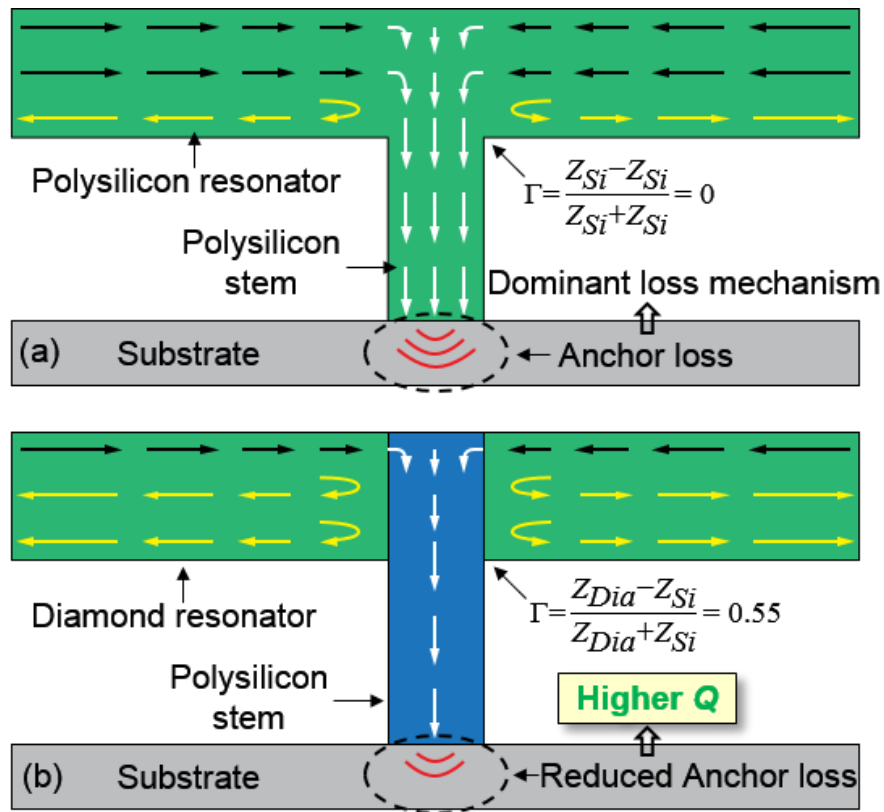


Figure 4.10: Schematics comparing anchor losses to substrate for (a) polysilicon disk with acoustic impedance matched polysilicon stem, and (b) for a polydiamond disk with a material mismatched polysilicon stem that results non-zero acoustic reflection coefficient at the resonator-anchor boundary.

#### 4.5.1 Material Mismatched Stems for Suppressing Anchor Loss

Anchor losses have long been identified as a major  $Q$  limiting mechanism for micromechanical devices, from the first MEMS-based resonators to reach VHF frequencies with high  $Q$  [103], to more recent rings [60], disks [30], and lamb wave structures [104]. VHF free-free beam resonators [103] were the first to employ quarter-wavelength supports attached at vibration mode nodal points to minimize energy coupled to the substrate via the supports, which is a technique still widely used in the latest generation of GHz devices [60][66] to effectively reduce anchor loss. Other strategies to mitigate anchor losses include Bragg reflectors [94], or photonic band gap structures [105] placed between the resonator and substrate, but these have so far not been as effectual as quarter-wavelength supports attached at nodal locations, at least from the perspective of attained maximum  $Q$ .

The key strategy common to all the aforementioned techniques is to create a large acoustic impedance mismatch at the resonator-anchor boundaries as an attempt to confine the acoustic energy within the resonator structure during resonance vibration, therefore prevent the energy dissipation to the substrate. Identifying this key observation, and further leveraging the very large

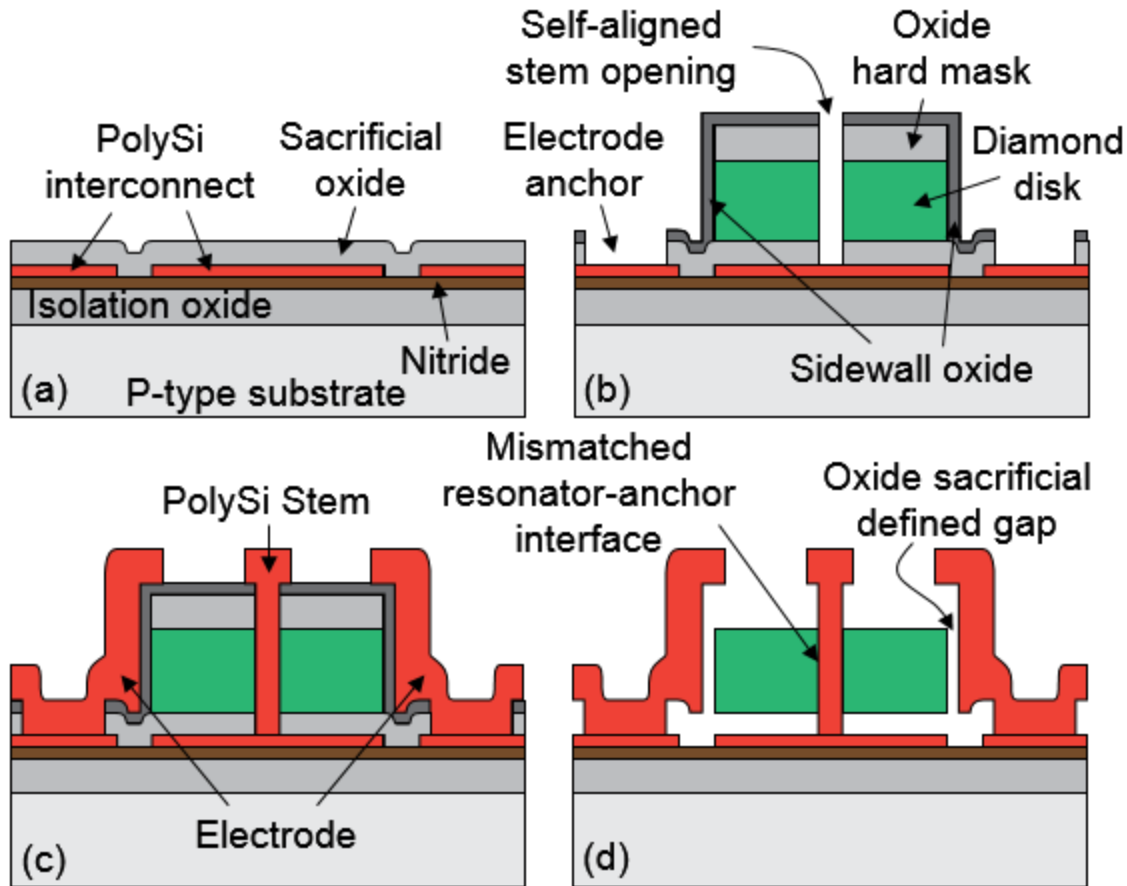


Figure 4.11: Cross-sections describing the five mask disk resonator fabrication process flow after (a) patterning interconnect and depositing bottom sacrificial oxide, (b) diamond deposition and etch using the oxide hard mask, followed by opening stem and electrode anchor openings, (c) depositing electrode and self-aligned stem using boron doped-poly followed by patterning, and (d) resonator freed after 49 wt. % HF release.

acoustic impedance mismatch between polydiamond and other common micromachinable materials, the work of [30] used MPCVD polydiamond as the disk material, but polysilicon for the anchoring stem, to induce a material mismatch between the disk and the stem that reflects energy back into the disk structure, counteracting the energy leakage that would otherwise occur.

The degree of reflection can be modeled analogously to electrical transmission lines to generate a non-zero reflection coefficient for acoustic waves at the resonator-anchor boundary, inhibiting energy from flowing through the stem into the substrate, as depicted in Figure 4.10. Here, the stem fabricated in the same material as the disk does little impede energy flow, whereas an acoustic impedance mismatched stem, where acoustic impedance is defined as

$$Z_{Acoustic} = \sqrt{E \times \rho} \quad (4.1)$$

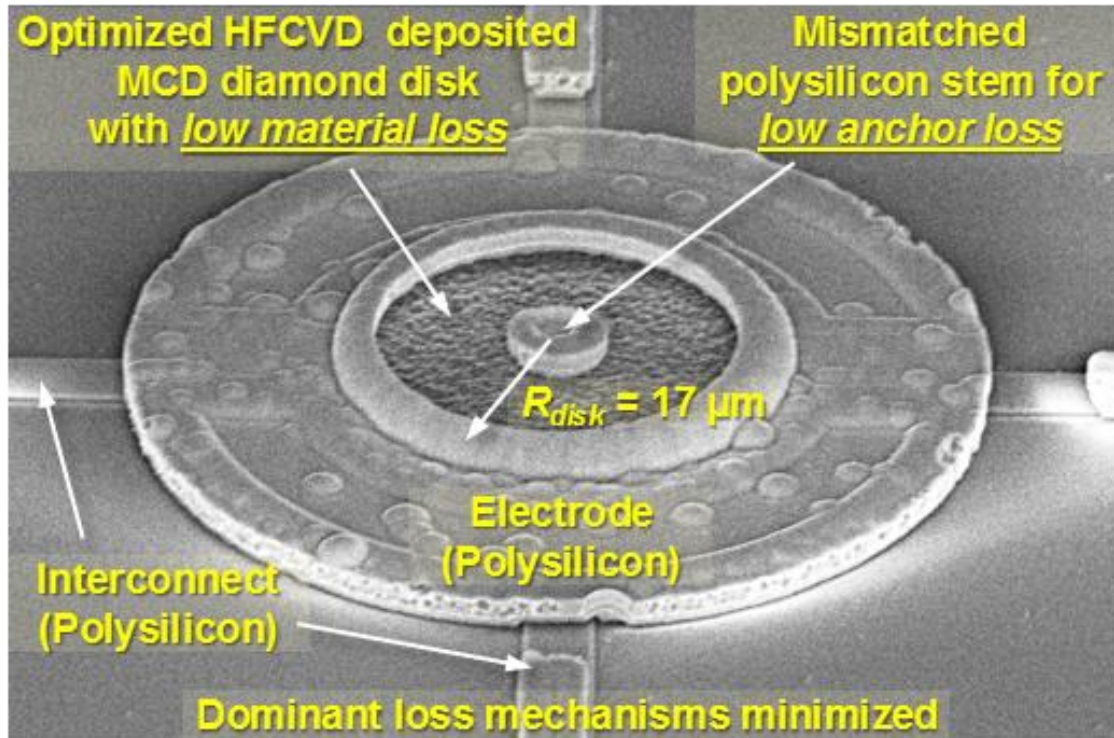


Figure 4.12: SEM image of a 327.8 MHz HFCVD microcrystalline polydiamond radial contour mode disk resonator with a fully surrounding electrode used for high frequency quality factor performance evaluation.

suppresses the energy loss to the substrate. This design strategy allowed the device of [30] to achieve measured  $Q$ 's as high as 55,300 at 498 MHz, corresponding to an impressive  $f \times Q$  product of  $2.75 \times 10^{13}$  that set a record for on-chip room temperature resonators at the time of its publication.

In order to suppress competing loss mechanisms that can mask the intrinsic HFCVD polydiamond  $Q$  most effectively, this study borrows from that of [30] in its use of polydiamond, but in this case using HFCVD to achieve potentially even better film quality at lower cost instead of MPCVD, and polysilicon for the mismatched stem material.

#### 4.5.2 Five-Mask Fabrication Process for High Frequency Contour Mode Micromechanical Disk Resonators

HFCVD polydiamond disk resonators studied in this work are fabricated using a five mask process similar to that of [30], where Figure 4.11 provides cross-section views of important process steps. The primary difference here is using an HFCVD diamond reactor that allows conformal and uniform film deposition over multiple large area wafers simultaneously at low cost per run, instead of an MPCVD tool that in [30] was limited to single small area depositions.

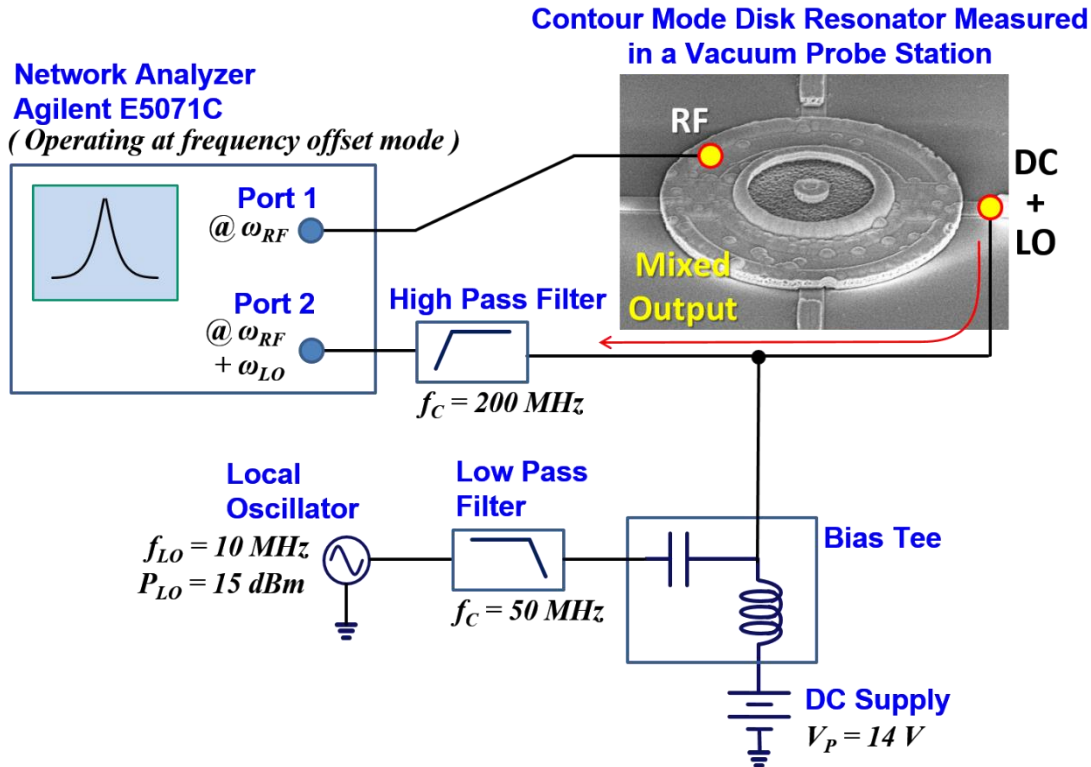


Figure 4.13: Schematic of the one-port mixing measurement setup used for contour mode disk resonator response measurements.

The process starts with p++ doping of 6" silicon wafers in a solid source boron furnace, followed by successive LPCVD depositions of 2 $\mu\text{m}$  LTO and 500nm nitride as electrical isolation layers. Then 500nm polysilicon is LPCVD deposited and solid source boron doped, and etched to create the electrical interconnect layer. The following blanket LPCVD deposited 700nm thick LTO layer serves as the bottom sacrificial oxide film, as seen in Figure 4.11(a).

The following structural polydiamond deposition starts with seeding the wafers with diamond nanoparticles by spin coating a liquid loaded with hydrocarbon nanoparticles prepared by ultrasonic agitation of fine diamond powder in methanol [98]. Seeded wafers are transferred to the sp3 model 650 HFCVD reactor pictured in Figure 4.2 to grow 2 $\mu\text{m}$  thick in-situ boron doped microcrystalline diamond using recipe named MCD<sup>2</sup> in Table 4-II, which provided the highest intrinsic material quality factor for low frequency folded-beam resonators in section 4.4.3.

A 1.2 $\mu\text{m}$  LPCVD deposited blanked oxide layer serves as an etch hard mask with high etch selectivity to diamond, as selectivity of photoresist to diamond is very low. The oxide hard mask also serves as a vertical sacrificial spacer between the disk resonator and electrodes that will be formed in the following steps. The resonator structure etched into the oxide hard mask and then the polydiamond film. The 80nm capacitive actuation gap between the disk and the electrode is then defined by a sidewall sacrificial oxide layer, where LPCVD deposition of high temperature

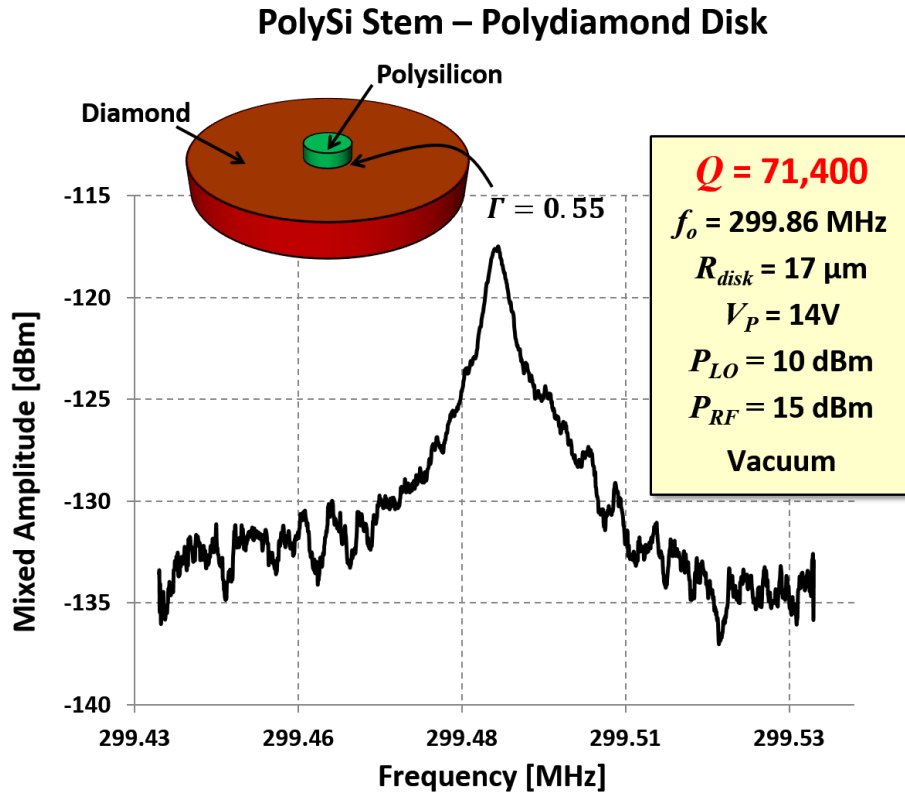


Figure 4.14: Measured frequency response (using mixing) for a contour mode disk resonator fabricated in HFCVD polydiamond and employing a material-mismatched polysilicon stem.

oxide using 40 sccm of DCS and 100 sccm of  $\text{N}_2$  flow at  $835^\circ\text{C}$  with 300 mTorr pressure provides uniform, conformal and pinhole free deposition of the sidewall sacrificial coating to ensure high yield.

The anchor openings used to tether the disk resonator by its stem and electrodes are then lithographically de-fined and etched into oxide, yielding the cross-section shown in Figure 4.11(b). A  $3\mu\text{m}$  thick solid-source boron doped polysilicon film then conformally fills the stem and electrode anchor openings, which is then patterned to create the fully surrounding electrode and the aforementioned material mismatched stems as shown in Figure 4.11(c). The final step involves 49 wt.-% percent liquid HF release that free the resonator and creates the cross-section presented in Figure 4.11(d). Figure 4.12 presents an SEM image of the polydiamond resonator studied in this work that has disk radius of  $R_{disk} = 17 \mu\text{m}$ , an acoustic impedance mismatched polysilicon stem with  $2 \mu\text{m}$  diameter, and a fully surrounding electrode with  $d_o = 80 \text{ nm}$  lateral capacitive actuation gap.

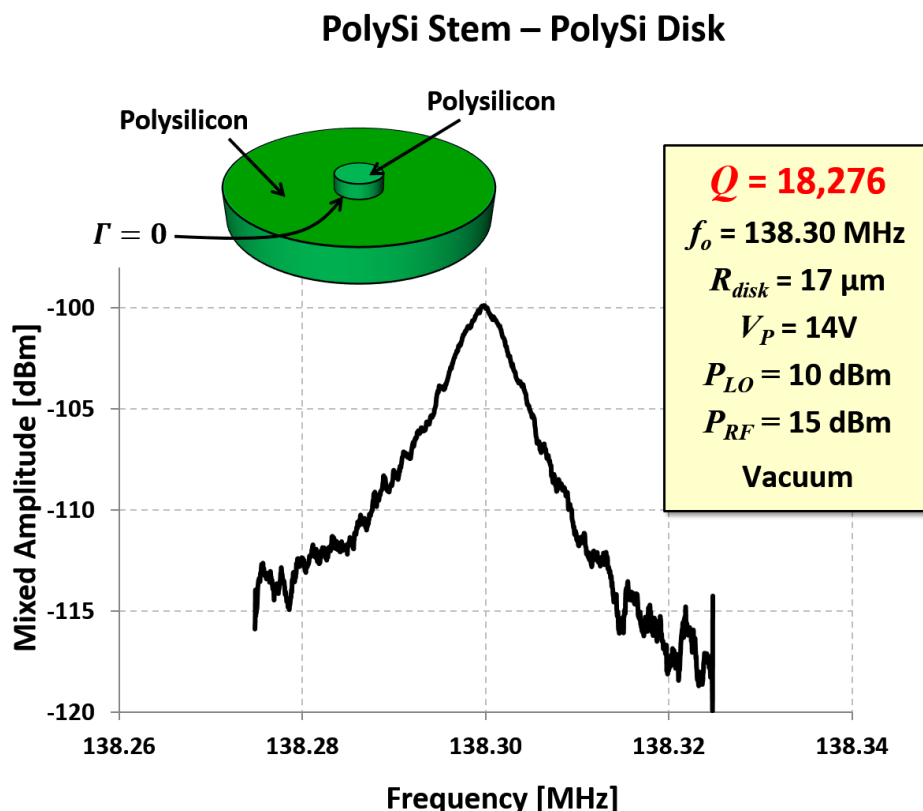


Figure 4.15: Measured frequency response for a contour mode disk resonator fabricated entirely in polysilicon, with identical geometry as the diamond disk of Figure 4.14.

### 4.5.3 Measurement Results

A Lakeshore model FWPX probe station provided 50  $\mu\text{Torr}$  vacuum and probing to allow room temperature frequency characteristic measurements using the mixing measurement setup [11] depicted Figure 4.13. Here, a bias tee combines a 10-MHz local oscillator signal with a DC bias voltage to generate the resonator voltage required for mixing measurement; and an Agilent E5071C Network Analyzer sources out of its port 1 an input RF signal that sweeps over a 100 kHz span centered at 10 MHz below the expected resonance frequency. As detailed in [11], the RF and LO signals mix via the square-law voltage-to-force transfer function of the input capacitive transducer, generating a force at their sum frequency, which equals the resonance frequency of the resonator, allowing port 2 of the network analyzer to sense the resonant peak without interference from feedthrough.

Figure 4.14 and Figure 4.15 present measured frequency characteristics for HFCVD diamond and polysilicon disks, identically dimensioned, both with polysilicon stems. The polydiamond disk with material-mismatched polysilicon stem exhibits a very high  $Q$  of 71,400 at 299.86 MHz, which

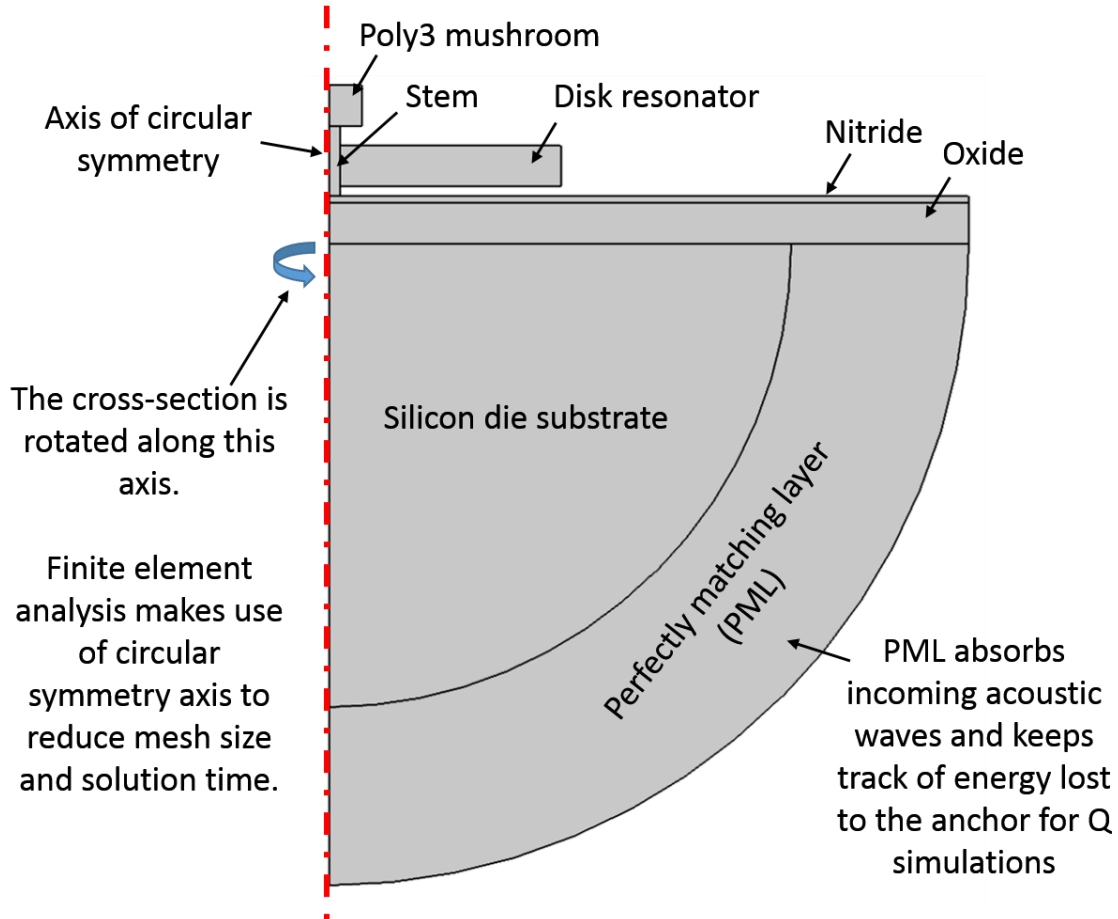


Figure 4.16: 3-D solid model of the disk resonator structure that implements the resonator disk, anchor, and Si substrate regions. The utilizes the circular axi-symmetry of the structure to simplify the finite element solution formulation, which leads to easier meshing of the structure and faster solution times.

is the highest series resonant  $Q$  measured at this frequency for an on-chip micromechanical resonator at room temperature. The polysilicon disk, on the other hand, not only resonates at a much lower frequency of 158.3 MHz, but since it lacks a material-mismatched stem, also posts a much lower  $Q$  of only 20,912, which is  $3.4\times$  lower than that of the acoustic impedance mismatched diamond device. The measured results clearly confirm the efficacy of stem-to-disk material mismatching to suppress energy loss to the substrate, and provide resounding testament to the utility of HFCVD polydiamond material for high frequency micromechanical resonators.

#### 4.5.4 Finite Element Analysis of Acoustic Impedance Mismatched Stems

##### 4.5.4.1 Anchor Loss Simulations using COMSOL

A comparison of the measurement results presented in Figure 4.14 and Figure 4.15 clearly demonstrates the efficacy of acoustic impedance mismatched stems to minimize anchor losses.



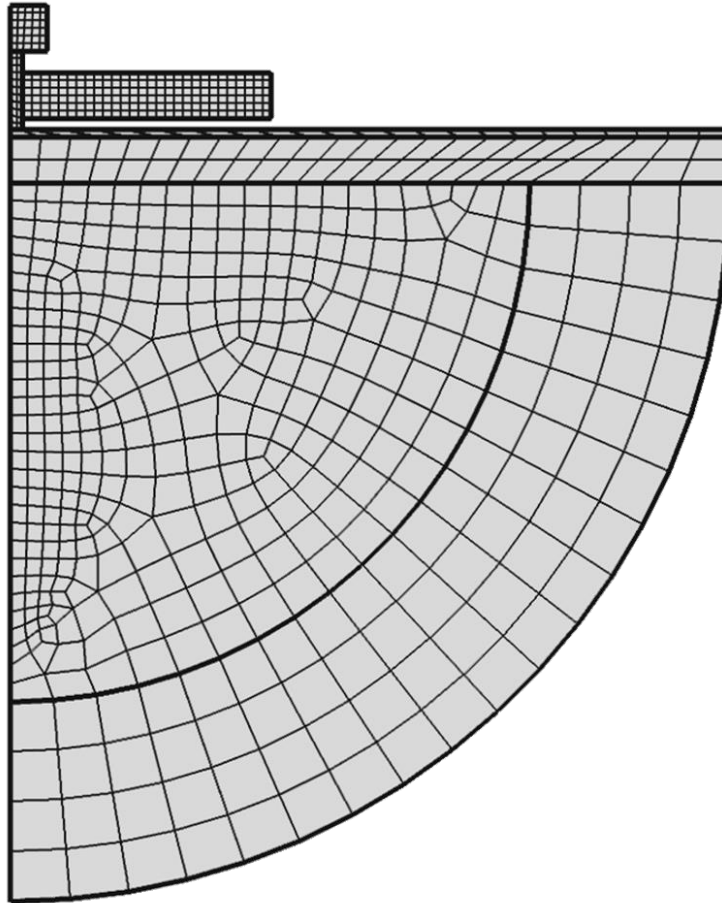


Figure 4.17: Area mesh applied to the solid model presented in Figure 4.16.

This section further supports the idea of confining the acoustic energy inside the disk by creating an impedance mismatch at the disk-anchor boundary by simulating the energy loss lost to the substrate via finite element simulation. To this end, a 3-D solid model of the disk resonator, the anchor, and the substrate is created using COMSOL, as illustrated in Figure 4.16. This model utilizes the circular axial-symmetry of the structure by creating a 2-D cross-section of the complete structure. This allows creating a uniform and good quality area mesh in a very short time, as illustrated in Figure 4.17. The meshed area is then swept 360° along the central symmetry axis as indicated in Figure 4.16.

The perfectly matching layer (PML) feature of COMSOL is key to accurately simulating the acoustic energy lost to the substrate via the anchor. As seen in Figure 4.16, the PML layer surrounds the Si substrate as a sphere, because the anchor connection to the substrate behaves like a point source that dissipates acoustic energy as semi-spherical acoustic waves. The FEA mesh used in this analysis utilizes four PML elements across the spherical PML volume, as shown in Figure 4.17. This number is chosen by a mesh convergence analysis that optimized the thickness of the PML layer thickness and number of elements. Using less than four elements across the PML layer

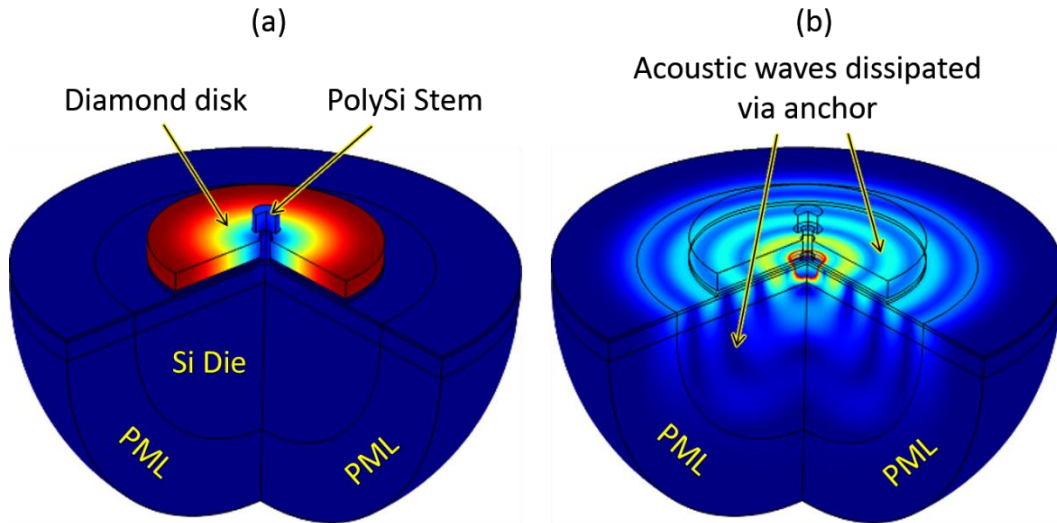


Figure 4.18: (a) Fundamental contour mode shape simulation result of the resonator model that uses polydiamond as the disk resonator and polysilicon as the stem anchor material. (b) Focusing on the acoustic waves launched in the Si substrate via the anchor. Here the PML layer perfectly absorbs the energy emanating from the anchor-substrate interface.

thickness, or using a thinner PML volume results in some of the acoustic waves reflect back from the PML layer. The configuration illustrated in Figure 4.17; however, allows the PML layer to act like a semi-infinite volume that absorbs all the incoming acoustic energy. The incoming acoustic energy signifies, of course, the energy lost to the substrate via the anchor. As a result, calculating the ratio of the total energy in the system vs. the energy absorbed by the PML volume gives the anchor-loss limited  $Q$  of the resonator structure.

Disk resonators that were measured in Section 4.5.3 are modelled with identical geometry (i.e. disk radius, thickness, stem diameter, etc.), using the solid modelling approach described above. Then FEA modal analysis is used to simulate the fundamental contour mode vibration for both acoustic impedance mismatched and regular stem cases to predict the anchor loss dominated  $Q$ . Figure 4.18 presents the FEA simulated contour-mode vibration mode shape result for the acoustic impedance mismatched polydiamond disk – polysilicon stem case. Here, Figure 4.18(a) illustrates the vibrating disk structure that assumes breathing contour mode shape with maximum displacement at the disk periphery at 299.8 MHz. Since the disk edges move a lot more than the rest of the system as indicated by the color map, the anchor and the substrate appear as not moving at all. This, however, is misleading as seen in Figure 4.18(b) that focuses on the motion of the anchor and the Si substrate. Here, the acoustic waves that couple to the Si substrate from the anchor are clearly visible. Choosing a sufficiently thick PML layer ensures all the energy propagating in the substrate gets absorbed by the PML layer as indicated by the color map. Insufficient PML modelling would result in artificial standing wave solutions and taint the simulated  $Q$  results.

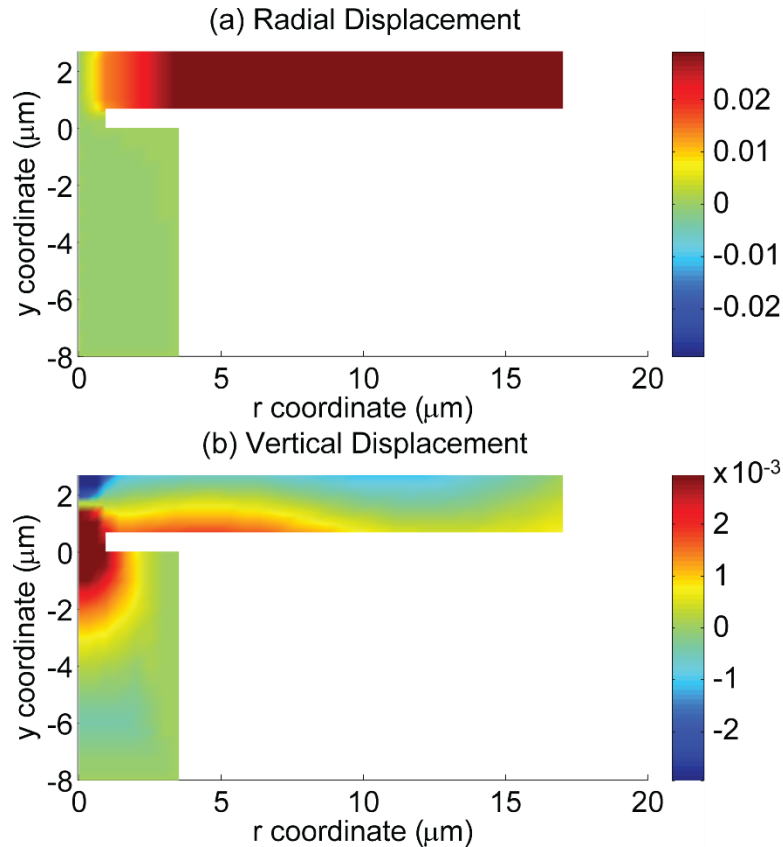


Figure 4.19: Anchor loss simulated (a) radial displacement, and (b) vertical displacement results for the contour mode shape obtained via HiQLab.

#### 4.5.4.2 Anchor Loss Simulations via HiQLab

Accurate anchor loss simulations are very valuable as a resonator design tool since they allow the designer optimize the anchor for different material combinations, such as the polydiamond-polysilicon system presented in this section. Therefore, it is no surprise that studies on closed form expressions and numerical analysis tools that calculate anchor dissipation are abundant in literature [106][107][108][109]. However, most of these studies focus on specific resonator geometries, and their accuracy is always in question given the complexity of the anchor dissipation mechanisms.

Therefore, this study used a second FEA analysis tool called HiQLab to simulate the anchor of the disk resonators presented in Section 4.5.3 in addition to the COMSOL analysis described in Section 4.5.4.1. Comparing the results of two separate analysis tools allows running two independent numerical studies. This study checks if the results of both studies agree with each other as well as with the measurement results to support the use of FEA optimized acoustic impedance mismatched anchor designs for future resonator designs.

Using HiQLab as the second FEA tool of choice in addition to COMSOL is very suitable, because the HiQLab program is developed specifically to predict the anchor loss dominated Q in vibrating disk structures with very similar geometries to those presented in this dissertation [109].

Table 4-IV: Comparison of the measured resonator  $Q$ 's and FEA simulation results.

<b>Disk Material</b>	<b>Stem Material</b>	<b>Measured <math>Q</math></b>	<b>COMSOL Simulated <math>Q</math></b>	<b>HiQLab Simulated <math>Q</math></b>
Diamond	PolySi	71,400	78,285	76,695
PolySi	PolySi	20,912	20,371	26,450
Diamond	Diamond	NA	41,578	52,486

The solid modelling approach used in HiQLab also utilizes the circular symmetry of the disk resonator structure to simplify the meshing and PML formation. However, unlike COMSOL, HiQLab uses a rectangular block for the Si substrate and PML sections. Figure 4.19 presents the contour-mode vibration simulation results calculated by HiQLab for the radial and vertical directed acoustic waves occurring in the mismatched stem polydiamond resonator. Similar to the COMSOL case, the PML layer that surrounds the substrate block absorbs the energy lost to the substrate as indicated by the displacement contour color map.

#### 4.5.4.3 Anchor Loss Simulation Results

Table 4-IV presents the anchor loss simulation results for the polydiamond disk – polysilicon anchor and polysilicon disk – polysilicon anchor cases with acoustic impedance mismatched and regular stems, respectively. This table also compares the simulation results with the measured data presented in Figure 4.14 and Figure 4.15. The first observation is that simulation results obtained by the two FEA tools agree well with each other. Two independent numerical analysis setups providing very close results raise the confidence level for the simulation tools for anchor loss analysis.

More importantly, the simulated results agree very well with the measured data. This result confirms our initial hypothesis that claimed the VHF-UHF frequency vibrating disks are limited by the anchor loss, and other loss mechanisms such as phonon-phonon dissipation and TED is negligible compared to the energy lost to the anchor. Therefore, the acoustic impedance mismatched anchor design detailed in Section 4.5.1, as well as other novel anchor design techniques such as the hollow stem design introduced by [110] is vital to achieve the  $Q$ 's exceeding 30,000 frequencies exceeding 1 GHz demanded by low loss narrow band receiver front end designs.

## 4.6 Conclusion

The very impressive  $Q$ 's of 146,580 at 232.4 kHz and 71,400 at 299.86 MHz measured for the folded-beam and disk resonators of this work, respectively, are considerably higher than previously achieved on similar devices constructed using microwave CVD polydiamond (or any other material, for that matter). These results now elevate hot filament CVD polydiamond as one of the

(if not the) most compelling material to use for high frequency on-chip micromechanical resonators. The material used here further exhibits an acoustic velocity of 18,516 m/s, which is now the highest to date among available surface micromachinable materials.

The optimized HFCVD diamond material is combined by an acoustic impedance mismatched anchor design borrowed from [30] helped create high  $Q$  disk resonators with a low cost, high wafer throughput process. The acoustic impedance mismatched anchor design is analyzed via two separate FEA analysis tools, which validated that using different materials with a large acoustic impedance difference confines the acoustic energy in the disk resonator instead of losing the energy to the substrate. The FEA simulation results showed very good agreement with the measure data, which suggests FEA analysis as a valuable anchor design tool for future disk resonator designs.

It is very possible that this new polydiamond recipe can eventually enable  $Q > 30,000$  at GHz frequencies, and work to demonstrate this continues. If achievable with adequately small motional impedance (which will take some work as elaborated in Chapter 3), a paradigm-shift in the design of next generation RF communication transceivers might be possible, such as described in [81], where channel-selecting RF filter banks enabled by  $Q$ 's this high remove all interferers from the signal directed to demodulation electronics, allowing realization of a fast, low power frequency gating spectrum analyzer that in turn enables true software-defined cognitive radio.

## Chapter 5

# PASSBAND-CORRECTED HIGH REJECTION RF CHANNEL-SELECT MICROMECHANICAL VIBRATING DISK FILTERS

---

---

This chapter introduces a 39nm-gap capacitive transducer, voltage-controlled frequency tuning, and a stress relieving coupled array design that enables a 0.09% bandwidth 223.4-MHz channel-select filter with only 2.7dB of in-band insertion loss and 50dB of out-of-channel interferer rejection. This amount of rejection is more than 23dB better than a previous capacitive-gap transduced filter design that did not benefit from sub-50nm gaps. It also comes in tandem with a 20dB shape factor of 2.7 realized by a hierarchical mechanical circuit design utilizing 206 resonant micromechanical circuit elements, all contained in an area footprint (sans bond pads) of only  $600\mu\text{m}\times 420\mu\text{m}$ . The key to such low insertion loss for this tiny percent bandwidth is  $Q$ 's  $>8,800$  supplied by polysilicon disk resonators employing for the first time capacitive transducer gaps small enough to generate coupling strengths on the order of  $(C_x/C_o) \sim 0.1\%$ , which is a  $6.1\times$  improvement over previous efforts. Defensive strategies built into the array-composite design hierarchy counter process variations via electrical stiffness tuning, and alleviate stress by allocating displacement-buffer devices to increase filter performance and yield. This filter is the first demonstrated that truly offers low insertion loss and high rejection channel-selection for ultra-low power communication front-ends targeted for autonomous sensor networks.

### 5.1 Introduction

The power consumption of a radio generally goes as the number and strength of the RF signals it must process [10]. In particular, a radio receiver would consume much less power if the signal presented to its electronics contained only the desired signal in a tiny percent bandwidth frequency channel, rather than the typical mix of signals containing unwanted energy outside the desired

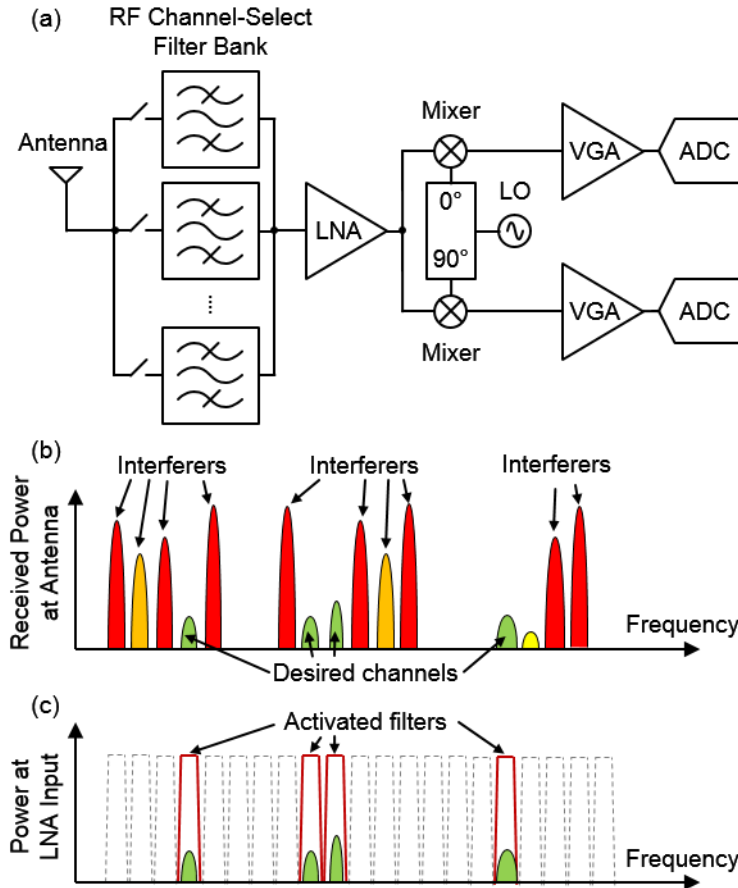


Figure 5.1: (a) Direct conversion receiver architecture combined with an RF-channel select filter bank capable of eliminating in-band blockers directly at the RF front-end. (b) Cartoon description of the typical power spectrum received at the antenna. (c) On/off configuration of the filters in the RF channelizing filter bank that selects only the desired channels.

channel that may be much stronger than the desired signal, e.g. by 70dB for the W-CDMA standard [3]. The more unwanted energy present, the higher the dynamic range required of the electronics, hence, the larger the power consumption. Unfortunately, a lack of filters capable of selecting single channel bandwidths at RF forces the front-ends of contemporary receivers to accept unwanted signals, and thus, to operate with sub-optimal efficiency.

It is no surprise, then, that attempts to realize RF filters with percent bandwidths on the order of 0.1% sufficient to remove all interfering signals, leaving only energy in the desired RF channel, are abundant in the literature. Because the bandwidths of such RF channel-selecting filters are so small, and technologies capable of attaining the needed  $Q$ 's are generally not widely tunable, much of the research has focused on micro-scale filters that can assemble into banks of weakly tunable filters, *cf.* Figure 5.1, to cover a target communication band.

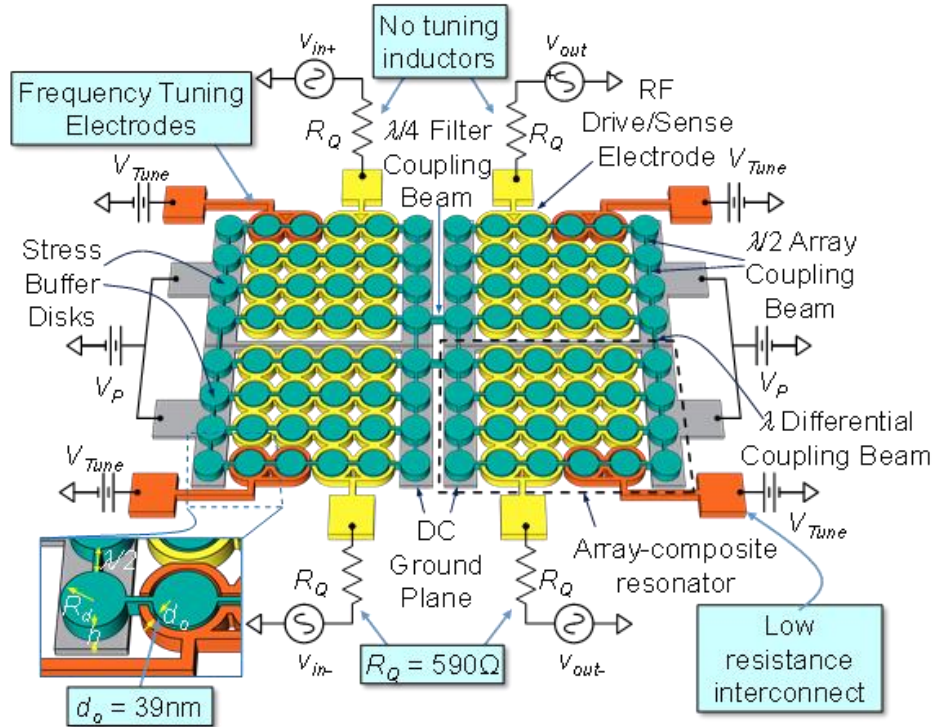


Figure 5.2: The improved filter design of this work with indicated improvements over to the filter design presented in [23]; in the preferred bias and excitation configuration used to evaluate filter performance.

Because of its tiny size and ability to attain very high  $Q$ , many research approaches to RF channel-selection focus on MEMS technology. These studies employ various resonator technologies using piezoelectric [17][18][19][20], internal dielectric [21][22], and capacitive [23][24] actuation. Unfortunately, so far none of the explored approaches truly achieves the needed performance, which demands not only small percent bandwidth, but also low passband insertion loss and high stop-band rejection. Several approaches explored thus far use resonators, e.g., based on piezoelectric materials [17][18], that lack the needed  $Q$  to achieve low insertion loss in so small a percent bandwidth. For example, one attempt to use conventional attached-electrode piezoelectric resonators does achieve the needed 0.1% bandwidth, but only with excessive passband loss on the order of 15dB [17], which is clearly not permissible immediately after the antenna.

On the other hand, approaches that attain sufficient  $Q$ 's on the order of 10,000, e.g., capacitive-gap transduced resonators, so far do not possess enough electromechanical coupling to attain 50dB stop-band rejection at UHF. In particular, although the design of [23] achieves the needed 0.06% bandwidth with an insertion loss of only 2.5 dB, it does so with only 27dB of stop-band rejection. It also re-quires rather large termination impedances on the order of 1.5 k $\Omega$  that necessitate the use of inductors to resonate out shunt input and output capacitance. Finally, its yield of devices with adequately small passband ripple is quite low.



More recent work using a “capacitive-piezoelectric” transducer that combines capacitive and piezoelectric transduction to realize a resonator with simultaneous high  $Q$  and coupling [111] seems poised to eventually achieve RF channel-select filters with appropriate insertion loss and stop-band rejection characteristics. The work of [111]; however, demonstrates only a single-resonator that provides only a 2-pole frequency shaping transfer function. Most RF front-ends require at least 4-pole shaping characteristics, so work is still needed to generate an appropriate filter response. Perhaps most importantly, if one transducer technology alone—e.g., one of capacitive-gap or piezoelectric, but not both—can be shown sufficient to achieve the needed filter characteristic, then this would likely be the more cost effective approach.

This chapter focuses on the degree to which capacitive-gap transduced micromechanical resonators can achieve the aforementioned RF channel-selecting filters. It aims to first show theoretically that with appropriate scaling capacitive-gap transducers are strong enough to meet the needed coupling requirements; and second, to fully detail an architecture and design procedure needed to realize said filters. Finally, this chapter provides an actual experimentally demonstrated RF channel-select filter designed using the above procedures and confirming theoretical predictions.

The overall micromechanical circuit design hierarchy used here builds upon micromechanical vibrating disk resonators presented in Chapter 2, and uses a combination of capacitive actuation gap scaling elaborated in Chapter 3, coupled array-composites [14], electrical stiffness tuning [15], [16], and fabrication process improvements to attain unprecedented RF channel-select performance. It specifically modifies the design of [23] to that of Figure 5.2, which points out the major design changes. Now, smaller electrode-to-resonator gaps on the order of 39nm amplify the input/output electromechanical coupling by more than  $8.6\times$ , which directly contributes to a larger stop-band rejection and removes the need for inductors. The new design also introduces additional electrodes around disks specifically tasked for frequency tuning to-wards higher device yield; as well as carefully designed electrode-less buffer devices that alleviate post-fabrication stress, thereby also contributing to higher yield.

Combined, these design changes yield a 223.4-MHz two-resonator filter that employs 206 resonant micromechanical elements to realize a channel-selecting 0.09%-bandwidth while achieving only 2.7dB of in-band insertion loss together with 50dB of out-of-channel stop-band rejection. This amount of rejection is more than 23dB better than that of [23] and comes in tandem with a 20dB shape factor of 2.7 commensurate with its use of two array-composite resonators.

But again, we start with filter theory and design specifications.

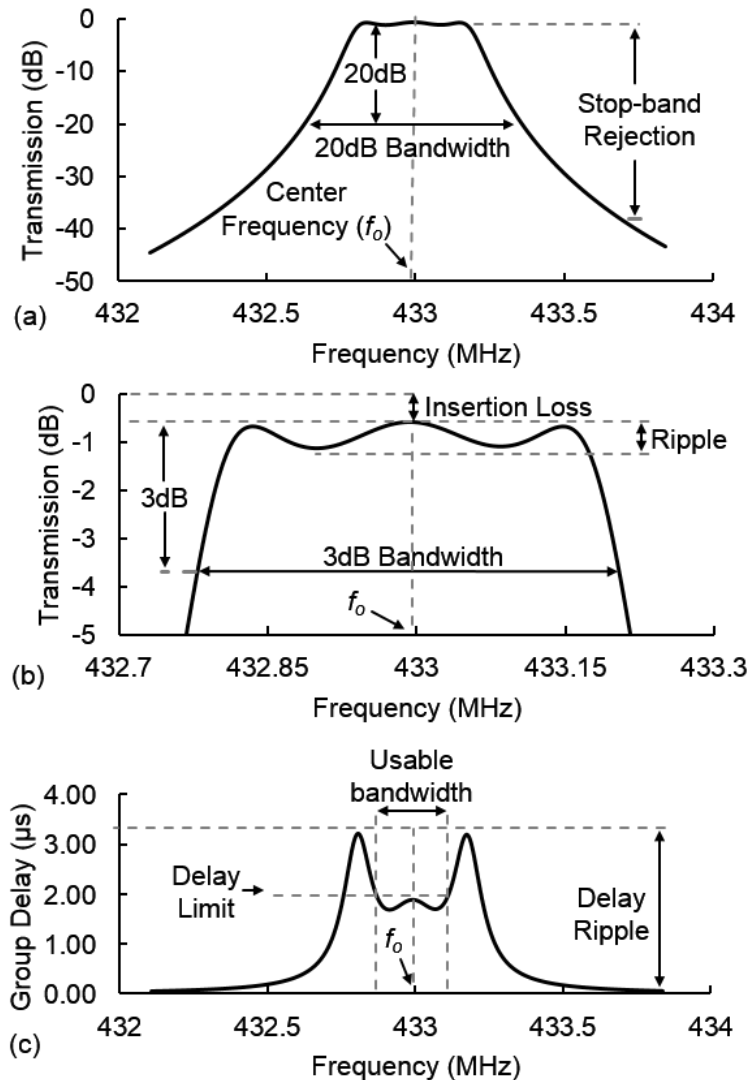


Figure 5.3: Schematic description of (a) transmission amplitude, (b) 3dB passband zoomed, and (c) group delay response metrics used to specify a bandpass filter.

## 5.2 Filter Design Specifications

Figure 5.3 presents the transmission response of a third-order bandpass filter and identifies important performance metrics [25], including insertion loss, stopband rejection, passband ripple, group delay ripple, and 20dB shape factor. A common way to achieve filter characteristics as in Figure 5.3 is to link multiple two-pole resonators together by coupling elements of some form, as shown in Figure 5.4(a) [26]. Figure 5.4(b) presents one possible implementation that employs series LCR resonator tanks coupled by shunt capacitors to mimic the structure of (a). Here, the res-

onators realize bandpass biquad transfer functions that when coupled by the shunt capacitors assemble into a frequency response as shown in Figure 5.4(c), where three mode peaks ensue, separated by frequency spans governed by coupling strength. Termination of the filter by resistors  $R_Q$  then effectively loads the resonators, loading their  $Q$ 's and widening their responses so that they add constructively in the passband to form the flat response of Figure 5.4(d). Phasing of resonator currents also induces subtraction of their responses outside the passband, thereby providing rejection in the stopband.

The desired filter amplitude response, cf. Figure 5.3(a), minimizes the passband insertion loss, ripple, and the filter shape factor, the latter defined here by the ratio of the 20dB bandwidth to the 3dB bandwidth; and maximizes the stopband rejection. The group delay characteristic [25] illustrated in Figure 5.3(c) is a measure of the degree to which the filter phase response deviates from the ideal linear-phase response. Not only must the group delay be below a certain threshold, its ripple must also be small. As a consequence, in the plot of Figure 5.3(c), only the region of filter bandwidth indicated between the large group delay peaks is actually usable. Note that Chebyshev and Elliptic type filters display a rippled group delay over the passband as seen in Fig. 3(c), whereas Bessel type filters achieve maximally flat group delay at the expense of increased shape factor [25].

It should be noted that the smaller the percent bandwidth of the filter, the larger the group delay in the usable bandwidth region. Thus, at first glance, it might seem that the 0.1%-bandwidth RF channel-select filters targeted by this work are not usable in a practical application, since they will have larger group delay than the 3%-bandwidth filters typically used in wireless handsets. Such worries, however, are unfounded, since smaller bandwidth signals can withstand larger group delay. In brief, the important thing is that the bit period-to-group delay ratio be above a certain threshold. The smaller the bandwidth of signal, the larger its bit period, hence the larger the permissible group delay.

Group delay is determined primarily by the filter type, i.e., Chebyshev, Butterworth, etc., and bandwidth. Although filter type also governs passband insertion loss  $IL$  and stopband rejection, these very important metrics also depend heavily on the performance of the resonators constituting the filter, particularly their quality factor  $Q$  and their input/output transducer coupling, the latter gauged by the  $(C_x/C_o)$  ratios of the end resonators in Figure 5.4(b). In brief, sufficient  $Q$  is needed for low filter insertion loss; and sufficient electromechanical coupling for proper termination of the filter with minimal passband distortion and large stopband rejection.

### 5.3 Needed $Q$ and Coupling

Whether or not high resonator  $Q$ , strong transducer coupling  $(C_x/C_o)$ , or a simultaneous combination of both, are needed, depends largely on the percent bandwidth of the filter to be realized.

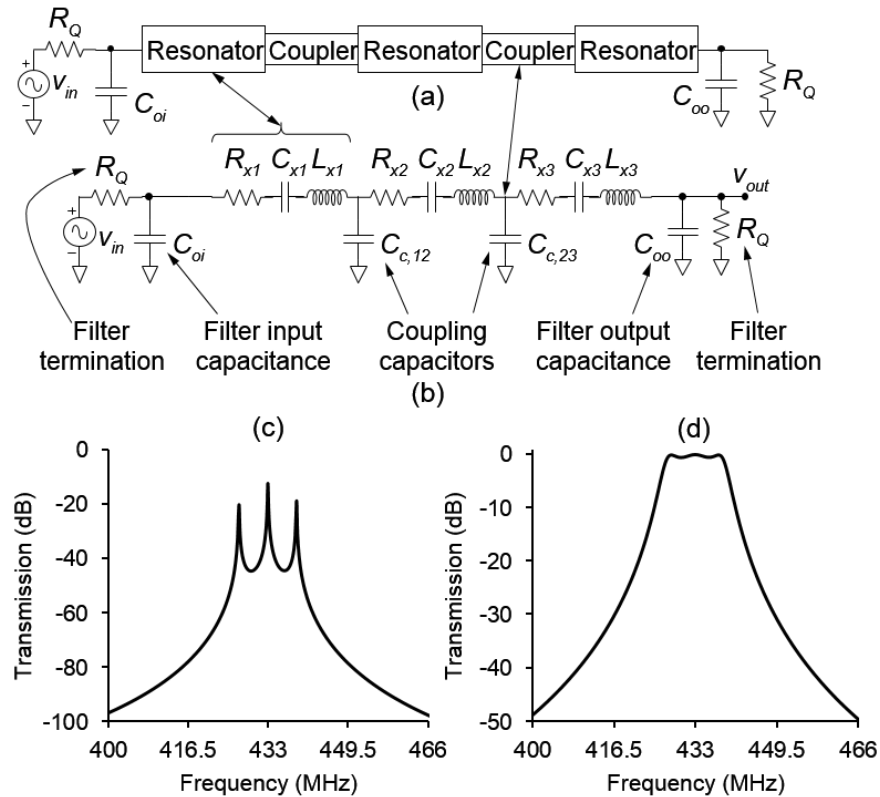


Figure 5.4: (a) Schematic description of general implementation topology of a band-pass filter consisting of a chain of discrete resonator tanks linked with coupling elements. (b) Electrical equivalent circuit representation of the generic filter network with  $LCR$  tanks representing the resonator elements and shunt capacitors modeling the coupling between adjacent resonators. (c) The three mode peaks that ensue from the coupled high  $Q$  resonators. (d) Terminated filter response after  $Q$ -control with termination resistors  $R_Q$ .

In particular, the small percent bandwidth filters needed for the aforementioned RF channel-selection application require resonators with large  $Q$  to avoid excessive insertion loss, but do not require large  $(C_x/C_o)$ .

### 5.3.1 Needed Quality Factor

The insertion loss of a front-end filter is perhaps its most important performance metric. Indeed, the positioning of this filter directly after the antenna and before the amplifier, cf. Figure 5.1, means that its loss cannot be attenuated by amplifier gain. As a result, the filter  $IL$  ends up adding directly to the receiver noise figure, so often has the greatest impact on overall receiver sensitivity.

The insertion loss of any coupled-resonator filter is primarily determined by the ratio of constituent resonator  $Q$  to overall filter quality factor  $Q_f$  [26], or

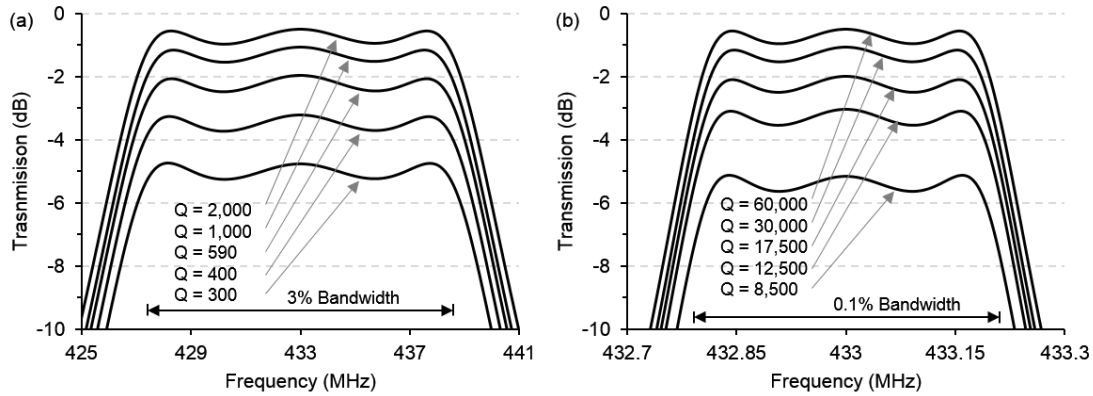


Figure 5.5: Simulated frequency characteristics for the 433-MHz three-resonator filter with varying constituent resonator  $Q$ 's, illustrating how resonator  $Q$  governs the insertion loss of a filter. (b) For an insertion loss less than 2dB, resonator  $Q$ 's must be larger than 590 for a 3% bandwidth filter. (c) When the filter bandwidth shrinks to 0.1%, even higher resonator  $Q > 17,500$ , is needed.

$$q_o = \frac{Q}{Q_f} \quad (5.1)$$

where  $Q_f$  takes the form

$$Q_f = \frac{f_o}{B} \quad (5.2)$$

where  $f_o$  and  $B$  are filter center frequency and 3dB bandwidth, respectively. The filter type and order set the minimum  $q_o$  required to achieve a desired  $IL$ . Here, filter cookbooks [26] readily provide  $q_o$  values for various filter types and insertion losses. For example, the minimum  $q_o$  required for less than 2 dB  $IL$  for a 2<sup>nd</sup> order Chebyshev filter is 9.7; it increases to 18.6 and 31.1 for third and fourth order filters, respectively [26]. Note that the relation between the quantity set by (5.1) and the filter  $IL$  is independent of the resonator technology used to implement the filter.

From (5.1), the higher the filter  $Q_f$ , the narrower the fractional bandwidth, and the higher the constituent resonator  $Q$  needed to maintain low insertion loss. Thus, high resonator  $Q$  becomes especially important for the small percent bandwidth RF channel-selecting filter targeted, here—much more so than a conventional 3% band-select filter used in today's wireless handsets.

Figure 5.5 illustrates the  $Q$  dependency by comparing simulated frequency responses of a three-resonator, 0.5dB-ripple, Chebyshev filter operating at 433 MHz for band-select and channel-select cases with 3% and 0.1% fractional bandwidths, respectively, with varying constituent resonator  $Q$ 's. Here, large resonator  $Q$  clearly minimizes insertion loss, regardless of the percent bandwidth. However, to achieve the same insertion loss, a filter with a smaller percent bandwidth requires resonators with larger  $Q$  than one with a large percent bandwidth. For example, the filter

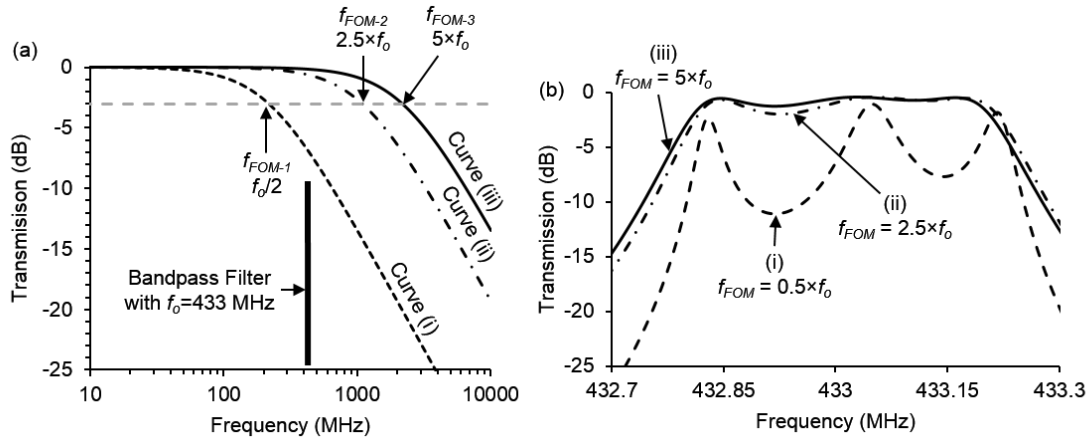


Figure 5.6: Simulations illustrating the degree to which low-pass filtering by shunt parasitic capacitance impacts passband flatness for a three-resonator filter, cf. Figure 5.3, operating at center frequency  $f_0 = 433$  MHz. Here, the filter response curves in (b) correspond to the parasitic low-pass filter cases in (a), for which (i)  $f_{FOM} = 0.5 f_0$ , (ii)  $f_{FOM} = 2.5 f_0$ , and (iii)  $f_{FOM} = 5 f_0$ .

with 3% 3dB-bandwidth shown in Figure 5.5(a) requires resonator  $Q$ 's of 590 to achieve an insertion loss of 2dB. However, when the bandwidth shrinks to the 0.1% required for RF channel-selection (at 433MHz with a 433kHz bandwidth), the required  $Q$  for 2 dB insertion loss increases to 17,500 as shown in Figure 5.5(b). The requirement becomes more stringent as frequencies increase or bandwidths decrease. For example, a 30-kHz bandwidth at 433MHz corresponds to a percent bandwidth of 0.007%, for which  $Q$  the required for less than 2dB insertion loss rises to 240,000. They become less stringent as the filter order reduces. For example, a second order version of the 0.1%-bandwidth, 433-MHz filter requires resonator  $Q$ 's of only 9,600 to achieve less than 2dB of insertion loss.

### 5.3.2 Needed Electromechanical Coupling Strength

The electromechanical coupling requirement is related to proper impedance termination of a given filter. In particular, the flat passbands shown in Figure 5.3(b) and Figure 5.4(d) are achieved via termination resistors  $R_Q$ 's that load both input and output ports, as shown in Figure 5.4(a). Here, the  $R_Q$ 's essentially load the  $Q$ 's of the filter end resonators, smoothing out the passband ripple in the process. If the filter had no shunt capacitance  $C_o$  at its input and output, then the value of  $R_Q$  can be as large or small as needed, with no limit.

The presence of  $C_o$ , however, places an upper limit on the value of  $R_Q$ . In an actual physical realization, load capacitance  $C_L$  from leads or other electrically connected structures to the substrate joins  $C_o$  to further limit  $R_Q$ . In particular,  $R_{Ql}$  and  $(C_{o1}+C_L)$  combine to form a low pass filter (LPF) that greatly attenuates and distorts the filter response if its cut-off frequency is below the filter center frequency  $f_0$ , such as depicted by curve (i) in Figure 5.6(a), which distorts the filter

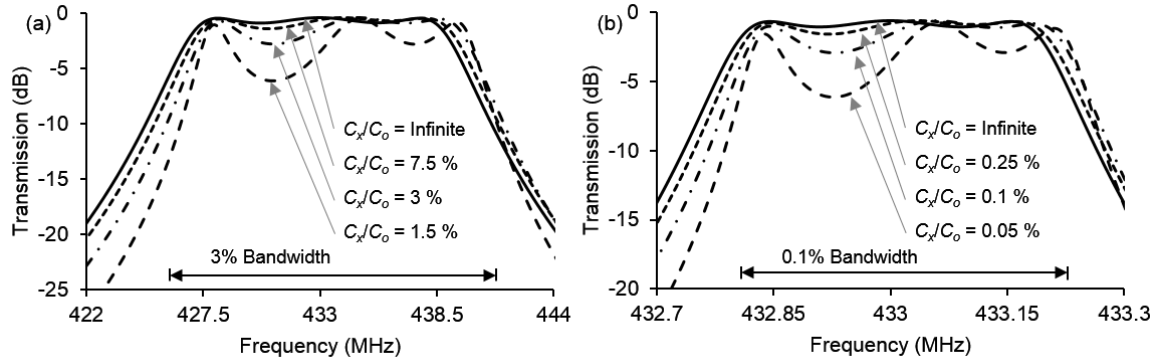


Figure 5.7: Simulated plots of responses for (a) a 3% bandwidth and (b) a 0.1% bandwidth 3-resonator Chebyshev filter with 0.5dB designed ripple for varying values of transducer ( $C_x/C_o$ ). Here, the simulations assume resonator  $Q$ 's of 2,500 in (a), and 50,000 in (b).

passband as shown in Figure 5.6(b). Here, the low pass cut-off frequency is labeled  $f_{FOM}$  to emphasize its role as a figure of merit for a given resonator/filter design, where the higher its value, the less pass-band distortion incurred. Even if  $f_{FOM}$  is higher than the filter's center frequency, cf. curve (ii) with simulated response in Figure 5.6(b), phase shift from the LPF can still generate significant passband distortion that may or may not be acceptable, depending upon the application. Thus, it is not enough for  $f_{FOM}$  to just be higher than  $f_o$ . As a rule of thumb, for the case of a three-resonator Chebyshev BPF, the amount of passband distortion introduced by the parasitic LPF is generally acceptable when  $f_{FOM}$  is more than 2.5 times the BPF center frequency, as shown in curve (ii).

For the case where  $C_o$  dominates over  $C_L$ , the quantity ( $C_x/C_o$ ) becomes a very convenient figure of merit for comparison of electromechanically transduced resonators to be used in a filter. In this case, a rule of thumb to avoid passband distortion upon proper termination stipulates that the transducer coupling at the input and output resonators of a given filter should satisfy

$$(C_x/C_o) > \xi \cdot P_{BW} \quad (5.3)$$

where  $P_{BW}$  is the percent bandwidth of the filter; and  $\xi$  is 2.5 for a low insertion loss 3-resonator Chebyshev filter, and  $\sim 6$  for a 3-resonator linear phase filter.

Figure 5.7 illustrates the dependence of passband distortion on ( $C_x/C_o$ ) by plotting simulated responses for (a) a 3% bandwidth and (b) a 0.1% bandwidth 3-resonator Chebyshev filter with 0.5dB designed ripple for varying values of transducer ( $C_x/C_o$ ). As shown, the passband of the filter in Figure 5.7(a) remains relatively undistorted until the transducer ( $C_x/C_o$ ) drops to below 7.5%, at which point an amount of extra ripple equal to the original 0.5dB ripple superimposes atop the passband for a total of 1dB ripple. On the other hand, the passband ripple of the 0.1% bandwidth filter of Figure 5.7(b) worsens to 1dB when ( $C_x/C_o$ ) drops to a much smaller 0.25%. Note that the passband distortions for both filters conform to the guideline of (5.3).

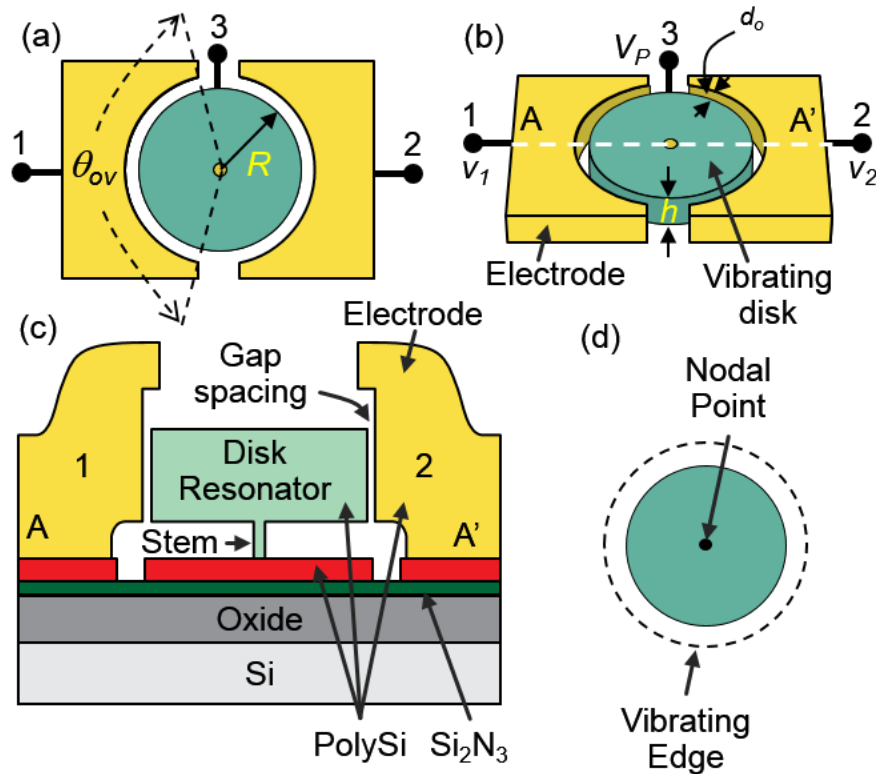


Figure 5.8: Pictorial summary for a micromechanical disk resonator with two in-put/output ports and a resonator body port. (a) Layout view. (b) Perspective view (c) Cross-section view. (d) Radial-contour mode shape.

From Figure 5.7, the smaller the percent bandwidth, the smaller the needed  $(C_x/C_o)$ . In particular, for the 0.1% bandwidth often required for RF channel-selection,  $(C_x/C_o)$  need only be  $\sim 0.25\%$ . It is important to note that the needs of a 0.1% RF channel-select filter differ significantly from those of conventional 3% band-select filters used in today's handsets. In particular, conventional 3% filters put a premium on strong coupling, where  $(C_x/C_o) \sim 7\%$  is often needed, and not so much on  $Q$ , for which 500 is often acceptable as in Figure 5.5(a). On the other hand, a 0.1% RF channel-select filter places a high premium on  $Q$ , which must often be greater than 10,000, and not so much on  $(C_x/C_o)$ , for which values on the order of only 0.25% are acceptable.

## 5.4 Simplified Description of the Vibrating Disk Filter Operation

The mechanical filter of this work is much like the filter of Figure 5.3(b), except that instead of  $LCR$  tanks constrained to  $Q$ 's below 100, it uses mechanically coupled arrays of vibrating micromechanical resonators [101] capable of achieving  $Q$ 's exceeding 10,000. As shown in Figure 5.8(a), each such resonator comprises an electrically conductive disk surrounded by electrodes



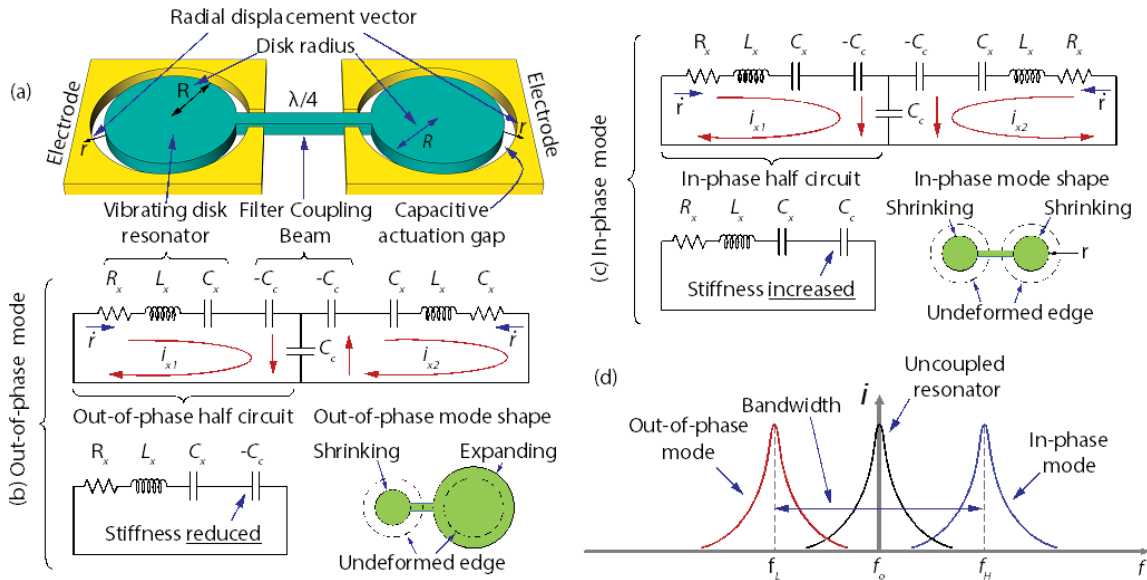


Figure 5.9: (a) Schematic description of a mechanically coupled two-resonator filter. Equivalent circuit models for the (b) lower frequency out-of-phase, and (c) higher frequency in-phase filter mode shapes. (d) Motional current spectra for the uncoupled vibrating disk, and the lower and higher frequency filter modes.

spaced by small gap spacing do from its perimeter, and supported at its center by a stem post, as described in Figure 5.8(c).

To operate the disk, a dc-bias voltage  $V_P$  is applied to its conductive structure (via terminal 3) and ac voltages  $v_i = V_i \cos(2\pi f t)$  are applied at each of its electrodes. The combinations of DC and AC voltages applied across each electrode-to-resonator gap generate forces on the disk structure at frequency  $f$  that then actuate the disk into vibration with amplitude governed by its high  $Q$  force-to-velocity band-pass biquad transfer function. In particular, when  $f$  matches the disk resonance frequency  $f_o$ , the disk responds by vibrating with a large resonance amplitude in the radial-contour mode shape depicted in Figure 5.8(d), where the disk expands and contracts around its circumference in a motion reminiscent of breathing. Vibration of the disk gives rise to time-varying capacitors at each electrode-to-resonator interface. Since these capacitors have DC bias voltages across them, they generate currents given by  $i_o = V_p dC/dt$  that then serve as outputs.

Unfortunately, the tiny size of a single disk relegates it to high impedance. For example, a  $6.3\mu\text{m}$ -radius 433-MHz disk with 100nm electrode-to-resonator gaps and a DC-bias voltage of 15 V posts a motional resistance  $R_x$  of 71.8 k $\Omega$ , which is much too large to match to other system components, e.g., the antenna. To remedy this, the design this work employs not one, but several disks with combined inputs and outputs that generate input and output currents larger than that of a single device by a factor equal to the number of disks used. In effect, an array of  $N$  disks generates  $N\times$  greater output current for the same input voltage amplitude, effectively reducing the overall impedance by  $N\times$ .

Ignoring the arraying for now (for simplicity), Figure 5.9 presents a simplified two-resonator version a micromechanical disk filter for the purposes of explaining its operation. Here, the two disks coupled by a single quarter-wavelength extensional mode beam are identical in all respects, i.e., they have the same resonance frequency. From a mechanical perspective, mechanical coupling of the two resonators creates a two degree of freedom mechanical system that effectively splits the originally identical resonance frequencies of the disks apart into two mode frequencies, i.e., eigenstates, that now define the passband of the filter response. The two modes can be characterized as out-of-phase, where the two resonators vibrate with opposite phase, i.e., one expanding while the other contracts at a given instant, cf. Figure 5.9(b); and in-phase, where the disks expand and contract in unison, cf. Figure 5.9(c).

The mechanism by which the quarter-wavelength coupling beam splits frequencies is perhaps best described via the electrical equivalent circuit for this system, shown in Figure 5.9 [46]. Here,  $LCR$  tanks model each disk resonator, while a T-network of capacitors models the quarter-wavelength coupling beam, essentially treating it as an acoustic transmission line. As shown in [46], the values of the  $L_x$ ,  $C_x$ , and  $R_x$  elements in the  $LCR$ 's are derived directly from the values of mass, stiffness, and damping of the actual resonators.

In the lower frequency out-of-phase mode described in Figure 5.9(b) the coupling spring experiences no strain, since the adjacent disk edges displace in opposite radial directions. This means the current into the leftmost (input) disk at resonance, given by

$$i_x = \frac{V_i}{R_x} \quad (5.4)$$

is positive; and the current going into the rightmost (output) disk is negative, i.e., current flows out of the disk into the output electrode. Thus, current flows through the device, from input to output. This means the motional currents indicated as  $i_{x1}$  and  $i_{x2}$  in the electrical equivalent circuit flow in the same clockwise directions around their respective meshes. They thus cancel in the shunt capacitor  $C_c$ , which means the voltage drop across the shunt arm of the coupling beam T-network equals zero. This then yields the half circuit for the system shown in Figure 5.9(b), where a capacitor of value  $-C_c$  adds in series to the motional  $C_x$  of the mechanical resonator, lowering the mesh frequency from that of the original resonator down to the lower mode frequency  $f_L$  given by

$$f_L = \frac{1}{2\pi} \sqrt{\frac{1}{L_x} \left( \frac{1}{C_x} - \frac{1}{C_c} \right)} \quad (5.5)$$

In the higher frequency in-phase mode, where both disks vibrate in unison, the coupling spring now experiences strain. This adds stiffness to the system, raising its frequency over that of the original resonators. From the electrical equivalent circuit perspective, the motional currents  $i_{x1}$  and  $i_{x2}$  in each resonator tank now flow in opposite directions around their respective meshes, which means they add in the shunt  $C_c$  arm of the T-network. Each mesh thus absorbs half of the shunt  $C_c$

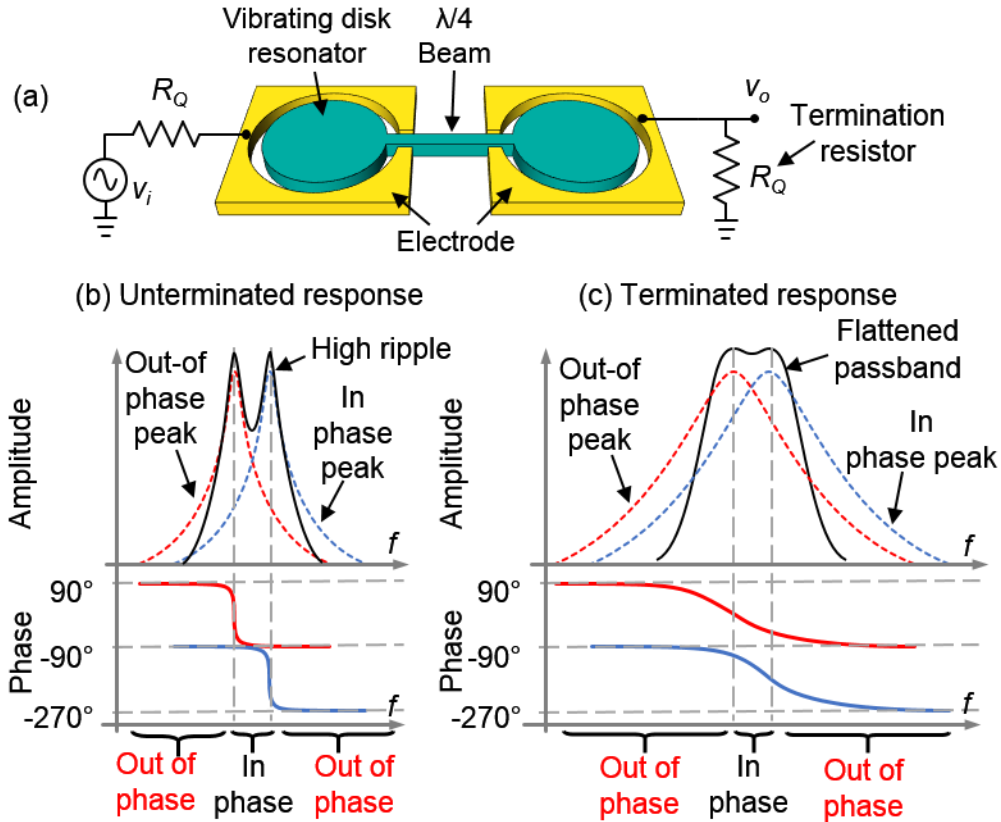


Figure 5.10: (a) Mechanically coupled two-resonator filter with termination resistors  $R_Q$  added for  $Q$ -control. (b) Addition of in-phase and out-of-phase mode shape transfer functions to create the unterminated filter response. (c) Terminated filter response after  $Q$ -control with termination resistors  $R_Q$ .

to yield the overall half circuit shown in Figure 5.9(c), where now a positive  $C_c$  adds in series to the motional capacitance  $C_x$ . This raises the mesh frequency to

$$f_H = \frac{1}{2\pi} \sqrt{\frac{1}{L_x} \left( \frac{1}{C_x} + \frac{1}{C_c} \right)} \quad (5.6)$$

Figure 5.9(d) plots the motional current amplitude spectrum for an uncoupled individual constituent disk resonating at frequency  $f_o$  alongside the coupled out-of- and in-phase mode frequencies at  $f_o - B_{sep}/2$  and  $f_o + B_{sep}/2$ , respectively, where  $B_{sep} = f_H - f_L$  is the frequency span that separates the modes. The out-of-phase and in-phase resonance transfer functions illustrated in Figure 5.9(d) correspond to the orthogonal eigenvectors of the coupled two-resonator system shown in Figure 5.9(a). Thus, the sum of these transfer functions generates the overall filter transfer function, as illustrated in Figure 5.10(b). Note that the relative phase between these modes plays a crucial role in shaping the overall filter response. In particular, the out-of-phase and in-phase modes have the same phase between the mode peaks, so add constructively within the filter passband to form a flatter response in this region. Outside the peaks, their phases differ by  $180^\circ$ , which means they

subtract outside the passband, yielding a steeper roll-off to the stopband and a higher overall stopband rejection.

However, as shown in Figure 5.10(a), addition in the pass-band will not yield a flat passband if the  $Q$ 's of the constituent resonators are too high. Indeed, to permit a flat passband, the signal power of each mode spectrum at the frequency directly between the peaks must be approximately equal to half that at the peaks themselves. This is where the termination impedances shown in Figure 5.3 and again in Figure 5.10 become important. These termination resistors  $R_Q$  load the  $Q$ 's of the resonators, broadening their peaks and effectively raising their power levels at frequencies away from resonance. To attain half power between the peaks, the resonator  $Q$ 's must be reduced to approximately that of the filter, or

$$q_n Q_f = Q \left( \frac{R_x}{R_x + R_Q} \right) \rightarrow R_Q = R_x \left( \frac{Q}{q_n Q_f} - 1 \right) \quad (5.7)$$

where  $q_n$  is a modification factor that depends upon the filter order and type, i.e., Chebyshev, Butterworth, and that can be found in filter cookbooks [26]. Upon inclusion of termination resistors  $R_Q$ , the flattened passband response in Figure 5.10(c) ensues. It should be noted that the  $R_Q$ 's are out-side the filter structure, so their loading of the resonator  $Q$ 's does not affect the insertion loss of the filter. The insertion loss for this two-resonator filter is in fact given by

$$IL = \frac{R_Q + R_x}{R_Q} = \frac{Q}{Q - q_n Q_f} \quad (5.8)$$

From Figure 5.10(c), it is clear that with quarter-wavelength coupling the center frequency of the Figure 5.10 filter equals the (common) frequency of its constituent resonators; and its 3dB bandwidth is a bit more than the total separation  $B_{sep}$  afforded by the coupler strength, captured by the value of  $C_c$ . Using (5.5) and (5.6), the mode peak separation takes the form

$$B_{sep} = \frac{C_x}{C_c} f_o = \frac{k_c}{k_m} f_o \quad (5.9)$$

where the last form recognizes that  $C_x$  and  $C_c$  are proportional to the inverse dynamic stiffnesses  $k_m$  and  $k_c$  of the coupled resonators [46]. Since filter bandwidth is usually defined as the 3dB bandwidth, a modification factor  $k_{ij}$  applied to (5.9) yields the more common form

$$B = \frac{k_c}{k_m k_{ij}} f_o \quad (5.10)$$

where  $B$  is the 3dB bandwidth, and  $k_{ij}$  refers to the modification factor needed for the coupler between the  $i^{th}$  and  $j^{th}$  resonators in a multi-resonator filter.  $k_{ij}$  values are widely tabulated in filter cookbooks [26] for a variety of filter types and orders.

## 5.5 Actual Filter Structure and Operation

Although the actual filter that will be experimentally demonstrated in Chapter 6 essentially operates as described in the previous section, its overall structure is substantially more complicated, mainly in the interest of maximizing performance. Again, Figure 5.2 presents the perspective-view schematic of the entire mechanical filter circuit in a preferred differential input/output configuration, showing all applied voltages and termination impedances, and pointing out key differences with the previous one of [23] that allow the present design to achieve much improved performance. As Figure 5.2 shows, the filter comprises 96 disks mechanically coupled by 110 beams. Many of the disks are surrounded by electrodes spaced only 39nm from their edge side-walls to serve as either input/output or mechanisms for frequency tuning. Array composite resonators are clearly discernable, and their use represents a first level of hierarchy in an overall hierarchical design reminiscent of those used in complex VLSI transistor circuits, but here used to achieve a complex MSI mechanical filter circuit. There are in fact four levels of hierarchy:

### *1<sup>st</sup> Level: Radial-Contour Mode Disk Resonator*

The polysilicon contour mode disk resonator depicted in Figure 5.8 and described in Section 2.2 comprises the unit element and 1<sup>st</sup> level of hierarchy in the mechanical circuit. In Figure 5.2, all disks are  $h=3\mu\text{m}$ -thick with  $R=12.1\mu\text{m}$  radii, so share a common radial-contour mode resonance frequency that sets the center frequency of the overall filter.

### *2<sup>nd</sup> Level: Disk Array-Composite*

To reduce termination impedance and raise stiffness to facilitate small bandwidth, four array-composites of half-wavelength coupled disks make up the 2<sup>nd</sup> level of hierarchy. Each combines and raises currents, thereby reducing motional resistance, hence, filter termination impedance.

### *3<sup>rd</sup> Level: Differential Array-Composite*

To enable differential I/O, a 3<sup>rd</sup> level of hierarchy couples pairs of array-composites via full-wavelength beams. This forces them to vibrate 180° out-of-phase, thereby enabling differential mode operation that cancels feedthrough to enable large stopband rejection.

### *4<sup>th</sup> Level: Coupled Resonator Filter*

A 4<sup>th</sup> level of hierarchy couples the differential blocks via quarter-wavelength beams that split their resonances, generating the desired passband and promoting signal subtraction in the stopband that increases rejection.

To operate the filter, a DC voltage  $V_P$  is applied to the conductive structure to amplify forces and electrical outputs, and differential electrical inputs are applied through termination impedances

Table 5-I: Filter Design Equations and Procedure Summary.

<p>Given the following parameters:  <u>Design goals:</u> <math>f_o, B, R_Q, w_{c,min}</math>  <u>Filter type specifications:</u> <math>q_i, k_{ij}, c</math>  <u>Resonator &amp; material properties:</u> <math>Q, E, \rho, \kappa_{mat}, \sigma_{f,Single}</math>  <u>Find:</u> <math>R, N, N_{ioe}, N_t, d_o, V_P, V_{Tune}, \lambda, w_c, h</math>.</p> <ol style="list-style-type: none"> <li>Solve (5.11) for the disk radius <math>R</math> for the given filter center frequency <math>f_o</math>.</li> <li>Choose resonator material thickness <math>h</math>.</li> <li>Determine the minimum array size achievable with the critical beam dimension <math>w_{c,min}</math> that meets the desired filter bandwidth <math>B</math> specification using (5.12).</li> <li>Solve (5.13)-(5.14) simultaneously for <math>d_o</math> and <math>V_P</math> to meet the desired filter termination value <math>R_Q</math> while achieving sufficient <math>C_x/C_o</math>.</li> <li>Solve (5.15) for the sufficient number of tuning electrodes <math>N_t</math> and tuning voltage <math>V_{Tune}</math> to correct the expected single resonator frequency deviation <math>\sigma_{f,Single}</math>.</li> <li>Determine the acoustic wavelength <math>\lambda</math> by (5.16) for the <math>\lambda/4</math> filter, <math>\lambda/2</math> array-composite, and <math>\lambda</math> differential couplers.</li> <li>Solve (5.17) for the <math>\lambda/4</math> filter coupling beam width <math>w_c</math> that realizes the desired bandwidth <math>B</math>.</li> <li>Use (5.18)-(5.21) to calculate all needed component values to simulate the filter response using the filter electrical equivalent circuit.</li> </ol>	Mechanical Design Variables	Disk radius	$R = \frac{K_{mat}}{2f_o} \sqrt{\frac{E}{\rho}}$	(5.11)
		Minimum array size	$N \geq w_{c,min} \frac{2}{\pi^2 K_{mat}^2 \chi k_{ij} \lambda} \frac{f_o}{B}$	(5.12)
		Required gap and bias voltage for sufficient $C_x/C_o$	$\frac{V_P^2}{d_o^3} \geq c \frac{B}{f_o} \frac{\pi^3 \chi K_{mat}^2 E}{\epsilon_o R \theta_{ov}} \frac{N}{N_{RF}}$	(5.13)
		Required gap and bias voltage for proper filter termination impedance $R_Q$	$\frac{V_P^2}{d_o^4} = \left( \frac{Q}{Q_f q_i} - 1 \right) \left( \frac{2\pi K_{mat} \chi}{Q \epsilon_o^2} \sqrt{\frac{E}{\rho}} \right) \left( \frac{N}{N_{ioe}^2} \right) \left( \frac{1}{h R \theta_{ov}^2} \right) \frac{1}{R_Q}$	(5.14)
		Number of tuning electrodes	$N_t = \frac{\left( \sigma_{f,Single} \frac{2\sqrt{N} \pi^3 K_{mat}^2 \chi E d_o^3}{\epsilon_o \theta_{ov} R} - N_{RF} V_P^2 \right)}{(V_{Tune} - V_P)^2}$	(5.15)
		Wavelength for coupling beam designs	$\lambda = \frac{1}{f_o} \sqrt{\frac{E}{\rho}}$	(5.16)
		$\lambda/4$ filter coupling beam width	$w_c = N \frac{B}{f_o} \frac{2k_{re} k_{ij} l_c}{\pi h E}$	(5.17)
		$\lambda/4$ filter coupling beam lumped model component	$c_c = \frac{2l_c}{\pi E h w_c}$	(5.18)
Filter Electrical Equivalent Circuit Components	Array-composite core $lcr$ components	$r_{xA} = \frac{2\pi \chi \rho \pi R^2 h}{NQ}$ $l_{xA} = N \chi \rho \pi R^2 h$ $c_{xA} = \frac{1}{N \pi^3 K_{mat}^2 \chi E h}$	(5.19)	
	Filter input/output port electro-mechanical coupling coefficient and static overlap capacitance	$\eta_{eA} = \frac{V_P}{d_o^2} N_{ioe} \epsilon_o \theta_{ov} R h$ $C_{oA} = N_{ioe} \times \frac{\epsilon_o \theta_{ov} R h}{d_o}$	(5.20)	
	Tuning electrode port electro-mechanical coupling coefficient and static overlap capacitance	$\eta_t = \frac{V_P}{d_o^2} N_t \epsilon_o \theta_{ov} R h$ $C_{tA} = N_t \times \frac{\epsilon_o \theta_{ov} R h}{d_o}$	(5.21)	

(governed by design) to the left-hand terminals. These electrical signals are converted to mechanical (e.g., velocity) signals that are processed mechanically by the frequency response of the structure and then converted back to electrical signals at the outputs.

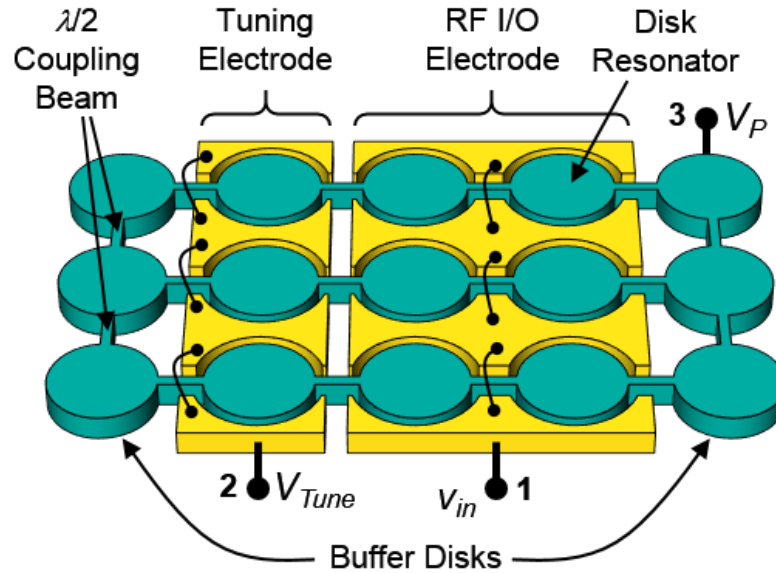


Figure 5.11: Schematic description of a  $\lambda/2$  coupled array-composite resonator with dedicated tuning electrodes and outer buffers disk-resonators for defensive design against in-plane structural film stress.

## 5.6 Detailed Filter Design

Given the design hierarchy from the previous section, a sensible design procedure now emerges:

- 1) Design the fundamental micromechanical radial-contour mode disk building block to resonate at the filter center frequency  $f_o$  with the needed  $Q$  and coupling strength ( $C_x/C_o$ ) with given values of dc-bias  $V_P$  and electrode-to-resonator gap spacing  $d_o$ .
- 2) Assemble disks into array-composites to achieve a specific termination resistance  $R_Q$ , linearity spec, and bandwidth. Here, the array size  $N$  is key to maintaining practically realizable filter coupling beam dimensions for the chosen filter bandwidth  $B$ .
- 3) Design quarter-wavelength filter coupling beams that yield the desired filter passband.
- 4) Convert the design from single-ended to differential.
- 5) Simulate the filter electrical equivalent circuit and verify satisfactory operation in the electrical domain.

Table 5-I captures this design procedure and provides a preview of the relevant governing equations. The remainder of this chapter now expands on the detailed procedures and formulations needed to completely execute each stage of the design process.

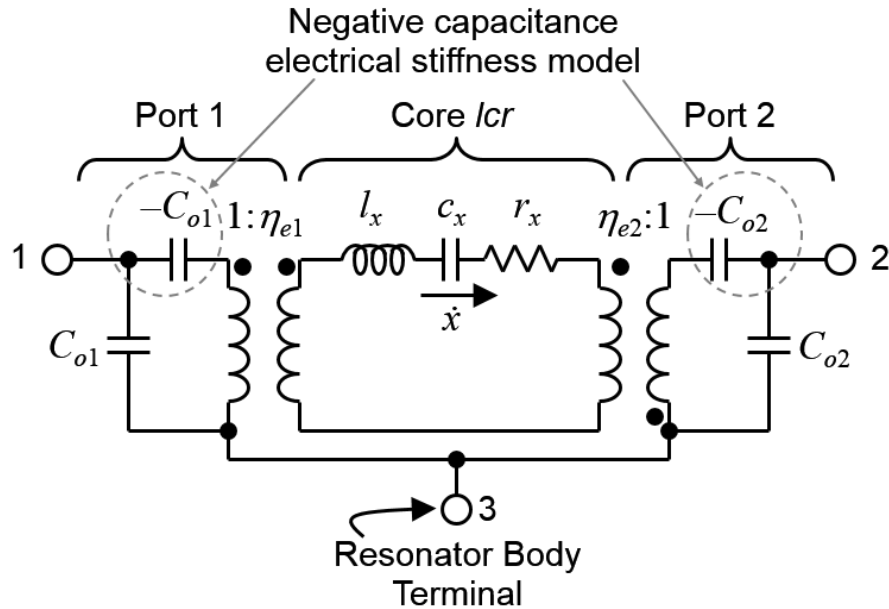


Figure 5.12: Negative capacitance small-signal AC equivalent circuit for a two-port capacitive gap transduced micromechanical resonator, such as that of Figure 5.8, when operating in the radial-contour mode

## 5.7 Radial Contour-Mode Disk Design

The radial-contour mode disk used in this work offers an excellent combination of high  $Q$ , reasonable coupling (when small gaps are used), and perhaps equally important, mechanical circuit design flexibility. The last of these derives from the fact that a lateral mode disk like that shown in Figure 5.8(d) is isotropic around its circumference, i.e., it ideally presents the same loading or response at any point on its outside edges. This means that radial beams can attach and couple to a given disk at any angle and still elicit the same response. Such coupling flexibility is quite welcome when complex coupling geometries are required, like the array of Figure 5.11.

The literature is abundant with capacitively-transduced radial-contour mode disk resonators capable of  $Q$ 's greater than 29,300 at 153-MHz in polysilicon structural material [110], and greater than 55,000 at 497 MHz in polydiamond [30]. Thus, from the perspective of achievable frequency and  $Q$ , the chosen disk resonator design seems adequate for RF channel-selection, at least for the example shown in Figure 5.5.

From the perspective of electromechanical transducer coupling strength, however, the disk resonators so far re-ported in the literature have been lacking. For example, the 153-MHz polysilicon disk of [110] posted a  $(C_x/C_o)$  of only 0.0003%, while the higher frequency 497-MHz was even poorer, on the order of only 0.00005%. Section 5.3.2 mentioned that  $(C_x/C_o)$  need not be large



for RF channel-selection, but these values are abysmal. If disk resonators are to be useful, their design must allow several orders of magnitude improvement in these numbers.

Fortunately, the literature provides comprehensive and experimentally confirmed models for radial-contour mode disk resonators that allow accurate prediction of design-driven performance improvements. Section 2.2 of this dissertation and Table 2-I already summarized the equivalent circuit, c.f. Figure 5.12, and expressions for elements, respectively, which details the most recent radial-contour mode disk model using a negative capacitance concept. Using formulations from Section 2.2, the electromechanical coupling factor for a radial-contour mode disk takes the form

$$\frac{C_x}{C_o} = \frac{V_P^2}{d_o^3} \frac{\epsilon_o R \theta_{ov}}{\pi^3 \chi K_{mat}^2 E} \quad (5.22)$$

where  $V_P$  is the dc-bias applied between the disk resonator and the surrounding electrodes,  $d_o$  is the capacitive actuation gap spacing,  $\epsilon_o$  is the permittivity of vacuum,  $R$  is the disk radius,  $\theta_{ov}$  is the angular overlap between the electrode and the disk in radians, and  $E$  is the Young's modulus of the resonator structural material. Figure 5.8 schematically illustrates these design variables.  $\chi$  is a constant that relates the static mass  $M_{tot}$  of the disk to its dynamic mass  $m_m$  as

$$m_m = \chi M_{tot} = \chi \rho \pi R^2 h \quad (5.23)$$

where  $\rho$  is the resonator structural material density.  $\chi$  can be derived by consideration of the total kinetic energy of the resonant disk structure and its radial velocity at the disk edges; and equals  $\chi = 0.763, 0.967, 0.987$  for a disk operating in its first, second, and third radial-contour modes, respectively [28].

Since (5.23) depends on disk radius  $R$ , it is a function of disk resonance frequency  $f_{nom}$  that derives from the simultaneous solution of

$$\frac{\zeta}{\xi} \cdot \frac{J_0(\zeta/\xi)}{J_1(\zeta/\xi)} = 1 - \sigma, \quad \xi = \sqrt{\frac{2}{1 - \sigma}} \quad (5.24)$$

and

$$\zeta = 2\pi f_{nom} R \sqrt{\frac{\rho(2 + 2\sigma)}{E}} \quad (5.25)$$

where  $\sigma$  and is the Poisson ratio of the structural material. Although the solution of (5.24)-(5.25) as described provides an accurate value for the resonance frequency of the con-tour mode, it does not readily impart design insight. To provide better insight to variable dependencies, rearrangement and simplification of (5.24)-(5.25) yields the closed form

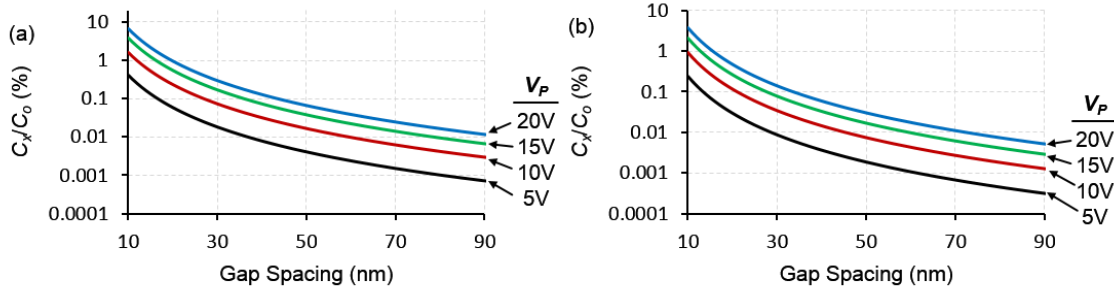


Figure 5.13: Simulated plot of  $C_x/C_o$  for a polysilicon contour mode disk resonator with fully surrounding electrodes plotted as a function of the electrode-to-resonator gap spacing for four different bias voltages operating at (a) 433 MHz, and (b) 1.2 GHz.

$$f_{nom} = \frac{K_{mat}}{2R} \sqrt{\frac{E}{\rho}} \quad (5.26)$$

where  $K_{mat}$  is a dimensionless frequency parameter that depends upon the structural material and is independent of radius. For polysilicon  $K_{mat} = 0.654$ . Solving for  $R$  and then inserting into (5.22) yields the expression for electro-mechanical coupling as a function of resonance frequency

$$\frac{C_x}{C_o} = \frac{V_P^2}{d_o^3} \frac{1}{f_o} \frac{\epsilon_o \theta_{ov}}{2\pi^3 \chi K \sqrt{E\rho}} \quad (5.27)$$

From (5.27), a reduction in electrode-to-resonator gap spacing  $d_o$  is clearly the most effective approach to raising  $(C_x/C_o)$ , given the third power dependence. In fact, reducing  $d_o$  from the 80 nm used for the 163-MHz disk of [23] to 48nm would result in a  $(C_x/C_o)$  equal to 0.1% for a 14V dc-bias voltage—a 4.6 times increase that makes possible a 0.1%-bandwidth two-resonator filter at this frequency. At higher frequency, the dependence on radius shown in (5.22) reduces the efficacy of gap scaling, but certainly does not negate it. In particular, for the 1.2 GHz disk of [30] a smaller gap of 18.5 nm would be needed to achieve a  $(C_x/C_o)$  of 0.1% for a 15V dc-bias voltage that would permit a 0.1%-bandwidth two-resonator filter. This gap is small, but not unreasonable for existing nanofabrication technologies.

Figure 5.13 plots  $(C_x/C_o)$  versus gap spacings below 100nm for radial-contour mode disks at various frequencies and dc-bias voltages. Interestingly, capacitive-gap transducers with gaps below 10 nm have potential to achieve  $(C_x/C_o) > 10\%$  at usable RF frequencies. Electromechanical coupling this high is actually not unheard of for capacitive-gap transducers. For example, the clamped-clamped beam resonators used in the HF filter of [31] posted  $(C_x/C_o)$ 's on the order of 14.8% at  $V_P = 35V$ .

It should be mentioned that adequate  $(C_x/C_o)$  does not guarantee an impedance match with the stages before and after the eventual filter using a given disk resonator. Unfortunately, the tiny size of a single disk relegates it to high impedance. Taking the example of a two-resonator Chebyshev

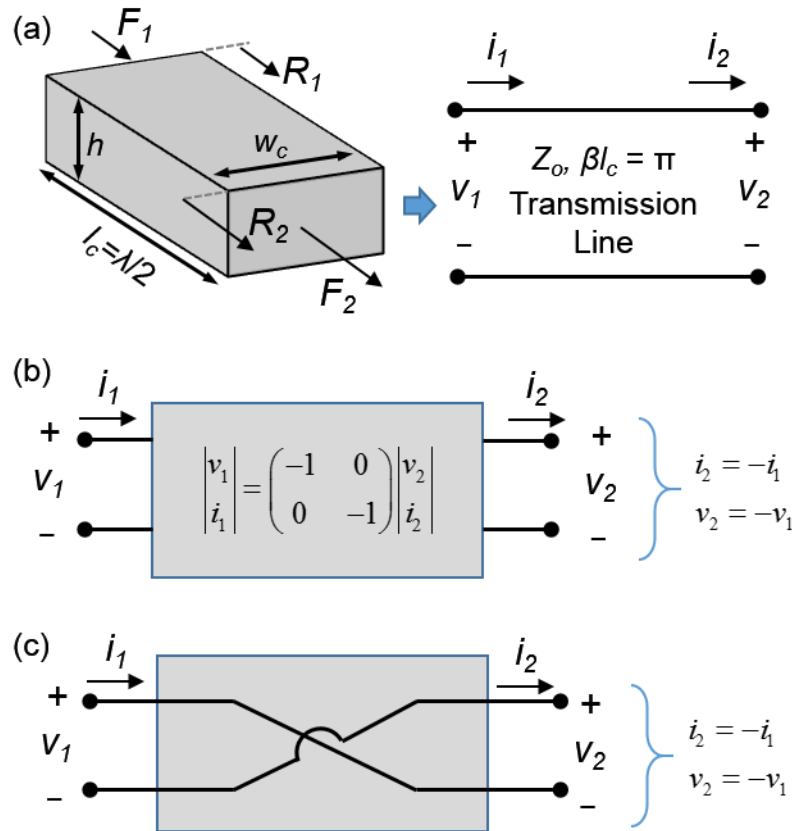


Figure 5.14: (a) Schematic view of a  $\lambda/2$  array coupling beam, and its acoustic transmission equivalent representation with acoustic impedance  $Z_o$  and electrical length  $\beta l_c = \pi$ . (b) ABCD matrix representation for the acoustic transmission line formed by the  $\lambda/2$  beam. (c) Electrical equivalent circuit representation of the  $\lambda/2$  beam.

filter with  $q_n = 1.9497$  [26] and  $Q/Q_f = 9.5$  for less than 2dB insertion loss, (5.7) predicts that a match to a  $50\Omega R_Q$  termination requires a motional resistance  $R_x$  of 12.9 k $\Omega$ ; and a match to 200 $\Omega$  requires that  $R_x$  be 51 k $\Omega$ . In this regard, the 163-MHz disk of the previous paragraph has an  $R_x$  of 11.8 k $\Omega$  for  $Q = 10,500$ ,  $h = 3 \mu\text{m}$ ,  $d_o = 80\text{nm}$ , and  $V_P = 14\text{V}$  as reported in [23]; while that of the 1.2-GHz disk [30] is 87.8 k $\Omega$  for  $Q = 12,050$ ,  $d_o = 90\text{nm}$ ,  $h = 3 \mu\text{m}$ , and  $V_P = 20 \text{V}$ ; both too large for a match to either 50 $\Omega$  or 200 $\Omega$ .

The solution: Arraying to further lower  $R_x$ .

## 5.8 Disk Array-Composite Design

Section 5.5 and Figure 5.2 described the strategy and utility of arraying  $N$  disk resonators to attain a combined output current  $N$  times larger than that of a single resonator for the same input voltage, i.e., a motional resistance  $N$  times smaller. Of course, the currents of the devices in an

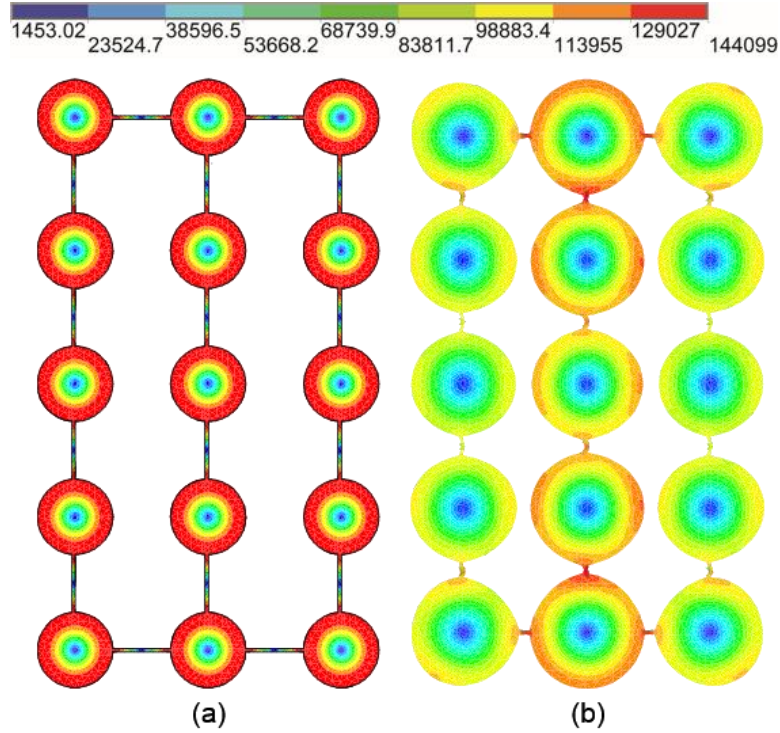


Figure 5.15: Finite element modal analysis result for a  $3 \times 5$  disk resonator array coupled with (a) ideal  $\lambda/2$  length beams, and (b) non-ideal  $0.6\lambda$  length beams with process variations. The color map legend indicates local mode shape displacement with arbitrary units.

array sum constructively only if all devices vibrate in phase and at the same frequency. To insure this, as depicted in Figure 5.11, the disks in the array are mechanically coupled by half-wavelength beams that effectively transform the array into a single multi-resonator composite device in which all constituent disks vibrate in unison at one mode frequency. Here, the use of half-wavelength coupling links ideally selects one desired mode and rejects all other possible modes. The result: An array-composite resonator with substantially lower impedance and greater power handling than a single one of its constituents.

The action of the half-wavelength extensional-mode coupling beams is perhaps best understood by closer inspection of the beam itself, depicted in Figure 5.14, and its defining chain matrix, which relates the force  $F$  and the velocity  $\dot{R}$  on both ends of the beam (cf. Figure 5.14(a)), taking the form [27]

$$\begin{bmatrix} F_1 \\ \dot{R}_1 \end{bmatrix} = \begin{bmatrix} \cos(\beta l_c) & jY_o \sin(\beta l_c) \\ jZ_o \sin(\beta l_c) & \cos(\beta l_c) \end{bmatrix} \begin{bmatrix} F_2 \\ \dot{R}_2 \end{bmatrix} \quad (5.28)$$

where  $Z_o$  and  $\beta$ , are the characteristic acoustic impedance and propagation constant, respectively, defined in terms of beam thickness  $h$ , beam width  $w_c$ , beam length  $l_c$ , and material properties  $E$  and  $\rho$  as

$$Y_o = \frac{1}{Z_o} = \frac{1}{hw_c \sqrt{\rho E}}, \quad \beta = \frac{\omega}{v_p}, \quad v_p = \sqrt{\frac{E}{\rho}} \quad (5.29)$$

where  $v_p$  is the acoustic velocity.

Considering the beam as a mechanical transmission line with acoustic wavelength  $\lambda$  at the desired vibration mode frequency defined as

$$\lambda = \frac{1}{f_o} \sqrt{\frac{E}{\rho}} \quad (5.30)$$

and setting the coupling beam length to half-wavelength,  $\beta l_c = \beta \lambda / 2 = \pi$  in (5.28), which then yields

$$\begin{aligned} \begin{bmatrix} F_1 \\ \dot{R}_1 \end{bmatrix} &= \begin{bmatrix} -1 & 0 \\ 0 & -1 \end{bmatrix} \begin{bmatrix} F_2 \\ \dot{R}_2 \end{bmatrix} \\ F_1 &= -F_2, \quad R_1 = -R_2 \end{aligned} \quad (5.31)$$

Equation (5.31) states that half-wavelength coupling enforces equal force and displacement amplitudes with opposite phases at the coupling beam ends. In other words, it forces the disks attached at the ends of the extensional coupling to vibrate in unison, i.e., with the same phase. From Figure 5.9 and the discussion of Section 5.4, this means it forces the highest frequency mode and rejects all other modes. Ideally, the in-phase mode would be the only one permissible under half-wavelength coupling. Figure 5.15(a) presents the FEA-simulated mode shape for a  $5 \times 3$  half-wavelength-coupled array showing identical contour-mode shapes for all resonators.

To lend more insight into the action of the half-wavelength beams, Figure 5.14(a) presents a schematic view of the  $\lambda/2$  coupling beam and its acoustic transmission line equivalent model for which (5.31) governs the force-to-displacement transfer function at the beam ends. Here, the direct electromechanical analogy [112] models the force and displacement applied on the ends of the beam as the voltages and currents, respectively, across the ports of the transmission line. It is important to note that the width of the  $\lambda/2$  beam does not affect its network properties defined by (5.31). Thus, the width of the  $\lambda/2$  couplers typically equals the minimum achievable critical dimension of the fabrication technology. A wider beam width would still mathematically satisfy (5.31), but would risk perturbing the vibration mode shape of the adjacent connected disks.

To provide a more visual circuit model, Figure 5.14(b) equates the  $\lambda/2$  beam to a two-port network using the ABCD matrix of (5.31), which then further simplifies to the electrical equivalent circuit of Figure 5.14(c). This cross-coupled circuit clearly shows that the  $\lambda/2$  beam acts to invert the phase of the motions at its ends, consistent with the previous discussion.

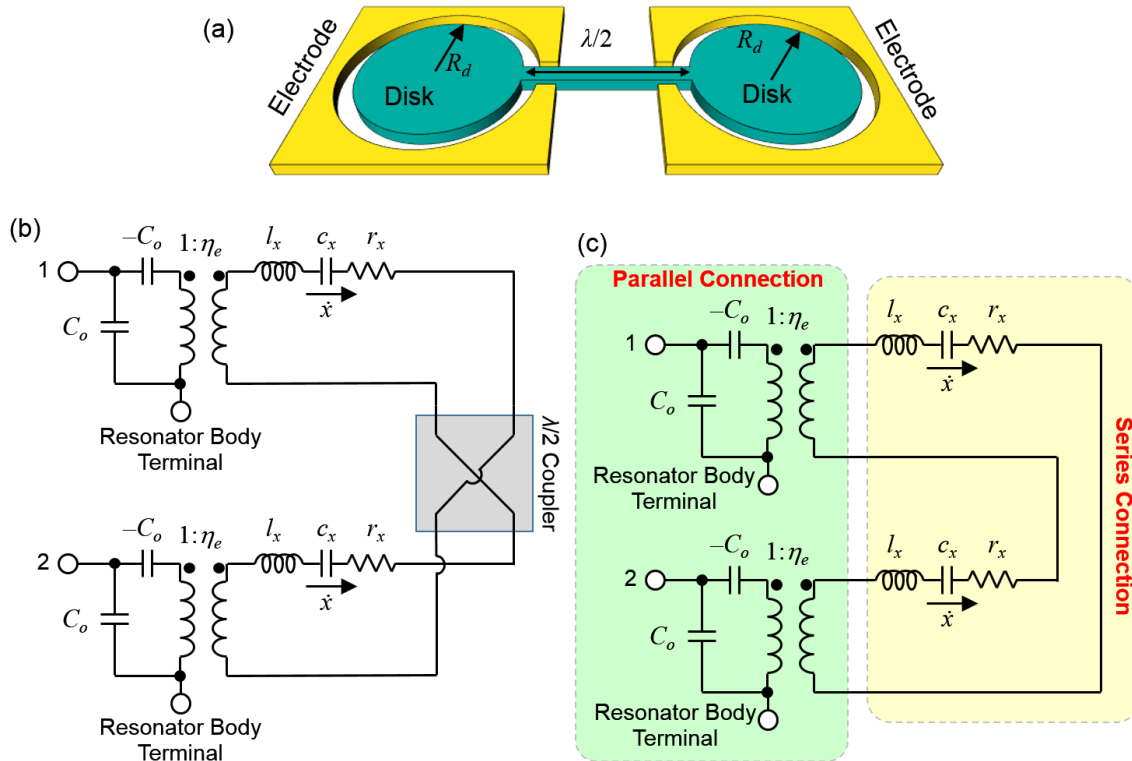


Figure 5.16: (a) Schematic view a two-resonator network coupled with a half-wavelength beam. (b) Electrical equivalent circuit representation of the two-resonator array-composite that combines the circuits presented in Figure 5.12 and Figure 5.14(c); and (c) the same circuit after re-drawing the element connections to identify the series and parallel connected sections.

### 5.8.1 Array-Composite Equivalent Circuit

The electrical equivalent circuit for the  $\lambda/2$ -coupled two-disk array-composite of Figure 5.16(a) results via simple combination of the electrical equivalent circuit representations of the  $\lambda/2$  beam presented in Figure 5.14(c) and the circuit model of a single disk resonator presented in Figure 5.12. Figure 5.16(b) does just this. Redrawing the circuit then yields the visually simpler version of Figure 5.16(c) that better elucidates the series and parallel connected components. Here, it is no surprise that the core  $lcr$  elements modeling the vibrating disks cascade in series, since  $\lambda/2$ -coupling forces the disks to vibrate in-phase with identical mode shapes. As a consequence, their dynamic stiffnesses, masses, and damping losses add linearly. Similarly, since the electrodes modeled by the transformers are in parallel, the forces exerted by the electrodes add cumulatively to generate a total combined force  $N_{ioe}$  times larger than that of a single electrode, where  $N_{ioe}$  is the number of driven input/output electrodes, each fully surrounding a disk.

Given these, the total effective equivalent circuit for an  $N$ -resonator  $\lambda/2$ -coupled array-composite becomes that presented in Figure 5.11, where expressions for the elements and turns ratio now take on the following forms:

$$\begin{aligned}\eta_{eA} &= N_{ioe} \times \eta_e \\ r_{xA} &= N \times r_x \\ l_{xA} &= N \times l_x \\ c_{xA} &= \frac{1}{N} \times c_x\end{aligned}\quad (5.32)$$

where  $\eta_{eA}$  is the electromechanical coupling coefficient at the array-composites input-output electrode. Similarly,  $r_{xA}$ ,  $l_{xA}$ , and  $c_{xA}$  represent the core- $lcr$  values that model the equivalent damping, dynamic mass, and inverse dynamic stiffness of the array-composite, respectively.

### 5.8.2 Array-Composite Motional Resistance

With electrodes in parallel and all disks vibrating in unison, the currents flowing into the electrodes now add in phase, allowing for a total current  $N_{ioe}$  times that of a single electrode fully surrounding a single disk. Since the current increases for the same input voltage, the motional resistance of the structure decreases to

$$R_{xA} = \frac{N}{N_{ioe}^2} R_x \quad (5.33)$$

where  $R_{xA}$  and  $R_x$  represent the motional resistance of the array-composite and a single disk resonator, respectively. The corresponding expression for the filter termination resistance follows from inserting (5.33) in (5.7) as

$$R_Q = \left( \frac{Q}{q_i Q_f} - 1 \right) \frac{N}{N_{ioe}^2} R_x \cong \frac{Q}{q_i Q_f} \frac{N}{N_{ioe}^2} \frac{r_x}{\eta_e^2} \quad (5.34)$$

where rewriting single resonator's damping term  $r_x$  in terms of the resonator  $Q$ , dynamic mass  $l_x$ , and electromechanical coupling coefficient  $\eta_e$  leads to

$$R_Q = \frac{1}{Q_f} \frac{N}{N_{ioe}^2} \frac{2\pi f_o l_x}{q_i \eta_e^2} \quad (5.35)$$

Rewriting the  $l_x$  and  $\eta_e$  terms in (5.35) in terms of the fundamental design variables yields

$$R_Q = \frac{f_o}{Q_f} \frac{N}{N_{ioe}^2} \frac{d_o^4}{V_P^2} \frac{2\pi^2 \chi \rho}{q_i h \epsilon_o^2 \theta_{ov}^2} \quad (5.36)$$

The right-hand-most form of (5.34) addresses the specific case where the filter insertion loss is low, i.e., the resonator  $Q$  much larger than the filter  $Q_f$ . In this case, the value of  $R_Q$  is independent

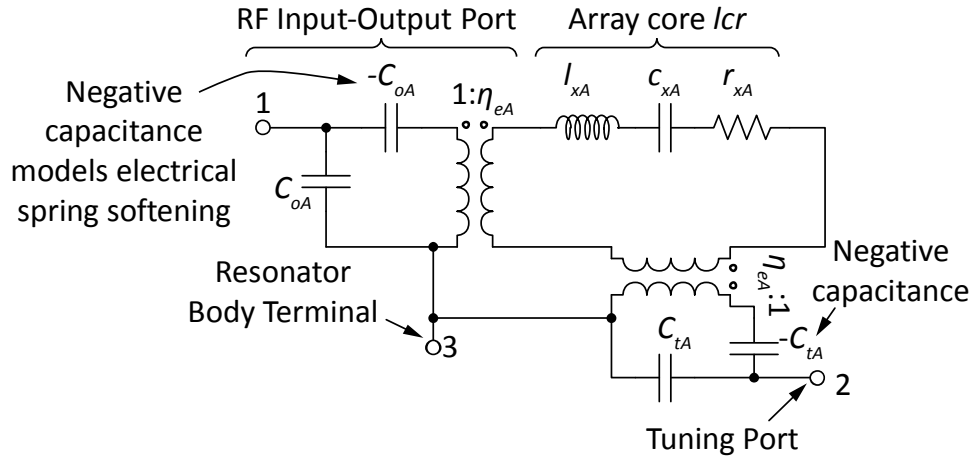


Figure 5.17: Electrical equivalent circuit of an array-composite resonator with RF input-output and electrical stiffness tuning ports.

of the unloaded resonator  $Q$ , and the best knobs to use to specify its value become the electrode-to-resonator gap spacing  $d_o$  (with a 4<sup>th</sup> power dependence) and the dc-bias voltage  $V_P$  (with a square-law dependence).

Taking as an example the 433-MHz disk resonator of Section 5.4, a single polysilicon disk resonating at 433 MHz with  $Q$  of 20,000, 80nm gaps, 15V dc-bias, thickness  $h = 3\mu\text{m}$ , and fully surrounding electrodes, i.e.  $\theta_{ov} = 2\pi$  would exhibit a motional resistance  $R_x$  of 14.7 k $\Omega$ , which is much too high to match to adjacent stages in a receiver. In contrast, combination of 90 resonators into a disk array-composite, as in Figure 5.11, allows summation of output currents towards a motional resistance of now only 163  $\Omega$ . For a three-resonator Chebyshev filter with 0.1% percent bandwidth, (5.36) sets the required termination resistance at 1.9 k $\Omega$ . Fig. 17 plots termination resistance  $R_Q$  versus number of 433-MHz based resonators in the array-composite for two different gap spacing examples of 80nm and 40nm, showing the ease by which this method specifies the filter termination resistance.

### 5.8.3 Array-Composite Power Handling

In addition to motional resistance, the power handling of an array-composite improves over that of a single constituent resonator. This is obvious, given that the current is now distributed among  $N_{ioe}$  devices, so any detrimental effects, e.g., heating, are lessened by approximately the factor  $N_{ioe}$ .

Third-order intermodulation distortion is often a good gauge for the largest input power acceptable to a given circuit element or system block. For practical applications, the third-order intermodulation intercept point  $IIP_3$ , defined as the input power at which the output powers due to an input at the carrier frequency and at two frequencies equally spaced from it are equal, is a good



metric for device or circuit linearity. [56] already developed an expression governing the  $IIP_3$  of a radial-contour mode disk resonator, repeated here for convenience as follows:

$$\begin{aligned}
 P_{V^2X} &= \frac{2\omega_o Q V_p^2 \epsilon_o A_o}{d_o [2\Theta_1 + \Theta_2]} \\
 P_{VX^2} &= \frac{2}{3} \frac{\omega_o Q d_o^2 k_{re}}{\Theta_1 [\Theta_1 + 2\Theta_2]} \\
 P_{X^3} &= \frac{\omega_o Q d_o^5 k_{re}^2}{3\epsilon_o A_o V_p^2 \Theta_1^2 2\Theta_2}
 \end{aligned} \tag{5.37}$$

where  $A_o$  is the electrode-to-resonator overlap area of a single disk resonator.  $\Theta_1$  and  $\Theta_2$  model the degree to which the resonator's amplitude transfer function attenuates the blocker input tones. Here, the  $P_{V^2X}$  and  $P_{VX^2}$  terms emanate from nonlinear voltage and displacement interactions, and the  $P_{X^3}$  term derives from purely nonlinear displacement interactions. The parallel combination of these three resonator non-linearity sources yield the final compact  $IIP_3$  power expression

$$P_{IIP_3} = P_{V^2X} \parallel P_{VX^2} \parallel P_{X^3} \tag{5.38}$$

It is important to observe that all of the three terms in (5.37) are linearly proportional to the array size  $N$ , i.e.

$$\begin{aligned}
 P_{V^2X}^{Array} &= N \times P_{V^2X} = \frac{2\omega_o Q V_p^2 \epsilon_o N A_o}{d_o [2\Theta_1 + \Theta_2]} \\
 P_{VX^2}^{Array} &= N \times P_{VX^2} = \frac{2}{3} \frac{\omega_o Q d_o^2 N k_{re}}{\Theta_1 [\Theta_1 + 2\Theta_2]} \\
 P_{X^3}^{Array} &= N \times P_{X^3} = \frac{\omega_o Q d_o^5 N k_{re}^2}{3\epsilon_o A_o V_p^2 \Theta_1^2 2\Theta_2}
 \end{aligned} \tag{5.39}$$

As a result, for the case of  $N$  mechanically coupled resonators, (5.39) leads to

$$P_{IIP_3}^{Array} = N \times P_{IIP_3} \tag{5.40}$$

where clearly  $IIP_3$  improves with the number of resonators  $N$ .

#### 5.8.4 Array-Based Mechanical Impedance Tailoring

It should be noted that coupling all resonators in this way does more than merely add currents to lower motional impedance and raise power handling. In fact, one of the most useful characteristics of an array-composite for filter design is the degree to which the impedance presented to an electrical or mechanical input/output port can be tailored. Indeed, for filter design purposes, the ability to tailor the impedance presented to an attached coupling beam is instrumental to bandwidth specification.

The amount of impedance tailoring available is readily apparent when determining the impedance seen into one port in the array-composite equivalent circuit of Figure 5.16(c) with the other port grounded. In particular, grounding port 2 yields the circuit of Figure 5.17, where port 1 essentially couples to an effective resonator with mass, stiffness, and damping values all twice as large as that of a single resonator. This means the resistance looking into the electrode is twice as large as that of a single disk. In addition, the stiffness presented to a mechanical structure, e.g., a coupling beam, attached to the left-side disk's edge is twice as large as that of a single disk resonator. It is easy to see that if there were  $N$  disk resonators in the composite array, then the resistance or stiffness would be  $N$  times larger. Thus, the number of resonators  $N$  used in a mechanically coupled array-composite acts as a knob to control the electrical or mechanical impedance presented by any of its resonators.

As will be seen, the dynamic stiffness presented at a coupling location very much controls the specific bandwidth of a given filter design. The ability to raise the presented stiffness by arraying equates to an ability to achieve a smaller percent bandwidth filter, such as needed for RF channel-selection.

### 5.8.5 Non-I/O Disks

The disks beyond those used for input/output, shown in Fig. 2, alleviate practical issues caused by finite fabrication tolerances that introduce device mismatch; and fabrication stress that can debilitate a large mechanical circuit like that of Fig. 2. These extra disks add to the total disk count in an array-composite, so further raise the impedance seen into each individual disk (either electrically or mechanically). As will be seen next, they also lower the effective electromechanical coupling of a disk array-composite.

## 5.9 Minimum Electromechanical Coupling Strength for the Chosen Bandwidth

Although array size strongly influences the impedance presented by the combined array-composite input terminal, it does not raise the electromechanical coupling strength, gauged by the ratio of motional-to-static input capacitance ( $C_{xA}/C_{oA}$ ). For the case where all disks possess I/O electrodes and all electrodes are hooked in parallel, i.e.  $N = N_{ioe}$ , ( $C_{xA}/C_{oA}$ ) follows readily by simply taking the ratio of

$$C_{xA} = N_{ioe}^2 \mathcal{N}_e^2 \frac{C_{xA}}{N} = \frac{N_{ioe}^2 V_P^2}{N} \frac{h(\epsilon_o R \theta_{ov})^2}{d_o^4 \pi^3 \chi K_{mat}^2 E} \quad (5.41)$$

and

$$C_{oA} = N_{ioe} C_o = N_{ioe} \frac{\varepsilon_o R \theta_{ov} h}{d_o} \quad (5.42)$$

, which yields

$$\frac{C_{xA}}{C_{oA}} = \frac{V_P^2}{d_o^3} \frac{\varepsilon_o R \theta_{ov}}{\pi^3 \chi K_{mat}^2 E} \quad (5.43)$$

Here,  $(C_{xA}/C_{oA})$  does not change with the number of I/O disks.

If, on the other hand, non-I/O disks are included, as described in Section 5.8.5, the expression for electromechanical coupling strength becomes

$$\frac{C_{xA}}{C_{oA}} = \frac{N_{ioe}}{N} \frac{V_P^2}{d_o^3} \frac{\varepsilon_o R \theta_{ov}}{\pi^3 \chi K_{mat}^2 E} \quad (5.44)$$

where  $N$  is the total number of mechanically coupled disks that include both the I/O and non-I/O disks, therefore  $N_{ioe}/N$  term in (5.44) is always less than one. In either (5.43) or (5.44), the only free variables are  $V_P$  and  $d_o$ , as the rest are fixed by the chosen center frequency  $f_o$ . Also, note that (5.43) does not depend on array size. This means that for a given filter design adequate electromechanical coupling  $(C_{xA}/C_{oA})$  to meet the requirement of (5.3) must be insured via proper choice of dc-bias  $V_P$  and electrode-to-resonator gap  $d_o$  scaling [35].

To gauge how the minimum  $C_{xA}/C_{oA}$  required to avoid passband distortion for a given filter bandwidth  $B$  scales with frequency, one can use (5.36) and (5.44) to rewrite (5.3) as

$$B \cdot \left( \frac{V_P^2}{d_o^3} \right) \cdot \left( \frac{q_i \varepsilon_o \theta_{ov} N_{ioe}}{2\pi^3 \chi K_{mat} N \sqrt{E\rho}} \right) > \xi \quad (5.45)$$

The terms in the rightmost parentheses in (5.45) are filter design constants, which leaves the bias voltage  $V_P$  and the capacitive actuation gap spacing  $d_o$  are the primary design knobs to satisfy (5.45) for a given  $B$ . It is important to observe that (5.45) is independent of the disk radius, i.e. the filter center frequency  $f_o$ . Therefore, the  $C_{xA}/C_{oA}$ , and thus the directly related capacitive actuation gap  $d_o$  and bias voltage  $V_P$ , remains constant over frequency for the desired filter bandwidth  $B$ .

## 5.10 Filter Passband Specification

Section 5.4 described how mechanical coupling of two identical single disk resonators, or more preferably identical array-composites that behave as single disks with reduced  $R_x$ , creates a two degree of freedom system with two closely spaced modes that constitute the filter passband, as described in Figure 5.9. A more explicit expression for the bandwidth of the filter follows from

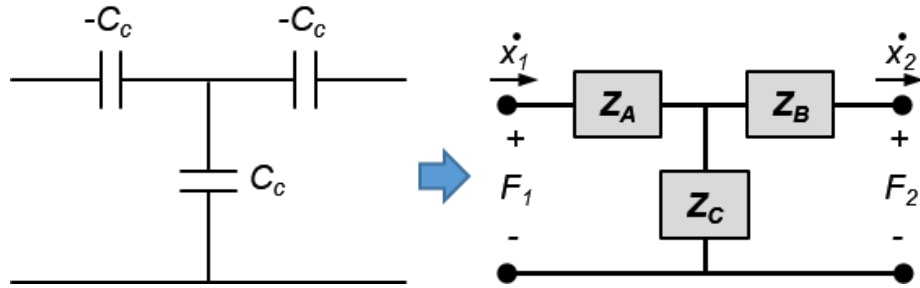


Figure 5.18: Transmission line model equivalent of the  $\lambda/4$  beam electrical equivalent circuit.

(5.10), which accounting for the stiffness transformation afforded by arraying described by (5.32), yields

$$B = \frac{k_{c,ij}}{k_{reA}} \frac{f_o}{k_{ij}} = \frac{k_{c,ij}}{k_{re}} \frac{f_o}{Nk_{ij}} \quad (5.46)$$

While any coupling beam length can be chosen to provide the dynamic stiffness  $k_{c,ij}$  for the required filter bandwidth in (5.46), beams with lengths matching odd multiples of the quarter-wavelength, i.e.  $\lambda/4$ , form a special case where the derivative of the dynamic stiffness of the beam with respect to the beam length becomes zero [27]. Therefore,  $\lambda/4$  filter coupling beams minimize the sensitivity of the filter bandwidth to process variations in beam length.

### 5.10.1 Electrical Equivalent Circuit of $\lambda/4$ Coupling Beams

As described in Section 5.8.1, the characteristics of a small cross-section coupling beam vibrating in extensional mode are similar to the behavior of an electrical transmission line, and can be described in ABCD matrix form by (5.28). The special case of quarter-wavelength filter coupling beams with  $l_c = \lambda/4$  sets the electrical length of the transmission line equivalent representation of the beam as  $\beta l = \pi/2$  in (5.28), which then yields the ABCD matrix expression for a  $\lambda/4$  coupling beam as

$$\begin{bmatrix} F_1 \\ \dot{R}_1 \end{bmatrix} = \begin{bmatrix} 0 & jY_o \\ jZ_o & 0 \end{bmatrix} \begin{bmatrix} F_2 \\ \dot{R}_2 \end{bmatrix} \quad (5.47)$$

Here, the  $\lambda/4$  coupling beam acts as an impedance inverter commonly used in ladder filter design [113].

As introduced in 5.4, a T-network of capacitors, as shown in Figure 5.9, captures the electrical equivalent lumped circuit model of the  $\lambda/4$  coupling beam. Figure 5.18 presents the transmission line representation of this T-network of capacitors, where the terms  $Z_A$ ,  $Z_B$ , and  $Z_C$  model the series

and shunt arm impedances. Equating the ABCD matrices of the circuit presented in Figure 5.18 [113] and (5.47) leads to

$$\frac{1}{Z_c} = jZ_o \rightarrow j\omega_o c_c = jh\omega_c \sqrt{\rho E} \quad (5.48)$$

; which yields the expression for the dynamic stiffness of the  $\lambda/4$  filter coupling beam, denoted as  $k_c$ , in terms of the beam dimensions as

$$k_c = \frac{1}{c_c} = \frac{\pi E}{2} \frac{hw_c}{l_c} \quad (5.49)$$

where  $w_c$  is the width of the coupling beam, and  $l_c$  is the beam length that may equal any odd multiple of  $\lambda/4$ .

### 5.10.2 $\lambda/4$ Coupling Beam Width & Array Size

Inserting (5.30) and (5.49) in (5.46) provides the filter band-width expression in terms of fundamental device geometry and material properties given by

$$B = \frac{w_c}{N} \left( f_o^2 \frac{2}{\pi^2 K_{mat}^2 \chi k_{ij}} \sqrt{\frac{\rho}{E}} \right) \quad (5.50)$$

The only free variables to set the filter bandwidth  $B$  in (5.50) are the  $\lambda/4$  beam width  $w_c$  and the array size  $N$ , where the remaining terms given in the parentheses are fixed by other filter specifications.

It is important to observe from (5.50) that very small bandwidths may require excessively narrow beam widths, especially if the array-composite design approach is not used, i.e.  $N = 1$ . The array-composite resonators allow the designer to keep  $w_c$  wider than the critical dimension  $w_{c,min}$  that can be reliably manufactured by the available micro-fabrication techniques as described by

$$w_c = N \left( \frac{B}{f_o} \right) \frac{\pi^2 K_{mat}^2 \chi k_{ij}}{2 f_o} \sqrt{\frac{\rho}{E}} > w_{c,min} \quad (5.51)$$

Taking as an example the 433-MHz disk resonator of Section 5.8, using single polysilicon disk resonators to form a second order Chebyshev filter not only requires an impractically high termination resistance exceeding 10 k $\Omega$ , but also requires an unfeasibly narrow  $\lambda/4$  coupling beam width of 22nm with  $N = 1$  in (5.51). Here, increasing the array size to  $N = 50$  adjusts the beam width to  $w_c = 1.1\mu\text{m}$  that can now be reliably etched into 3 $\mu\text{m}$  polysilicon using DRIE, with the added benefit of low sub-1k $\Omega$  filter termination resistances.

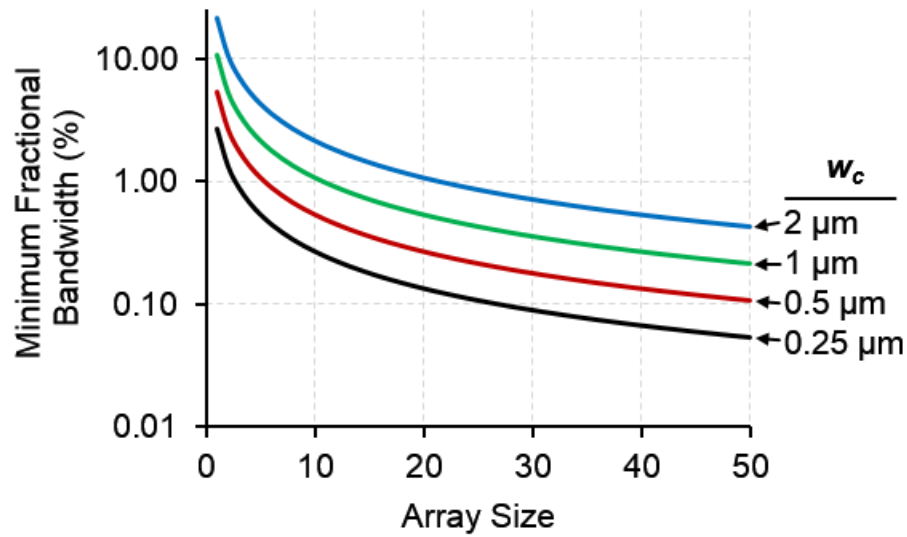


Figure 5.19: Simulated curves of minimum achievable fractional bandwidth as a function of array size for different minimum coupling beam widths for a 2<sup>nd</sup> order Chebyshev filter operating at 1 GHz fabricated using polysilicon.

Equation (5.51) indicates that filters with very small fractional bandwidth  $P_{BW} = B/f_o$ , such as the RF channel-select filters at the focus of this work, must have their array size  $N$  greater than a minimum number  $N_{min}$  set by  $w_{c,min}$  according to

$$N \geq N_{min} = \frac{w_{c,min}}{P_{BW}} \frac{2f_o}{\pi^2 K_{mat}^2 \chi k_{ij}} \sqrt{\frac{E}{\rho}} \quad (5.52)$$

regardless of other filter specifications such as filter termination resistance or layout area. Figure 5.19 plots the minimum achievable fractional bandwidth  $P_{BW}$  for a 2<sup>nd</sup> order Chebyshev filter operating at 1 GHz fabricated using polysilicon for different minimum filter coupling beam widths via (5.52). These curves demonstrate the wide fractional filter bandwidth range achievable by mechanically coupled disk filters, where larger array sizes enable smaller fractional bandwidths desired for channel-select applications.

The large  $\lambda/2$  coupled array sizes indicated in Figure 5.19 may raise area and cost concerns; however, the disks that form the array have tiny dimensions that scale inversely proportional to frequency. For example, a 0.1% fractional bandwidth 2<sup>nd</sup> order filter operating at 1 GHz with 0.25 $\mu$ m wide coupling beams requires  $N=25$   $\lambda/2$  coupled resonators per array-composite. As illustrated in Figure 5.2, a second order differential filter comprises four array-composites, which in this case leads to  $N=25$  resonators in each quadrant. This 100-coupled disk resonator circuit would consume only 110 $\mu$ m  $\times$  110 $\mu$ m die area (assuming electrode routing is done in another layer as in CMOS), where each disk has a diameter of only 5.4 $\mu$ m. To put this tiny footprint in perspective,

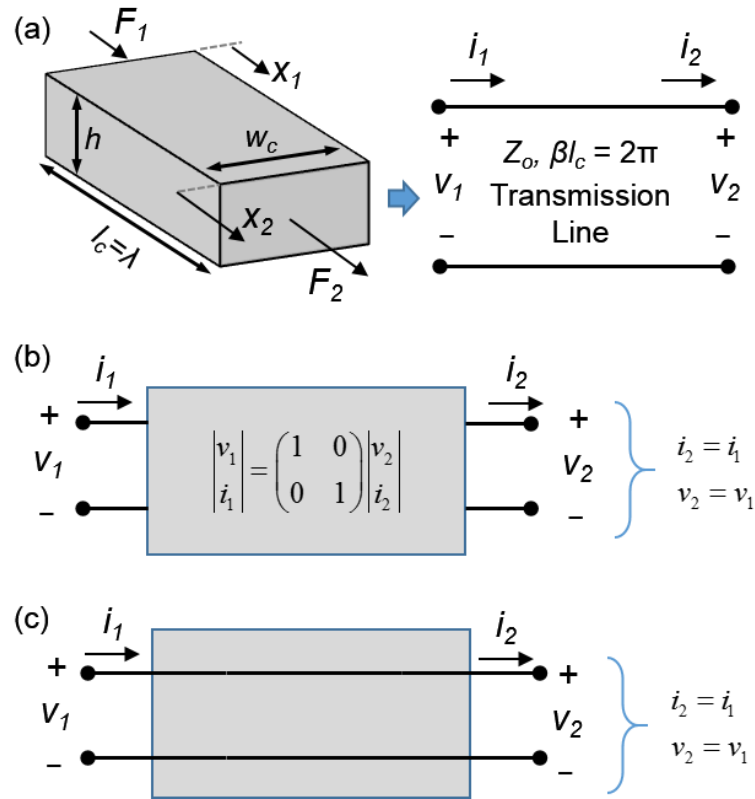


Figure 5.20: (a) Schematic view of a  $\lambda$  array coupling beam, and its acoustic transmission equivalent representation with acoustic impedance  $Z_o$  and electrical length  $\beta l_c = 2\pi$ . (b) ABCD matrix representation for the acoustic transmission line formed by the  $\lambda$  beam. (c) Electrical equivalent circuit representation of the  $\lambda$  beam.

one can amass 2025 similar filters in a  $5\text{mm} \times 5\text{mm}$  chip towards devising a low cost, programmable mode-selectable RF channelizing filter bank for a communication standards agnostic receiver front-end.

## 5.11 Differential Mechanical Design

Differential filters with electrically and mechanically symmetric drive and sense has two advantages over their single-ended counterparts:

- 1) Spurious modes close to the filter center frequency that stem from the non-idealities of the complex mechanical circuit get suppressed [23].
- 2) Feedthrough currents flowing through the parasitic capacitors formed by the electrode-disk overlap and the substrate cancel since they are common-mode signals.

Much like differential transistor pair design, creating the micromechanical resonator circuit in two symmetric halves in the mechanical domain that are forced to resonate at the same vibration

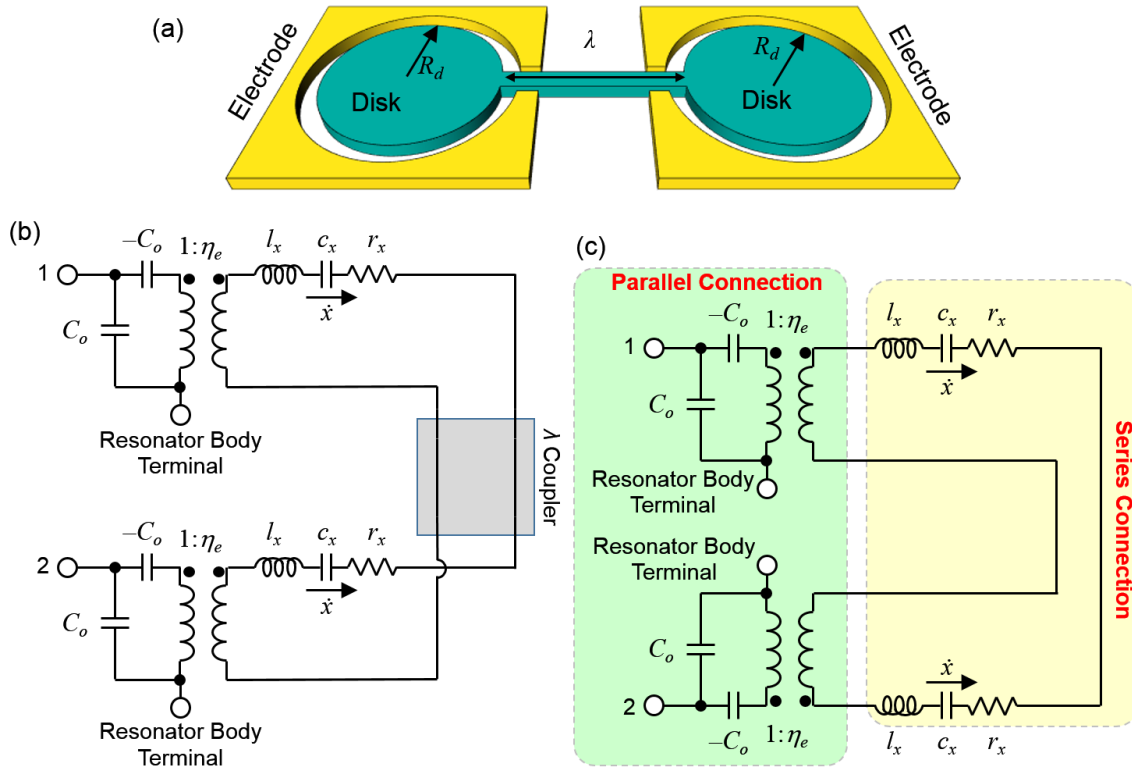


Figure 5.21: (a) Schematic view a two-resonator network coupled with a full-wavelength beam. (b) Electrical equivalent circuit representation of the two-resonator differential array-composite that combines the circuits presented in Figure 5.12 and Figure 5.20 (c); and (c) the same circuit after re-drawing the element connections to identify the series and parallel connected sections.

frequency but  $180^\circ$  out of phase yields the desired differential operation. Similar to the analysis presented in Section 5.8.1 for  $\lambda/2$  beams that enforce in-phase vibration, the electrical transmission line analogy outlined by (5.28) also enables coupling beams that enforce differential vibration. Here, setting the beam length  $l_c$  to the full wavelength  $\lambda$  so that the electrical length becomes  $\beta l_c = \beta \lambda = 2\pi$  yields the ABCD matrix given by

$$\begin{bmatrix} F_1 \\ \dot{R}_1 \end{bmatrix} = \begin{bmatrix} 1 & 0 \\ 0 & 1 \end{bmatrix} \begin{bmatrix} F_2 \\ \dot{R}_2 \end{bmatrix} \quad (5.53)$$

$$F_1 = F_2, \quad R_1 = R_2$$

The  $R_1 = R_2$  condition in (5.53) is only possible when one of the coupled disks contract while the other expands to keep the displacement magnitude and direction on both ends of the coupling beam identical. As a result, the  $\lambda$ -coupled disks assume the same vibration frequency but out-of-phase displacement.



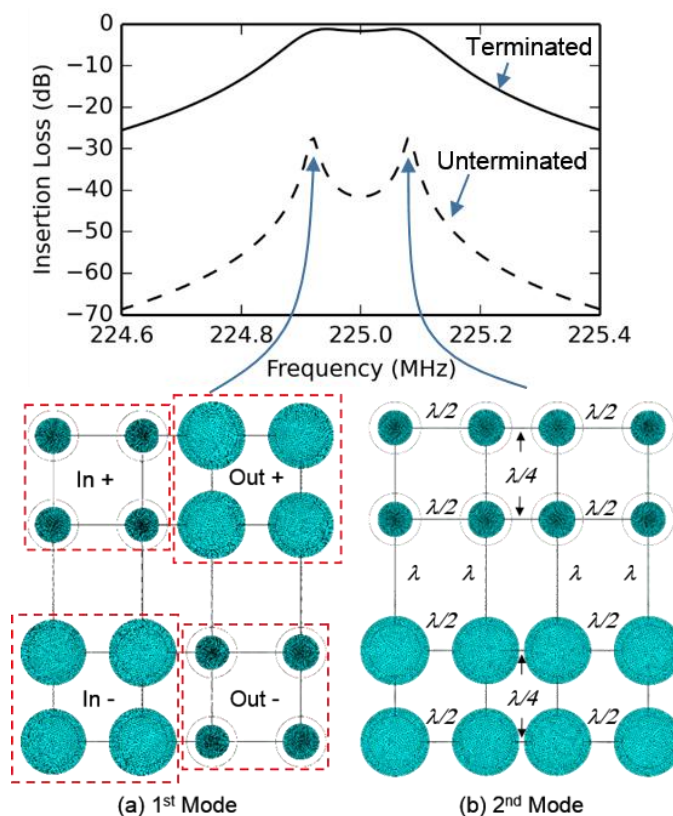


Figure 5.22: FEA simulation of mode shapes of disk resonators coupled with various wavelength optimized coupling beams where  $\lambda$ -coupling enforces differential vibration of upper and lower halves, and  $\lambda/4$  beams realize (a) out-of-phase (lower frequency) and (b) in-phase (higher frequency) filter modes.

Similar to Figure 5.14 that explains the in-phase  $\lambda/2$  coupler model, Figure 5.20 illustrates the equivalent circuit model for the full-wavelength differential coupler. Here, the width of the  $\lambda$  differential coupler does not change its network properties at resonance, much like the  $\lambda/2$  coupler, and typically equals the minimum critical dimension to avoid loading the disk resonators by unnecessarily wide coupling beams.

Figure 5.21 illustrates the electrical equivalent circuit for a  $\lambda$ -coupled differential disk pair, which follows from the inspection of the equivalent circuit of a single disk resonator given by Figure 5.12 and the circuit model for the  $\lambda$  coupler given by Figure 5.20(c). Similar to the  $\lambda/2$  coupled case presented in Figure 5.16(c), the core-*lcr* circuits of the  $\lambda$ -coupled disks add in series. However, in contrast to the  $\lambda/2$  coupled case, the electrodes of the  $\lambda$ -coupled pair combine in parallel with differential polarity. Therefore, the electrodes must be driven differentially, i.e. with  $180^\circ$  phase difference relative to each other, to avoid cancelling the motional currents generated by the individual disks.

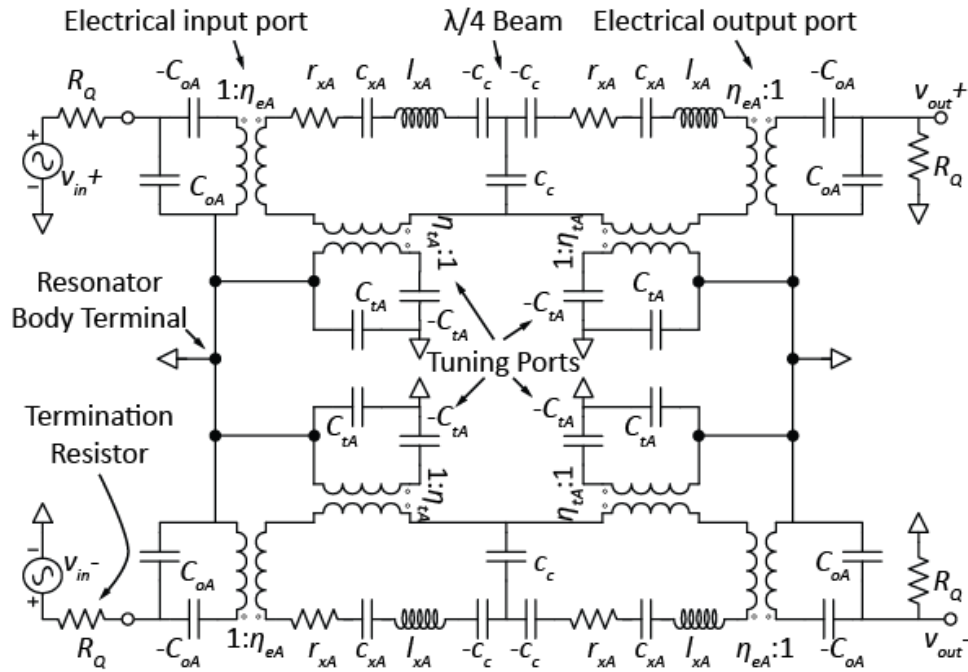


Figure 5.23: Electrical equivalent circuit for a 2<sup>nd</sup> order differential filter.

### 5.11.1 Differential Filter Structure Design Summary

To visually convey how the overall differential filter structure functions, Figure 5.22 presents the expected properly terminated filter frequency response for a simplified 4-disk-array version of this design, with dotted lines to show its unterminated response, and with FEA-simulated vibration mode shapes corresponding to each peak of the response. Here, the  $\lambda/2$  beams facilitate the first level of hierarchy by combining four disk resonators in each quadrant to create array-composites that act as a single disk, but with  $4\times$  less  $R_x$ . Then,  $\lambda$ -coupling of the array-composites in the upper and lower halves of the mechanical circuit enforces an out-of-phase motion to enable differential actuation of the filter. Finally, the mode that actuates the quarter-wave coupling springs the least generates the low frequency peak, cf. Figure 5.22(a); while the mode that flexes these couplers the most specifies the high frequency one, cf. Figure 5.22(b). When the filter is terminated, loading of the resonators widens their frequency response spectra, allowing them to add constructively between peaks and subtract outside, yielding the desired filter response.

## 5.12 Filter Electrical Equivalent Circuit Model

Much like their transistor circuit counterparts, the design of micromechanical circuits benefits immensely from behavioral models that capture their electrical response in SPICE [42]. To this end, previous sections employed electromechanical analogies to capture the functionality added

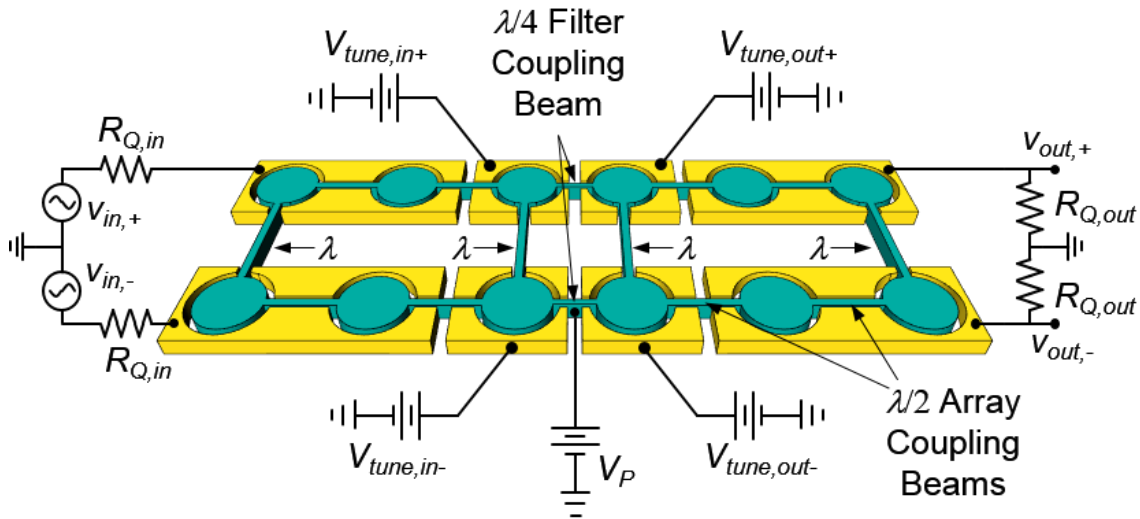


Figure 5.24: Schematic description of a 2<sup>nd</sup> order differential filter.

by each level of hierarchy. The overall filter equivalent circuit combines these sub-circuits as modules and accurately captures the filter electrical behavior for arbitrary termination impedances.

Figure 5.23 presents the electrical equivalent circuit for a 2<sup>nd</sup> order differential filter, such as the one schematically illustrated in Figure 5.24. Here, the three resonators coupled with  $\lambda/2$  array coupling beams in each quadrant of Figure 5.24 resonate in-phase to act as a single array-composite resonator, and thus can be modeled by the circuit of Figure 5.17. Next,  $\lambda/4$  filter coupling beams couple the two array-composites to form the two poles of the 2<sup>nd</sup> order filter network, as represented by the T-network of capacitors illustrated in Figure 5.18 combining the equivalent circuit model of the two array-composites. Finally,  $\lambda$  differential coupling beams force the upper and lower symmetric halves of the mechanical network to oscillate out-of-phase, as captured by the electrically balanced differential drive and sense for the symmetric upper and lower half-circuits presented in Figure 5.23.

### 5.13 Summary of Filter Design Procedure and Equations

Table 5-I presents the equations in a design flow that achieves the desired filter response with a specific center frequency, bandwidth, and filter termination resistance. These equations generate specific values for all mechanical geometry variables necessary for the filter layout, such as disk radii, and beam widths; and process design variables such as resonator material thickness and capacitive actuation gap spacing. In addition, Table 5-I provides the values for all the elements in the small-signal equivalent circuit of Figure 5.23 that enables SPICE simulated design verification.

Table 5-II: 2<sup>nd</sup> Order Differential Chebyshev Polysilicon Vibrating Disk Filter Design  
Examples Assuming  $V_P = 15V$ ,  $h = 3\mu\text{m}$ , and  $w_{c,min} = 0.25\mu\text{m}$

Filter Specifications			Calculated Design Variables									
$f_o$ (MHz)	$B$ (kHz)	$IL$ (dB)	Minimum Required $Q$	$C_x/C_o$ (%)	$d_o$ (nm)	$R_Q$ ( $\Omega$ )	$R$ ( $\mu\text{m}$ )	$\lambda/4$ ( $\mu\text{m}$ )	$w_c$ ( $\mu\text{m}$ )	$N$	Area ( $\mu\text{m} \times \mu\text{m}$ )	Area ( $\text{mm}^2$ )
10	30	2	3,250	3.32	40	522	270.9	207.1	2.9	1	1300×1920	2.496
30	30	2	9,500	1.11	40	377	90.3	69.0	0.3	1	640×435	0.278
50	30	2	16,000	0.66	40	174	54.2	41.4	0.35	3	1035×390	0.404
100	30	2	32,000	0.33	40	59	27.1	20.7	0.26	9	520×575	0.299
250	250	2	9,500	0.19	35	318	10.8	8.3	0.31	8	285×155	0.044
433	250	2	16,500	0.08	40	240	6.3	4.8	0.26	20	210×180	0.038
433	500	2	8,200	0.11	35	506	6.3	4.8	0.26	10	210×90	0.019
900	250	2	34,000	0.04	40	52	3.0	2.3	0.25	84	295×130	0.038
900	500	2	17,000	0.06	30	95	3.0	2.3	0.25	42	145×130	0.019
900	1000	2	8,500	0.15	30	125	3.0	2.3	0.25	21	145×65	0.009
1200	1000	2	11,500	0.11	25	63	2.3	1.7	0.28	42	110×100	0.011
1800	250	2	68,500	0.02	40	15	1.5	1.2	0.25	340	210×185	0.039
1800	500	2	34,500	0.04	30	16	1.5	1.2	0.25	170	180×110	0.020
1800	1000	2	17,500	0.08	25	32	1.5	1.2	0.25	85	180×55	0.010
2400	1000	2	23,000	0.06	25	18	1.1	0.9	0.25	150	120×80	0.010
3000	1000	2	28,500	0.05	25	12	0.9	0.7	0.25	230	150×65	0.010

### 5.13.1 Filter Design Examples

Table 5-II presents example designs for various 2<sup>nd</sup> order Chebyshev differential filters with center frequencies ranging between 10 MHz to 3 GHz. The columns grouped under the ‘filter specifications’ section of Table 5-II specify the filter center frequency and bandwidth as design objectives. Then, following the filter design procedure outlined in the previous sections, which Table 5-I neatly summarizes, yields the values for the design variables listed under the ‘Calculated Design Variables’ section of Table 5-II that satisfy the corresponding filter specifications. All designs use 3 $\mu\text{m}$  thick polysilicon as the disk resonator structural material, and assume a dc-bias voltage  $V_P = 15V$  and minimum resolvable coupling beam width of  $w_{c,min} = 0.25\mu\text{m}$ .

Table 5-II illustrates the one-to-one relation between the communication standard requirements that typically trans-late to a filter spectral mask, and the geometrical dimensions of the final on-silicon filter product. A key advantage of the filter design procedure of this paper is that the lateral dimensions (instead of the thickness) of the surface micromachined elements specify the associated filter de-sign variables such as the center frequency and the band-width, and the corresponding electrical equivalent circuit variable values. Therefore, the whole structure is amenable to automatic generation by a CAD program [10]. Such a program could also generate the layout required to achieve a specific filter response, making the realization of a VLSI circuit of such filters as convenient as it is for transistor IC design.

As Table 5-II demonstrates, the capacitive actuated vibrating disk filter technology can adapt to challenging filter specifications over a wide frequency range by adjusting its numerous design

knobs, such as the gap spacing and array size. Table 5-II makes it clear that the combination of capacitive actuation gap scaling and the array-composite design is key towards achieving RF channel-selection at 1GHz and beyond with a small area footprint. The design examples dispel various doubts about feasibility of such filters, e.g. layout area of arrays as large as  $N = 230$  disks, where the total filter area at 3 GHz can be as small as  $0.01\text{mm}^2$ ; in other words, 2500 of such filters in a  $5\text{mm}\times 5\text{mm}$  chip.

## 5.14 Conclusion

This chapter introduced a design flow for micromechanical RF channel-select filters capable of eliminating strong adjacent channel blockers directly after the antenna, which greatly reduces power consumption in RF front-ends. The design stack starts with high- $Q$  disk resonators as the primary building block that enables low filter passband loss for tiny fractional bandwidths, in contrast to the previous efforts in literature that suffered high  $IL$  due to insufficient  $Q$ . Capacitive actuation gap scaling over-comes the inadequate electromechanical coupling that limited the performance of previous capacitive actuated filter efforts. Then, the array-composite design approach uses the vibrating disks with high  $Q$  and sufficient  $C_x/C_o$  as building blocks towards reducing the filter termination impedance, followed by the next level of hierarchy that couples array-composites with full-wavelength beams for differential operation. Finally, identical differential array-composite blocks coupled with quarter-wavelength beams generate the desired filter passband. A filter electrical equivalent circuit built using modules that use electromechanical analogies for each level of the design hierarchy captures the electrical behavior of the filter as a final design verification tool.

Perhaps the most significant contribution of this work is the demonstration of an intuition based mechanical circuit design flow that works just as powerful as those used in the transistor world to enhance functionality via a hierarchical building block approach. The following chapter of this dissertation will demonstrate the efficacy of the design principles outlined in this chapter through the fabrication and measurement of a 224 MHz 0.09% bandwidth RF channel-select filter, where the measured performance supports the accuracy of the models used to design the filter.

# Chapter 6

## PRACTICAL FILTER IMPLEMENTATION & EXPERIMENTAL RESULTS

This chapter presents the fabrication and measurement results of an RF channel-select filter created using the theory and design procedure elaborated in Chapter 5. The introduction of a 39nm-gap capacitive transducer, voltage-controlled frequency tuning, and a stress relieving coupled array design has enabled a 0.09% bandwidth 223.4 MHz channel-select filter with only 2.7dB of in-band insertion loss and 50dB rejection of out-of-band interferers. This amount of rejection is more than 23dB better than a previous capacitive-gap transduced filter design [23] that did not benefit

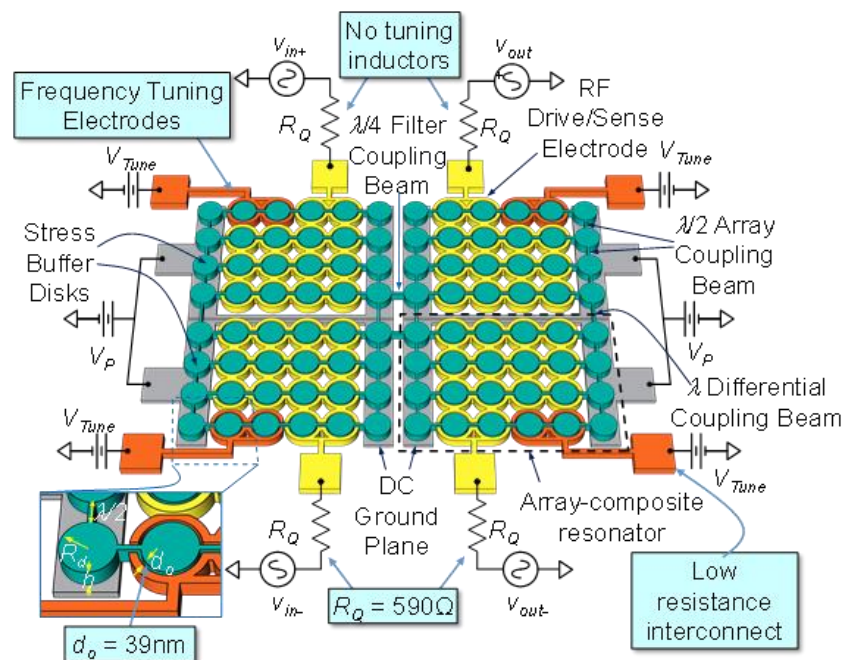


Figure 6.1: Schematic description of the designed 2nd order differential filter with electrical drive and sense setup used in measurement.

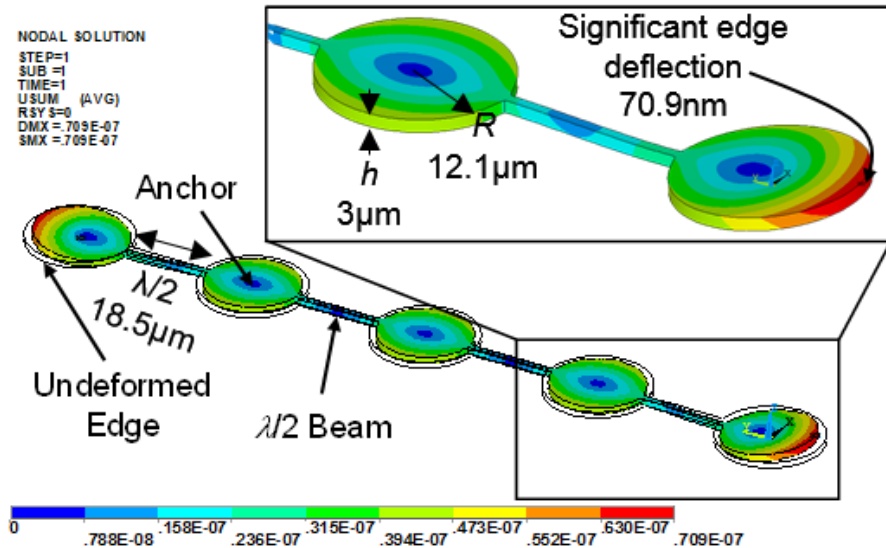


Figure 6.2: Finite element static analysis result of a  $5 \times 1$  polysilicon disk resonator array under 500MPa compressive stress. Each disk is anchored at the center by a stem post of  $2\mu\text{m}$  diameter, and connected to the adjacent disk with  $\lambda/2$  long beams. The color-map legend indicates the displacement in meters.

from sub-50nm gaps. It also comes in tandem with a 20dB shape factor of 2.7 realized by a hierarchical mechanical circuit design utilizing 206 micromechanical circuit elements, all contained in an area footprint of only  $600\mu\text{m} \times 420\mu\text{m}$ . The key to such low insertion loss for this tiny percent bandwidth is  $Q's > 8,800$  supplied by polysilicon disk resonators employing for the first time capacitive transducer gaps small enough to generate coupling strengths of  $C_x/C_o \sim 0.1\%$ , which is a  $6.1 \times$  improvement over previous efforts [23]. The filter structure utilizes electrical tuning to correct frequency mismatches due to process variations, where a dc tuning voltage of 12.1 V improves the filter insertion loss by 1.8 dB and yields the desired equiripple passband shape. An electrical equivalent circuit is presented that captures not only the ideal filter response, but also parasitic non-idealities that create electrical feed-through, where simulation of the derived equivalent circuit matches measured filter spectrum closely both in-band and out-of-band.

## 6.1 Introduction

The ever-increasing demand for wireless interconnectivity continues to motivate efforts on paradigm shifting transceiver designs, such as the software defined [14] and cognitive radio [2]. Practical implementation of such radios with low cost and low power consumption can benefit immensely from RF channel-selecting front-end filter banks [10] and/or chip-scale frequency gating spectrum analyzers [114]. Such advanced RF front-end hardware, however, requires high fre-

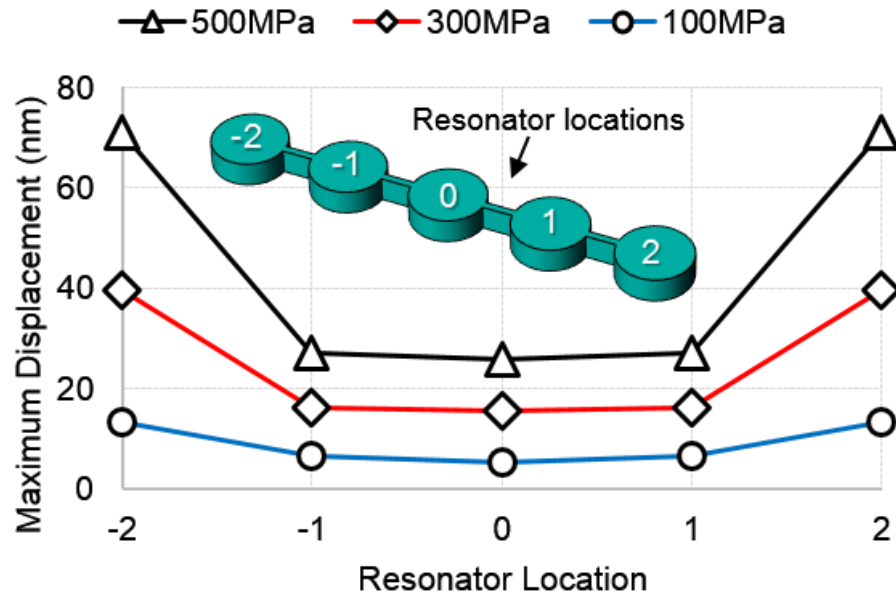


Figure 6.3: Plot of FEA static analysis result for maximum static displacement under three different structural film stress scenarios for the device of Figure 6.2.

quency resonators with simultaneous high  $Q$  (e.g.  $> 15,000$  at 1 GHz) and sufficient electromechanical coupling (e.g.  $C_x/C_o > 0.1\%$ ) as building blocks for low insertion loss narrow-band filters with fractional bandwidths on the order of 0.1% or less [46].

This chapter complements the previous one, where Chapter 5 detailed a comprehensive design procedure to realize the aforementioned low insertion loss RF channel-select filter banks using high  $Q$  vibrating micromechanical disks. This part follows up with an actual RF channel-select filter realized using the procedures elaborated in Chapter 5.

The demonstrated 223.4-MHz second order Chebyshev filter, cf. Figure 6.1, employs 206 resonant micromechanical elements to realize a channel-selecting 0.09%-bandwidth while achieving only 2.7dB of in-band insertion loss together with 50dB of out-of-channel stop-band rejection. This amount of rejection is 25dB better than that of previous capacitive actuated channel-select filter efforts [23], and comes in tandem with a 20dB shape factor of 2.7 commensurate with its use of two array-composite resonators. Capacitive actuation gaps scaled down to 39nm and a bias voltage of 14V achieves sufficient transducer coupling strength  $C_x/C_o = 0.1\%$  and a low filter termination impedance of only 590 $\Omega$ . As shown in Figure 6.1, the filter comprises 96 disks mechanically coupled by 110 beams. The clearly discernable mechanically coupled resonator arrays implement a design hierarchy reminiscent of complex VLSI transistor circuits, but here used to achieve a complex MSI mechanical filter circuit.

Unlike the ideal filter treated in Chapter 5, the real filter has non-idealities such as structural film stress, parasitic trace resistance, and process variations. Therefore, this chapter focuses on the



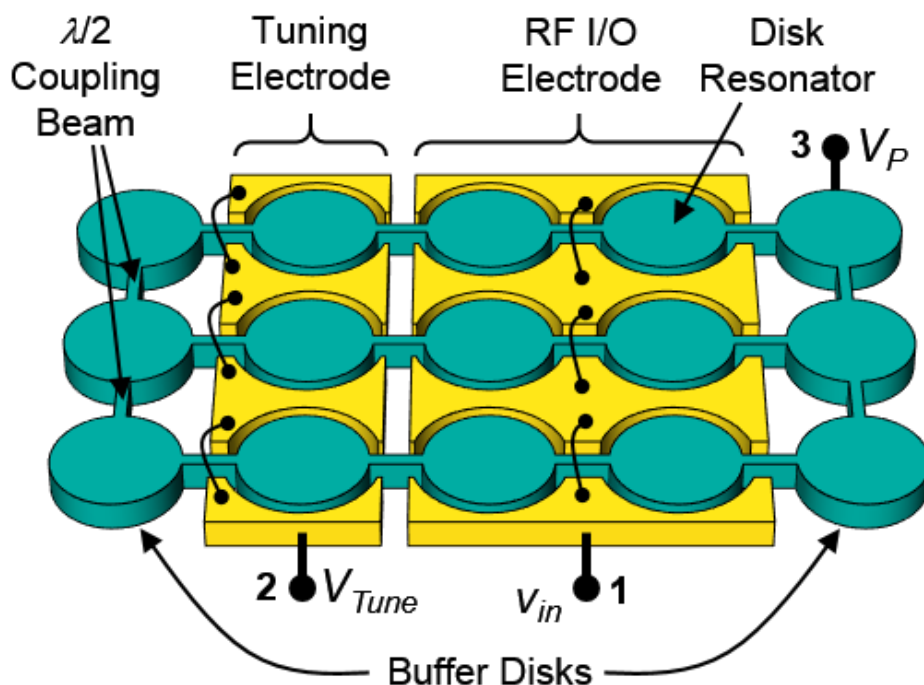


Figure 6.4: Schematic description of a  $\lambda/2$  coupled array-composite resonator with dedicated tuning electrodes and outer buffers disk-resonators for defensive design against in-plane structural film stress.

practical implementation of a filter that accounts for these non-idealities. Specifically, the design illustrated in Figure 6.1 introduces additional electrodes around disks specifically tasked for frequency tuning towards higher device yield to combat device mismatch; as well as carefully designed electrode-less buffer devices that alleviate post-fabrication stress, thereby also contributing to higher yield. In addition, the  $3\mu\text{m}$ -thick Phosphorus doped polysilicon interconnect of the structure achieves a sufficiently low trace resistance of  $0.8\ \Omega/\text{square}$  and mitigates parasitic  $Q$  loading and electrical feedthrough problems. This part also enhances the ideal filter equivalent circuit presented in Chapter 5 with additional circuit elements that capture the effects of the non-idealities, and confirms the theoretical predictions of the simulated filter equivalent circuit with measured results. The following sections will elaborate on the practical challenges of small percent bandwidth channel-select filters, and present solutions that improve yield and repeatability.

## 6.2 Defensive Design against Film Stress

Chapter 5 emphasized the importance of small electrode-to-resonator gaps that amplify the input/output electromechanical coupling and directly contribute to large stop-band rejection. However, one consequence of array-composites with tiny gaps is a higher susceptibility to stress, where mechanically linking adjacent resonators introduces a fabrication pitfall. The residual in-plane

stress in the resonator structural film accumulates a lateral strain through the cascade of coupled resonators that maximizes at the resonators located at the exterior of the array.

Figure 6.2 illustrates this effect for a linear array of five contour mode disk resonators designed to operate at 224MHz with 12.1 $\mu\text{m}$  disk radius and 3 $\mu\text{m}$  thickness coupled with  $\lambda/2$  length beams, where stem posts of 2 $\mu\text{m}$  diameter and 0.5 $\mu\text{m}$  height anchor each disk at the center. The presented finite element static analysis result with 500 MPa in-plane compressive structural film stress displays significant displacement that maximizes for the resonators at both ends of the array. Here, the edge resonators displace by 70.9nm, which is 2.62 $\times$  larger compared to the maximum displacement observed for the adjacent inner resonator. Figure 6.3 plots the FEA result for the maximum static displacement of each disk along the same 5 $\times$ 1 resonator array for three different stress values, and demonstrates that the resonators placed at the boundaries of the array structure displace drastically more than the interior ones even for modest amounts of film stress. Clearly, the edge-resonators risk failure by tip-ping against the surrounding electrode that can be apart by as little as 40nm, or become more likely to electrically pull-in due to the reduced electrode-to-resonator gap.

Eliminating surrounding electrodes on these boundary devices and allocating them as buffer resonators, as depicted in Figure 6.4, solves this problem, and increases device yield significantly for sub-50nm gap array-composite resonators. The design trade-off that reduces the available electrode area is negligible compared to the vastly improved device robustness, since increasing the number of arrayed resonators to achieve the desired coupling costs a small area given the tiny footprint of micromechanical disk resonators that scales down quadratically with increasing frequency.

### 6.3 Electrical Equivalent Circuit with Parasitic Elements & Modeling Electrical Feedthrough

Chapter 5 introduced an electrical equivalent circuit that models the ideal filter behavior by combining electromechanical analogies developed for the hierarchical modules that comprise the filter, which proved to be a valuable design verification tool to confirm the desired electrical response resulting from the mechanical design choices. However, this circuit ignored the parasitic effects, such as the influence of the electrical resistance of the dc-bias lines and the  $\lambda/4$  filter coupling beams on the filter stop-band rejection. An accurate electrical model of the dominant parasitic feedthrough currents provides mechanical design insights towards suppressing them. This section identifies the dominant parasitic feedthrough current paths in the filter structure presented in Figure 6.1 towards capturing the electrical behavior of the filter not only in the pass-band, but also in the stopband by simulating the filter stop-band rejection accurately.

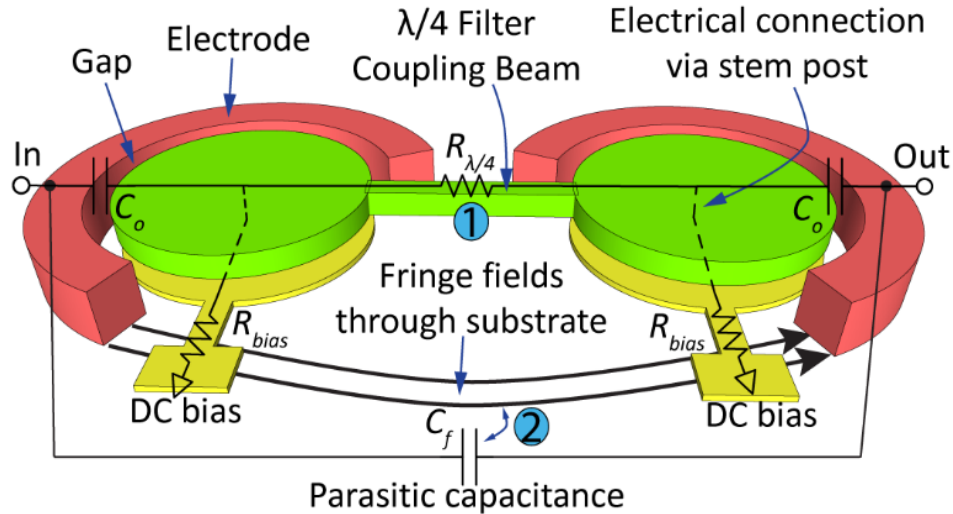


Figure 6.5: Schematic description of dominant electrical feedthrough paths in a two-resonator filter, where the path marked 1 indicates parasitic currents flowing through the coupling beam and path marked 2 describes the parasitic capacitance formed between the input and output electrodes through the substrate.

Excessive electrical feedthrough causes significant pass-band distortion, and reduces the out-of-band rejection of the filter that impedes the channel-select filter's capability to eliminate strong out-of-channel blockers. There are two dominant electrical feedthrough paths in the mechanically coupled disk network depicted in Figure 6.1 fabricated using conductive polysilicon. Figure 6.5 schematically describes how these paths form in a simplified two-resonator filter example, where the resonators represent the differential actuated array-composites on the right and left halves of Figure 6.1. As highlighted in Figure 6.5, the dominant parasitic electrical feedthrough paths form through the following mechanisms:

- 1) Via the electrode-to-disk static overlap capacitors  $C_o$  and the filter conductive coupling beam with electrical resistance  $R_{beam}$ .
- 2) Through the silicon substrate modelled by the parasitic capacitance  $C_f$  formed by the fringing fields between the input and output electrodes.

The following sections will introduce the electrical equivalent circuit model that captures the behavior of these feedthrough paths.

### 6.3.1 Filter Electrical Equivalent Circuit with Parasitic Elements

Figure 6.6 presents a filter electrical equivalent circuit that builds on the simpler version provided in Figure 5.23 of Chapter 5 by adding electrical models that describe the two dominant parasitic feedthrough mechanisms illustrated in Figure 6.5. The highlighted areas enclosed with in the labeled rectangles on the circuit schematic indicate the circuit elements dedicated to model these feedthrough paths. Here, a resistive voltage divider models the feedthrough path flowing

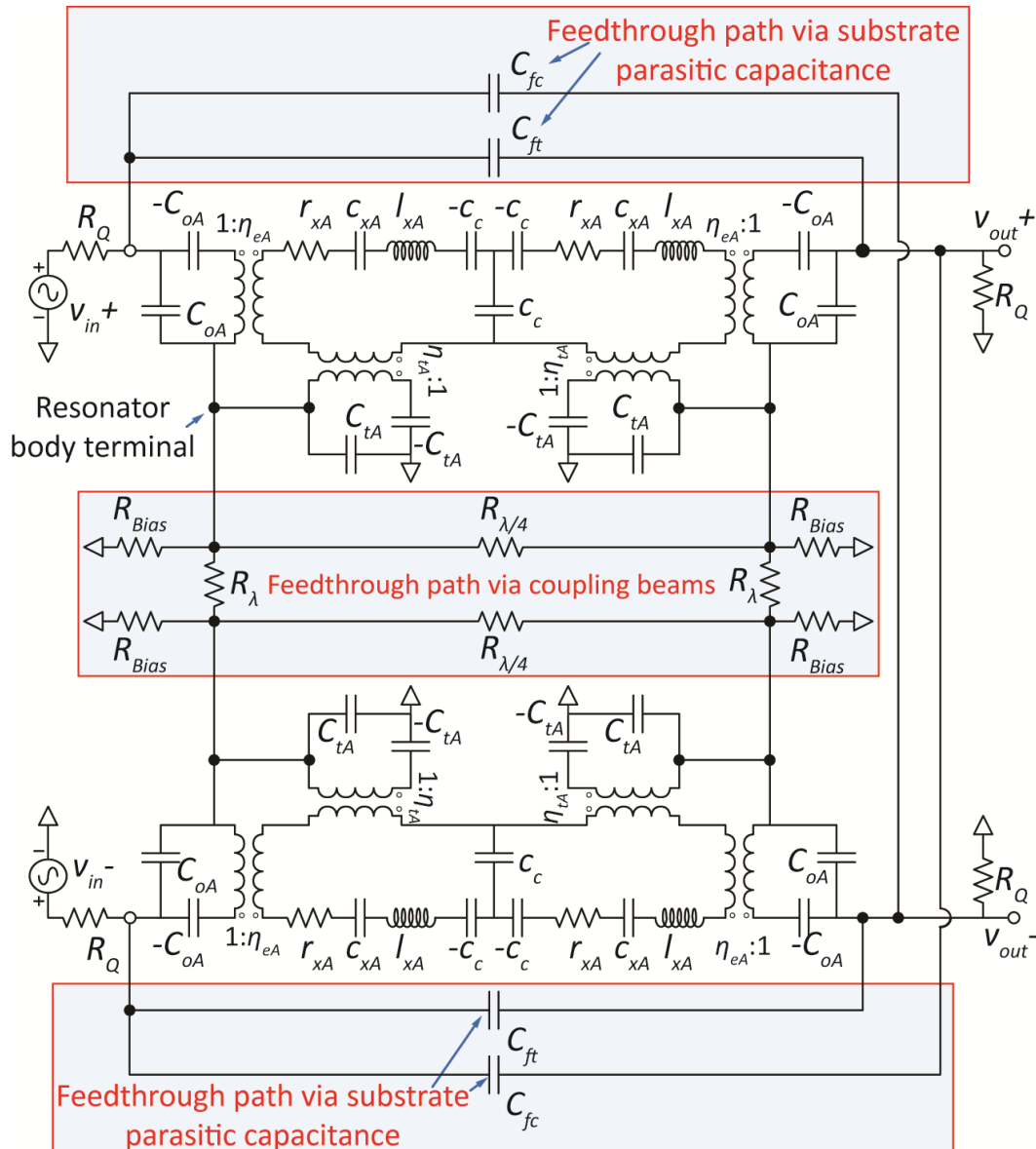


Figure 6.6: Electrical equivalent circuit for a 2<sup>nd</sup> order differential micromechanical disk filter. This circuit improves upon the version presented in Chapter 5 by introducing parasitic electrical feedthrough models as marked in the highlighted rectangular areas, describing two dominant feedthrough paths as feedthrough via coupling beams, and through the substrate parasitic capacitances.

across the coupling beams, where resistors labeled  $R_\lambda$  and  $R_{\lambda/4}$  represent the electrical resistance of the  $\lambda$  and  $\lambda/4$  beams that couple the array-composite resonators, respectively, analogous to the case described as path-1 in Figure 6.5.

Similarly, the four  $R_{bias}$  resistor elements in Figure 6.6 capture the resistance of the traces between the dc-bias source that acts as an ac-ground sink and the disk resonator body terminals of the four  $\lambda/2$  coupled array-composites in each quadrant of the filter network, as seen in Figure 6.1.

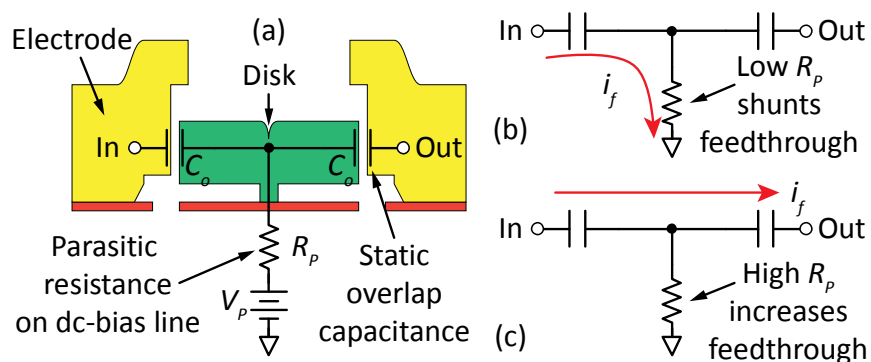


Figure 6.7: (a) Schematic describing the current divider formed by any dc-bias trace parasitic resistance and static electrode-disk overlap capacitors, where (b) very low trace resistance creates a sink for parasitic feedthrough current if and increases filter rejection as desired, and in contrast (c) high trace resistance cannot effectively shunt electrical feedthrough causes and leaks it to output electrode.

The voltage divider network formed by these resistor elements forms a bridge across the input and output electrodes, where the ac-ground provided by the dc-bias sources tries to shunt the feedthrough current before it reaches from the input to the output.

However, any resistance on the dc-bias path, as captured by the  $R_{bias}$  terms, hinders the suppression of the feedthrough as described in Figure 6.7, which emphasizes the importance of achieving low trace resistance, and thus the use of a  $3\mu\text{m}$  thick polysilicon film for the interconnect layer in this work. Of course, using non-conductive  $\lambda/4$  filter coupling beams would also suppress this feedthrough path as evident from the inspection of Figure 6.5 and Figure 6.6 with setting  $R_{\lambda/4} \approx \infty$ , which; however, would increase fabrication process complexity.

The second feedthrough path forms via fringing fields through the substrate between the input and output electrodes of the filter, which can accrue a significant lateral area to form sufficiently strong fringe fields and cause significant parasitic coupling between the input and output ports, as illustrated by the feedthrough path-2 in Figure 6.5. The equivalent circuit presented in Figure 6.6 models this path with four parasitic capacitors coupled across the four RF input/output ports of the filter. Here, capacitors labeled  $C_{fi}$  capture the parasitic coupling across ports with the same differential drive polarity, e.g.  $v_{in+}$  and  $v_{out+}$ ; and capacitors labeled  $C_{fc}$  model the cross-coupling between opposite polarity ports, e.g.  $v_{in-}$  and  $v_{out+}$ .

### 6.3.2 Filter Design Insights from Inspection of the Electrical Equivalent Circuit

Chapter 5 breaks down the design complexity of the complete mechanical filter circuit into easier to handle fundamental building blocks with individual equivalent circuits to describe the ideal operation of the filter. The circuit presented in Figure 6.6 in this chapter; however, goes one step further by intuitively visualizing how various filter building blocks and non-ideal parasitic

elements interact on the system level. The improved circuit model of Figure 6.6 makes more obvious the design choices and topologies to optimize filter performance. Specifically, an inspection of the voltage dividers formed by the electrical components on the dominant feedthrough paths and termination resistors  $R_Q$  suggests using lower termination resistor values to minimize the parasitic feedthrough coupled across the in-put and output ports. To illustrate, the ratio of the applied positive polarity input voltage  $v_{in+}$  leaking to the positive polarity output electrode  $v_{out+}$  through the parasitic capacitance  $C_f$  in dB scale is given by

$$\frac{v_{out+}}{v_{in+}} = 20 \log_{10} \left( \frac{R_Q}{2R_Q + 1/(j\omega C_f)} \right) \quad (6.1)$$

where reducing  $R_Q$  from  $5k\Omega$  to  $50\Omega$  would decrease the feedthrough level by 40dB for typical  $C_f$  values  $\sim 5$ fF. This observation justifies the use of  $\lambda/2$  coupled array-composites that trades of the filter area (i.e. the number of arrayed resonators) to reduce the termination resistance value for high stopband rejection, in addition to easier impedance matching to the rest of the receiver chain.

Inspecting the dominant electrical feedthrough paths presented in Figure 6.6 also justifies the added fabrication process complexity induced by the  $3\mu\text{m}$  thick phosphorus doped polysilicon traces in this study, given their low sheet resistance of  $0.8 \Omega/\text{square}$ . Low parasitic trace resistance minimizes parasitic  $Q$  loading and avoid undue insertion loss due to low loaded resonator  $Q$ . Low interconnect resistance becomes more important as electrode-to-resonator gaps shrink to yield correspondingly small motional resistances that are more easily loaded by the interconnect resistance. Disks operating in radial contour modes benefit especially more from reduced parasitic trace resistances, since the resonant motional currents enter or leave both input and output electrodes in phase [28], so are subject to resistive loading from dc-bias lines, as well from in-put/output lines, which degrades the  $Q$  and the strongly related filter insertion loss.

Minimizing the resistance on the dc-bias trace also provides high filter stopband rejection and avoids passband shape distortion. The resistance of dc-bias line interconnect forms a current divider between the electrode-to-resonator overlap capacitors across input/output electrodes and the dc-bias source that acts as an ac-ground, as de-scribed in Figure 6.7(a). A low dc-bias path resistance forms a sink for electrical feedthrough currents by shunting them before they reach the output electrode, as depicted in Figure 6.7(b). In contrast, a high resistance between the dc-bias source and the disk resonator directs the feedthrough currents to the output port instead of the sink formed by the dc-bias source, cf. Figure 6.7(c), where they will mask the de-sired motional current of the device and pose a bottleneck for the filter stopband rejection.

Another important design insight inferred from studying the electrical equivalent circuit of Figure 6.6 is the crucial importance of symmetry in micromechanical filter design. A perfectly symmetric network with differential drive and sense completely suppresses electrical feedthrough since parasitic currents are common mode signals that are an-nulled by the infinite common mode rejection ratio of a fully balanced ideal system, much like the CMRR of a transistor differential

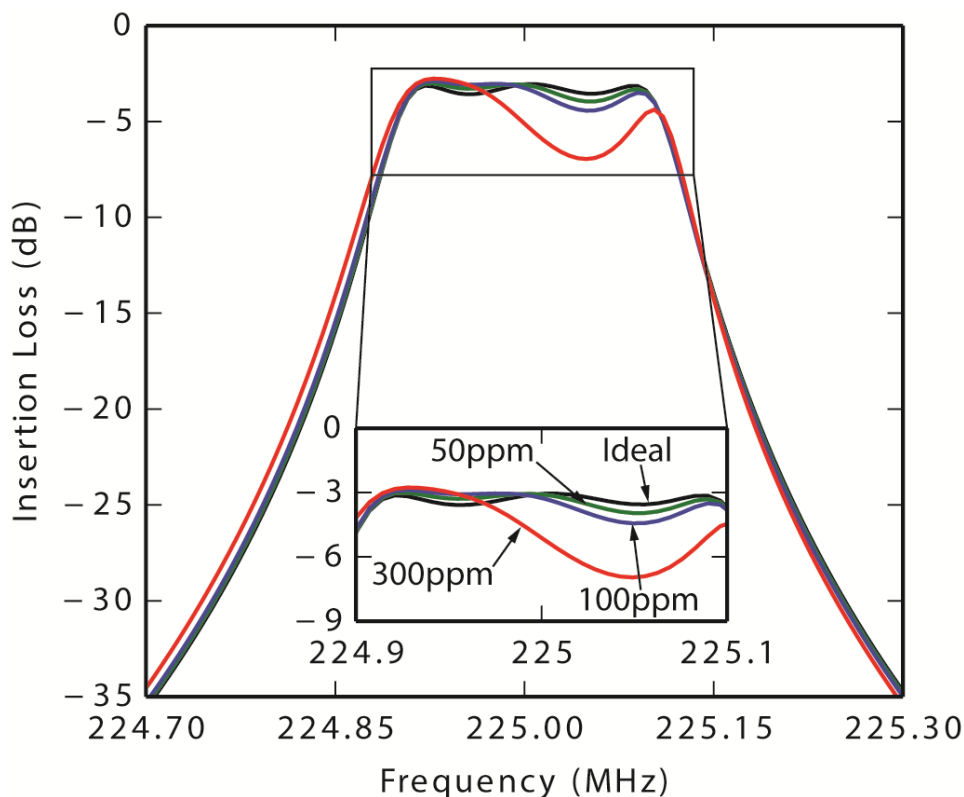


Figure 6.8: Simulated frequency response spectra for a 225-MHz three-pole, i.e. three-resonator, 0.5dB-ripple, Chebyshev filter with 0.1% bandwidth, for different amounts of resonator-to-resonator mismatching. For each mismatch case, adjacent resonators experience the indicated frequency deviation in opposite directions to simulate the worst-case mismatch scenario.

pair circuit. Of course, any practical filter implementation will suffer non-idealities that will deviate from the perfectly symmetric filter layout, as well as phase and impedance imbalances in the external electrical drive and sense circuitry, which reduces the CMRR and limits the feedthrough rejection performance of the filter.

In addition to suppressing electrical feedthrough, a symmetric and differentially balanced mechanical and electrical design suppresses the spurious vibration mode shapes that may otherwise arise in the complex mechanical network fabricated with a finite production precision. Here, the differential operation induced by the  $\lambda$ -coupling trades off filter footprint area with substantially increased filter performance. The differential design that uses two symmetric halves with  $180^\circ$  out-of-phase vibration mode shapes covers double the area of a single-ended filter, yet in return it suppresses the electrical feedthrough and unwanted spurious modes, both of which interfere with selective frequency filtering required from a channel-select filter.

## 6.4 Electrical Stiffness Tuning of Frequency Mismatches

Small percent bandwidth filters present challenges in not only insertion loss, but also yield and repeatability. Indeed, the smaller the percent bandwidth, the smaller the allowable mismatch between resonators. For example, as illustrated by the simulations of Figure 6.8, 0.1% bandwidth requires resonator-to-resonator frequency matching to better than 50 ppm to constrain mismatch-added pass-band ripple to less than 0.5dB over the designed 0.5dB. So far, single disk resonators (such as used in this work) post frequency standard deviations on the order of  $\sigma_{f,Single} = 316$  ppm [115], which is clearly short of the requirement. For this reason, only a small number of the mechanical filters fabricated in [23] actually had acceptable passband distortion. Yields of course must be much higher if high volume production is needed.

From [115], it is true that array-composites of resonators can be manufactured with better matching than any one of their constituents, by a factor equal to  $\sqrt{N}$ , where  $N$  is the number of resonators in the array. Thus, the 24 resonators (including non-I/O ones) used in each differential array-composite pair of Figure 6.1 should improve the standard deviation by  $4.9\times$  to 64.5 ppm. Unfortunately, this is still not sufficient.

Dedicating part of the resonators exclusively for electrical stiffness tuning [37], as shown in Figure 6.4, solves this problem by adjusting the dynamic stiffness of the array-composite by applying dc tuning voltages that modify the electrical stiffness term derived in Chapter 2

$$k_{e,Tune} = \frac{\eta_{tA}^2}{C_{tA}} \quad (6.2)$$

to pull the resonance frequency to its ideal value, where  $\eta_{tA}$  and  $C_{tA}$  are the electromechanical coupling coefficient and static electrode overlap capacitance for the tuning electrode port of the array-composite. This electrical tuning strategy is a unique advantage of capacitively transduced resonators over their counterparts, such as piezoelectric devices, which allows real time correction of resonance frequency against not only process variations [116], but also aging and temperature drift [32].

The effective dynamic stiffness  $k_{reA}$  of an array-composite after considering the electrical spring softening effect induced by the RF input-output electrode that adds a constant frequency shift for the chosen  $V_P$ , and the tunable shift adjusted by  $V_{Tune}$  follows as

$$k_{reA} = k_{mA} - k_{e,ioe} - k_{e,Tune} = k_{mA} - \frac{\eta_{eA}^2}{C_{oA}} - \frac{\eta_{tA}^2}{C_{tA}} \quad (6.3)$$

where  $k_{mA}$  is the dynamic stiffness of the array-composite with no voltage applied between the disk resonators and the surrounding electrodes, and the terms  $k_{e,ioe}$  and  $k_{e,Tune}$  represent the electrical



stiffness values stemming from the RF input-output and electrical tuning ports, respectively. The array resonance frequency  $f_{oA}$  after spring softening effects becomes

$$f_{oA} = \sqrt{\frac{k_{reA}}{m_{mA}}} = \sqrt{\frac{k_{mA} - k_{e,Total}}{m_{mA}}} = f_{nom} \sqrt{1 - \frac{k_{e,Total}}{k_{mA}}} \quad (6.4)$$

where  $k_{e,Total} = k_{e,ioe} + k_{e,Tune}$ , and  $f_{nom}$  is the nominal resonance frequency of a single disk with no voltages applied. The normalized frequency tuning range in ppm follows from the Taylor series expansion of (6.4) as

$$\begin{aligned} \Delta f_{ppm} &= \frac{f_{nom} - f_{oA}}{f_{nom}} \times 10^6 = \frac{1}{2} \frac{k_{e,Total}}{k_{mA}} \times 10^6 \\ &= \left( N_t (V_{Tune} - V_P)^2 + N_{RF} V_P^2 \right) \frac{C_{oi}}{d_o^2} \frac{1}{2Nk_m} \times 10^6 \end{aligned} \quad (6.5)$$

The filter designer should choose the variables in (6.5) to satisfy

$$\Delta f_{ppm} \geq \frac{\sigma_{Single}}{\sqrt{N}} \quad (6.6)$$

condition in order to ensure sufficient tuning for correcting the worst-case mismatch scenarios within the available tuning voltage  $V_{Tune}$  range.

As illustrated in Figure 6.1, the filter presented in this work uses  $N_t = 2$  of its  $N = 24$  array resonators for frequency tuning that generates a frequency tuning pull of 3 ppm/V. This, however, is sufficient to traverse the expected (64.5-50=14.5) ppm frequency pull needed to correct for differential array-composite pair mismatch, and thus, is sufficient to correct mismatch-generated passband distortion towards higher manufacturing yields.

## 6.5 Design Parameters for the Fabricated 224 MHz, 0.1% Bandwidth Channel-Select Filter

This section summarizes the design parameters of the fabricated micromechanical disk filter that successfully realizes <0.1% fractional bandwidth while maintaining low insertion loss. To this end, a differential coupled disk resonator filter comprising 96 resonators and a total of 206 resonant elements, cf. Figure 6.1, is designed with the procedure elaborated in Chapter 5. The primary design goals are a center frequency of  $f_o = 224\text{MHz}$  with  $B = 224\text{kHz}$  (i.e. 0.1%) bandwidth, and sub 1-k $\Omega$  termination resistors fabricated using the process flow described in Section 6.6 with the minimum resolvable critical dimension of  $w_{c,min} = 1\mu\text{m}$ . The filter structural material is polysilicon with elastic properties listed as Young's modulus  $E = 158\text{GPa}$ , density  $\rho = 2300\text{ kg/m}^3$ , and Poisson ratio  $\sigma = 0.226$ .

Table 6-I: Summary of Filter Design Procedure and Equivalent Circuit Element Values

Design Procedure		Parameter	Source	Design	Simulated	Unit	
<p>Given: <math>f_o, B, w_{c,min}</math>  Goals: <math>IL &lt; 3\text{dB}, R_Q &lt; 1\text{k}\Omega</math>  Find: <math>R_Q, d_o, V_P, N, N_{RF}, N_b, N_s</math></p> <ol style="list-style-type: none"> <li>Choose <math>E, \rho, \sigma</math> by choice of structural material.</li> <li>Choose thickness <math>h</math>, determine resonator <math>Q</math>.</li> <li>Start with a single disk resonator to oscillate at 224 MHz in the fundamental contour mode shape, where solution of (5<sup>†</sup>) yields <math>R = 12.1\mu\text{m}</math></li> <li>Solve for minimum number of resonators in array-composites to satisfy (26<sup>†</sup>) with <math>w_{c,min} = 1\mu\text{m}</math> that leads to <math>N = 24</math>.</li> <li>Allocate <math>N_b = 6</math> resonators as stress-relief buffers, <math>N_t = 2</math> as tuning resonators and the remaining <math>N_{ioe} = 16</math> for RF drive and sense.</li> <li>Determine minimum electromechanical coupling strength via (27<sup>†</sup>) leading to <math>C_x/C_o \geq 0.09\%</math>, which can be chosen by (28<sup>†</sup>) as <math>d_o = 40\text{nm}</math> and <math>V_P = 14\text{V}</math> (among various other combinations) to ensure a high yield process with reasonably sized gaps and low risk of electrostatic pull-in.</li> <li>Calculate <math>\lambda</math>, and design <math>\lambda/4, \lambda/2</math> and <math>\lambda</math> coupling beams.</li> <li>Calculate filter termination resistor value via (2<sup>†</sup>) as <math>580\Omega</math>, meeting <math>&lt; 1\text{k}\Omega</math> design goal.</li> <li>Calculate voltage-to-force electromechanical coupling coefficient <math>\eta_e</math> for each port.</li> <li>Calculate electrical equivalent circuit variables.</li> <li>Convert the single ended design to differential, and finally create the electrical equivalent circuit and compare simulated results with measurement data.</li> </ol>	Filter Specs.	Frequency, $f_o$	Spec.	224	<b>223.4</b>	MHz	
		Bandwidth, $B$	Spec.	224	<b>209</b>	kHz	
		Fractional bandwidth	Spec.	0.1	<b>0.09</b>	%	
		Insertion Loss, $IL$	Measured	2.70	<b>2.73</b>	dB	
		Minimum beam width, $w_{c,min}$	Process	1	1	$\mu\text{m}$	
		Out-of-band rejection	Measured	50	50	dB	
	Single Disk Resonator		Disk radius, $R$	(5.11)	12.1	<b>12.12</b>	$\mu\text{m}$
			Disk thickness, $h$	Process	3	3	$\mu\text{m}$
			Resonator quality factor, $Q$	Measured	10,000	<b>8,830</b>	-
			Electrode span angle, $\theta_{ov}$	Layout	$165^\circ$	$165^\circ$	$^\circ$
	Array & Coupling Beam Design		Resonator per array, $N$	(5.12)	24	24	-
			Number of buffer res., $N_b$	Layout	6	6	-
			Number of tuning res., $N_t$	Layout	2	2	-
			Number of input res., $N_{ioe}$	Layout	16	16	-
			Acoustic quarter-wavelength, $\lambda/4$	(5.16)	9.26	<b>9.27</b>	$\mu\text{m}$
			Filter coupling beam width, $w_c$	(5.17)	1	1	$\mu\text{m}$
	Coupling Strength		Filter coupling beam capacitance, $c_c$	(5.18)	12.97	<b>12.95</b>	$\mu\text{F}$
			Electromechanical coupling coef. $C_x/C_o$	(5.44)	0.1	<b>0.1</b>	%
			Electrode-to-resonator gap, $d_o$	(5.14)	40	<b>39.1</b>	nm
			DC Bias Voltage, $V_P$	(5.14)	14	14	V
	Core Equivalent Circuit Variables		Filter termination resistor, $R_Q$	(5.36)	587	<b>590</b>	$\Omega$
			Inductance at disk-array perimeter, $l_{xA}$	(5.19)	58.13	<b>58.31</b>	pH
			Capacitance at disk-array perimeter, $c_{xA}$	(5.19)	8.69	8.69	nF
Resistance at disk-array perimeter, $r_{xA}$			(5.19)	9.81	<b>9.83</b>	$\mu\Omega$	
Tuning Port		RF input port static overlap cap., $C_{oA}$	(5.20)	636.1	<b>638.6</b>	fF	
		RF input port coupling coefficient, $\eta_{eA}$	(5.20)	222.6	<b>224.1</b>	$\mu\text{C}/\text{m}$	
		Tuning port static overlap cap., $C_{o,tA}$	(5.21)	90.87	<b>91.23</b>	fF	
Parasitic Elements		DC tuning voltage, $V_{tune}$	Measured	12.1	12.1	V	
		Tuning coupling coefficient, $\eta_{tA}$	(5.21)	4.31	<b>4.35</b>	$\mu\text{C}/\text{m}$	
		DC bias line resistance, $R_{bias}$	Measured	-	5	$\Omega$	
		Coupling beam resistance, $R_\lambda$	Measured	-	8	$\Omega$	
		Feedthrough capacitances, $C_{f,13}$ & $C_{f,14}$	Measured	-	9 & 7	fF	

Table 6-I presents the step-by-step application of the filter design procedure and equations derived in Part I of this paper, and tabulates the resulting design values chosen to meet the design specifications. This table also includes all geometric dimensions derived by the design procedure, and the resulting electrical equivalent circuit values to be used in the electrical model of Figure

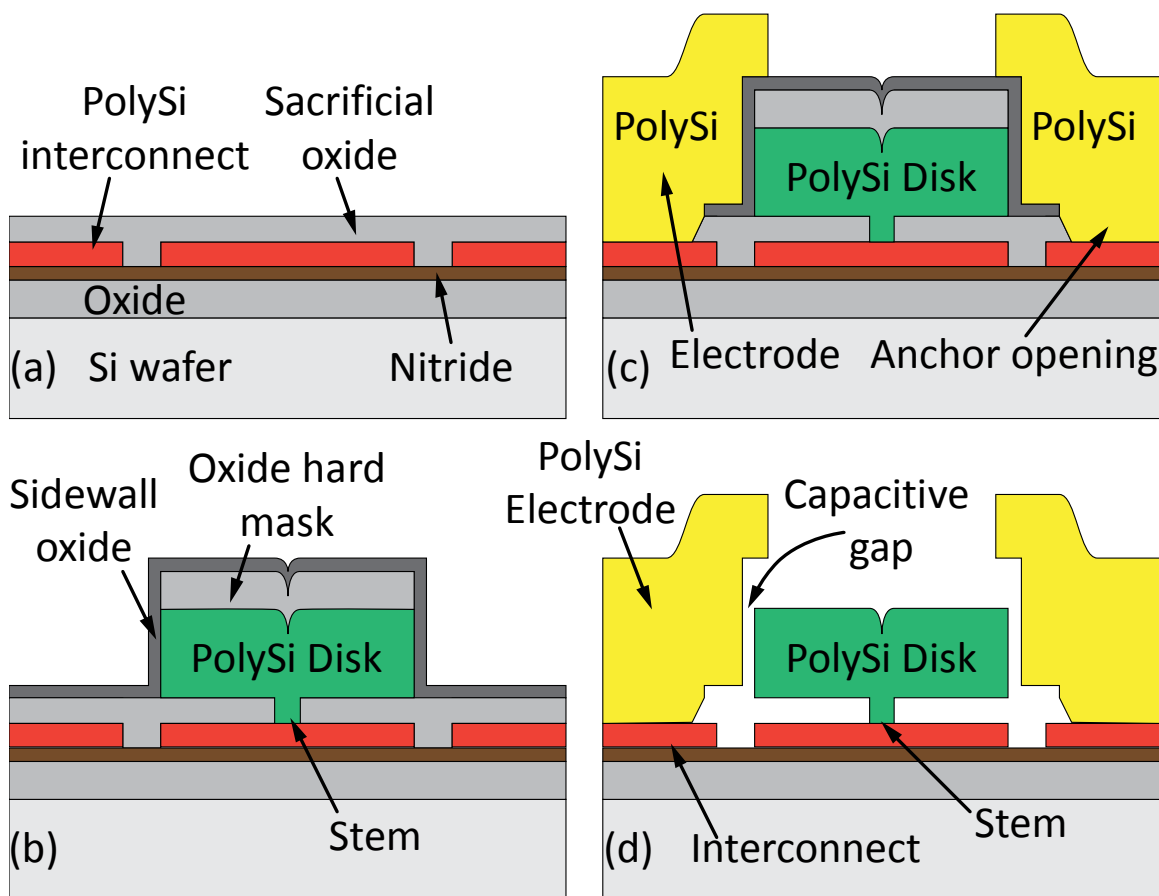


Figure 6.9: Cross-sections describing disk filter fabrication process flow after (a) patterning interconnect and depositing bottom sacrificial oxide, (b) depositing structural polysilicon over the stem opening followed by structural layer etch using an oxide hard mask and sidewall sacrificial oxide deposition, (c) opening electrode anchors that are later filled with doped polysilicon to be patterned to form electrodes, and (d) resonator freed after HF release.

6.6. Here the variables under the column labeled ‘Design’ indicate the initial design goals assumed during device layout, and the values typed in bold face under the column labeled ‘Simulated’ provide the actual measurement data obtained either directly from measured plots or curve fitted to data sets from the fabricated filter structure.

## 6.6 Fabrication Process

Pursuant to verifying the overall design strategy detailed in Chapter 5 of this dissertation, the polysilicon vibrating disk filters of this work are fabricated using a five mask process similar to that of [101] with the cross-sections of major process steps presented in Figure 6.9. The process starts on 6” blank Si wafers with successive LPCVD depositions of 2 μm LTO and 500 nm nitride

as electrical isolation layers. The following  $3\mu\text{m}$  thick LPCVD deposited phosphorus doped polysilicon layer is DRIE etched to form the interconnect layer with  $0.8\ \Omega/\text{square}$  sheet resistance. Then, a  $3.5\mu\text{m}$  LTO layer is blanket deposited to uniformly refill between the interconnect traces, which is then CMP'ed to selectively stop on the polysilicon traces. The CMP step eliminates the high topography created by the  $3\mu\text{m}$  thick interconnect routing to avoid ripples in the structural resonator film that will be deposited above the interconnect layer. In addition, the CMP step improves lithography accuracy of the succeeding stages. Next, a blanket LPCVD deposited  $500\text{nm}$  thick LTO film serves as the bottom sacrificial oxide layer with a uniform thickness over the flattened wafer surface, as depicted in Figure 6.9 (a). Circular stem openings with  $2\mu\text{m}$  diameter are then lithographically defined and etched into the bottom oxide film where the polysilicon interconnect serves as the etch stop.

The filter structural material comprises LPCVD deposited phosphorus doped  $3\mu\text{m}$  thick polysilicon that refills the stem openings etched in the previous step to form the anchor posts of the disk resonators. These mechanical anchors support the disk resonators at the contour mode vibration nodal point at the disk center, and connect the electrically conductive disk structures to the underlying interconnect layer. The next step deposits a  $1.2\mu\text{m}$  thick oxide to serve as a hard mask layer for the succeeding etching process. The layout pattern of the disk structures and coupling beams that forms the mechanical filter network is first etched into the oxide hard mask, and the photoresist layer patterned with the filter layout is then removed to avoid polymer formation and photoresist re-deposition on the etch sidewall during the following structural polysilicon etch step.

Realizing a smooth and vertical sidewall etch profile for the structural layer is vital in achieving high resonator  $Q$ , and producing the desired vibration mode shape and frequency with high yield. To this end, a polysilicon RIE etch recipe is developed using the gas flow rates of  $140\ \text{sccm}$  of HBr,  $14\ \text{sccm}$  of  $\text{Cl}_2$ , and  $5\ \text{sccm}$  of  $\text{O}_2$  at  $12\text{mTorr}$  pressure with  $250\text{W}$  and  $75\text{W}$  RF and wafer bias powers, respectively, using a Lam TCP 9400SE etch system. This recipe etches polysilicon at a rate of  $220\ \text{nm}/\text{min}$  with an oxide to polysilicon etch selectivity of  $16:1$ , and reduces the sidewall roughness observed for etch recipes that use higher  $\text{Cl}_2$  flow rates. The high selectivity between the oxide hard mask and the structural polysilicon film enables the desired vertical sidewalls and transfers the layout lateral dimensions to the structural polysilicon film with reduced uncertainty. HBr/ $\text{Cl}_2$  based etch chemistries form a side-wall polymer residue containing halogens and silicon oxide [117], which must be removed before the following high temperature deposition steps. Therefore, the wafers are immersed in a  $\text{H}_2\text{O}$  diluted  $50:1$  HF acid bath for 30 seconds and then rinsed with DI, followed by a 10 minutes immersion in DuPont EKC-270 post-etch residue remover heated to  $70^\circ\text{C}$  to remove the sidewall polymer residues.

The most critical step of the fabrication process is perhaps the following sidewall sacrificial oxide layer deposition that defines the  $39\text{nm}$  capacitive actuation gap between the disk and the surrounding electrodes. Here, the LPCVD deposition of high temperature oxide (HTO) using  $40\text{sccm}$  of DCS and  $100\text{sccm}$  of  $\text{N}_2\text{O}$  flow with  $600\text{mTorr}$  process pressure at  $835^\circ\text{C}$  coats a uniform, conformal, and pinhole free layer of HTO over the vertical disk sidewalls, as illustrated in

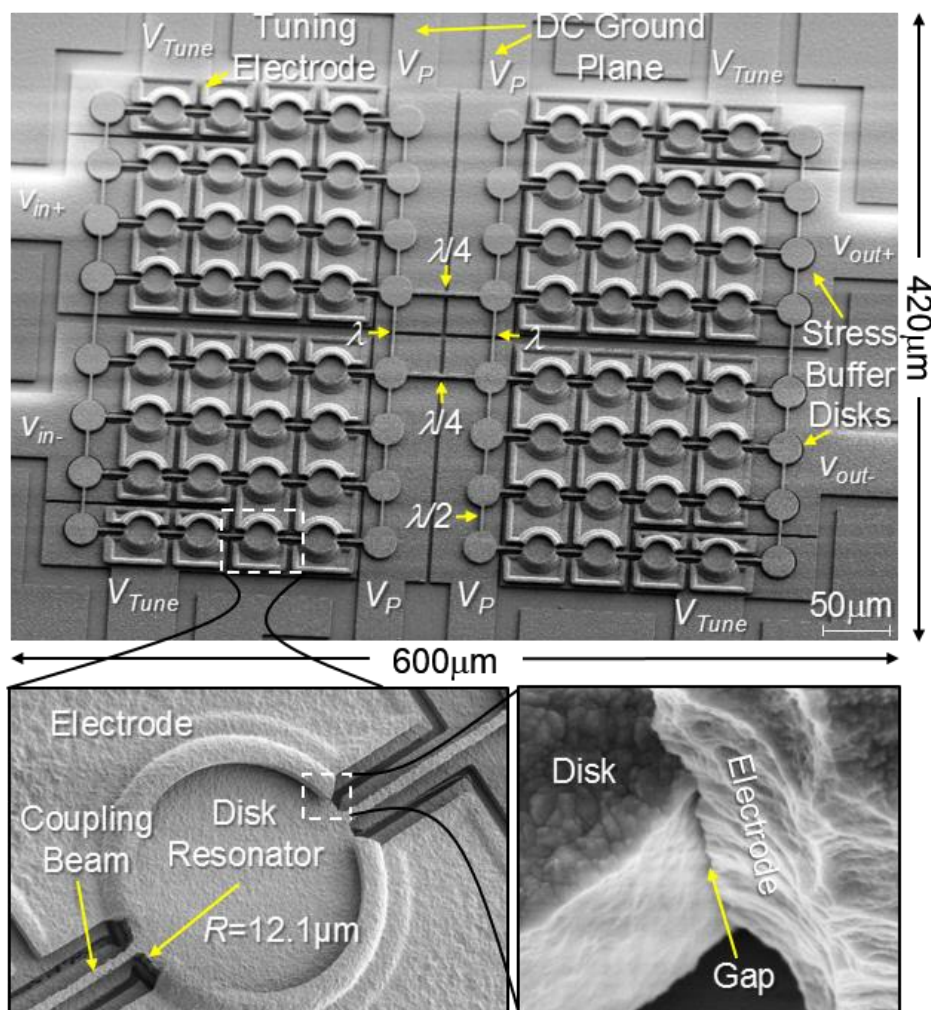


Figure 6.10: SEM image of a fabricated and released 2<sup>nd</sup> order differential filter described schematically in Figure 6.1. The inset on the right zooms in the disk resonator that constitutes the building block of the filter network. The inset on the right focuses on the capacitive actuation gap that forms between the disk resonator and the surrounding electrodes.

Figure 6.9(b). Then, the electrode anchor openings are etched into the bottom oxide sacrificial layer, followed by a blanket 3 $\mu$ m thick phosphorus doped polysilicon deposition. The final lithography and dry etch step creates the electrodes, as shown in Figure 6.9(c).

Completed wafers are diced and die-level released in 49 wt. % liquid HF that frees the filter structure with the final resonator cross-section schematic presented in Figure 6.9(d). Figure 6.10 shows the SEM image of a fabricated and released 2<sup>nd</sup> order differential filter that physically realizes the mechanical circuit schematically illustrated in Figure 6.1. The insets in Figure 6.1 focus on the disk resonator and coupling beams that constitute the filter network and the capacitive actuation gap formed between the disk resonator and the electrode. Finally, Appendix-A provides a

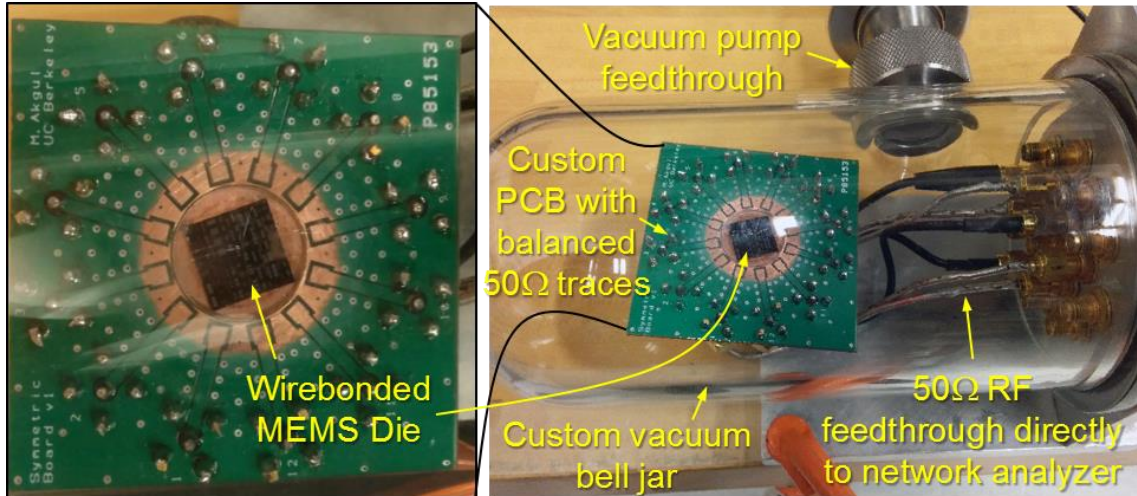


Figure 6.11: Vacuum measurement setup with  $50\Omega$  RF feedthroughs with matching electrical length for balanced differential measurement that connect the network analyzer directly to the wirebonded micromechanical filter.

detailed process traveler with step-by-step recipe details that were used to fabricate the devices presented in this dissertation.

## 6.7 Measurement Results

Pursuant to verifying the overall design strategy, micro-mechanical filters were fabricated using the process flow detailed in Section 6.6. Figure 6.10 presents the SEM of a fabricated differential filter matching the design of Fig. 1. Fabricated filters are tested with a four-port direct measurement setup using an Agilent E5071C network analyzer with the measurement plane moved to the filter bondpads using standard SOLT calibration. All measurement results presented in the following sections are obtained with 0dBm, i.e.  $0.225 V_{rms}$  signal amplitude, output power setting on all four ports of the network analyzer. The released MEMS die is housed in a custom-made vacuum bell jar providing  $30\mu\text{Torr}$  vacuum and wirebonded to a custom pcb that serves as a  $50\Omega$  fixture connecting directly to the network analyzer through coaxial cables as shown in Figure 6.11. All presented data is taken with  $50\Omega$  termination provided by the network analyzer ports on all four RF terminals of the filter, and the fixture simulator functionality of the network analyzer is then used to realize the differential drive and sense, and the purely resistive  $590\Omega$  termination without any other processing external to the network analyzer. Figure 6.1 presents the electrical configuration of the device under test, where a dc-bias voltage of  $V_P = 14\text{V}$  is applied to the conductive disk resonators through the underlying dc-ground plane. DC voltages are also applied to the indicated frequency tuning pads that direct them to electrodes capable of tuning frequency via voltage-controllable electrical stiffness.

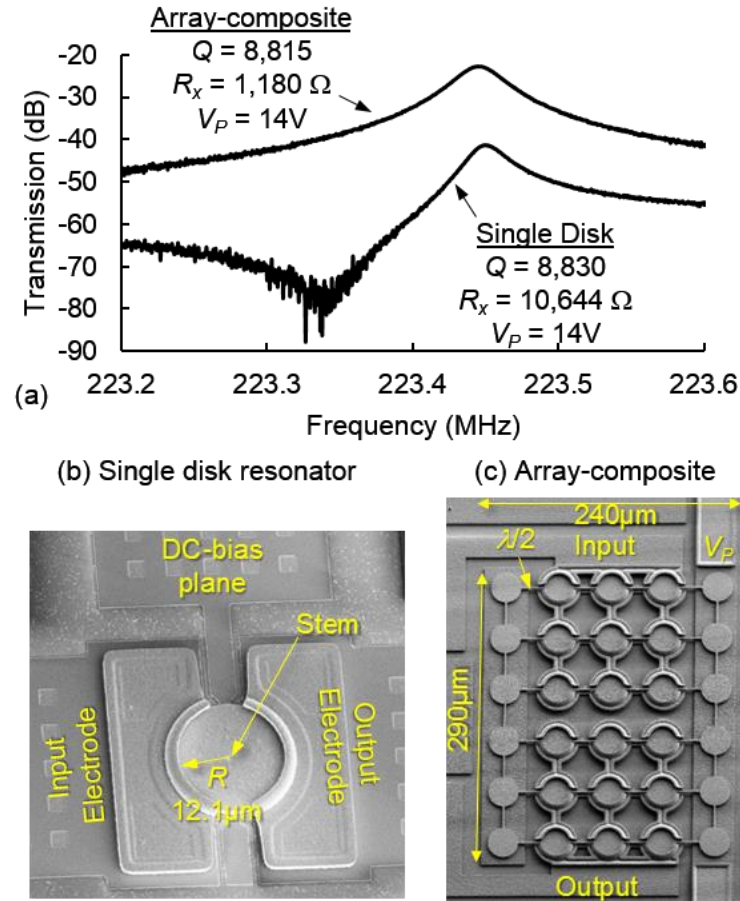


Figure 6.12: (a) Comparison of measured frequency spectrum of a single disk resonator and 30-resonator array-composite, and SEM images of the measured (b) single disk resonator, and (c) the array composite device.

### 6.7.1 Verification of $\lambda/2$ Coupled Array-Composite Operation

To demonstrate the added benefits by elevating the de-sign hierarchy from single disk resonators to  $\lambda/2$  coupled array-composites, Figure 6.12(a) compares the measured frequency spectrum obtained from a single disk resonator and a 30-resonator array-composite device. Figure 6.12 (b) and (c) show the SEM images of the measured single disk resonator and the  $5 \times 6$  array, respectively, both having disk radii of  $12.1 \mu\text{m}$  to operate at 223.4 MHz. Here, the array composite retains the high  $Q > 8,000$  of the single disk resonator, and reduces its motional resistance by  $9 \times$  from  $10,644 \Omega$  to  $1,180 \Omega$  for the same bias voltage of  $V_P = 14V$ .

The measured improvement in  $R_x$  agrees well with the theoretical expectation derived in (5.33), which is proportional to  $N / N_{ioe}^2$ , where  $N = 30$  is the total number of total disks including stress-buffer devices in the array perimeter, and  $N_{ioe} = 18$  is the number of resonators with surrounding

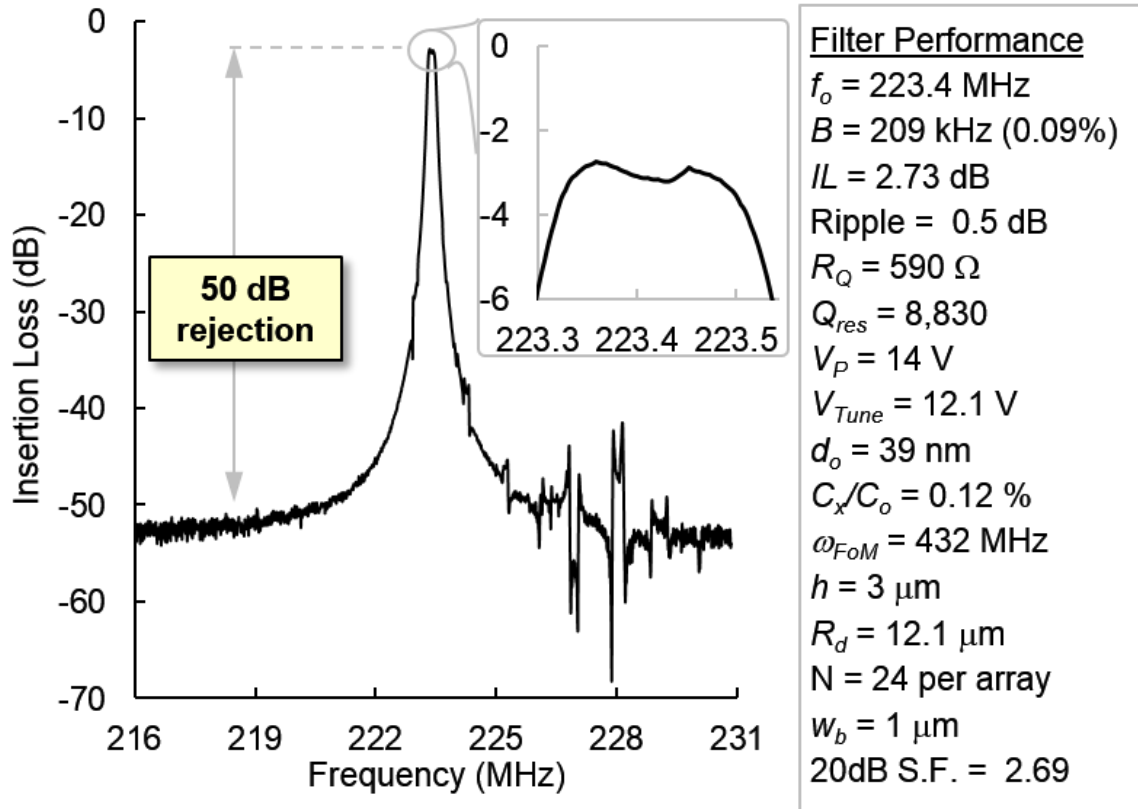


Figure 6.13: Measured terminated filter spectrum with the inset zooming on the 3dB passband, and the legend listing filter performance and design metrics.

input/output electrodes, which leads to an expected  $10.8 \times R_x$  reduction. The slight difference between the measured  $9 \times R_x$  improvement and the theoretical expectation can be attributed to small deviations from completely coherent in-phase summation of motional currents at the output electrode of the arrayed resonators. The presented disk array-composite mechanical circuit serves as a good example of enhancing functionality using a building block approach, where the array-composite displays a strong agreement between the measurement results and the predicted reduction in  $R_x$  while maintaining the high  $Q$  and the identical vibration frequency of a single disk device.

### 6.7.2 Terminated and Electrically Tuned Filter Spectrum

Figure 6.13 presents the tuned and terminated filter spectrum with an inset zoom-in on the passband showing centered at 224 MHz with 209 kHz, i.e. 0.09%, bandwidth with only 2.7dB insertion loss. Here, 590 $\Omega$  resistors terminate the filter as schematically described in Fig. 1, with a dc-bias voltage of 14V applied to the resonator body, and a dc tuning voltage of 12.1V is used to correct the filter passband. Small gaps combined with the symmetric and differential design lead to 50dB out-of-channel rejection and a 20-dB shape factor of 2.7. This amount of rejection is 23dB better than a previous capacitive gap transduced differential filter design [23] that did not benefit from low parasitic resistance traces. The 39nm capacitive transducer gaps of this work generate



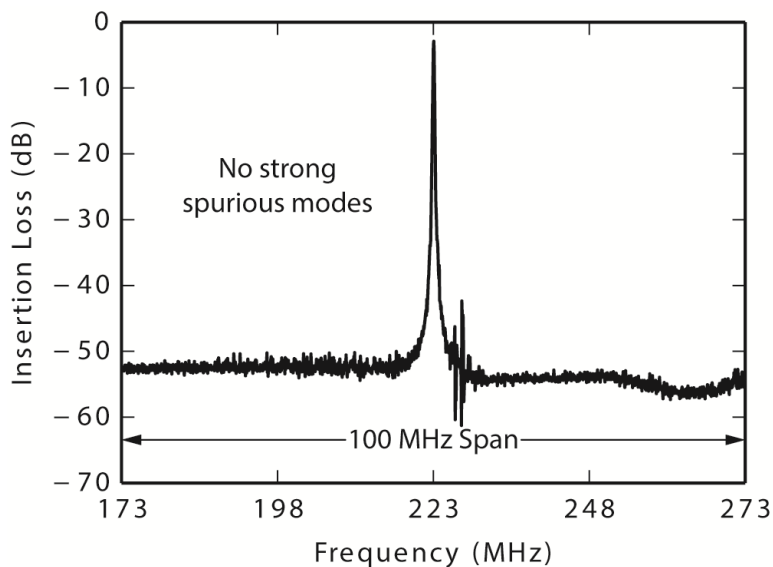


Figure 6.14: Measured terminated spectrum over 100 MHz span showing no strong spurious modes.

coupling strength of  $C_x/C_o = 0.1\%$ , which is a  $8.6\times$  improvement over previous efforts [23], and yields the desired undistorted equiripple passband displayed by the measured result.

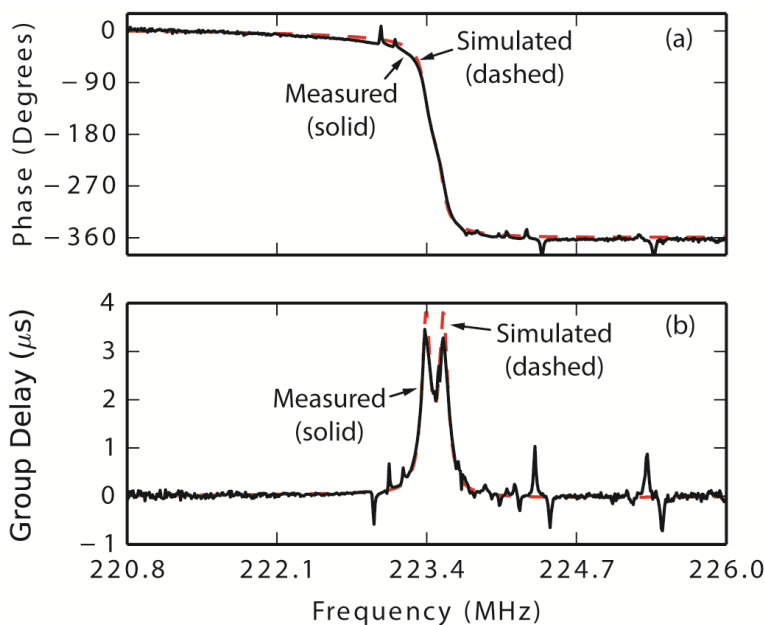


Figure 6.15: (a) Phase response, and (b) the corresponding group delay of the differential filter where the solid curves indicate measured data obtained under measurement conditions identical to Figure 6.13, and dashed lines indicate simulated response obtained from the electrical equivalent circuit of Figure 6.6 using the circuit element values listed in Table 6-I.

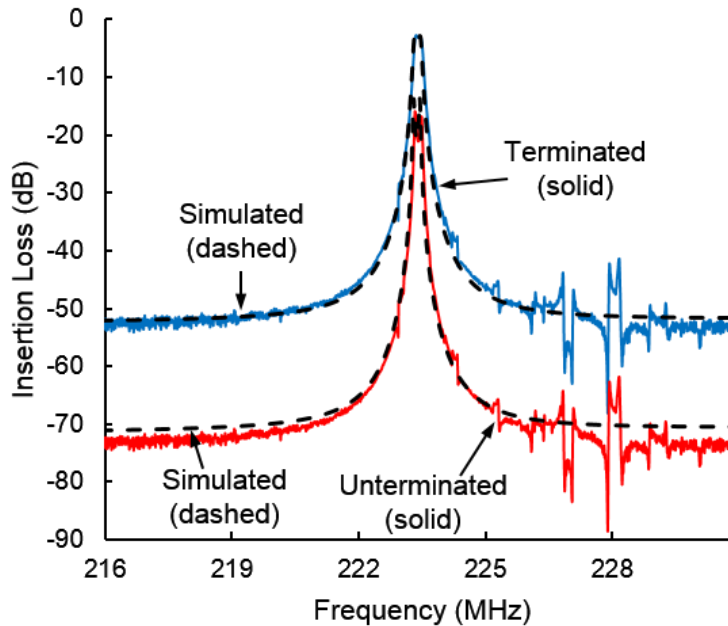


Figure 6.16: Comparison of 590 $\Omega$  terminated and unterminated (i.e. with 50 $\Omega$  termination) measured filter spectrum (solid lines), and electrical equivalent circuit simulation results for both cases shown as dashed lines.

Figure 6.14 presents the terminated spectrum over a 100MHz wide span showing no strong spurious modes, again achieved by differential design and tuning.

Figure 6.15(a) presents the measured phase response of the terminated filter. The filter group delay [25] presented in Figure 6.15(b) is the derivative of the phase response and is a measure of deviation from the ideal linear-phase response. Here, the filter displays an average group delay of 2.6  $\mu\text{s}$  over the 3dB passband with 1.2  $\mu\text{s}$  variation. The measured phase and group delay response presented as the solid curves in Figure 6.15 is in good agreement with the theoretical expectation indicated as dashed lines obtained by the electrical simulation of the equivalent circuit presented in Figure 6.6 using the circuit element values listed in Table 6-I.

### 6.7.3 Comparison of Measured & Simulated Results

Figure 6.16 presents the comparison of filter response with proper termination using 590 $\Omega$  resistors and the unterminated case, i.e. measurement with simply using 50 $\Omega$  port impedance of the network analyzer, where solid lines indicate measurement results. This figure also presents comparison to theoretical results as shown with the dashed line curves obtained by SPICE simulation of the circuit presented in Figure 6.6 with circuit element values provided in the ‘simulated’ column of Table 6-I, which show very good agreement with the measured data. The factors contributing to the accuracy of the presented equivalent circuit in capturing measured behavior for both in-passband and out-of-passband regions are:

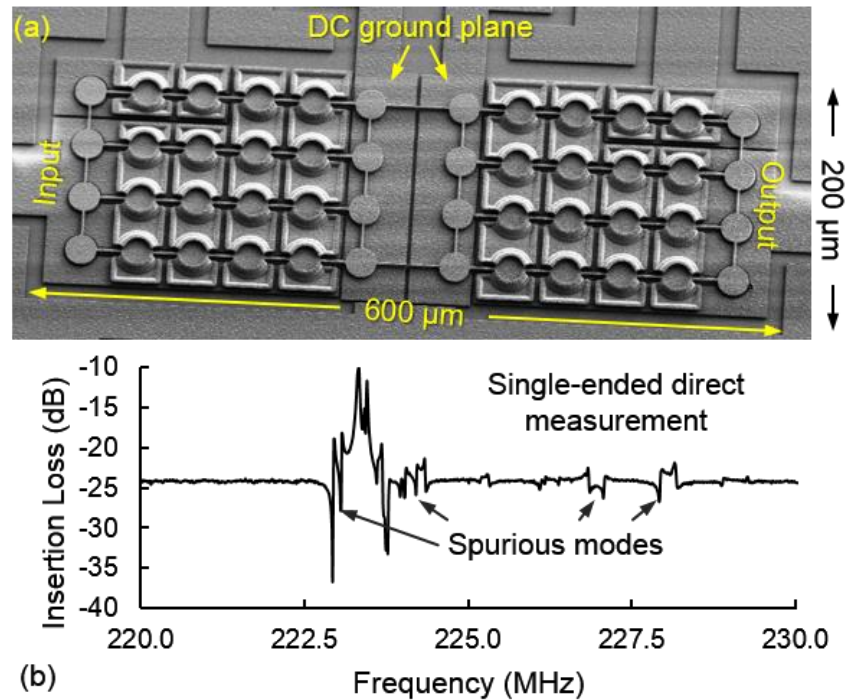


Figure 6.17: (a) SEM image and (b) measured  $590\Omega$  terminated frequency response of a single-ended version of the differential filter presented in Figure 6.10, emphasizing importance of differential design to suppress feedthrough and spurious modes.

- 1) Using the negative-capacitance model [9] for each electrical port that captures the electrical stiffness effects, and thus precise filter pole locations, properly for arbitrary port termination impedances.
- 2) Capturing the dominant feedthrough paths accurately as elaborated in Section 6.3.

#### 6.7.4 Measured Comparison of Differential & Single-Ended Filters

To verify the efficacy of a mechanically differential vibration mode shape engineered by  $\lambda$ -couplers in suppressing spurious modes and electrical feedthrough, the single ended version of the same filter design that does not use differential  $\lambda$ -couplers was also fabricated as presented in the SEM image of Figure 6.17(a). Lacking the electrical and mechanical symmetry and balance, this single ended version suffers greatly from feedthrough that limits its stop-band rejection to only 15dB as seen in the  $590\Omega$  terminated direct measurement result presented in Figure 6.17(b). The single ended network also suffers from numerous mechanical spurious modes that obstruct selective and controlled frequency selection capability of the filter.

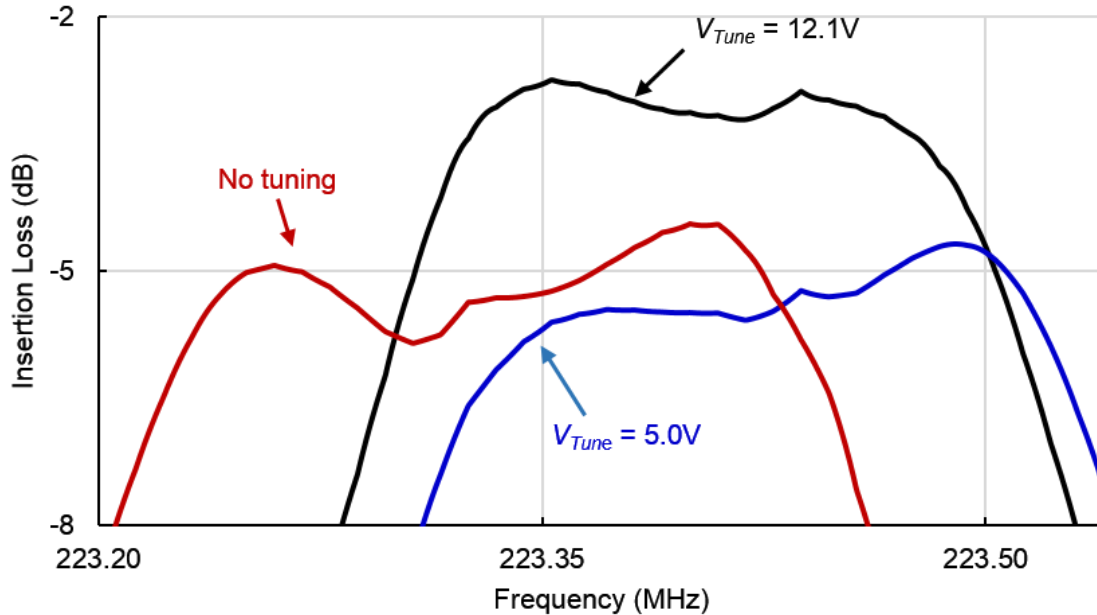


Figure 6.18: Measured comparison of terminated filter passband spectrum for varying tuning cases.

## 6.8 Electrical Stiffness Tuning Strategy

Post-fabrication electrical tuning was essential for successful implementation of the presented filter. Figure 6.18 emphasizes the importance of electrical tuning for this tiny percent bandwidth filter by demonstrating how proper tuning with 12.1V improves the passband shape and minimizes insertion loss compared to insufficient tuning with 5V and no tuning voltage applied cases. The optimum tuning voltage was determined empirically by varying  $V_{Tune}$  and simultaneously monitoring the resulting change in filter frequency response on a network analyzer, until symmetric passband ripple heights were observed around the filter center frequency, which is the expected equiripple passband shape of a Chebyshev filter. The tuning voltage that yields symmetrically positioned passband ripple peaks with equal height also achieves the minimum insertion loss as expected from the closer-to-ideal filter response. This observation is in-line with previous efforts on electrical tuning of kHz frequency capacitive comb-actuated filters [46][116], where positioning passband resonant peaks equidistant around the filter center frequency via electrical tuning minimized insertion loss and yielded the desired filter response. Automatic tuning techniques using intelligent transistor circuitry would certainly be beneficial in future filter implementations, not only as a low cost post-fabrication tuning method, but also for real-time adaptive compensation of frequency drift over time due to aging or temperature variations.

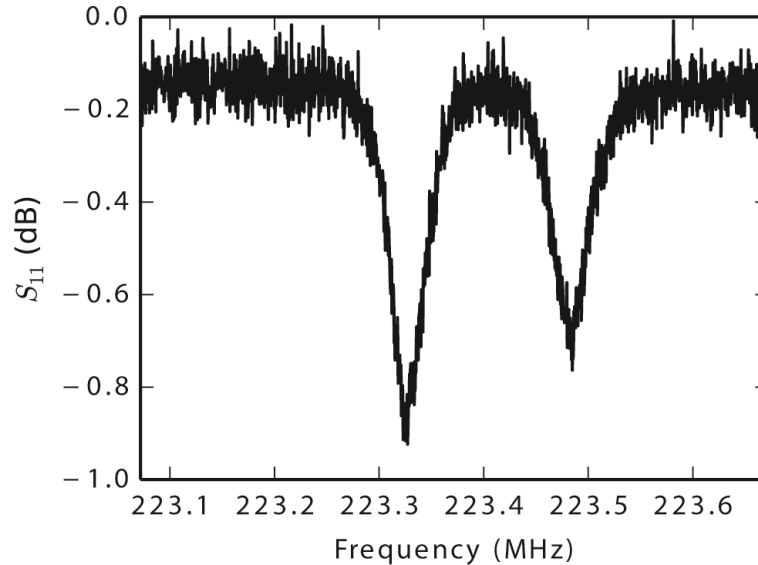


Figure 6.19: Measured return loss, i.e.  $S_{11}$ , data from the positive-input electrode of the differential filter under identical measurement conditions to those of Figure 6.13 with  $50\Omega$  termination.

## 6.9 Filter Power Handling Capability and Linearity

The results presented in Figure 6.13, Figure 6.14, and Figure 6.15 are measured with 0 dBm output power setting applied to all four ports of the network analyzer that corresponds to  $0.225 V_{rms}$  signal amplitude applied to the I/O electrodes of the filter. Since the device under test is not impedance matched to the  $50\Omega$  terminals of the network analyzer, a portion of the applied 0 dBm power will reflect back to the source as indicated by the return loss, i.e.  $S_{11}$ , data presented in Figure 6.19 obtained from the positive-input port of the filter with  $Z_o = 50\Omega$  termination. Here, the in-band return loss of 0.9 dB indicates that 81% of the 0 dBm, i.e. 1 mW, applied from the network analyzer port reflects back, and the actual power going through the filter network is  $190\mu\text{W}$ , i.e. -7.2 dBm, which is considerably above the GSM maximum in-band power specification of -26 dBm. As the zoomed-in inset that focuses on the filter passband presented in Figure 6.13 indicates, the filter does not suffer any distortion at -7.2 dBm drive power due to duffing non-linearity. Array-composite design improves the filter linearity with increasing array size, which is the key to achieve sufficient power handling in this study to avoid the pass-band distortion under strong drive that plagued previous capacitive filter implementations [31].

Figure 6.20 presents the simulated  $IIP_3$  of the second-order filter shown in Figure 6.10 as a function of the capacitive actuation gap spacing under the operating conditions listed in Table 6-I, assuming two equal amplitude tones placed at 200 kHz and 400 kHz offset from the filter center frequency.

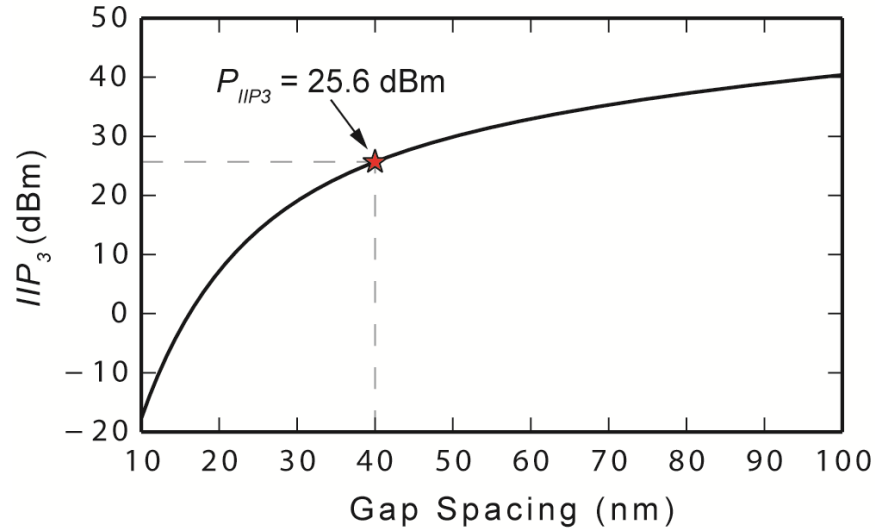


Figure 6.20: Simulated filter  $IIP_3$  for the 2<sup>nd</sup> order differential filter measured in this work calculated for  $V_p = 14$  V as a function of the capacitive actuation gap spacing. The labeled data point indicates the  $IIP_3$  for the gap spacing  $d_o = 40$  nm realized for the filter studied in this paper.

The  $IIP_3$  calculation formulates the nonlinear interactions between applied off-resonance electrical signals and the mechanical displacements they induce as elaborated in [56][118], and has proven very effective in predicting the  $IIP_3$  performance of various capacitive actuated multi-resonator systems, such as cc-beam resonators [118], contour-mode [65], and flexural-mode [119] vibrating disks with very good agreement to experimental data. As Figure 6.20 indicates, the 39 nm gap realized in this study attains an input referred  $IIP_3$  power of 25.6 dBm.

Off-chip passives and piezoelectrically actuated micro-resonators generally post  $IIP_3$ 's greater than 70 dBm [18], yet they lack the  $Q$ 's necessary for RF channel-selection. Can the capacitive actuated high- $Q$  passives that aim to eventually replace the conventional off-chip passives attain similar high  $IIP_3$  values, especially with tiny actuation gaps, e.g. 39 nm as in this work? The better question to ask, however, is “Do they need to?” The answer to the former question is most assuredly yes, as enabled by  $\lambda/2$  coupled array-composites that increase the  $IIP_3$  linearly proportional to the array size [56], where adjusting the array size allows satisfying virtually any desired linearity specification.

However, as elaborated in [65][12], relaxing the linearity of the RF, image-reject, and the IF filters in a superheterodyne GSM receiver, such as the one published in [120], from an  $IIP_3$  of 100 dBm to a mere 15 dBm reduces the cumulative  $IIP_3$  of the overall receiver by less than 0.1 dBm. The overall receiver linearity is dominated by elements placed towards the end of the receiver chain where the cumulative gain is much higher; therefore the linearity of the mixer, LNA, and the stopband rejection of the IF filter dominate the receiver linearity, as long as the  $IIP_3$  of the filters surpasses 15 dBm. This observation applies to more modern transceiver architectures, as well,

such as the direct-conversion receivers [5] that require a single filtering stage for reduced cost, where the  $IIP_3$  of the passive RF filter will have an even smaller effect on the receiver linearity. In summary, capacitive vibrating disk filters can provide more than sufficient linearity to meet the specifications of conventional and future transceiver architectures without facing the low  $Q$  challenge alternative resonator technologies face.

## 6.10 Conclusion

The combined 2.7dB passband insertion loss and 50dB stopband rejection of the demonstrated 206-element 0.09% bandwidth 223.4-MHz differential micromechanical disk filter represents a landmark for capacitive-gap transduced micromechanical resonator technology. This demonstration proves that the mere introduction of small gaps, on the order of 39 nm, goes a long way towards moving this technology from a research curiosity to practical performance specs commensurate with the needs of actual RF channel-selecting receiver front-ends. It also emphasizes the need for tuning and defensive stress-relieving structural design when percent bandwidths and gaps shrink, all demonstrated by the work herein.

Perhaps most encouraging is that the models presented in Chapter 5 of this study used to design the filter and predict its behavior seem to all be spot on. This means that predictions using these models foretelling 1-GHz filters with sub-200 $\Omega$  impedances enabled by 20nm-gaps might soon come true, bringing this technology ever closer to someday realizing the ultra-low power channel-selecting communication front-ends targeted for autonomous set-and-forget sensor networks [10]. Work towards these goals continues.

# Chapter 7

## CONCLUSIONS

---

---

This dissertation explored the degree to which capacitive-gap transduced micromechanical resonators can achieve the aforementioned RF channel-selecting filters. The thesis focused on four distinct methods that culminated in an actual experimentally demonstrated RF channel-select filter designed using the developed procedures and confirming theoretical predictions.

### 7.1 Achievements

The first method introduced in Chapter 2 explicitly models the electrical stiffness in a capacitive-gap transduced micromechanical resonator via a negative capacitance. The equivalent circuit of this chapter provides design insights that explain certain previously unexplained measured behavior, such as the reduction in efficacy of electrical stiffness when the resistances loading a resonator's input/output ports are large, which in turn led to incorrect experimental extraction of electrode-to-resonator gap spacings. This equivalent circuit provides more accurate methods for determining element values, where integration is employed to account for varying resonator mass and stiffness over a given electrode and where a single coupling coefficient models both electrical and mechanical aspects of a capacitive-gap transducer. These contributions make the described negative capacitance equivalent circuit a very useful tool for design of more complex micro-mechanical circuits demonstrated in this dissertation, as well future micromechanical RF channelizer designs that will follow up on this work.

The second method introduced in Chapter 3 improves the ALD-partial electrode-to-resonator gap filling technique and reduces the  $Q$ -limiting surface losses of previous renditions by adding an alumina pre-coating before ALD of the gap-filling high- $k$  dielectric, which increases the  $Q$  over the  $\sim 10,000$  of previous renditions by more than  $6\times$ . This work demonstrates the first VHF micro-mechanical resonators in any material, piezoelectric or not, to meet the simultaneous high  $Q$  ( $>50,000$ ) and low motional resistance ( $<200\Omega$ ) commonly desired in many RF and frequency



control applications. In doing so, it disproves to a large extent the common misconception that capacitively transduced resonators always exhibit high impedance.

The same ALD technique was also used to demonstrate substantial improvements in the far-from-carrier phase noise of oscillators referenced to stand-alone (as opposed to arrayed) capacitively transduced micromechanical disk resonators. The phase noise improvement is attained via the use of atomic layer deposition (ALD) to tune the electrode-to-resonator capacitive gaps. Specifically, ALD of about 30nm of Hafnia ( $\text{HfO}_2$ ) onto the surface of a released 60-MHz micromechanical disk resonator to reduce its effective resonator-to electrode gap size from 92nm to 32nm provides an increase in power handling leading to more than 15-20dB reduction in the far-from-carrier phase noise of an oscillator referenced to this resonator. This ALD-enabled nano-scale gap tuning provides a simple and effective method to satisfy increasing demands for higher short-term stability in frequency references for electronic applications.

The third method introduces a capacitively transduced micromechanical resonator constructed in hot filament CVD boron-doped microcrystalline diamond (MCD) structural material that posts a measured  $Q$  of 146,580 at 232.441 kHz, which is  $3\times$  higher than the previous high for conductive polydiamond. Moreover, radial-contour mode disk resonators fabricated in the same MCD film and using material mismatched stems exhibit a  $Q$  of 71,400 at 299.86 MHz, which is the highest series-resonant  $Q$  yet measured for any on-chip resonator at this frequency. The material used here further exhibits an acoustic velocity of 18,516 m/s, which is now the highest to date among available surface micromachinable materials. For many potential applications, the hot filament CVD method demonstrated in this work is quite enabling, since it provides a much less expensive method than microwave CVD based alternatives for depositing doped CVD diamond over large wafers (e.g., 8") for batch fabrication.

The final method presents a complete filter design hierarchy that achieves the desired filter response with a specific center frequency, bandwidth, and filter termination resistance. The design procedure culminates in specific values for all mechanical geometry variables necessary for the filter layout, such as disk radii, and beam widths; and process design variables such as resonator material thickness and capacitive actuation gap spacing.

Experimental results introduce a 39nm-gap capacitive transducer, voltage-controlled frequency tuning, and a stress relieving coupled array design that enable a 0.09% bandwidth 223.4 MHz channel-select filter with only 2.7dB of in-band insertion loss and 50dB rejection of out-of-band interferers. This amount of rejection is more than 23dB better than previous capacitive-gap transduced filter designs that did not benefit from sub-50nm gaps. It also comes in tandem with a 20dB shape factor of 2.7 realized by a hierarchical mechanical circuit design utilizing 206 micromechanical circuit elements, all contained in an area footprint of only  $600\mu\text{m}\times 420\mu\text{m}$ . The key to such low insertion loss for this tiny percent bandwidth is  $Q's > 8,800$  supplied by polysilicon disk resonators employing for the first time capacitive transducer gaps small enough to generate coupling strengths of  $C_x/C_o \sim 0.1\%$ , which is a  $6.1\times$  improvement over previous efforts. The filter

structure utilizes electrical tuning to correct frequency mismatches due to process variations, where a dc tuning voltage of 12.1 V improves the filter insertion loss by 1.8 dB and yields the desired equiripple passband shape. An electrical equivalent circuit is presented that captures not only the ideal filter response, but also parasitic non-idealities that create electrical feed-through, where simulation of the derived equivalent circuit matches measured filter spectrum closely both in-band and out-of-band.

The combined 2.7dB passband insertion loss and 50dB stopband rejection of the demonstrated 206-element 0.09% bandwidth 223.4-MHz differential micromechanical disk filter represents a landmark for capacitive-gap transduced micromechanical resonator technology. This demonstration proves that the mere introduction of small gaps, on the order of 39 nm, goes a long way towards moving this technology from a research curiosity to practical performance specs commensurate with the needs of actual RF channel-selecting receiver front-ends. It also emphasizes the need for tuning and defensive stress-relieving structural design when percent bandwidths and gaps shrink, all demonstrated by the work herein.

## 7.2 Future Research Directions

This dissertation identifies the following four aspects of RF channel-select filter design and treats each topic in detail:

1. Accurate electro-mechanical analogies that capture electrical spring softening and electrical tuning in an intuitive way.
2. Capacitive actuator gap scaling via partial ALD gap filling.
3. High  $Q$  – high acoustic velocity fabrication materials that can be deposited with low cost, high throughput methods.
4. A hierarchical mechanical circuit design reminiscent of transistor VLSI circuits that lends itself to SPICE simulations.

These design aspects will continue be important future micromechanical RF channelizer implementations. As a first step, a design that combines all these four techniques in one single device, i.e. a vibrating disk filter fabricated in polydiamond that benefits from  $\text{Al}_2\text{O}_3$ - $\text{TiO}_2$  ALD partial filled sub-20nm gaps, further augmented with electrical tuning to correct fabrication non-idealities can demonstrate a true RF channelizer operating at 1 GHz and beyond.

The true potential of this technology, however, expands far beyond this expectation. A strong advantage of the capacitive actuated vibrating disk filters is that lateral resonator layout dimensions, much like transistor circuit design, primarily determine the filter specification. As this dissertation elaborates, the filter design procedure follows a straightforward set of equations that directly correlate to a traditional ‘*filter spectral mask*’ specification, i.e. center frequency, stopband

rejection and roll-off rate, etc. This suggests that the design procedure can be fully CAD automated, where a program automatically calculates the optimum design metrics, such as disk array-composite sizes, number of tuning electrodes to cover all process corners, stress buffers for the expected film stress monitored from production data etc., and generates the filter layout with optimum area footprint.

The methods developed in this dissertation can also be combined with the recent very exciting techniques such as silicide induced gaps [70] to realize sub-20nm gaps. In addition, the recent developments in capacitive-piezoelectric  $Q$ -boosted high frequency resonators [111] that simultaneously achieve high  $Q$  and strong electromechanical coupling present exciting opportunities for RF channel-select filter bank designs.

In order to bring this technology ever closer to someday realizing the ultra-low power channel-selecting communication front-ends, and not just a research curiosity, we also need a solid approach to overcome fabrication induced non-idealities. The most important non-ideality is frequency mismatches among the multitude of individual resonators that constitute the filter. While this dissertation, as well as previous efforts [46][121], demonstrate successful filter passband tuning that corrects the frequency mismatches; the tuning approach is very empirical and is not amenable to mass production. Fortunately, recent studies [116] show promising results that may one day lead to computer automated post-fabrication tuning, or better yet on-chip CMOS integrated closed-loop feedback circuitry that continuously monitors the filter performance over aging and temperature drift.

Further design challenges, such as how to best handle the cumulative input capacitance of a bank of parallel-connected filters, will definitely arise as this technology matures towards practical implementation of advanced RF front-ends, such as on-chip spectrum analyzers or true cognitive radio with watch battery supplied power [81]. Nonetheless, this technology addresses the very fundamental low loss RF channel-selection design problem, which is achieving simultaneous high  $Q$  and sufficient electromechanical coupling. Considering the track record of the previous results demonstrated by the capacitive actuated vibrating disk resonators, and humbly adding the filter performance demonstrated by this dissertation; we can project that this technology is ever closer to someday realizing the ultra-low power channel-selecting communication front-ends targeted for autonomous set-and-forget sensor networks [10]. Work towards these goals continues.

## REFERENCES

---

- [1] K. S. Gilhousen, I. M. Jacobs, R. Padovani, A. J. Viterbi, J. LA Weaver, and C. E. Wheatley III, "On the capacity of a cellular CDMA system," *Veh. Technol. IEEE Trans. On*, vol. 40, no. 2, pp. 303–312, 1991.
- [2] D. Cabric, S. M. Mishra, and R. W. Brodersen, "Implementation issues in spectrum sensing for cognitive radios," in *Signals, systems and computers, 2004. Conference record of the thirty-eighth Asilomar conference on*, 2004, vol. 1, pp. 772–776.
- [3] European Telecommunications Standards Institute (ETSI), "Universal Mobile Telecommunications System (UMTS); User Equipment (UE) conformance specification; Part 1: Protocol conformance specification (3GPP TS 34.123-1 version 10.3.1 Release 10)." 2013.
- [4] E. H. Armstrong, "The super-heterodyne-its origin, development, and some recent improvements," *Radio Eng. Proc. Inst. Of*, vol. 12, no. 5, pp. 539–552, 1924.
- [5] A. A. Abidi, "Direct-conversion radio transceivers for digital communications," *Solid-State Circuits IEEE J. Of*, vol. 30, no. 12, pp. 1399–1410, 1995.
- [6] B. Razavi, *RF Microelectronics*, 2nd ed. New York: Prentice Hall, 2011.
- [7] R. C. Ruby, P. Bradley, Y. Oshmyansky, A. Chien, and J. D. Larson, "Thin film bulk wave acoustic resonators (FBAR) for wireless applications," in *2001 IEEE Ultrasonics Symposium. Proceedings. An International Symposium (Cat. No.01CH37263)*, Atlanta, GA, USA, pp. 813–821.
- [8] R. G. Kinsman, "A history of crystal filters," in *Frequency Control Symposium, 1998. Proceedings of the 1998 IEEE International*, 1998, pp. 563–570.
- [9] R. Ruby, P. Bradley, D. Clark, D. Feld, T. Jamneala, and K. Wang, "Acoustic FBAR for filters, duplexers and front end modules," in *Microwave Symposium Digest, 2004 IEEE MTT-S International*, 2004, vol. 2, pp. 931–934.
- [10] C.-C. Nguyen, "MEMS-based RF channel selection for true software-defined cognitive radio and low-power sensor communications," *Commun. Mag. IEEE*, vol. 51, no. 4, pp. 110–119, 2013.
- [11] A.-C. Wong and C. T.-C. Nguyen, "Micromechanical Mixer-Filters," *J. Microelectromechanical Syst.*, vol. 13, no. 1, pp. 100–112, Feb. 2004.
- [12] Y. Lin, "Low phase noise micromechanical reference oscillators for wireless communications," Ph.D. dissertation, University of Michigan, Ann Arbor, MI, USA, 2007.
- [13] A. A. Abidi, "The Path to the Software-Defined Radio Receiver," *IEEE J. Solid-State Circuits*, vol. 42, no. 5, pp. 954–966, May 2007.
- [14] J. Mitola, "The software radio architecture," *Commun. Mag. IEEE*, vol. 33, no. 5, pp. 26–38, 1995.

- [15] L. Kull, T. Toifl, M. Schmatz, P. A. Francese, C. Menolfi, M. Braendli, M. Kossel, T. Morf, T. Andersen, and Y. Leblebici, "A 35mW 8 b 8.8 GS/s SAR ADC with low-power capacitive reference buffers in 32nm Digital SOI CMOS," in *VLSI Circuits (VLSIC), 2013 Symposium on*, 2013, pp. C260–C261.
- [16] J. C. Rudell, J. A. Weldon, J.-J. Ou, L. Lin, and P. Gray, *An Integrated OSM/DECT Receiver: Design Specifications*. Citeseer, 1997.
- [17] T.-T. Yen, C.-M. Lin, Y.-J. Lai, D. Wittwer, M. A. Hopcroft, and A. P. Pisano, "Fine frequency selection techniques for aluminum nitride Lamb wave resonators," in *Frequency Control Symposium (FCS), 2010 IEEE International*, 2010, pp. 9–13.
- [18] C. Zuo, N. Sinha, M. B. Pisani, C. R. Perez, R. Mahameed, and G. Piazza, "Channel-Select RF MEMS Filters Based On Self-Coupled AlN Contour-Mode Piezoelectric Resonators," in *2007 IEEE Ultrasonics Symposium Proceedings*, New York, NY, USA, 2007, pp. 1156–1159.
- [19] B. Kim, R. H. Olsson, and K. E. Wojciechowski, "AlN Microresonator-Based Filters With Multiple Bandwidths at Low Intermediate Frequencies," *J. Microelectromechanical Syst.*, vol. 22, no. 4, pp. 949–961, Aug. 2013.
- [20] R. H. Olsson, C. M. Washburn, J. E. Stevens, M. R. Tuck, and C. D. Nordquist, "VHF and UHF mechanically coupled aluminum nitride MEMS filters," in *Frequency Control Symposium, 2008 IEEE International*, 2008, pp. 634–639.
- [21] D. Weinstein, H. Chandralalim, L. F. Cheow, and S. A. Bhave, "Dielectrically transduced single-ended to differential MEMS filter," in *Solid-State Circuits Conference, 2006. ISSCC 2006. Digest of Technical Papers. IEEE International*, 2006, pp. 1236–1243.
- [22] H. Chandralalim, D. Weinstein, L. F. Cheow, and S. A. Bhave, "High- $\kappa$  dielectrically transduced MEMS thickness shear mode resonators and tunable channel-select RF filters," *Sens. Actuators Phys.*, vol. 136, no. 2, pp. 527–539, May 2007.
- [23] S.-S. Li, Y.-W. Lin, Z. Ren, and C.-C. Nguyen, "An MSI micromechanical differential disk-array filter," in *Solid-State Sensors, Actuators and Microsystems Conference, 2007. TRANSDUCERS 2007. International*, 2007, pp. 307–311.
- [24] S.-S. Li, Y.-W. Lin, Z. Ren, and C.-C. Nguyen, "A micromechanical parallel-class disk-array filter," in *Frequency Control Symposium, 2007 Joint with the 21st European Frequency and Time Forum. IEEE International*, 2007, pp. 1356–1361.
- [25] A. S. Sedra and P. O. Brackett, *Filter Theory and Design: Active and Passive*. Beaverton, OR, USA: Matrix, 1978.
- [26] A. I. Zverev, *Handbook of filter synthesis*. New York: Wiley, 1967.
- [27] R. Johnson, *Mechanical filters in electronics*. Wiley, 1983.
- [28] M. Akgul, L. Wu, Z. Ren, and C. Nguyen, "A Negative Capacitance Equivalent Circuit Model for Parallel-Plate Capacitive-Gap Transduced Micromechanical Resonators," *IEEE Trans. UFFC*, vol. 61, no. 5, p. 849, May 2014.
- [29] M. Hikita, H. Kojima, T. Tabuchi, and Y. Kinoshita, "800-MHz high-performance SAW filter using new resonant configuration," *Microw. Theory Tech. IEEE Trans. On*, vol. 33, no. 6, pp. 510–518, 1985.
- [30] J. Wang, J. E. Butler, T. Feygelson, and C. T. . Nguyen, "1.51-GHz nanocrystalline diamond micromechanical disk resonator with material-mismatched isolating support," 2004, pp. 641–644.
- [31] F. D. Bannon, J. R. Clark, and C. T.-C. Nguyen, "High-Q HF microelectromechanical filters," *IEEE J. Solid-State Circuits*, vol. 35, no. 4, pp. 512–526, Apr. 2000.

- [32] W. T. Hsu and C. T. . Nguyen, "Stiffness-compensated temperature-insensitive micromechanical resonators," in *Micro Electro Mechanical Systems, 2002. The Fifteenth IEEE International Conference on*, 2002, pp. 731–734.
- [33] S. S. Li, Y. W. Lin, Z. Ren, and C. T. . Nguyen, "Self-switching vibrating micromechanical filter bank," in *Frequency Control Symposium and Exposition, 2005. Proceedings of the 2005 IEEE International*, 2006, p. 7.
- [34] L.-W. Hung, Z. A. Jacobson, Z. Ren, A. Javey, and C. T.-C. Nguyen, "Capacitive transducer strengthening via ALD-enabled partial-gap filling," in *Hilton Head*, 2008, vol. 8, pp. 208–211.
- [35] M. Akgul, B. Kim, Z. Ren, and C. T.-C. Nguyen, "Capacitively Transduced Micromechanical Resonators with Simultaneous Low Motional Resistance and  $Q > 70,000$ ," in *Tech. Digest, 2010 Solid-State Sensor, Actuator, and Microsystems Workshop*, Hilton Head, South Carolina, 2010, pp. 467–470.
- [36] G. Piazza, P. J. Stephanou, J. M. Porter, M. B. J. Wijesundara, and A. P. Pisano, "Low motional resistance ring-shaped contour-mode aluminum nitride piezoelectric micromechanical resonators for UHF applications," in *Micro Electro Mechanical Systems, 2005. MEMS 2005. 18th IEEE International Conference on*, 2005, pp. 20–23.
- [37] H. C. Nathanson, W. E. Newell, R. A. Wickstrom, and J. R. Davis Jr, "The resonant gate transistor," *Electron Devices IEEE Trans. On*, vol. 14, no. 3, pp. 117–133, 1967.
- [38] A. Partridge, J. K. Reynolds, B. W. Chui, E. M. Chow, A. M. Fitzgerald, L. Zhang, N. I. Maluf, and T. W. Kenny, "A high-performance planar piezoresistive accelerometer," *Microelectromechanical Syst. J. Of*, vol. 9, no. 1, pp. 58–66, 2000.
- [39] J. Bernstein, S. Cho, A. T. King, A. Kourepenis, P. Maciel, and M. Weinberg, "A micromachined comb-drive tuning fork rate gyroscope," in *Micro Electro Mechanical Systems, 1993, MEMS'93, Proceedings An Investigation of Micro Structures, Sensors, Actuators, Machines and Systems. IEEE.*, 1993, pp. 143–148.
- [40] N. Barbour and G. Schmidt, "Inertial sensor technology trends," *Sens. J. IEEE*, vol. 1, no. 4, pp. 332–339, 2001.
- [41] Y. Lin, W. C. Li, Z. Ren, and C. T. . Nguyen, "A Resonance Dynamical Approach to Faster, More Reliable Micromechanical Switches."
- [42] P. W. Tuinenga, *SPICE: A Guide to Circuit Simulation and Analysis Using PSpice*, 3rd ed. NJ: Prentice Hall, 1995.
- [43] Z. Hao, S. Pourkamali, and F. Ayazi, "VHF Single-Crystal Silicon Elliptic Bulk-Mode Capacitive Disk Resonators&#8212;Part I: Design and Modeling," *J. Microelectromechanical Syst.*, vol. 13, no. 6, pp. 1043–1053, Dec. 2004.
- [44] H. A. Tilmans, "Equivalent circuit representation of electromechanical transducers: I. Lumped-parameter systems," *J. Micromechanics Microengineering*, vol. 6, no. 1, p. 157, 1996.
- [45] Yu-Wei Lin, Seungbae Lee, Sheng-Shian Li, Yuan Xie, Zeying Ren, and C. T.-C. Nguyen, "Series-resonant VHF micromechanical resonator reference oscillators," *IEEE J. Solid-State Circuits*, vol. 39, no. 12, pp. 2477–2491, Dec. 2004.
- [46] K. Wang and C. T. . Nguyen, "High-order medium frequency micromechanical electronic filters," *Microelectromechanical Syst. J. Of*, vol. 8, no. 4, pp. 534–556, 1999.
- [47] J. Wang, Z. Ren, and C. Nguyen, "1.156-GHz self-aligned vibrating micromechanical disk resonator," *Ultrason. Ferroelectr. Freq. Control IEEE Trans. On*, vol. 51, no. 12, pp. 1607–1628, 2004.

- [48] M. Akgul and C. T.-C. Nguyen, "A passband-corrected high rejection channel-select micro-mechanical disk filter," in *Frequency Control Symposium (FCS), 2014 IEEE International*, 2014, pp. 1–6.
- [49] J. Wang, Y. Xie, and C.-C. Nguyen, "Frequency tolerance of RF micromechanical disk resonators in polysilicon and nanocrystalline diamond structural materials," in *Electron Devices Meeting, 2005. IEDM Technical Digest. IEEE International*, 2005, p. 4–pp.
- [50] M. Onoe, "Contour Vibrations of Isotropic Circular Plates," *J. Acoust. Soc. Am.*, vol. 28, no. 6, pp. 1158–1162, 1956.
- [51] M. Akgul, R. Schneider, Z. Ren, G. Chandler, V. Yeh, and C. T.-C. Nguyen, "Hot filament CVD conductive microcrystalline diamond for high Q, high acoustic velocity micromechanical resonators," in *Frequency Control and the European Frequency and Time Forum (FCS), 2011 Joint Conference of the IEEE International*, 2011, pp. 1–6.
- [52] B. Kim, M. Akgul, Y. Lin, W. C. Li, Z. Ren, and C. T. . Nguyen, "Acceleration sensitivity of small-gap capacitive micromechanical resonator oscillators," in *Frequency Control Symposium (FCS), 2010 IEEE International*, 2010, pp. 273–278.
- [53] S. Lee, M. U. Demirci, and C. T.-C. Nguyen, "A 10-MHz micromechanical resonator Pierce reference oscillator for communications," *Dig. Tech. Pap.*, pp. 10–14, 2001.
- [54] W.-L. Huang, Z. Ren, and C. T.-C. Nguyen, "Nickel vibrating micromechanical disk resonator with solid dielectric capacitive-transducer gap," in *International Frequency Control Symposium and Exposition, 2006 IEEE*, 2006, pp. 839–847.
- [55] D. Weinstein and S. A. Bhave, "Internal Dielectric Transduction in Bulk-Mode Resonators," *J. Microelectromechanical Syst.*, vol. 18, no. 6, pp. 1401–1408, Dec. 2009.
- [56] M. U. Demirci and C. T.-C. Nguyen, "Mechanically Corner-Coupled Square Microresonator Array for Reduced Series Motional Resistance," *J. Microelectromechanical Syst.*, vol. 15, no. 6, pp. 1419–1436, Dec. 2006.
- [57] L. Wu, M. Akgul, W.-C. Li, Y. Lin, Z. Ren, T. Rocheleau, and C. T.-C. Nguyen, "Micro-mechanical disk array for enhanced frequency stability against bias voltage fluctuations," in *European Frequency and Time Forum & International Frequency Control Symposium (EFTF/IFC), 2013 Joint*, 2013, pp. 547–550.
- [58] G. Piazza, "Integrated aluminum nitride piezoelectric microelectromechanical system for radio front ends," *J. Vac. Sci. Technol. Vac. Surf. Films*, vol. 27, no. 4, p. 776, 2009.
- [59] C. P. Yue and S. S. Wong, "On-chip spiral inductors with patterned ground shields for Si-based RF ICs," *Solid-State Circuits IEEE J. Of*, vol. 33, no. 5, pp. 743–752, 1998.
- [60] S.-S. Li, Y.-W. Lin, Y. Xie, Z. Ren, and C. T.-C. Nguyen, "Micromechanical 'hollow-disk' ring resonators," in *17th IEEE International Conference on Micro Electro Mechanical Systems. Maastricht MEMS 2004 Technical Digest*, Maastricht, Netherlands, pp. 821–824.
- [61] C. T.-C. Nguyen, "Integrated Micromechanical Radio Front-Ends," in *2008 International Symposium on VLSI Technology, Systems and Applications (VLSI-TSA)*, Hsinchu, Taiwan, 2008, pp. 3–4.
- [62] M. Akgul, Bongsang Kim, Li-Wen Hung, Yang Lin, Wei-Chang Li, Wen-Lung Huang, I. Gurin, A. Borna, and C. T.-C. Nguyen, "Oscillator far-from-carrier phase noise reduction via nano-scale gap tuning of micromechanical resonators," in *Solid-State Sensors, Actuators and Microsystems Conference, 2009. TRANSDUCERS 2009. International*, 2009, pp. 798–801.
- [63] "IEEE Standard on Piezoelectricity," *ANSIIEEE Std 176-1987*, p. 0\_1–, 1988.

- [64] Y. Lin, W.-C. Li, and C. T.-C. Nguyen, "A MEMS-based charge pump," in *VLSI Technology (VLSIT), 2013 Symposium on*, 2013, pp. T148–T149.
- [65] Y. W. Lin, S. S. Li, Z. Ren, and C. T. . Nguyen, "Third-order intermodulation distortion in capacitively-driven VHF micromechanical resonators," in *Proceedings of IEEE Int. Ultrasonics Sym.*, 2005, pp. 1592–1595.
- [66] G. Piazza, P. Stephanou, and A. Pisano, "One and two port piezoelectric higher order contour-mode MEMS resonators for mechanical signal processing," *Solid-State Electron.*, vol. 51, no. 11–12, pp. 1596–1608, Nov. 2007.
- [67] M. Rinaldi, C. Zuniga, and G. Piazza, "5-10 GHz AlN Contour-Mode Nanoelectromechanical Resonators," in *Micro Electro Mechanical Systems, 2009. MEMS 2009. IEEE 22nd International Conference on*, 2009, pp. 916–919.
- [68] C. Kampen, P. Evanschitzky, A. Burenkov, and J. Lorenz, "Lithography induced layout variations in 6-T SRAM cells," in *Simulation of Semiconductor Processes and Devices (SISPAD), 2010 International Conference on*, 2010, pp. 149–152.
- [69] T. J. Cheng and S. A. Bhawe, "High-Q, low impedance polysilicon resonators with 10 nm air gaps," in *Micro Electro Mechanical Systems (MEMS), 2010 IEEE 23rd International Conference on*, 2010, pp. 695–698.
- [70] L. W. Hung and T. C. . Clark, "Silicide-Based Release of High Aspect-Ratio Microstructures."
- [71] M. Leskelä and M. Ritala, "Atomic layer deposition (ALD): from precursors to thin film structures," *Thin Solid Films*, vol. 409, no. 1, pp. 138 – 146, 2002.
- [72] J. Robertson, "High dielectric constant oxides," *Eur. Phys. J. Appl. Phys.*, vol. 28, no. 3, pp. 265–291, Dec. 2004.
- [73] H.-E. Cheng, C.-M. Hsu, and Y.-C. Chen, "Substrate Materials and Deposition Temperature Dependent Growth Characteristics and Photocatalytic Properties of ALD TiO[sub 2] Films," *J. Electrochem. Soc.*, vol. 156, no. 8, p. D275, 2009.
- [74] A. C. Dillon, A. W. Ott, J. D. Way, and S. M. George, "Surface chemistry of Al<sub>2</sub>O<sub>3</sub> deposition using Al(CH<sub>3</sub>)<sub>3</sub> and H<sub>2</sub>O in a binary reaction sequence," *Surf. Sci.*, vol. 322, no. 1–3, pp. 230–242, Jan. 1995.
- [75] M. D. Groner, J. W. Elam, F. H. Fabreguette, and S. M. George, "Electrical characterization of thin Al<sub>2</sub>O<sub>3</sub> films grown by atomic layer deposition on silicon and various metal substrates," *Thin Solid Films*, vol. 413, no. 1–2, pp. 186–197, Jun. 2002.
- [76] M. A. Abdelmoneum, M. U. Demirci, and C.-C. Nguyen, "Stemless wine-glass-mode disk micromechanical resonators," in *Micro Electro Mechanical Systems, 2003. MEMS-03 Kyoto. IEEE The Sixteenth Annual International Conference on*, 2003, pp. 698–701.
- [77] Yu-Wei Lin, Sheng-Shian Li, Zeying Ren, and C. T.-C. Nguyen, "Low phase noise array-composite micromechanical wine-glass disk oscillator," in *IEEE International Electron Devices Meeting, 2005. IEDM Technical Digest.*, Tempe, Arizon, USA, pp. 278–281.
- [78] D. B. Leeson, "A simple model of feedback oscillator noise spectrum," *Proc. IEEE*, vol. 54, no. 2, pp. 329–330, Feb. 1966.
- [79] S. Lee and C. T. . Nguyen, "Mechanically-coupled micromechanical resonator arrays for improved phase noise," in *Frequency Control Symposium and Exposition, 2004. Proceedings of the 2004 IEEE International*, 2005, pp. 144–150.
- [80] Y. Xie, S.-S. Li, Y.-W. Lin, Z. Ren, and C. T.-C. Nguyen, "UHF micromechanical extensional wine-glass mode ring resonators," in *Electron Devices Meeting, 2003. IEDM '03 Technical Digest. IEEE International*, 2003, pp. 39.2.1–39.2.4.



- [81] C. Nguyen, "MEMS technology for timing and frequency control," *IEEE Trans. Ultrason. Ferroelectr. Freq. Control*, vol. 54, no. 2, pp. 251–270, 2007.
- [82] T. Mattila, J. Kiihamäki, T. Lamminmäki, O. Jaakkola, P. Rantakari, A. Oja, H. Seppä, H. Kattelus, and I. Tittonen, "A 12 MHz micromechanical bulk acoustic mode oscillator," *Sens. Actuators Phys.*, vol. 101, no. 1–2, pp. 1–9, Sep. 2002.
- [83] R. Tabrizian, M. Rais-Zadeh, and F. Ayazi, "Effect of phonon interactions on limiting the fQ product of micromechanical resonators," in *Solid-State Sensors, Actuators and Microsystems Conference, 2009. TRANSDUCERS 2009. International*, 2009, pp. 2131–2134.
- [84] V. B. Braginsky, V. P. Mitrofanov, and V. I. Panov, *Systems with Small Dissipation*. University Of Chicago Press, 1985.
- [85] T. L. Naing, T. Beyazoglu, L. Wu, M. Akgul, Z. Ren, T. O. Rocheleau, and C.-C. Nguyen, "2.97-GHz CVD diamond ring resonator with  $Q > 40,000$ ," in *Frequency Control Symposium (FCS), 2012 IEEE International*, 2012, pp. 1–6.
- [86] N. Sepulveda, D. M. Aslam, and J. P. Sullivan, "Polycrystalline Diamond RFMEMS Resonators with the Highest Quality Factors," in *Micro Electro Mechanical Systems, 2006. MEMS 2006 Istanbul. 19th IEEE International Conference on*, 2006, pp. 238–241.
- [87] S. Yugo, T. Kanai, T. Kimura, and T. Muto, "Generation of diamond nuclei by electric field in plasma chemical vapor deposition," *Appl. Phys. Lett.*, vol. 58, no. 10, p. 1036, 1991.
- [88] S. Matsumoto, Y. Sato, M. Tsutsumi, and N. Setaka, "Growth of diamond particles from methane-hydrogen gas," *J. Mater. Sci.*, vol. 17, no. 11, pp. 3106–3112, 1982.
- [89] R. Lifshitz and M. L. Roukes, "Thermoelastic damping in micro- and nanomechanical systems," *Phys Rev B*, vol. 61, no. 8, pp. 5600–5609, Feb. 2000.
- [90] K. Y. Yasumura, T. D. Stowe, E. M. Chow, T. Pfafman, T. W. Kenny, B. C. Stipe, and D. Rugar, "Quality factors in micron- and submicron-thick cantilevers," *Microelectromechanical Syst. J. Of*, vol. 9, no. 1, pp. 117–125, Mar. 2000.
- [91] Y.-H. Cho, A. P. Pisano, and R. T. Howe, "Viscous damping model for laterally oscillating microstructures," *Microelectromechanical Syst. J. Of*, vol. 3, no. 2, pp. 81–87, Jun. 1994.
- [92] M. Weinberg, R. Candler, S. Chandorkar, J. Varsanik, T. Kenny, and A. Duwel, "Energy loss in MEMS resonators and the impact on inertial and RF devices," in *Solid-State Sensors, Actuators and Microsystems Conference, 2009. Transducers 2009. International*, 2009, pp. 688–695.
- [93] S. A. Chandorkar, M. Agarwal, R. Melamud, R. N. Candler, K. E. Goodson, and T. W. Kenny, "Limits of quality factor in bulk-mode micromechanical resonators," in *Micro Electro Mechanical Systems, 2008. MEMS 2008. IEEE 21st International Conference on*, 2008, pp. 74–77.
- [94] B. P. Harrington and R. Abdolvand, "In-plane acoustic reflectors for reducing effective anchor loss in lateral–extensional MEMS resonators," *J. Micromechanics Microengineering*, vol. 21, no. 8, p. 085021, Aug. 2011.
- [95] Y. Hirose, S. Amanuma, and K. Komaki, "The synthesis of high-quality diamond in combustion flames," *J. Appl. Phys.*, vol. 68, no. 12, p. 6401, 1990.
- [96] S. W. Reeve, W. A. Weimer, and D. S. Dandy, "On the optimization of a dc arcjet diamond chemical vapor deposition reactor," *J. Mater. Res.*, vol. 11, no. 3, pp. 694–702, 1996.
- [97] W. C. Tang, T.-C. H. Nguyen, M. W. Judy, and R. T. Howe, "Electrostatic-comb drive of lateral polysilicon resonators," *Sens. Actuators Phys.*, vol. 21, no. 1–3, pp. 328–331, Feb. 1990.

- [98] M. P. Everson, "Studies of nucleation and growth morphology of boron-doped diamond microcrystals by scanning tunneling microscopy," *J. Vac. Sci. Technol. B Microelectron. Nanometer Struct.*, vol. 9, no. 3, p. 1570, May 1991.
- [99] J. E. Graebner, "Measurements of specific heat and mass density in CVD diamond," *Diam. Relat. Mater.*, vol. 5, no. 11, pp. 1366–1370, 1996.
- [100] J. E. Graebner, S. Jin, G. W. Kammlott, J. A. Herb, and C. F. Gardinier, "Unusually high thermal conductivity in diamond films," *Appl. Phys. Lett.*, vol. 60, no. 13, p. 1576, 1992.
- [101] J. R. Clark, W.-T. Hsu, M. A. Abdelmoneum, and C. T.-C. Nguyen, "High-Q UHF micro-mechanical radial-contour mode disk resonators," *J. Microelectromechanical Syst.*, vol. 14, no. 6, pp. 1298–1310, Dec. 2005.
- [102] J. Wang, Z. Ren, and C. T. . Nguyen, "Self-aligned 1.14-GHz vibrating radial-mode disk resonators," 2003, vol. 2.
- [103] Kun Wang, Ark-Chew Wong, and C. T.-C. Nguyen, "VHF free-free beam high-Q micro-mechanical resonators," *Microelectromechanical Syst. J. Of*, vol. 9, no. 3, pp. 347–360, 2000.
- [104] T.-T. Yen, A. P. Pisano, and C. T.-C. Nguyen, "High-Q capacitive-piezoelectric AlN Lamb wave resonators," in *Micro Electro Mechanical Systems (MEMS), 2013 IEEE 26th International Conference on*, 2013, pp. 114–117.
- [105] Y. A. Vlasov, X.-Z. Bo, J. C. Sturm, and D. J. Norris, "On-chip natural assembly of silicon photonic bandgap crystals," *Nature*, vol. 414, no. 6861, pp. 289–293, Nov. 2001.
- [106] A. Frangi, A. Bugada, M. Martello, and P. T. Savadkoochi, "Validation of PML-based models for the evaluation of anchor dissipation in MEMS resonators," *Eur. J. Mech. - ASolids*, vol. 37, no. 0, pp. 256 – 265, 2013.
- [107] S. Schmid and C. Hierold, "Damping mechanisms of single-clamped and prestressed double-clamped resonant polymer microbeams," *J. Appl. Phys.*, vol. 104, no. 9, p. -, 2008.
- [108] T. Koyama, D. S. Bindel, W. He, E. P. Quévy, S. Govindjee, J. W. Demmel, and R. T. Howe, "Simulation tools for damping in high frequency resonators," in *Sensors, 2005 IEEE*, 2005, p. 4–pp.
- [109] D. S. Bindel, E. Quevy, T. Koyama, S. Govindjee, J. W. Demmel, and R. T. Howe, "Anchor loss simulation in resonators," in *Micro Electro Mechanical Systems, 2005. MEMS 2005. 18th IEEE International Conference on*, 2005, pp. 133–136.
- [110] L. Wu, M. Akgul, Z. Ren, Y. Lin, W.-C. Li, and C.-C. Nguyen, "Hollow stems for higher micromechanical disk resonator quality factor," in *Ultrasonics Symposium (IUS), 2011 IEEE International*, 2011, pp. 1964–1967.
- [111] L.-W. Hung and C. T.-C. Nguyen, "Capacitive-piezoelectric AlN resonators with Q >12,000," in *Micro Electro Mechanical Systems (MEMS), 2011 IEEE 24th International Conference on*, 2011, pp. 173–176.
- [112] A. Bloch, "Electromechanical analogies and their use for the analysis of mechanical and electromechanical systems," *Electr. Eng. - Part Gen. J. Inst. Of*, vol. 92, no. 52, pp. 157–169, Apr. 1945.
- [113] D. Pozar, *Microwave Engineering*. Wiley, 1997.
- [114] C.-C. Nguyen, "Transceiver front-end architectures using vibrating micromechanical signal processors," in *Silicon Monolithic Integrated Circuits in RF Systems, 2001. Digest of Papers. 2001 Topical Meeting on*, 2001, pp. 23–32.

- [115] Y. Lin, W. C. Li, B. Kim, Y. W. Lin, Z. Ren, and C. T. . Nguyen, "Enhancement of micro-mechanical resonator manufacturing precision via mechanically-coupled arraying," in *Frequency Control Symposium, 2009 Joint with the 22nd European Frequency and Time forum. IEEE International*, 2009, pp. 58–63.
- [116] H. G. Barrow and C. T.-C. Nguyen, "A protocol for automated passband correction of high-order microelectromechanical filters," in *Frequency Control Symposium (FCS), 2014 IEEE International*, 2014, pp. 1–5.
- [117] C. C. Cheng, "Competitive halogenation of silicon surfaces in HBr/Cl<sub>2</sub> plasmas studied with x-ray photoelectron spectroscopy and in situ, real-time, pulsed laser-induced thermal desorption," *J. Vac. Sci. Technol. Vac. Surf. Films*, vol. 13, no. 4, p. 1970, Jul. 1995.
- [118] R. Navid, J. R. Clark, M. Demirci, and C. T. . Nguyen, "Micro Electro Mechanical Systems, 2001. MEMS 2001. The 14th IEEE International Conference on," 2001, pp. 228–231.
- [119] M. U. Demirci and C.-C. Nguyen, "Single-resonator fourth-order micromechanical disk filters," in *Micro Electro Mechanical Systems, 2005. MEMS 2005. 18th IEEE International Conference on*, 2005, pp. 207–210.
- [120] P. Orsatti, F. Piazza, and Q. Huang, "A 20-mA-receive, 55-mA-transmit, single-chip GSM transceiver in 0.25- $\mu\text{m}$  CMOS," *Solid-State Circuits IEEE J. Of*, vol. 34, no. 12, pp. 1869–1880, 1999.
- [121] M. A. Abdelmoneum, M. M. Demirci, S. S. Li, and C. T. . Nguyen, "Post-fabrication laser trimming of micromechanical filters," in *Electron Devices Meeting, 2004. IEDM Technical Digest. IEEE International*, 2004, pp. 39–42.

# APPENDIX A

## THICK-POLY INTERCONNECT FABRICATION

### PROCESS TRAVELER

---

---

1. Start with 10 blank Si wafers. Scribe wafers on the front, near right side of major flat
2. POCL3 dope only 2 wafers  
Tool: tystar13  
Recipe: 13POCL3A  
Temp: 1050°C  
Time: 02:00:00 + 01:00:00  
Note: Remove PSG after this step on these two wafers with msink8 5:1 BHF dip
3. Pre-furnace cleaning  
Tool: msink6, msink8  
Step: piranha clean  
Temp: 120°C
4. Isolation oxide deposition  
Tool: tystar12  
Recipe: 12SULTOA  
Temp: 450°C  
Time: 04:30:00  
Goal: 30,000Å
5. Isolation oxide densification  
Tool: tystar3  
Recipe: 3N2ANNLA  
Temp: 950°C  
Time: 00:30:00
6. Metrology: isolation oxide thickness  
Tool: Nanospec

Recipe: Program #1  
Result: \_\_\_\_\_(Å)

7. Standard UV resist coating – for PM marks  
Tool: svgcoat6  
Recipe: 1-2-1 (1.48 krpm spin speed)  
Temp: 130°C  
Note: Run three dummies first
8. Expose PM marks  
Tool: ASML  
Job: MAXFIELD\_DIE  
Field: PM layer  
Mask: COMBI reticle  
Energy: 18mJ
9. Develop PM marks  
Tool: svgdev6  
Recipe: 1-1-9  
Temp: 130°C  
Note: Run three dummies first
10. Hard bake resist  
Tool: uvbake  
Recipe: Program U
11. Etch PM marks into isolation oxide  
Tool: centura-mxp  
Recipe: MXP-OXSP-ETCH  
500W, 200mT, Ar:120, CF4:10, CHF3:50  
rate: 3,100A/min  
Time: 180 s  
Note: Inspect etched marks under microscope
12. Ash resist  
Tool: matrix  
Recipe: 400W  
Time: 150 s
13. Pre-furnace cleaning  
Tool: msink8, msink6  
Step: piranha clean  
Temp: 120°C
14. Isolation nitride deposition  
Tool: tystar17  
Recipe: LSNSTDA.017

100DCS, 25NH<sub>3</sub>, 140mTorr  
Temp: 835°C  
Time: 01:40:00  
Goal: 4,000Å

15. Thick poly interconnect deposition

Tool: tystar16  
Recipe: 10SUPLYA  
Temp: 615°C  
Time: 04:00:00  
Goal: 30,000Å  
Note: Add two 1,000Å oxide monitors

16. POCL<sub>3</sub> doping

Tool: tystar13  
Recipe: 13POCL3A  
Temp: 1050°C  
Time: 02:00:00 + 01:00:00  
Note: This serves as stress anneal as well

17. Clean PSG over poly

Tool: msink8  
Recipe: 5:1 BHF tank  
Time: 10 min

18. Metrology: Poly-1 thickness

Tool: Nanospec  
Recipe: Program #4  
Notes: Measure poly over 1,000Å oxide monitors  
Result: \_\_\_\_\_(Å)

19. Metrology: Poly-1 sheet resistance

Tool: resmap  
Notes: Measure poly over 1,000Å oxide monitors  
Result: \_\_\_\_\_(Ω/sq)

20. Standard UV resist coating – for Poly1

Tool: svgcoat6  
Recipe: 1-2-1 (1.48 krpm spin speed)  
Temp: 130°C  
Note: Run three dummies first

21. Expose interconnect

Tool: ASML  
Job: MAXFIELD\_DIE  
Field: Upper Right – layer 1  
Mask: ThickPlyRet1

Energy: 25mJ

Notes: Could try exposure matrix on dummy first

22. Develop resist

Tool: svgdev6

Recipe: 1-1-9

Temp: 130°C

Note: Run three dummies first

23. Descum

Tool: technics-c

Recipe: 50W, O<sub>2</sub> plasma

Time: 1 min

24. Hard bake resist

Tool: uvbake

Recipe: Program U

25. Etch thick poly

Tool: sts2

Recipe: DEEP SILICON 1

(Passivation: 7sec, 18mT, C<sub>4</sub>F<sub>8</sub>:80, Coil: 600W, Bias: 0W

Etch: 10sec, 35mT, SF<sub>6</sub>:130, O<sub>2</sub>:13, Coil:600W, Bias:20W)

Time: 42 cycles (17 sec per cycle)

26. Ash resist

Tool: matrix

Recipe: 400W

Time: 150 s

27. Pre-furnace cleaning

Tool: msink8, msink6

Step: piranha clean

Temp: 120°C

28. Planarization oxide deposition - HTO

Tool: tystar17

Recipe: HTOSTDA.017

Temp: 910°C

Time: 10:00:00

Goal: 35,000Å

29. CMP interconnect layer

Tool: cmp

Recipe: poly-on-oxide

Notes: CMP until all poly traces are exposed. Verify trace conductivity in probe station.

## 30. Cleaning after CMP

## Step-1

Tool: sinkcmp

Notes: QDR water rinse, 4 cycles. Follow with manual cleaning with sponge. Then the ultrasonic bath with 5% NH<sub>4</sub>OH in DI solution for 10 minutes.

## Step-2

Tool: misnk8

Notes: Piranha clean for 10 mins. Follow with QDR DI rinse. 5:1 BHF dip for 5 seconds, followed by QDR DI rinse. Then spin dry wafers.

## 31. SEM after CMP

Tool: LEO or FEI

Notes: Look for dishing, key holes, surface pitting, dried residue and other contamination.

## 32. Metrology: wafer bow

Tool: flexus

Note: High compressive stress expected from HTO thickness imbalance on the backside of the wafer after CMP

Result: \_\_\_\_\_(μm)

## 33. Etch backside oxide to correct wafer bow

Tool: sts-oxide

Recipe: Oxide etch (APS) no 1- 2  
(4mT, C<sub>4</sub>F<sub>8</sub>: 15, H<sub>2</sub>: 8, He: 174, RF: 1500W  
Bias: 350W, 0.3μm/min)

Time: 9min – check wafer bow in 3 min intervals

## 34. Metrology: wafer bow

Tool: flexus

Note: Accept if less than 15μm bow

Result: \_\_\_\_\_(μm)

## 35. Metrology: cmp'ed poly interconnect sheet res.

Tool: Wentworth probe station

Recipe: Use 4-pt probe test structure

Result: \_\_\_\_\_(Ω/sq)

## 36. Metrology: Feedthrough from just poly-1

Tool: Lakeshore probe station

Recipe: Use GSG probes, typical filter pads

Result: \_\_\_\_\_(dB)

## 37. Pre-furnace cleaning - for LSN wafers

Tool: msink8, msink6

Step: piranha clean

Temp: 120°C



38. Bottom sacrificial oxide deposition
  - Tool: tystar12
  - Recipe: 12SULTOA
  - Temp: 450°C
  - Time: 00:45:00
  - Goal: 5,000Å
  - Note: Add 2 blank Si monitor wafers
  
39. Bottom sacrificial oxide densification
  - Tool: tystar3
  - Recipe: 3N2ANNLA
  - Temp: 950°C
  - Time: 00:30:00
  
40. Metrology: Bottom sacrificial oxide thickness
  - Tool: Nanospec
  - Recipe: Program #1
  - Result: \_\_\_\_\_(Å)
  
41. Standard UV resist coating – for Stem
  - Tool: svgcoat6
  - Recipe: 1-2-1 (1.48 krpm spin speed)
  - Temp: 130°C
  - Note: Run three dummies first
  
42. Expose stem
  - Tool: ASML
  - Job: MAXFIELD\_DIE
  - Field: Upper Left – layer 2
  - Mask: ThickPlyRet1
  - Energy: 30mJ
  - Notes: Could try exposure matrix on dummy first
  
43. Develop resist
  - Tool: svgdev6
  - Recipe: 1-1-9
  - Temp: 130°C
  - Note: Run three dummies first
  
44. Descum
  - Tool: technics-c
  - Recipe: 50W, O<sub>2</sub> plasma
  - Time: 1 min
  
45. Hard bake resist
  - Tool: uvbake
  - Recipe: Program J

46. Etch stem holes in to oxide  
Tool: centura-mxp  
Recipe: MXP-OXSP-ETCH  
500W, 200mT, Ar:120, CF4:10, CHF3:50  
Rate: 3,100A/min  
Time: 180 s (includes 150% over etch)
47. Ash resist  
Tool: matrix  
Recipe: 400W  
Time: 150 s
48. Pre-furnace cleaning  
Tool: msink8, msink6  
Step: piranha clean  
Temp: 120°C
49. Wet HF dip before structural poly deposition  
Tool: msink6  
Step: 10:1 HF bath, right after piranha and QDR  
Time: 45 sec  
Note: Follow with standard QDR and spin dry, then go to poly furnace ASAP.
50. Structural poly deposition  
Tool: tystar10  
Recipe: 10SUPLYA  
Temp: 615°C  
Time: 04:00:00 – for 3um devices  
02:45:00 – for 2um devices  
Note: First run a dummy on 1000Å oxide test wafer with NO real wafers to determine the depositon rate and adjust the given times.  
Add two 1000Å test wafers with process wafers for etch tests.
51. POCL<sub>3</sub> doping  
Tool: tystar13  
Recipe: 13POCL3A  
Temp: 1050°C  
Time: 02:00:00 + 01:00:00  
Note: This serves as stress anneal as well
52. Clean PSG over poly  
Tool: msink8  
Recipe: 5:1 BHF tank  
Time: 10 min
53. Metrology: Poly-2 thickness  
Tool: Nanospec

Recipe: Program #4  
 Notes: Measure poly over 1,000Å oxide monitors  
 Result: \_\_\_\_\_(Å)

54. Metrology: Poly-2 sheet resistance

Tool: resmap  
 Notes: Measure poly over 1,000Å oxide monitors  
 Result: \_\_\_\_\_(Ω/sq)

55. Hard mask oxide deposition

Tool: tystar12  
 Recipe: 12SULTOA  
 Temp: 450°C  
 Time: 01:50:00  
 Goal: 12,000Å  
 Note: Add one blank Si monitor.

56. Hard mask oxide densification

Tool: tystar3  
 Recipe: 3N2ANNLA  
 Temp: 950°C  
 Time: 00:30:00

57. Metrology: hard mask oxide thickness

Tool: Nanospec  
 Recipe: Program #1  
 Result: \_\_\_\_\_(Å)

58. Standard UV resist coating – for Poly-2

Tool: svgcoat6  
 Recipe: 1-2-1 (1.48 krpm spin speed)  
 Temp: 130°C  
 Note: Run three dummies first

59. Expose Structural layer

Tool: ASML  
 Job: MAXFIELD\_DIE  
 Field: Lower Left – Field 3  
 Mask: ThickPlyRet1 reticle  
 Energy: 8mJ – or update as in note  
 Note: Run exposure matrix on dummy poly2+hard mask, pick the best energy

60. Develop Structural layer

Tool: svgdev6  
 Recipe: 1-1-9  
 Temp: 130°C  
 Note: Run three dummies first

61. Descum  
Tool: technics-c  
Recipe: 50W, O<sub>2</sub> plasma  
Time: 1 min
62. Hard bake resist  
Tool: uvbake  
Recipe: Program J
63. Etch Structure into oxide hard mask  
Tool: centura-mxp  
Recipe: MXP-OXSP-ETCH  
500W, 200mT, Ar:120, CF<sub>4</sub>:10, CHF<sub>3</sub>:50  
rate: 3,100A/min  
Time: 275 s (includes 20% over etch)  
Note: Etch conditioning dummies. SEM test wafer for hard mask on beams looking sharp and vertical before etching process wafers.
64. Ash resist  
Tool: matrix  
Recipe: 400W  
Time: 150 s
65. Etch Structure into Poly-2  
Tool: lam8  
Recipe: Custom recipe  
RF 250W, Bias 75W, 10mT, Cl<sub>2</sub>:14,  
HBr:140, O<sub>2</sub>:5  
rate: Obtain from test wafer  
Time: Obtain from test wafer  
Note: Monitor endpoint while etching. Etch test wafers and SEM them before etching process wafers.
66. Polymer removal after Lam8 etch  
Step 1  
Tool: msink18  
Recipe: EKC270, temperature: 70C, 10 minutes  
  
Step 2 (effective for HBr etches in literature)  
Tool: msink6  
Recipe: 20:1 HF bath  
Time: 45 sec
67. Etch backside oxide to correct wafer bow  
Tool: sts-oxide  
Recipe: Oxide etch (APS) no 1- 2

(4mT, C<sub>4</sub>F<sub>8</sub>: 15, H<sub>2</sub>: 8, He: 174, RF: 1500W, Bias: 350W, 0.3μm/min)  
 Time: 5min

68. Etch backside poly to correct wafer bow

Tool: sts2

Recipe: DEEP SILICON 1

(Passivation: 7sec, 18mT, C<sub>4</sub>F<sub>8</sub>:80, Coil: 600W, Bias: 0W

Etch: 10sec, 35mT, SF<sub>6</sub>:130, O<sub>2</sub>:13, Coil:600W, Bias: 20W)

Time: 32 cycles (17 sec per cycle)

69. Metrology: wafer bow

Tool: flexus

Note: Accept if less than 15μm bow

Result: \_\_\_\_\_(μm)

70. Clean wafers after backside etch

Tool: msink8, msink6

Step: piranha clean

Temp: 120°C

71. Sidewall Oxide Deposition – 50nm

Tool: tystar17

Recipe: HTOSTDA.017

Temp: 910°C

Time: Run monitor wafer, use past data for start

Goal: 5,00Å

72. Thick UV resist coating – for Anchor

Tool: svgcoat6

Recipe: 1-7-1 (1.00 krpm spin speed)

Temp: 140°C – IMPORTANT!

Note: Run three dummies first

73. Expose Anchor

Tool: ASML

Job: MAXFIELD\_DIE

Field: Lower Right – layer 4

Mask: ThickPlyRet1

Energy: 50mJ

Notes: Could try exposure matrix on dummy first

74. Develop resist

Tool: svgdev6

Recipe: 1-1-9

Temp: 110°C – IMPORTANT!

Note: Run three dummies first

75. Descum  
Tool: technics-c  
Recipe: 50W, O<sub>2</sub> plasma  
Time: 1 min
76. Hard bake resist  
Tool: 120°C oven  
Recipe: 12 hours bake
77. Etch anchor in to oxide  
Tool: centura-mxp  
Recipe: MXP-OXSP-ETCH  
500W, 200mT, Ar:120, CF<sub>4</sub>:10, CHF<sub>3</sub>:50  
rate: 3,100A/min  
Time: 180 s (includes 150% over etch)
78. Strip resist – wet sink  
Tool: msink1  
Recipe: PRS-3000 bath  
Time: 2 hours
79. Ash resist  
Tool: matrix  
Recipe: 400W  
Time: 150 s  
Note: This is precaution for residual resist and polymers.
80. Pre-furnace cleaning - for all (LSN & AlN) wafers  
Tool: msink8, msink6  
Step: piranha clean  
Temp: 120°C
81. Wet HF dip before electrode poly deposition  
Tool: msink6  
Step: 20:1 HF bath, right after piranha and QDR  
Time: 30 sec – be careful of the sidewall oxide!  
Note: Follow with standard QDR and spin dry, then go to poly furnace ASAP.
82. Electrode poly deposition  
Tool: tystar10  
Recipe: 10SUPLYA  
Temp: 615°C  
Time: 2:45:00 – for 2um  
Note: Add two 1000Å test wafers with process wafers for etch tests.

83. POCL<sub>3</sub> doping  
 Tool: tystar13  
 Recipe: 13POCL3A  
 Temp: 1050°C  
 Time: 02:00:00 + 01:00:00  
 Note: This serves as stress anneal as well
84. Clean PSG over poly  
 Tool: msink8  
 Recipe: 5:1 BHF tank  
 Time: 10 min
85. Metrology: Poly-3 thickness  
 Tool: Nanospec  
 Recipe: Program #4  
 Notes: Measure poly over 1,000Å oxide monitors  
 Result: \_\_\_\_\_(Å)
86. Metrology: Poly-3 sheet resistance  
 Tool: resmap  
 Notes: Measure poly over 1,000Å oxide monitors  
 Result: \_\_\_\_\_(Ω/sq)
87. CMP Electrode layer – on 8 wafers  
 Tool: cmp  
 Recipe: Poly-on-oxide  
 Notes: CMP until all poly traces are exposed. Verify trace conductivity in probe station.
- Cleaning after CMP  
 Step-1  
 Tool: sinkcmp  
 Notes: QDR water rinse, 4 cycles. Follow with manual cleaning with sponge. Then the ultrasonic bath with 5% NH<sub>4</sub>OH in DI solution for 10 minutes.
88. FOR ELECTRODE CMP WAFERS: Standard UV resist coating – for Poly-3  
 Tool: svgcoat6  
 Recipe: 1-2-1 (1.48 krpm spin speed)  
 Temp: 130°C  
 Note: Run three dummies first
89. FOR ELECTRODE CMP WAFERS: Expose electrode  
 Tool: ASML  
 Job: MAXFIELD\_DIE  
 Field: Upper Right – layer 1  
 Mask: ThickPlyRet2  
 Energy: 25mJ  
 Notes: Could try exposure matrix on dummy first

## 90. FOR NO ELECTRODE CMP WAFERS: Thick UV resist coating – for Electrode

Tool: svgcoat6

Recipe: 1-7-1 (1.00 krpm spin speed)

Temp: 140°C – IMPORTANT!

Note: Run three dummies first

## 91. Expose electrode

Tool: ASML

Job: MAXFIELD\_DIE

Field: Upper Right – layer 1

Mask: ThickPlyRet2

Energy: 55mJ

Notes: Could try exposure matrix on dummy first

## 92. Develop resist

Tool: svgdev6

Recipe: 1-1-9

Temp: 110°C – IMPORTANT!

Note: Run three dummies first

## 93. Descum

Tool: technics-c

Recipe: 50W, O<sub>2</sub> plasma

Time: 1 min

## 94. Hard bake resist

Tool: 120°C oven

Recipe: 12 hours bake

## 95. Etch Poly3

Tool: sts2

Recipe: DEEP SILICON 1

(Passivation: 7sec, 18mT, C4F8:80, Coil: 600W, Bias: 0W

Etch: 10sec, 35mT, SF6:130, O2:13, Coil:600W, Bias: 20W)

Time: 48 cycles (17 sec per cycle)

Note: Watch for stringers

## 96. Dice Wafers

## 97. RUN COMPLETE